

Doctoral thesis

Doctoral theses at NTNU, 2023:296

Tancredi Salamone

Proximity effects in nanostructures with geometric curvature for superconducting spintronics

NTNU
Norwegian University of Science and Technology
Thesis for the Degree of
Philosophiae Doctor
Faculty of Natural Sciences
Department of Physics



Norwegian University of
Science and Technology

Tancredi Salamone

Proximity effects in nanostructures with geometric curvature for superconducting spintronics

Thesis for the Degree of Philosophiae Doctor

Trondheim, September 2023

Norwegian University of Science and Technology
Faculty of Natural Sciences
Department of Physics



Norwegian University of
Science and Technology

NTNU

Norwegian University of Science and Technology

Thesis for the Degree of Philosophiae Doctor

Faculty of Natural Sciences

Department of Physics

© Tancredi Salamone

ISBN 978-82-326-7292-9 (printed ver.)

ISBN 978-82-326-7291-2 (electronic ver.)

ISSN 1503-8181 (printed ver.)

ISSN 2703-8084 (online ver.)

Doctoral theses at NTNU, 2023:296

Printed by NTNU Grafisk senter

Abstract

In this thesis we consider hybrid structures of superconductors and geometrically curved magnetic materials. In these structures the proximity effect induces superconducting correlations in the magnetic material and we study how these correlations are influenced by geometric curvature and magnetic properties. We have conducted theoretical and numerical investigations in order to unveil new properties and effects for applications in the field of superconducting spintronics. The findings of our research are reported in the 3 publications enclosed to this thesis. In Paper I, we show that geometric curvature induces long-range supercurrents and a tunable $0 - \pi$ transition in Josephson junctions with curved ferromagnetic weak links. In Paper II, we demonstrate how geometric curvature produces a superconducting spin-valve effect in hybrid structures of superconductors and curved ferromagnets. In Paper III, we present a mechanism producing superconductivity in high magnetic field in multiband superconductors. In the main text of the thesis we present the basic instruments and theories, as well as the main results obtained for the realization of the enclosed publications. We also report original work, currently being prepared for publication, on non-equilibrium dynamics, and on ferromagnetic and antiferromagnetic helices proximity coupled to superconductors.

Preface

This thesis is submitted in partial fulfilment of the requirements for the degree of philosophiae doctor at the Norwegian University of Science and Technology (NTNU). The research presented in this thesis and the enclosed papers [1–3] was conducted as part of a three-year graduate programme in physics. It also included 30 ECTS credits of coursework. My research has been supervised by Dr. Sol H. Jacobsen, with Professor Jacob Linder as co-supervisor.

This research was funded via the “Outstanding Academic Fellows” programme at NTNU, the Research Council of Norway Grant No. 302315, as well as through its Centres of Excellence funding scheme, Project No. 262633, “QuSpin.”. Most of the computations carried out during the research have been performed on the SAGA supercomputer provided by UNINETT Sigma2 - the National Infrastructure for High Performance Computing and Data Storage in Norway.

Acknowledgements

First of all I am extremely grateful to my supervisor Sol H. Jacobsen for allowing me to work on this exciting project. Moving to Norway for my PhD was not an easy decision in the first place, but thanks to your support and guidance, as well as your kindness, I was able to overcome this challenge and grow as a researcher. Thank you for sharing your passion with me, I enjoyed the three years we worked together very much and I am sure I could not have had a better supervisor.

I would like to thank Morten Amundsen and Henning G. Hugdal for all the helpful and interesting discussions we had in our weekly meeting together with Sol. I had the opportunity to learn a lot in those meetings and it has been a great pleasure collaborating with you. I would also like to thank Mathias B. M. Svendsen, Alv Skarpeid and Magnus S. Skjærpe, who I had the chance to collaborate with during and after their Master at NTNU. Many thanks for being such nice persons and office mates to Frode S. Strand, who I hope is still cooking pasta all'amatriciana with guanciale, Håkon Ivarssønn Røst, and Verena J. Brehm, who I also want to thank together with her boyfriend Max Haas for the many invites for very nice dinners and board game evenings at their place. I also want to thank all the people at QuSpin, especially Eirik Erlandsen and Karen-Elisabeth Sødahl for helping me when I first moved here, all those I had the pleasure to go together at the APS March Meeting 2023 in Las Vegas: Lina Johnsen Kamra, Jonas Lidal, Kristian Mæland, Jeroen Danon and Bjørnulf Brekke, who I also thank for the nice interesting conversations on superconducting diode problems, Niels Henrik Aase and Asle Sudbø for checking the free energy in the multiband superconductivity project, Matthias Hartl, Christian S. Johnsen, Vemund Falch, and all the people I had nice conversations with during our breaks.

I also wish to thank my family, who despite the physical distance were always able to show me their love and support. A big thank goes also to my friends back in Italy for being there every time I was back in Italy as well as remotely. Speaking of friends, I should not forget to mention my flatmates, who I spent a lot of time with either at home or around Norway and without whom I would not have enjoyed my time here as much as I did. Finally, I must also thank all the new friends I met here

in Trondheim, with a special mention to my climbing friends.

Publications

1. Tancredi Salamone, Mathias B. M. Svendsen, Morten Amundsen, and Sol Jacobsen,
Curvature-induced long-range supercurrents in diffusive superconductor-ferromagnet-superconductor Josephson junctions with a dynamic $0 - \pi$ transition.
Physical Review B **104**, L060505 (2021). (Letter)
2. Tancredi Salamone, Henning G. Hugdal, Morten Amundsen, and Sol H. Jacobsen,
Curvature control of the superconducting proximity effect in diffusive ferromagnetic nanowires.
Physical Review B **105**, 134511 (2022).
3. Tancredi Salamone, Henning G. Hugdal, Sol H. Jacobsen, and Morten Amundsen,
High magnetic field superconductivity in a two-band superconductor.
Physical Review B **107**, 174516 (2023).

Contents

Units and Notations	xv
1 Introduction	1
1.1 Spintronics	1
1.2 Ferromagnetism	3
1.3 Antiferromagnetism	4
1.4 Superconductivity	6
1.4.1 Symmetry of the Superconducting Order Parameter	8
1.5 Superconducting Spintronics	9
1.5.1 Proximity Effects and Role of Spin-Orbit Coupling	10
2 Superconductivity	13
2.1 Macroscopic Theory of Superconductivity	13
2.1.1 London Equations	13
2.1.2 Ginzburg-Landau Theory	14
2.1.3 Flux Quantization	16
2.1.4 Type I and Type II Superconductors	16
2.2 Microscopic (BCS) Theory of Superconductivity	17
2.2.1 Cooper Pairs	18
2.2.2 The Attractive Interaction	18
2.2.3 BCS Theory in the Green's Function Formalism	19
2.3 High Magnetic Field Superconductivity in a Two-band Superconductor	24
2.3.1 Brief Overview on Multiband Superconductors	25
2.3.2 Pauli-Chandrasekhar-Clogston Limit	26
2.3.3 Hamiltonian for a two-band superconductor	26
2.3.4 Green's function of the system	28
2.3.5 Gap equation for the interband order parameter	29
2.3.6 Gap equation for the intraband order parameters	31

2.3.7	Linearized gap equation for coupled interband and intra-band order parameters	32
2.3.8	Results for a Two-Band Superconductor	32
3	Fabrication Techniques for Curved Nanostructures	39
3.1	Standard Fabrication Techniques	39
3.2	Lithography Techniques	40
3.3	Glancing Angle Deposition	42
3.4	Focused Electron Beam Induced Deposition	43
4	Curvature-Induced Effects and Theory of Curved Nanostructures	45
4.1	Theoretical Framework for Curved Nanostructures	45
4.1.1	Frenet-Serret frame	45
4.1.2	Curvature Induced Spin-Orbit Coupling	49
4.2	Curvature-Induced Effects	50
4.2.1	Non-magnetic Systems	50
4.2.2	Micromagnetic Theory for Ferromagnetic Systems	51
4.2.3	Antiferromagnetic Systems	54
5	Diffusive Theory of Superconductivity	57
5.1	Usadel Equation	57
5.1.1	Green's function in the Keldysh formalism	57
5.1.2	Quasiclassical Approximation	59
5.1.3	The Dirty Limit	60
5.1.4	Boundary Conditions	62
5.1.5	Riccati Parametrization	63
5.1.6	Weak Proximity Effect	64
5.2	Observables	65
5.2.1	Density of States	65
5.2.2	Proximity-Induced Magnetization	66
5.2.3	Charge Current Density	67
5.2.4	Spin Current Density	68
5.3	Diffusion Equation in Curved Systems	68
5.3.1	Covariant Hamiltonian for Curved Geometries	69
5.3.2	Effective Hamiltonian for Curved Nanowire	69
5.3.3	Usadel equation for curved nanowires	70
5.3.4	Riccati parametrization	72
5.3.5	Weak proximity effect equations	73
5.3.6	Diffusion Equation in Nonequilibrium	75

6	Curvature Effects in Superconductor-Ferromagnet Hybrid Structures	79
6.1	Diffusive SFS Josephson Junctions with Curved Ferromagnetic Weak Link	79
6.1.1	Diffusive equations	80
6.1.2	Dynamic $0 - \pi$ transition and long-ranged currents	81
6.2	Diffusive SF hybrid nanowires with curvature	85
6.2.1	Diffusive Equations and Weak Proximity Effect	86
6.2.2	Triplet spin-valve effect controlled by curvature	88
6.3	Diffusive SFS Josephson Junctions with Ferromagnetic Helix	92
6.3.1	Current-Phase Relation	93
6.3.2	Magnetization	94
6.3.3	Spin Current	95
6.4	Non Equilibrium Spin Currents in Diffusive NFS hybrid structure with curved ferromagnet	97
7	Curvature Effects in Superconductor-Antiferromagnet Hybrid Structures	101
7.1	Diffusive Theory of Curved Antiferromagnetic Metals	101
7.1.1	Tight Binding Hamiltonian	102
7.1.2	Usadel Equation	104
7.1.3	Boundary Conditions	105
7.2	Usadel Equation for Curved Antiferromagnets	106
7.2.1	Riccati Parametrization	106
7.2.2	Weak Proximity Effect	107
7.3	Diffusive Superconducting-Antiferromagnetic Helix Hybrid Nanowire	109
7.3.1	Density of States	109
7.3.2	Magnetization	111
8	Outlook	113
	References	117
	Publications	145

Units and Notations

In this thesis we will use SI units. In some occasions and only when specified, we will set the reduced Planck's constant and Boltzmann's constant to unity, $\hbar = 1$, $k_B = 1$.

We will follow the conventional notations used in literature, with scalars identified by symbols in italic and vectors in bold italic. Unit vectors in Cartesian coordinates are identified by \hat{e}_x , \hat{e}_y and \hat{e}_z .

We will often deal with equations involving matrices of different dimensions. No special notation for 2×2 matrices has been introduced, when present their nature will be specified in the text. Matrices with higher rank are identified with a specific notation, \hat{M} represents a 4×4 matrix, and \check{M} represents a 8×8 matrix. We will also consider vectors with matrix components, such as the Pauli vector $\boldsymbol{\sigma} = \sigma_x \hat{e}_x + \sigma_y \hat{e}_y + \sigma_z \hat{e}_z$, with the 2×2 Pauli matrices

$$\sigma_x = \begin{pmatrix} 0 & 1 \\ 1 & 0 \end{pmatrix}, \quad \sigma_y = \begin{pmatrix} 0 & -i \\ i & 0 \end{pmatrix}, \quad \sigma_z = \begin{pmatrix} 1 & 0 \\ 0 & -1 \end{pmatrix}.$$

When considering superconductivity we will often refer to a 4×4 space, a combination of spin and particle-hole spaces. Matrices in this space will be represented through the basis matrices $\hat{\tau}_0$, being the 4×4 identity matrix, $\hat{\tau}_1$, $\hat{\tau}_2$, and $\hat{\tau}_3$, corresponding to the Kronecker product of the Pauli matrices in spin space and the identity matrix in electron-hole space.

We will often consider curvilinear orthonormal coordinates, where covariant basis vectors are represented by \mathbf{e}_α and unit basis vectors by \hat{e}_α , with the index $\alpha = \{T, N, B\}$ identifying the tangential, normal and binormal components. The geometry of the space in a general curved structure will be described through the three orthonormal unit vectors $\hat{\mathcal{T}}$, $\hat{\mathcal{N}}$ and $\hat{\mathcal{B}}$, representing tangential, normal and binormal directions. These three unit vectors will be used to define the Pauli vector in the curved framework having components $\sigma_{T,N,B} = \boldsymbol{\sigma} \cdot \{\hat{\mathcal{T}}, \hat{\mathcal{N}}, \hat{\mathcal{B}}\}$.

Chapter 1

Introduction

Throughout this work we will study the effects arising when a superconductor (S) is coupled with curvilinear ferromagnets (Fs) and antiferromagnets (AFs). We will present the theoretical tools needed to investigate heterostructures formed by these two categories of materials. We will then perform numerical simulations for different types of hybrid nanostructures and show the appearance of interesting phenomena. These phenomena can open new possibilities for the design of novel devices for superconducting spintronics applications.

In this introductory chapter, we will first give a brief summary of the field of spintronics and its applications. We will then introduce ferromagnets and antiferromagnets, two classes of materials often used in spintronics devices. We will conclude with an introduction to superconductivity and how it can be exploited for new spintronics applications through the field of superconducting spintronics.

1.1 Spintronics

Spintronics is a relatively young field which uses the *spin* of solid-state systems instead of or in conjunction with the electric charge to transport information, similarly to what is done in electronics with the transport of charge alone.

The word spin refers to the intrinsic angular momentum of particles, which behave as if they were spinning around their own axis. Considering electrons, their spin when measured can be in one of two states, identified as *spin-up* and *spin-down*, with respect to a certain axis, associated with clockwise and counter-clockwise rotation, respectively. The spin s of an electron can be detected through its associated magnetic moment $\boldsymbol{\mu}_s \simeq -(e\hbar/m_e)\mathbf{s}$, where e is the electron charge, m_e its mass and \hbar is the reduced Planck's constant. Typical materials where the electron spin plays a crucial role are called *ferromagnets*. In these materials, like iron, the majority of the spins are aligned in the same direction as a result of

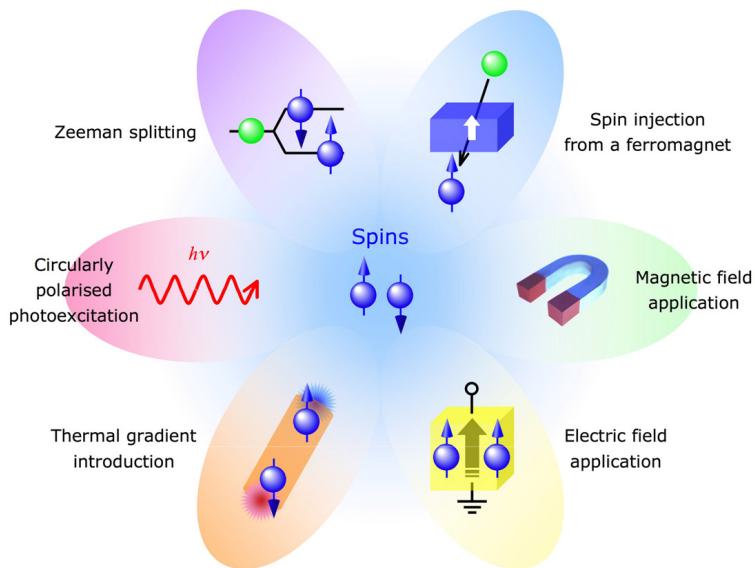


Figure 1.1: Methods used for the generation of spin-polarized electrons. Reproduced with permission from [4] Copyright 2014, IOP Publishing.

the *exchange interaction*, a quantum mechanical consequence of the Coulomb interaction and the Pauli exclusion principle. An important class of ferromagnets is that of half metals, materials conducting only electrons with a certain spin orientation.

In spintronics, one studies how the spin of electrons interact with their surroundings in solid-state materials to create devices with reduced power consumption and increased memory capacity, compared to traditional electronics devices. An important aspect, for the realization of spintronics devices, is the generation of spin-polarized electrons, which can be done in different ways [4]: spin injection from a ferromagnet, application of magnetic or electric fields, Zeeman splitting, circularly polarized photoexcitation, or introduction of a thermal gradient (see Fig. 1.1). A typical example is spin injection in a normal metal from a ferromagnetic material through ohmic contacts or tunneling barriers. Other relevant mechanisms are represented by spin relaxation and spin dephasing, affecting for how long the system retains a certain spin orientation. The time scales of these processes need to be large enough so that the electrons can travel a sufficient distant to be detected before their spin decays.

The first examples of spintronics related effects are tunneling magnetoresistance (TMR) [5] and giant magnetoresistance (GMR) [6, 7], which have both been used for the realization of hard disk drives (HDD) for data storage. TMR is observed in

trilayers, consisting of two ferromagnets separated by an insulating barrier, and the effect consists in different tunneling of electrons when the magnetizations of the two ferromagnets are parallel or antiparallel. Similarly, GMR is observed in devices where two ferromagnets are separated by a metallic barrier. In both cases, a measure of the efficiency of devices is given by the magnetoresistance ratio, corresponding to the resistance change between antiparallel and parallel configurations relative to the resistance of the parallel configuration. After its first observation below 4.2K in 1975 [5], TMR was achieved at room temperature with magnetoresistance ratios slightly above 10% in 1995 [8, 9]. Since then higher ratios have been achieved, up to 70% [10], $\sim 220\%$ [11] in 2004, and an impressive 604% [12] in 2008. GMR was discovered in 1988, later than TMR, with a resistance change of $\sim 50\%$ at 4.2K [6, 7]. However, GMR was observed earlier than TMR at room temperature, with a magnetoresistance ratio of 65% in 1991 [13], and therefore was the first of the two to be used in HDDs. Given the better performance of TMR devices, HDDs later moved from GMR to TMR, with an increase in capacity of almost four times in the last decade [14]. Moreover, TMR is used for the realization of magnetoresistive random access memory (MRAM) devices, using magnetization to store data [15].

1.2 Ferromagnetism

Ferromagnetism refers to the characteristic of some materials, such as iron, cobalt and nickel, to have a spontaneous magnetization even in the absence of an external magnetic field, below a certain temperature known as the Curie Temperature. Above the Curie temperature, a paramagnetic state is realized. In these materials, the majority of magnetic moments of atoms or molecules are aligned in the same direction¹. As stated in the previous section, this alignment is generally a consequence of Coulomb repulsion between electrons in combination with the exchange interaction, a quantum mechanical effect arising from the Pauli exclusion principle. When two electrons are on the same atom the exchange energy generally favors a triplet state, *i.e.* electrons with parallel spin, consistently with Hund's rules². On the contrary, when the two electrons sit on two different atoms, the exchange energy will favor the singlet state.

In ferromagnetic materials the exchange interaction lowers the energy of the configuration where the spins of electrons are aligned. Consequently, this interaction

¹In most ferromagnets this is not true throughout the whole sample. Typical ferromagnetic materials consists of multiple macroscopic domains with a spontaneous magnetizations, with the magnetization of each domain pointing in a different direction. Ferromagnets in which the conduction electrons have all the same spin direction are named half-metals.

²Hund's rules are those followed by electrons when filling atomic orbitals. They state that electrons singly occupy orbitals at the same level with aligned spins before doubly occupying any orbital.

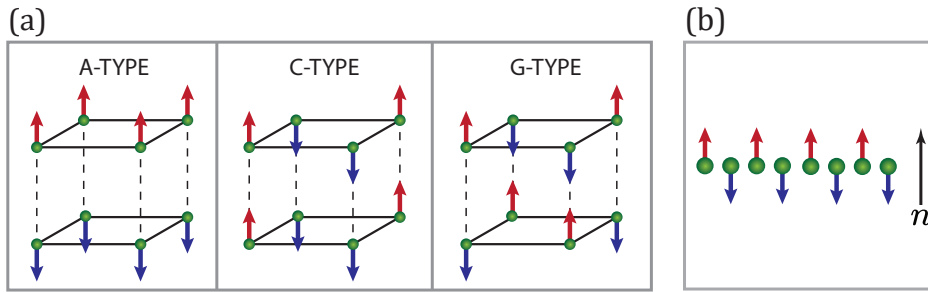


Figure 1.2: (a) A-, C- and G-type orderings on a cubic lattice. (b) Orientation of the Néel vector n (black arrow) in a AF chain.

gives rise to an effective magnetic field, the *exchange field*, experienced by an electron due to the surroundings. The strength of the exchange field is determined by the strength of the exchange interaction and spins align with its direction. We will later use the exchange field to describe ferromagnets in the diffusive theory.

Ferromagnetic materials are widely used in conventional and superconducting spintronics. Their importance in the context of superconducting spintronics lies in the proximity effect, which occurs when a superconductor is placed in contact with another normal material. Due to the proximity effect, the superconducting properties are partly transferred in the adjacent material. In a superconducting-ferromagnetic hybrid structure, the superconductivity inside the ferromagnet acquires interesting properties, which we will describe later in this introduction. At the same time an inverse proximity effect is observed, a magnetization is induced in the superconductor causing the superconductivity in the superconductor to be slightly suppressed. We will deal more specifically with the proximity effect later in this thesis.

1.3 Antiferromagnetism

Contrary to ferromagnetism, antiferromagnetism identifies materials where neighbouring magnetic moments tend to align antiparallel to each other. Therefore, antiferromagnets exhibit a net zero magnetization, despite the presence of local individual magnetic moments. Similarly to ferromagnetism, this phenomenon arises from the exchange interaction, which owing to specific material properties, can favor antiparallel configurations. In general, antiferromagnetism is realized at temperatures below the Néel temperature, while for higher temperatures paramagnetism occurs.

There are different types of antiferromagnetic ordering in multilayered structures, the three most common types are depicted in Fig. 1.2(a). An A-type AF occurs for ferromagnetic intraplanar coupling and antiferromagnetic interplanar

coupling, B-type for antiferromagnetic intraplanar coupling and ferromagnetic interplanar coupling, C-type for both intraplanar and interplanar antiferromagnetic coupling.

Often antiferromagnetism occurs in systems which can be separated into two distinct sublattices. In each of the two sublattices the magnetic moments point all in the same direction, and opposite to the other sublattice. This allows to define the total magnetizations of the two sublattices, whose sum gives the total magnetization in the AF, equal to zero, and whose difference is a quantity named the *Néel vector*, the antiferromagnetic order parameter. An important instrument in describing AFs, the Néel vector identifies the direction along which the magnetic moments of the two sublattices are antiparallel, as depicted in Fig. 1.2(b) with a black arrow.

Unlike for ferromagnets, the inclusion of AFs in the context of spintronics happened only recently³. Owing to their stability in magnetic fields, absence of stray fields and ultrafast dynamics, AFs could eventually substitute ferromagnets in spintronics devices and potentially revolutionise the field. The first applications of AFs in spintronics came in magnetic recording devices, exploiting the interface coupling between ferromagnets and AFs. Other early applications came with antiferromagnetic spin valves and tunnel junctions, where spin transfer torque is used to control the AF order parameter [19, 20]. The spin transfer torque could allow the switching of the Néel vector, providing the writing operation in AF-based MRAMs. Various experiments successfully achieved manipulation of the AF order parameter in spintronics devices [21–24].

Recently, much attention has been placed in the control of the interfacial spin ordering, rather than the bulk. For instance, control of interfacial spins has been achieved in antiferromagnetic-ferromagnetic-heavy metal heterostructures [25–27]. Depending on the AF type, the ordering at the interface of AFs can be defined as *compensated*, *i.e.* antiferromagnetic ordering parallel to the interface, or *uncompensated*, *i.e.* ferromagnetic ordering, achieved by an interface, *e.g.* along the plane of an A-type, or a diagonal cut along C- or G-types, see Fig. 1.2(a). In this context, theoretical studies have focused on the role of the interface ordering in antiferromagnetic-superconducting heterostructures [28–34]. For instance, Ref.[28] studied the influence of the uncompensated and compensated ordering on the bound states formed at the interface between an antiferromagnet and a superconductor. Moreover, in Ref.[33] it was shown that through a compensated interface it is possible to control the superconducting critical temperature in an AF-S-F heterostructure.

Moreover, the ultrafast dynamics in AFs could enable information processing and storage in the terahertz-frequency regime. For instance, a terahertz writing speed has been reported in an antiferromagnetic memory device [35], and ultrafast

³For reviews on antiferromagnetic spintronics, see[16–18].

terahertz radiation has been used to drive spin-lattice coupling in the AF CoF₂ [36]. Furthermore, it has been shown that ultrafast spin-lattice coupling induces emission of terahertz coherent magnons, *i.e.* collective excitations of the spin structure, in bilayers made of the AF insulator NiO and Pt [37].

1.4 Superconductivity

The phenomenon of superconductivity was first discovered in 1911 by H. K. Onnes [38], with observation of zero direct current resistance in mercury when cooled down below a certain critical temperature. A vanishing electrical resistance, or perfect conductivity is the first defining characteristic of superconductivity. The second fundamental feature is perfect diamagnetism, *i.e.* the expulsion of magnetic fields from the interior of a material, known as the Meissner effect [39]. The first phenomenological theory of superconductivity was developed in 1935 by the Londons [40], describing the two fundamental electrodynamic properties [41]. However, for decades, scientists failed in formulating a full theory of superconductivity, until in 1957 Bardeen, Cooper and Schrieffer [42], developed a microscopic theory, known as BCS theory. In this theory, they showed that even a weak attractive interaction can produce bound pairs of electrons, known as Cooper pairs, with equal and opposite spins and momenta, which can be loosely identified as the superconducting charge carriers. The BCS theory well describes the so-called conventional superconductors, a category comprising materials which are metallic at room temperatures, such as Hg, Pb, and Nb, with typically low critical temperature, the highest at atmospheric pressure being 39K for MgB₂ [43].

For a long time, all the superconductors discovered well agreed with the BCS theory. Nowadays these compounds are named conventional superconductors, while superconductors which do not follow the BCS theory are labeled as unconventional superconductors.

Another breakthrough in the field was the discovery in 1987 of superconductivity up to 40K in a La-Ba-Cu-O compound [45]. This was then followed by the discovery of superconductivity in many other cuprate compounds, with the highest critical temperature of 138K achieved in HgBa₂Ca₂Cu₃O_{8+ δ} at ambient pressure [46] and 164K at 45GPa [47]. These high critical temperatures are the reason why cuprates are defined as high temperature superconductors. Another family of superconductors belonging to this category is that of iron-based superconductors, with the highest critical temperature achieved for FeSe thin films grown on doped SrTiO₃ above 100K [48]. Both cuprates and iron-based superconductors are unconventional superconductors. Other unconventional superconductors include heavy-fermion compounds, such as UPt₃, strontium ruthenate Sr₂RuO₄, carbon-based and nickel-based superconductors. Different families of superconductors are

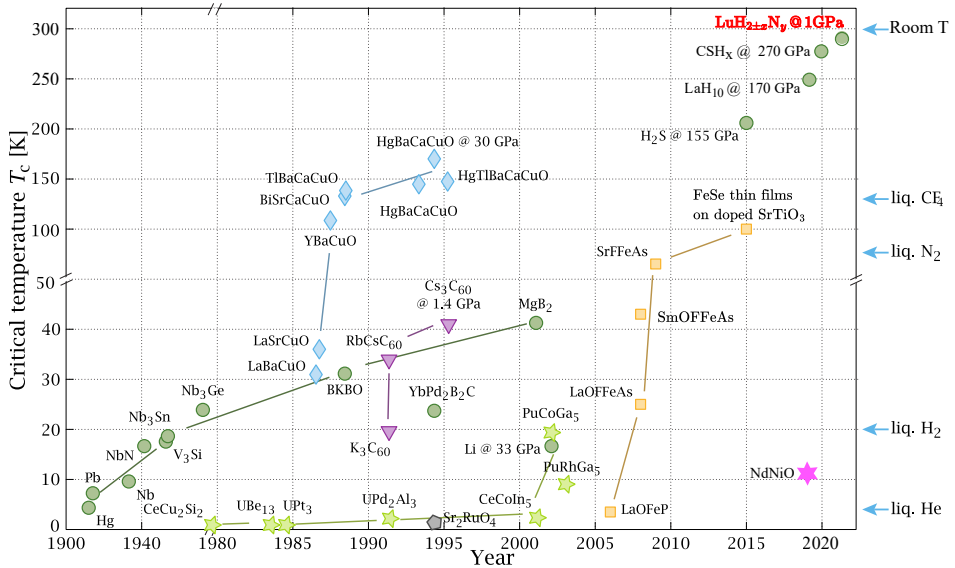


Figure 1.3: Historic timeline of discovered superconductors, with different symbols identifying different categories, green circles for conventional superconductors, blue diamonds for cuprates, orange squares for iron based superconductors, green stars for heavy fermion superconductors, purple triangles for carbon-based superconductors, grey pentagon for strontium ruthenate, six-point pink star for nickel-based superconductor. For reference we added in red the recent highly disputed hydride compound from Ref.[44]. Adapted from P. J. Ray/CC BY-SA 4.0/Wikimedia.

reported in Fig. 1.3, with the date of their discovery and their critical temperature.

An important goal in the research of new superconductors is achieving room temperature superconductivity. Critical temperatures close to room temperature have been achieved at extremely high pressures first in sulfur hydride, with a T_c of 203K at 155GPa [49], and later in lanthanum hydride, with $T_c = 250$ K at 270GPa [50]. Earlier this year, room temperature superconductivity at near-ambient pressure has been reported in a N-doped lutetium hydride, with a critical temperature of 294K at 1GPa [44]. However, this study is the object of great debate about irregularities and scientific misconduct, given the recent retraction by Nature of a previous similar study on the observation of room temperature superconductivity in a carbonaceous sulfur hydride. The reason for the retraction is the use of a “non-standard, user-defined procedure” of noise subtraction applied to raw data used to generate the magnetic susceptibility plots. It must also be noted that a more recent study performed on the same material as the one used in Ref.[44], was not able to reproduce near-ambient superconductivity [51]. Therefore, the claim of an achievement of superconductivity at ambient conditions must be taken with extreme caution.

One of the most common applications of superconductors is that of superconducting electromagnets, for the generation of high magnetic fields through superconducting coils. Despite having to be cooled down to cryogenic temperatures, superconducting electromagnets are energetically more efficient than their non-superconducting counterpart, since they can support much larger currents without any energy dissipation and generate higher magnetic fields. For this reason they are commonly used in nuclear magnetic resonance and magnetic resonance imaging machines, in magnetic confinement fusion reactors, in particle accelerators and in magnetic levitation trains. In 2019 scientists at the US National High Magnetic Field Laboratory (NHMFL) were able to generate a magnetic field of 45.5T through a cuprate superconductor [52]. This is currently the highest magnetic field intensity reached for a static magnetic field. Higher intensities, of the kilotesla order, can be achieved without superconductors, but with pulsed magnetic fields [53].

Superconductors are also used to realize devices known as Josephson junctions. In their most basic version they consist of two superconductors coupled via a weak link, which can be a material or a physical constriction. Owing to the superconducting properties, a direct supercurrent can flow in this device without any applied voltage, this is known as the DC Josephson effect. If a DC voltage is applied instead, an alternating current flows through the device, realizing the AC Josephson effect. Josephson junctions are used to realize *superconducting quantum interference devices* (SQUIDs), which are extremely sensitive devices for magnetic field measurements, and in superconducting qubits for quantum computing applications.

1.4.1 Symmetry of the Superconducting Order Parameter

As stated above, superconductivity is characterized by bound pairs of electrons. Therefore, the superconducting order parameter is identified as a two-fermion correlation function, which must obey Fermi statistics, *i.e.* the order parameter must be antisymmetric. This imposes restriction on the nature of the superconducting correlations. For instance, in most superconductors electron pairs are bound together in a spin-singlet state, which is antisymmetric, meaning that the orbital part must be symmetric, or even under parity. Therefore, for a spin-singlet state, the spatial or momentum symmetry of the order parameter must be *s-wave*, as in conventional BCS superconductors, or *d-wave*, as in cuprates, and so on. Conversely, if the Cooper pairs are in a spin-triplet state, the orbital part needs to be antisymmetric, with spatial symmetry being *p-wave*, *f-wave*, and so on.

The states mentioned so far refer to equal time pairing, since the time coordinate is often not taken into account, as in the BCS theory. However, considering the

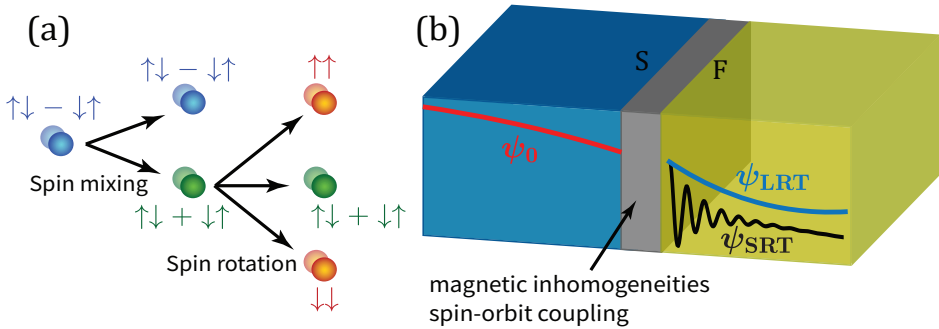


Figure 1.4: Singlet to triplet conversion, (a) conversion from singlet to long-range triplets through spin mixing and spin rotation, (b) proximity effect between a superconductor and a ferromagnet: the presence of magnetic inhomogeneities or spin-orbit coupling provides long-range triplet generation. Based on figure in [55].

possibility for electrons to pair at different times, provides an additional symmetry of the order parameter. For even in time pairing the above discussion remains valid. The situation is different when superconducting correlations are odd in time or frequency. This state is known as odd-frequency pairing and opens the possibility for s-wave triplet or p-wave singlet states. This pairing can occur in superconducting heterostructures such as those considered in this thesis and has recently become of interest for the field of superconducting spintronics, given its robustness against magnetic fields and impurity scattering⁴.

1.5 Superconducting Spintronics

As we discussed above, spintronics has the potential to realize more efficient nanodevices, while superconductivity provides dissipationless charge transport. Therefore, the combination of spintronics and superconductivity in the field of superconducting spintronics [55, 56], provides further advances in the realization of new energy efficient, high-performance devices, since it permits all the operations typical of conventional spintronics with the advantage of no heat loss by virtue of the dissipationless currents provided by superconductors.

Generally, superconductivity and ferromagnetism are two competing phases, since typically superconductivity is characterized by Cooper pairs in a singlet state, *i.e.* electrons with opposite spins, while ferromagnetism tends to align the spins, making superconducting pairing energetically unfavourable. However, a solution to this problem is provided by the superconducting proximity effect. This process occurs when a superconductor is put in contact with another non-superconducting

⁴For a review on odd-frequency pairing see [54].

material, resulting in the superconducting correlations leaking into the other material and electrons into the superconductor.

1.5.1 Proximity Effects and Role of Spin-Orbit Coupling

The proximity effect is the reason why hybrid structures of superconductors and ferromagnets are of particular importance in superconducting spintronics [57–59]. In diffusive heterostructures, covering a broad range of commonly available materials which may have impurities or suboptimal interface transparencies, conventional superconducting s-wave correlations typically penetrate only a short distance into a ferromagnet, proportional to $\sqrt{D_F/\hbar}$, where D_F is the diffusion constant and \hbar the magnitude of the exchange field of the ferromagnet.

At the SF interface, singlet correlations are also converted into the so-called short-range triplet (SRT) correlations, carrying no net spin projection along the quantization axis and decaying with the same length scale of the singlet correlations, but this time with an oscillatory behavior. However, it was demonstrated that equal spin triplet correlations can be generated by means of magnetic inhomogeneities [60, 61], *i.e.* non constant magnetization orientation, through the processes of spin mixing and spin rotation [55, 56, 62], see Fig. 1.4. This conversion occurs as follows. In the spin mixing process, when a Cooper pair enters the interface with a ferromagnet, the wave function acquires a spin dependent phase shift, due to the spin-splitting field of the ferromagnet. The resulting wave function is a combination of spin-singlet and spin-triplet with no net spin, or SRT, contributions. The presence of an additional spin-splitting field aligned along a different axis provides a new quantization axis with respect to which the SRT state is a combination of equal-spin pairs, with up and down spin. The spin rotation process thus causes the different spin-triplet components to transform into each other. These correlations, not being affected by any pair-breaking due to the exchange field, penetrate for longer distances in the ferromagnet of order $\sqrt{D_F/T}$, where T is the temperature, and are therefore named long-range triplet (LRT) correlations.

Magnetic inhomogeneities can be achieved through multiple misaligned magnetic layers [63], or rotating exchange textures such as those present in Holmium [64]. In 2006, came the first experimental observation of LRT correlations, through the measurement of a triplet supercurrent in a Josephson Junction with the half-metallic ferromagnet CrO_2 as weak link [65]. However, this observation was not supported by a clear conversion mechanism. More robust observations, cementing the understanding of the role of magnetic inhomogeneities, came in 2010, with the two separate observations of long-range supercurrents in Josephson junctions containing magnetic multilayers [63], and holmium [64]. Since then many other experimental observations with different setups followed [63, 64, 66–71], showing

the promising potential of superconducting spintronics and its applications.

Other than through magnetic inhomogeneities, it is possible to achieve LRT conversion with the presence of spin-orbit coupling (SOC) [72, 73]. SOC corresponds to the interaction of a particle momentum with its spin, originating when electrons move in an electric field \mathbf{E} . In its rest frame, an electron moving with momentum \mathbf{p} experiences an effective magnetic field $\mathbf{B}_{\text{eff}} \sim \mathbf{p} \times \mathbf{E}$. The energy of the electrons in this magnetic field is given by the Zeeman coupling $\mu_B \boldsymbol{\sigma} \cdot \mathbf{B}_{\text{eff}}$, leading to a spin-orbit coupling $H_{SO} \sim \mu_B \mathbf{E} \cdot (\mathbf{p} \times \boldsymbol{\sigma})$. In solids, SOC originates when the crystal structure lacks inversion symmetry, and can be of the Dresselhaus [74] or Rashba [75] type. Dresselhaus coupling occurs in systems lacking an inversion center, and in a 2D electron-gas confined along the \hat{z} direction it has the following form:

$$H_D = \frac{\beta}{\hbar} (p_y \sigma_y - p_x \sigma_x), \quad (1.1)$$

where β is the Dresselhaus coupling constant. In a 2D electron gas where the inversion symmetry is broken along the \hat{z} direction, either due to the crystal structure itself or due to interface with other materials, Rashba SOC can be written as:

$$H_R = \frac{\alpha}{\hbar} (\mathbf{p} \times \boldsymbol{\sigma}) \cdot \hat{z}, \quad (1.2)$$

where α is the Rashba coupling constant. Being derived for 2D electron gases, these two forms of SOC are useful approximations for thin film heterostructures.

Through its effect on the triplet correlations, SOC produces many interesting effects. In general the interplay between SOC and exchange interaction in superconducting ferromagnetic hybrid structure, induces a strong coupling between charge, spin and superconducting phase, *e.g.* allowing for control of the magnetoelectric effect in Josephson junctions [76] and the magnetoresistance in thin metal films [77]. Furthermore it was recently shown that this control can be exploited to realize a Josephson phase-battery [78]. The study of SF bilayers, showed that presence of SOC in the F provides control of the critical temperature of the hybrid structure [79, 80], realizing the so-called superconducting spin-valve effect. Moreover, it was shown that SOC allows to generate spin-polarized supercurrents in SFS Josephson junctions [81] and to obtain a giant proximity effect in a π -biased SFS junction, in contrast with the suppression in absence of SOC [82]. Investigations of a hybrid SF nanowire with intrinsic SOC and applied voltage bias, showed that SOC facilitates the tuning of the magnetization [83].

In this thesis we will show that geometric curvature allows for geometric control of magnetic textures and SOC, and can represent an alternative for achieving long-range supercurrents, as shown in Paper I [1], or superconducting spin-valve effect, as shown in Paper II [2].

Chapter 2

Superconductivity

In this chapter we will first give an overview of the first successful theories of conventional superconductivity¹. We will start by discussing the first phenomenological theory of superconductivity provided by the Londons [40] and then show how this theory is incorporated in the Ginzburg-Landau theory of superconductivity, describing superconductors at the macroscopic level. We will then present the BCS or microscopic theory of superconductivity. We will conclude by demonstrating a new mechanism allowing for superconductivity at high magnetic fields.

2.1 Macroscopic Theory of Superconductivity

For years after the discovery of superconductivity, a microscopic understanding of this phenomenon had been missing. Nonetheless, scientists successfully described superconductors by formulating macroscopic and phenomenological theories, which we will introduce in the following.

2.1.1 London Equations

The London equations provided the first description of the two basic electrodynamic properties of superconductors. The two equations proposed by the Londons in 1935 [40] govern the microscopic electric field \mathbf{E} and microscopic magnetic field \mathbf{h} , and they can be written as:

$$\frac{\partial \mathbf{j}_s}{\partial t} = \frac{n_s e^2}{m} \mathbf{E}, \quad (2.1a)$$

$$\nabla \times \mathbf{j}_s = -\frac{n_s e^2}{m} \mathbf{h}, \quad (2.1b)$$

¹We will not discuss unconventional superconductivity here, for a review see *e.g.* [84].

where \mathbf{j}_s is the total supercurrent and n_s is the number density of superconducting electrons. The first equation, Eq. (2.1a), describes perfect conductivity, stating that superconducting electrons accelerate in an applied electric field since they do not experience any scattering. The second equation, Eq. (2.1b) can be combined with the Maxwell equation in static electric field $\nabla \times \mathbf{h} = 4\pi\mathbf{j}_s/c$. Taking the curl of Eq. (2.1b) and using the second Maxwell's equation $\nabla \cdot \mathbf{h} = 0$, we can write:

$$\nabla^2 \mathbf{h} = \frac{4\pi n_s e^2}{mc^2} \mathbf{h}. \quad (2.2)$$

Considering a superconductor occupying the space for $z > 0$ in an applied field along x and intensity H_0 , the microscopic magnetic field inside the superconductor can be obtained from Eq. (2.2). The solution is $h(z) = H_0 \exp(-z/\lambda_L)$, where

$$\lambda_L = \sqrt{\frac{mc^2}{4\pi n_s e^2}}, \quad (2.3)$$

is the London penetration depth. Thus, the magnetic field penetrates inside the superconductor for a distance λ_L and is screened from its interior. This shows that for 2D materials we expect magnetic fields to penetrate superconductors.

2.1.2 Ginzburg-Landau Theory

In 1950 another step forward in the study of superconductivity was provided by Ginzburg and Landau [85], who formulated a theory from which the London equations can be derived. Despite being a phenomenological theory, it was later shown by Gor'kov in 1959 [86], that it can also be derived microscopically, demonstrating its fundamental importance.

The Ginzburg-Landau (GL) theory describes the superconducting electrons through the complex order parameter ψ in the context of Landau's theory of second order phase transitions. The theory is based on a free energy expansion in terms of ψ :

$$F_S = F_N + \alpha |\psi|^2 + \frac{1}{2} \beta |\psi|^4 + \frac{1}{2m^*} \left| \left(-i\hbar\nabla + \frac{e^*}{c} \mathbf{A} \right) \psi \right|^2 + \frac{h^2}{8\pi}, \quad (2.4)$$

where F_N is the free energy of the normal state, m^* and e^* are effective mass and charge, respectively, \mathbf{A} is the vector potential and $\mathbf{h} = \nabla \times \mathbf{A}$ is the microscopic magnetic field. The parameters α and β are phenomenological constants, with β assumed to be independent of temperature, while $\alpha \equiv \alpha(T) = (T - T_c)\alpha'$. Minimization of the free energy by taking variation of ψ , ψ^* and \mathbf{A} gives the following two field equations:

$$\frac{1}{2m^*} \left(-i\hbar\nabla + \frac{e^*}{c} \mathbf{A} \right)^2 \psi + \alpha\psi + \beta\psi |\psi|^2 = 0, \quad (2.5a)$$

$$\mathbf{j}_s = \frac{e^*}{m^*} \left[i\frac{\hbar}{2} (\psi^* \nabla \psi - \psi \nabla \psi^*) - \frac{1}{c} |\psi|^2 \mathbf{A} \right]. \quad (2.5b)$$

As a simple case we consider a homogeneous system, which from Eq. (2.5a) in the absence of any magnetic field has the following two solutions:

$$\psi = 0, \quad |\psi| = \sqrt{-\frac{\alpha'}{\beta}(T - T_c)}. \quad (2.6)$$

The first solution describes the normal state and the second is valid only for $T < T_c$. It is clear that the superconducting solution leaves a freedom in the choice of the phase of the order parameter $\psi = |\psi| \exp(i\phi)$, which is crucial when including spatial variations of ψ since it ensures that the free energy and physical observables are gauge invariant. The invariance of the magnetic field under the gauge transformation $\mathbf{A} \rightarrow \mathbf{A}' = \mathbf{A} - \nabla\chi$, imposes a simultaneous transformation on the phase $\phi \rightarrow \phi' = \phi - e^*\chi/\hbar^2$.

Another simple case to consider is the one dimensional case with $\mathbf{h} = 0$. The first GL equation becomes:

$$-\frac{\hbar^2}{2m^*} \frac{d^2\psi}{dz^2} + \alpha(T)\psi + \beta\psi |\psi|^2 = 0. \quad (2.7)$$

Defining the dimensionless order parameter $f = (\beta/|\alpha(T)|)^{1/2}\psi$, Eq. (2.7) reads

$$-\xi(T)^2 \frac{d^2f}{dz^2} + f^3 - f = 0, \quad (2.8)$$

where

$$\xi(T) = \frac{\hbar}{\sqrt{2m^*\alpha'(T_c - T)}}, \quad (2.9)$$

is the GL coherence length, defining the characteristic length scale for the spatial variation of the order parameter.

Now let us consider a uniform order parameter $|\psi|_\infty = \sqrt{n_s^*}$, defining an effective superconducting electron density. The supercurrent expression of Eq. (2.5b), takes the following form:

$$\mathbf{j}_s = -\frac{(e^*)^2 n_s^*}{m^* c} |\psi|^2 \mathbf{A}, \quad (2.10)$$

corresponding to the second London equation Eq. (2.1b), with the penetration depth:

$$\lambda(T) = \sqrt{\frac{m^* \beta c^2}{4\pi(e^*)^2 \alpha'(T_c - T)}}. \quad (2.11)$$

2.1.3 Flux Quantization

The GL equation for the supercurrent Eq. (2.5b) allows to verify the quantization of the flux in a superconductor. Substituting $\psi = |\psi| \exp(i\phi)$ in Eq. (2.5b) gives:

$$\mathbf{A} + \frac{m^* c}{(e^*)^2 |\psi|^2} \mathbf{j}_s = -\frac{\hbar c}{e^*} \nabla \phi. \quad (2.12)$$

Integrating this equation on a path C lying entirely in the superconductor we have:

$$\oint d\mathbf{l} \cdot \mathbf{A} + \frac{m^* c}{(e^*)^2} \oint \frac{d\mathbf{l} \cdot \mathbf{j}_s}{|\psi|^2} = -\frac{\hbar c}{e^*} \oint \mathbf{l} \cdot \nabla \phi. \quad (2.13)$$

In order for the order parameter to be single valued, the integral on the right side must be equal to a multiple of 2π . With this and using Stokes' theorem to rewrite the first term, we obtain:

$$\int d\mathbf{S} \cdot \mathbf{h} + \frac{m^* c}{(e^*)^2} \int \frac{d\mathbf{l} \cdot \mathbf{j}_s}{|\psi|^2} = n\Phi_0, \quad (2.14)$$

where n is an integer number and $\Phi_0 = 2\pi\hbar c/e^*$ is the flux quantum. The term on the left side of Eq. (2.14) is named fluxoid, and is the magnetic flux plus an additional contribution arising from the induced supercurrent.

2.1.4 Type I and Type II Superconductors

With Eqs. (2.9) and (2.11) we have defined two characteristic length scales for the superconductor. It is then possible to introduce the following dimensionless Ginzburg-Landau parameter

$$\kappa \equiv \frac{\lambda}{\xi}. \quad (2.15)$$

The importance of this parameter was demonstrated by Abrikosov [89], by studying the energy associated with a surface separating normal and superconducting regions, σ_{ns} , in an applied magnetic field H_c . This surface energy determines the behavior of a superconductor in an applied magnetic field, defining the distinction between type I and type II superconductors, realized for $\sigma_{ns} > 0$ ($\kappa < 1/\sqrt{2}$) and $\sigma_{ns} < 0$

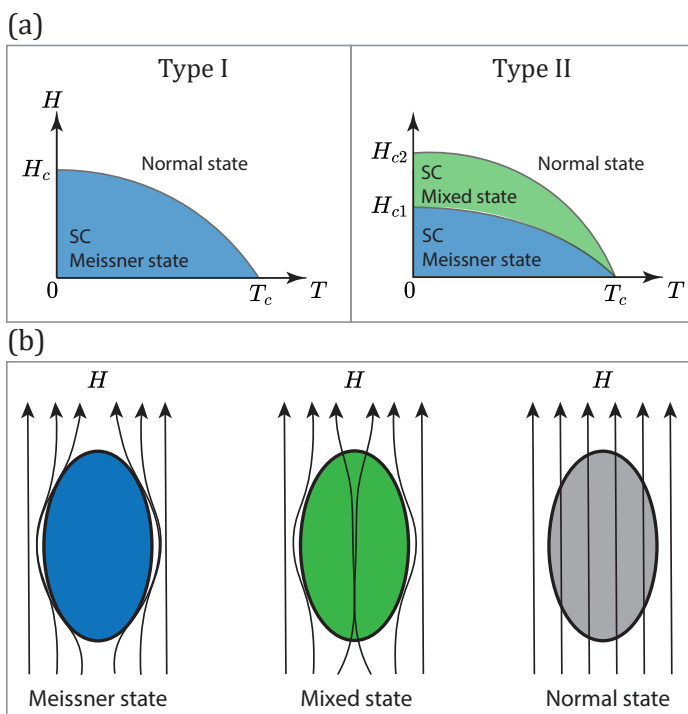


Figure 2.1: (a) Phase diagram in the HT plane for type I (left) and type II (right) superconductors. (b) Illustration of the magnetic field lines in the Meissner state (left), mixed state (center) and normal state (right). Based on figures in [87, 88].

($\kappa > 1/\sqrt{2}$), respectively. In type I superconductors, the positive surface energy makes the sample spatially homogeneous, presenting a Meissner effect up to a certain critical field H_c . On the other hand a type II superconductor exhibit an intermediate or mixed state when the magnetic field exceeds a lower critical field H_{c1} , where some magnetic flux penetrates the superconductor in quantized flux lines. The amount of penetrating flux increases with the magnetic field until at a certain upper critical field H_{c2} there is a transition from the mixed to normal state.

2.2 Microscopic (BCS) Theory of Superconductivity

Here we present the microscopic theory introduced by Bardeen, Cooper and Schrieffer [42]. This theory describes how an effective attractive interaction between electrons, mediated by phonons, leads to the formation of bound pairs of electrons, usually called Cooper pairs [90].

2.2.1 Cooper Pairs

The underlying idea of the BCS theory, that a weak attractive interaction can bind electrons in pairs, was first introduced by Cooper [90] in 1956. In his simple model, Cooper showed that the Fermi sea becomes unstable with respect to the formation of at least one bound pair, as long as an attractive interaction is present, no matter how weak.

The general approach is to add two electrons to the Fermi sea at $T = 0$, assuming that these extra electrons only interact with each other. After defining a wave function of the two electrons one inserts it into the Schrödinger equation and calculate the energy eigenvalue associated to it. Introducing the approximation that the potential $V_{\mathbf{k}\mathbf{k}'}$, representing the scattering of a pair of electrons with momenta $(\mathbf{k}, -\mathbf{k})$ to $(\mathbf{k}', -\mathbf{k}')$, is equal to $-V$ for states with an energy cutoff $\hbar\omega_c$ away from the Fermi energy E_F , and $V_{\mathbf{k}\mathbf{k}'} = 0$ otherwise, it can be shown that the energy eigenvalue is [41]:

$$E \approx 2E_F - 2\hbar\omega_c e^{-2/N(0)V}, \quad (2.16)$$

where $N(0)$ is the density of states at the Fermi level and $\hbar\omega_c$ a characteristic energy. The energy of Eq. (2.16) shows that there is a bound state with negative energy with respect to the Fermi surface.

2.2.2 The Attractive Interaction

To show how an attractive interaction can originate we consider the bare Coulomb interaction $V(r) = e^2/r$ between two electrons at a distance r and calculate its Fourier transform for unit normalization volume $V(\mathbf{q}) = 4\pi e^2/q^2$. Taking into account the screening due to the conducting electrons, described through the Thomas-Fermi approximation of the dielectric function $\epsilon(\mathbf{q}) = 1 + k_s^2/q^2$, where $k_s^{-1} \approx 1\text{\AA}$ is the screening length, the interaction is reduced by a factor $\epsilon^{-1}(\mathbf{q})$:

$$V(\mathbf{q}) = \frac{4\pi e^2}{q^2 + k_s^2}, \quad (2.17)$$

which is still positive. To obtain a negative interaction we consider ion motion, adding the phonon, *i.e.* lattice vibrations, contribution to the screening². The physical picture behind this is that a moving electron attracts the ions, producing a polarized region of positive charge. This region of excess positive charge in turn attracts a second electron, thus causing an effective attractive interaction.

²Phonons are not the only option for a negative interaction, but it was the first and the most common. Other suggestions exist as valid extensions to BCS.

Considering electron-phonon interaction, if an electron is scattered from momentum \mathbf{k} to \mathbf{k}' , the phonon will carry a momentum $\mathbf{q} = \mathbf{k} - \mathbf{k}'$. A realistic phonon contribution to the screening [41] is proportional to $(\omega^2 - \omega_q^2)^{-1}$, with ω_q being the phonon frequency. It is clear that if $\omega < \omega_q$ the contribution is negative, so for electron energy difference larger than $\hbar\omega_q$ the effective interaction becomes repulsive. This means that the cutoff energy $\hbar\omega_c$ of the effective attractive interaction introduced in the previous section should be of the order of the characteristic energy of phonons, the Debye energy $\hbar\omega_D$. A treatment of the electron-phonon coupled system through a jellium model (homogeneous electron gas) gives the following effective interaction [91]:

$$V(\mathbf{q}) = \frac{4\pi e^2}{q^2 + k_s^2} \frac{\omega^2}{\omega^2 - \omega_q^2}. \quad (2.18)$$

This interaction is clearly attractive for every $\omega < \omega_q$, but must not be considered as an universally reliable expression, it is rather meant to illustrate that it is possible to achieve an effective attractive interaction between electrons using simple considerations.

The phonon-mediated mechanism for the attractive interaction has been the first one to be discovered. Different mechanisms have been proposed, *e.g.* antiferromagnetic spin fluctuations in cuprates and iron based superconductors or the Kohn-Luttinger mechanism [92] in twisted bilayer graphene.

It is important to note that, although the BCS theory was developed based on the conventional mechanism for s-wave singlet superconductivity, it can be generalized to different pairing mechanisms and symmetries, such as p-wave and d-wave, and to spin-triplet superconductivity.

2.2.3 BCS Theory in the Green's Function Formalism

Here we present a derivation of the BCS theory through the Green's function formalism [86, 93, 94]. We will start by considering the following grand canonical Hamiltonian for an electron gas with an attractive interaction, in absence of magnetic fields and with $\hbar = 1$:

$$\begin{aligned} \hat{H} = \hat{H}_0 + \hat{V} = & - \sum_{\sigma} \int d\mathbf{r} \psi_{\sigma}^{\dagger}(\mathbf{r}) \left(\frac{\nabla^2}{2m} - \mu \right) \psi_{\sigma}(\mathbf{r}) \\ & - \frac{1}{2} g \sum_{\sigma\sigma'} \int d\mathbf{r} \psi_{\sigma}^{\dagger}(\mathbf{r}) \psi_{\sigma'}^{\dagger}(\mathbf{r}) \psi_{\sigma'}(\mathbf{r}) \psi_{\sigma}(\mathbf{r}), \end{aligned} \quad (2.19)$$

where the field operator $\psi_{\sigma}^{\dagger}(\mathbf{r})$ ($\psi_{\sigma}(\mathbf{r})$) creates (annihilates) a particle in position \mathbf{r} with spin σ , and $g > 0$ is the strength of the interaction. We will now introduce

a mean-field version of the Hamiltonian of Eq. (2.19) in the Cooper channel, *i.e.* including the pairing of electrons with opposite spins in a bound Cooper pair, and ignore all other channels. This is done by considering the following effective Hamiltonian:

$$\hat{H}_{\text{eff}} = \hat{H}_0 - g \int d\mathbf{r} \left\{ \langle \psi_{\downarrow}^{\dagger}(\mathbf{r}) \psi_{\uparrow}^{\dagger}(\mathbf{r}) \rangle \psi_{\uparrow}(\mathbf{r}) \psi_{\downarrow}(\mathbf{r}) + \psi_{\downarrow}^{\dagger}(\mathbf{r}) \psi_{\uparrow}^{\dagger}(\mathbf{r}) \langle \psi_{\uparrow}(\mathbf{r}) \psi_{\downarrow}(\mathbf{r}) \rangle \right\}, \quad (2.20)$$

where the angle brackets represent an ensemble average evaluated with \hat{H}_{eff} . We now define the imaginary-time Heisenberg operators

$$\psi_{H\sigma}(\mathbf{r}, \tau) = \exp\left(\hat{H}_{\text{eff}}\tau\right) \psi_{\sigma}(\mathbf{r}) \exp\left(-\hat{H}_{\text{eff}}\tau\right), \quad (2.21a)$$

$$\psi_{H\sigma}^{\dagger}(\mathbf{r}, \tau) = \exp\left(-\hat{H}_{\text{eff}}\tau\right) \psi_{\sigma}^{\dagger}(\mathbf{r}) \exp\left(\hat{H}_{\text{eff}}\tau\right), \quad (2.21b)$$

whose time evolution is given by

$$\frac{\partial \psi_{H\sigma}(x)}{\partial \tau} = \left(\frac{\nabla^2}{2m} + \mu \right) \psi_{H\sigma} - g \langle \psi_{\uparrow} \psi_{\downarrow} \rangle \psi_{H\sigma'}^{\dagger}, \quad (2.22a)$$

$$\frac{\partial \psi_{H\sigma}^{\dagger}}{\partial \tau} = - \left(\frac{\nabla^2}{2m} + \mu \right) \psi_{H\sigma}^{\dagger} - g \langle \psi_{\uparrow} \psi_{\downarrow} \rangle \psi_{H\sigma'}, \quad (2.22b)$$

where $x \equiv (\mathbf{r}, \tau)$. We can now define the following single particle Green's function:

$$G(x, x') = - \langle T_{\tau} \{ \psi_{H\uparrow}(x) \psi_{H\uparrow}^{\dagger}(x') \} \rangle, \quad (2.23)$$

where T_{τ} represents the imaginary time-ordered product. By using Eqs. (2.22a) and (2.22b) we get the following equation for the Green's function:

$$\left(- \frac{\partial}{\partial \tau} + \frac{\nabla^2}{2m} + \mu \right) G(x, x') = \delta(x - x') + g \langle \psi_{\uparrow}(\mathbf{r}) \psi_{\downarrow}(\mathbf{r}) \rangle \langle T_{\tau} \{ \psi_{\downarrow}^{\dagger}(x) \psi_{\uparrow}^{\dagger}(x') \} \rangle, \quad (2.24)$$

where $\delta(x - x') \equiv \delta(\mathbf{r} - \mathbf{r}') \delta(\tau - \tau')$. By inspection of this equation it appears natural to introduce two additional Green's functions, also called anomalous Green's functions:

$$F(x, x') = - \langle T_{\tau} \{ \psi_{H\uparrow}(x) \psi_{H\downarrow}(x') \} \rangle, \quad (2.25a)$$

$$F^{\dagger}(x, x') = - \langle T_{\tau} \{ \psi_{H\downarrow}^{\dagger}(x) \psi_{H\uparrow}(x') \} \rangle. \quad (2.25b)$$

For a time-dependent Hamiltonian the Green's function G , F and F^\dagger depend only on the time difference $\tau - \tau'$, so that it is possible to define the superconducting order parameter as:

$$\Delta(\mathbf{r}) = gF(\mathbf{r}\tau, \mathbf{r}'\tau) = -g\langle\psi_\uparrow(\mathbf{r})\psi_\downarrow(\mathbf{r})\rangle. \quad (2.26)$$

Similarly to the case of G it is possible to obtain the equation of motion for F and F' . With the use of the definitions Eqs. (2.23), (2.25a), (2.25b) and (2.26) we can write the equation of motion for G , F and F^\dagger

$$\left(-\frac{\partial}{\partial\tau} + \frac{\nabla^2}{2m} + \mu\right)G(x, x') = \delta(x - x') - \Delta(\mathbf{r})F(x, x'), \quad (2.27a)$$

$$\left(-\frac{\partial}{\partial\tau} + \frac{\nabla^2}{2m} + \mu\right)F(x, x') = \Delta(\mathbf{r})G(x, x'), \quad (2.27b)$$

$$\left(\frac{\partial}{\partial\tau} + \frac{\nabla^2}{2m} + \mu\right)F^\dagger(x, x') = \Delta^*(\mathbf{r})G(x, x'), \quad (2.27c)$$

which are known as the Gorkov equations. It is possible to rewrite Eqs. (2.27a) to (2.27c) in a more compact form by introducing the two-component Nambu field operator $\Psi_H^\dagger(x) = (\psi_\uparrow^\dagger(x), \psi_\downarrow(x))$ and the 2×2 Green's function:

$$\mathcal{G}(x, x') = \begin{pmatrix} G(x, x') & F(x, x') \\ F^\dagger(x, x') & -G(x, x') \end{pmatrix}. \quad (2.28)$$

This allows us to write the following equation of motion:

$$\mathcal{D}_x\mathcal{G}(x, x') = \hat{\tau}_0\delta(x - x'), \quad (2.29)$$

where $\hat{\tau}_0$ is the 2×2 identity matrix and we have define the following differential operator:

$$\mathcal{D}_x = \begin{pmatrix} -\frac{\partial}{\partial\tau} + \frac{\nabla^2}{2m} + \mu & \Delta(\mathbf{r}) \\ \Delta^*(\mathbf{r}) & -\frac{\partial}{\partial\tau} - \frac{\nabla^2}{2m} - \mu \end{pmatrix}. \quad (2.30)$$

Since we have a time independent Hamiltonian with no external magnetic fields, the Green's functions of the system are functions of $\tau - \tau'$ and $\mathbf{r} - \mathbf{r}'$. We then consider the following Fourier representation for the Green's function:

$$\mathcal{G}(x - x') = \frac{1}{\beta(2\pi)^3} \sum_n \int d\mathbf{k} e^{-i\omega_n(\tau - \tau') + i\mathbf{k}\cdot(\mathbf{r} - \mathbf{r}')} \mathcal{G}(\mathbf{k}, \omega_n), \quad (2.31)$$

where $\omega_n = (2n + 1)\pi/\beta$ are the Matsubara fermionic frequencies and $\beta = (k_B T)^{-1}$. In our case it is sufficient to consider the Gorkov equations Eqs. (2.27a) and (2.27c) together with the gap equation Eq. (2.26), taking the following form:

$$(i\omega_n - \xi_k)G(\mathbf{k}, \omega_n) + \Delta F^\dagger(\mathbf{k}, \omega_n) = 1, \quad (2.32a)$$

$$(-i\omega_n - \xi_k)F^\dagger(\mathbf{k}, \omega_n) - \Delta^* G(\mathbf{k}, \omega_n) = 0, \quad (2.32b)$$

$$\Delta^* = \frac{g}{\beta} \sum_n e^{-i\omega_n \zeta} F^\dagger(\mathbf{r} = 0, \omega_n), \quad (2.32c)$$

where $\xi_k = k^2/(2m) - \mu$ and $\zeta = 0^+$. The solutions for the normal and anomalous Green's functions are easily found to be:

$$G(\mathbf{k}, \omega_n) = -\frac{i\omega_n + \xi_k}{\omega_n^2 + E_k^2}, \quad (2.33a)$$

$$F^\dagger(\mathbf{k}, \omega_n) = \frac{\Delta^*}{\omega_n^2 + E_k^2}, \quad (2.33b)$$

where we have defined $E_k = \sqrt{\xi_k^2 + \Delta^2}$. It is useful to get a partial fraction decomposition of F^\dagger in order to evaluate the order parameter from Eq. (2.32c). We can use the residue theorem, the function $(\omega_n^2 + E_k^2)^{-1}$ has singularities in $i\omega_n = \pm E_k$, so that its partial fraction decomposition can be obtained by calculating the residues of the function in its singularities. The decomposition reads:

$$f(i\omega_n) \equiv \frac{1}{\omega_n^2 + E_k^2} = \frac{A_k}{i\omega_n - E_k} + \frac{B_k}{i\omega_n + E_k}, \quad (2.34a)$$

$$A_k = \text{Res}_{z=E_k} f(z) = \lim_{z \rightarrow E_k} (z - E_k) f(z) = -\frac{1}{2E_k}, \quad (2.34b)$$

$$B_k = \text{Res}_{z=-E_k} f(z) = \lim_{z \rightarrow -E_k} (z + E_k) f(z) = \frac{1}{2E_k}. \quad (2.34c)$$

This allows us to rewrite the anomalous Green's function as

$$F^\dagger(\mathbf{k}, \omega_n) = -\frac{\Delta^*}{2E_k} \left(\frac{1}{i\omega_n - E_k} - \frac{1}{i\omega_n + E_k} \right). \quad (2.35)$$

Since we are considering conventional s-wave superconductivity and we are in absence of magnetic fields, the order parameter Δ can be taken real. The self-consistent gap equation Eq. (2.32c) takes the following form:

$$\Delta = -\frac{g}{\beta(2\pi)^3} \sum_n \int d\mathbf{k} \frac{\Delta}{2E_k} \left(\frac{1}{i\omega_n - E_k} - \frac{1}{i\omega_n + E_k} \right). \quad (2.36)$$

We can sum over the Matsubara frequencies by using the identity $\beta^{-1} \sum_n (i\omega_n \mp E_k)^{-1} = n_F(\pm E_k)$, where $n_F(E) = (e^{\beta E} + 1)^{-1}$ is the Fermi function. With this, Eq. (2.36) becomes:

$$\frac{1}{g} = \frac{1}{(2\pi)^3} \int d\mathbf{k} \frac{1}{2E_k} \tanh(\beta E_k/2), \quad (2.37)$$

where we used the fact that $n_F(E) - n_F(-E) = -\tanh(\beta E/2)$. The next step is to replace the integration in momentum space with an integration over the energies:

$$\frac{1}{(2\pi)^3} \int d\mathbf{k} \rightarrow \int d\xi N(\xi), \quad (2.38)$$

where $N(\xi)$ is the density of states. Given the origin of the attractive interaction, the energy integral has a cutoff at ω_D . Furthermore, since ω_D is much smaller than the Fermi energy we can approximate the density of states with its value at the Fermi surface $N(0)$. The gap equation thus reads:

$$\frac{1}{gN(0)} = \int_0^{\omega_D} \frac{d\xi}{\sqrt{\xi^2 + \Delta^2}} \tanh\left(\beta\sqrt{\xi^2 + \Delta^2}/2\right). \quad (2.39)$$

This equation allows to calculate the gap function for any temperature, and it is usually solved numerically, except the limiting cases $T = 0$ and $T = T_c$. At zero temperature $\tanh(\cdot) \rightarrow 1$, so that we can write:

$$\frac{1}{gN(0)} = \int_0^{\omega_D} \frac{d\xi}{\sqrt{\xi^2 + \Delta_0^2}} = \ln \frac{\sqrt{\omega_D^2 + \Delta_0^2} + \omega_D}{\Delta_0} \approx \ln \frac{2\omega_D}{\Delta_0}, \quad (2.40)$$

where we have used the fact that $\omega_D \gg \Delta_0$. We then obtain the following expression for the gap at zero temperature

$$\Delta_0 \approx 2\omega_D e^{-1/(gN(0))}. \quad (2.41)$$

In the opposite limit $T = T_c$ we can set $\Delta = 0$ and obtain the following equation for the critical temperature:

$$\frac{1}{gN(0)} = \int_0^{\omega_D} \frac{d\xi}{\xi} \tanh\left(\frac{\xi}{2T_c}\right). \quad (2.42)$$

In order to calculate the integral we introduce the dimensionless variable $x = \xi/(2T_c)$, and then integrate by parts:

$$\begin{aligned} \int_0^{\frac{\omega_D}{2T_c}} \frac{dx}{x} \tanh(x) &= [\ln(x) \tanh(x)]_0^{\frac{\omega_D}{2T_c}} - \int_0^{\frac{\omega_D}{2T_c}} dx \frac{\ln(x)}{\cosh^2(x)} \\ &\approx \ln\left(\frac{\omega_D}{2T_c}\right) - \int_0^{\infty} dx \frac{\ln(x)}{\cosh^2(x)} \\ &\approx \ln\left(\frac{2\omega_D e^\gamma}{\pi T_c}\right), \end{aligned} \quad (2.43)$$

where we made use of the fact $\omega_D \gg T_c$ and we have approximated the definite integral as

$$\int_0^{\infty} dx \frac{\ln(x)}{\cosh^2(x)} \approx -\ln\left(\frac{4e^\gamma}{\pi}\right), \quad (2.44)$$

with $\gamma \approx 0.577$ Euler's constant. With this we obtain the following expression for the critical temperature

$$T_c = \frac{2e^\gamma \omega_D}{\pi} e^{-1/(gN(0))} = \frac{e^\gamma}{\pi} \Delta_0. \quad (2.45)$$

Combining Eqs. (2.41) and (2.45) we obtain the universal value for the ratio between Δ_0 and T_c [41, 94]

$$\frac{\Delta_0}{T_c} = \pi e^{-\gamma} \approx 1.76, \quad (2.46)$$

which is independent of the material under consideration.

2.3 High Magnetic Field Superconductivity in a Two-band Superconductor

So far we have considered systems where only one band is in the proximity of the Fermi level. In the following we take a step forward in the study of superconductivity, by considering multiband superconductors. With multiband superconductor we refer to a system having multiple bands close to the Fermi level where superconducting pairing can occur. This fact provides additional possibilities for the pairing, since now the electrons forming the Cooper pairs have also a band index. Therefore, it is in principle possible to have both *intra*band Cooper pairs, *i.e.* the electrons forming the pair come from the same band, and *inter*band Cooper pairs, *i.e.* electrons coming from two distinct bands. We will first present the theoretical

formalism for multiband superconductivity with an external spin-splitting field, and we will then employ it to study a two-band superconductor with spin-splitting induced by an in-plane external magnetic field. As presented in Paper III [3], we show that this system can host superconductivity at values of the external magnetic field significantly higher than the usual limiting values for single band superconductors.

2.3.1 Brief Overview on Multiband Superconductors

Experimental studies on multiband superconductors have shown that these systems can host interesting effects not achievable in single band systems. For instance, in Ref.[95] it was demonstrated that MgB_2 , the first-ever discovered multiband superconductor, can host Leggett modes, *i.e.* collective excitations corresponding to relative phase fluctuations between two order parameters. More recently, these modes have also been optically-controlled [96], showing the possibility to control collective superconducting excitations through electromagnetic radiation. Moreover, spontaneous time reversal symmetry breaking has been reported in $\text{Ba}_{1-x}\text{K}_x\text{Fe}_2\text{As}_2$, Sr_2RuO_4 , UPt_3 and many other multiband systems³.

The first extensions of the Bardeen–Cooper–Schrieffer (BCS) theory to multiband systems were provided by Suhl, Matthias and Walker [98] and Moskalenko [99]. Since then, many studies have focused on a theoretical understanding of the effects of a multiband description of superconductors. For instance, it has been shown that two band superconductors can present a crossover from the weak coupling (BCS) state of Cooper pairs to a Bose-Einstein condensate (BEC) of strongly-coupled di-fermionic molecules [100–102].

In general, if two bands are close to each other or hybridized, it is possible to obtain interband Cooper pairs (see *e.g.* [103]), where the electrons comprising the pairs come from two distinct bands. Research on interband pairing has been rather limited, but studies have found that it affects collective excitations [104] and Josephson tunneling [105] and that it can induce odd-frequency pairing [106]. Furthermore, it is a crucial factor in demonstrating the presence of an anomalous Hall effect in Sr_2RuO_4 [107], it can produce gapless states [108], and it influences the BCS-BEC crossover [109].

It is worth noting that in the literature the term interband pairing is sometimes used to refer to the hopping of intraband pairs, *i.e.* formed by electrons in the same band, between different bands, also called pair-hopping. Here, when using the term interband we will always mean Cooper pairs formed by electrons in distinct bands.

Among multiband superconductors, MgB_2 and Fe-Based Superconductors (FeBS) exhibit high critical temperatures and critical magnetic fields. For instance, the critical temperature is 39K for MgB_2 [43], 55K for $\text{SmO}_{1-x}\text{F}_x\text{FeAs}$ [110]

³For an exhaustive review see [97].

and 65K in FeSe films on SrTiO₃ substrate [111], whereas the zero temperature estimated values of the critical field are 25T in single crystal MgB₂ [112], 70T in C-doped MgB₂ thin films [113] and up to 300T in FeBS [114–119].

2.3.2 Pauli-Chandrasekhar-Clogston Limit

A superconductor in external magnetic field is subject to two effects which are detrimental to superconductivity: the orbital and Pauli paramagnetic pairbreaking effects [120, 121]. The orbital effect describes the breaking of Cooper pairs when the kinetic energy of electrons, resulting from the momentum acquired in a magnetic field, exceeds the superconducting gap. On the other hand, paramagnetic pairbreaking occurs when Cooper pairing becomes energetically unfavourable as the Zeeman energy of the electrons overcomes the superconducting gap. This happens when the exchange energy reaches a value given by the Pauli, or equivalently the Chandrasekhar-Clogston, limit $h_c = \Delta_0/\sqrt{2} = 1.86T_c$, where Δ_0 is the value of the superconducting gap at zero temperature and zero applied field, and T_c is the superconducting critical temperature.

Different mechanisms leading to a violation of this limit, or to an enhancement of critical fields, have been proposed theoretically. For instance, it has been shown that scattering by non-magnetic impurities enhances the upper critical field in dirty two-band superconductors [122, 123], while application of a voltage bias in superconducting ferromagnetic heterostructures allows to recover superconductivity above the limiting value [124, 125]. Other studies have shown that the multiband nature of the system also allows to overcome the limit, such as, *e.g.* the proximity of two bands to each other [126–128], or pair-hopping in three band superconductors [129, 130]. Furthermore, many experimental works have reported evidence for critical magnetic field violating the above limits in various superconductors, *e.g.* NbSe₂ [131, 132], iron pnictides [133, 134], lanthanide infinite-layer nickelate [135], moiré graphene [136], organic superconductors [137, 138], Eu-Sn molybdenum chalcogenide [139], URhGe [140], and UTe₂ [141].

2.3.3 Hamiltonian for a two-band superconductor

We consider a two-band superconducting thin-film with both intra- and interband spin-singlet superconducting coupling, and an in-plane external magnetic field producing Zeeman splitting. We ignore orbital pair-breaking effects and assume the system does not experience any magnetic flux. The mean-field Hamiltonian of the system is the following:

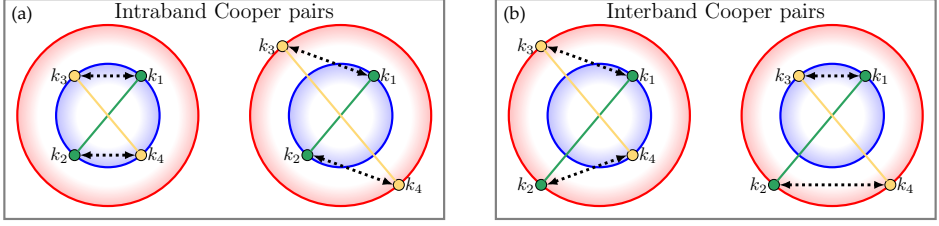


Figure 2.2: Illustration of some of the superconducting pairing processes possible in a two-band system for (a) intraband and (b) interband Cooper pairs. The red and blue circles represent the Fermi surfaces of the two bands, the green and yellow lines identify the electrons forming the Cooper pairs and the dotted lines indicates the scattering processes.

$$\begin{aligned} \mathcal{H} = & \sum_{\mathbf{k}\sigma} (\xi_{\mathbf{k}}^{(1)} - E_c - \sigma h) c_{\mathbf{k}\sigma}^{(1)\dagger} c_{\mathbf{k}\sigma}^{(1)} + \sum_{\mathbf{k}\sigma} (\xi_{\mathbf{k}}^{(2)} + E_c - \sigma h) c_{\mathbf{k}\sigma}^{(2)\dagger} c_{\mathbf{k}\sigma}^{(2)} \\ & - \sum_{\mathbf{k}} \sum_{\alpha, \alpha'=1,2} \left(\Delta_{\alpha\alpha'}(\mathbf{k}) c_{\mathbf{k}\uparrow}^{(\alpha)\dagger} c_{-\mathbf{k}\downarrow}^{(\alpha')\dagger} + \text{h.c.} \right), \end{aligned} \quad (2.47)$$

where the operator $c_{\mathbf{k}\sigma}^{(\alpha)\dagger}$ ($c_{\mathbf{k}\sigma}^{(\alpha)}$) creates (destroys) an electron in band α with dispersion $\xi_{\mathbf{k}}^{(\alpha)} = \varepsilon_{\mathbf{k}}^{\alpha} - \mu$ and spin σ , E_c is half the band separation and h is the externally applied in-plane magnetic field. The superconducting order parameters $\Delta_{\alpha\alpha'}(\mathbf{k})$ are defined by the following generalization of Eq. (2.26):

$$\Delta_{\alpha\alpha'}(\mathbf{k}) = \frac{T}{V} \sum_{\omega_n} \sum_{\beta, \beta'=1,2} \sum_{\mathbf{k}'} g_{\alpha\alpha', \beta\beta'}(\mathbf{k}, \mathbf{k}') F^{\beta\beta'}(\mathbf{k}', \omega_n), \quad (2.48)$$

where $\omega_n = (2n + 1)\pi/\beta$ is the fermionic Matsubara frequency and $F^{\beta\beta'}$ is the anomalous component of the Green's function. The terms Δ_{11} and Δ_{22} represent the intraband order parameters, while $\Delta_{12} = \Delta_{21}$ is the interband order parameter.

The superconducting coupling tensor $g_{\alpha\alpha', \beta\beta'}(\mathbf{k}, \mathbf{k}')$ defines the different coupling processes. The terms $g_{\alpha\alpha, \alpha'\alpha'}$ describe hopping of intraband Cooper pairs between the same band ($\alpha = \alpha'$) or different bands ($\alpha \neq \alpha'$). This last term is often referred to in the literature as interband scattering, or pair hopping, and must not be confused with the use we make of the term interband. Processes involving interband pairs instead are described by the elements $g_{\alpha\alpha', \beta\beta'}$ with $\alpha \neq \alpha'$ and/or $\beta \neq \beta'$. In Fig. 2.2 we illustrate the pairing processes we will consider in the following.

2.3.4 Green's function of the system

In the basis defined by $\hat{\psi}_{\mathbf{k}}^\dagger = \left(c_{\mathbf{k}\uparrow}^{(1)\dagger}, c_{-\mathbf{k}\downarrow}^{(1)}, c_{\mathbf{k}\uparrow}^{(2)\dagger}, c_{-\mathbf{k}\downarrow}^{(2)} \right)$ the inverse Green's function for the Hamiltonian of Eq. (2.47) is:

$$\mathcal{G}_0^{-1} = \begin{pmatrix} (i\omega_n + h)\hat{\tau}_0 - \tilde{\xi}_1\hat{\tau}_3 + \Delta_{11}\hat{\tau}_1 & \Delta_{12}\hat{\tau}_1 \\ \Delta_{12}\hat{\tau}_1 & (i\omega_n + h)\hat{\tau}_0 - \tilde{\xi}_2\hat{\tau}_3 + \Delta_{22}\hat{\tau}_1 \end{pmatrix}, \quad (2.49)$$

where $\tilde{\xi}_1 = \xi_{\mathbf{k}}^{(1)} - E_c$, $\tilde{\xi}_2 = \xi_{\mathbf{k}}^{(2)} + E_c$ and we restricted to s-wave pairing (real order parameter). The two branches of the BCS quasiparticle excitation spectrum, E_+ and E_- , are obtained by defining $\det\mathcal{G}_0^{-1} \equiv (\tilde{\omega}_n^2 + E_+^2)(\tilde{\omega}_n^2 + E_-^2)$, where $\tilde{\omega}_n = \omega_n - ih$. Inverting Eq. (2.49) we obtain the Green's function of the system:

$$\mathcal{G}_0(\mathbf{k}, \omega_n) = \frac{1}{\det\mathcal{G}_0^{-1}} \begin{pmatrix} \hat{\mathcal{A}}^{11}(\mathbf{k}, \tilde{\omega}_n) & \hat{\mathcal{A}}^{12}(\mathbf{k}, \tilde{\omega}_n) \\ \hat{\mathcal{A}}^{21}(\mathbf{k}, \tilde{\omega}_n) & \hat{\mathcal{A}}^{22}(\mathbf{k}, \tilde{\omega}_n) \end{pmatrix}, \quad (2.50)$$

where $\det\mathcal{G}_0^{-1} = (\tilde{\omega}_n^2 + E_+^2)(\tilde{\omega}_n^2 + E_-^2)$ with $\tilde{\omega}_n = \omega_n - ih$. The two branches have the following expression:

$$E_{\pm}^2 = \frac{1}{2} \left\{ \tilde{E}_1^2 + \tilde{E}_2^2 + 2|\Delta_{12}|^2 \pm \left[\left(\tilde{E}_1^2 + \tilde{E}_2^2 + 2|\Delta_{12}|^2 \right)^2 - 4 \left(\tilde{E}_1^2 \tilde{E}_2^2 + |\Delta_{12}|^4 + 2\tilde{\xi}_1 \tilde{\xi}_2 |\Delta_{12}|^2 - 2\text{Re} \left\{ \Delta_{11} \Delta_{22} \Delta_{12}^* \right\} \right) \right]^{\frac{1}{2}} \right\}. \quad (2.51)$$

The components of the 2×2 matrices $\hat{\mathcal{A}}^{\alpha\beta}(\mathbf{k}, \omega_n)$ are:

$$\begin{aligned} \left[\hat{\mathcal{A}}^{11}(\mathbf{k}, \tilde{\omega}_n) \right]_{11} &= - \left(i\tilde{\omega}_n + \tilde{\xi}_1 \right) \left(\tilde{\omega}_n^2 + \tilde{\xi}_2^2 + |\Delta_{22}|^2 \right) \\ &\quad - |\Delta_{12}|^2 \left(i\tilde{\omega}_n + \tilde{\xi}_2 \right), \end{aligned} \quad (2.52a)$$

$$\left[\hat{\mathcal{A}}^{11}(\mathbf{k}, \tilde{\omega}_n) \right]_{12} = \Delta_{11} \left(\tilde{\omega}_n^2 + \tilde{\xi}_2^2 + |\Delta_{22}|^2 \right) - \Delta_{12}^2 \Delta_{22}^*, \quad (2.52b)$$

$$\begin{aligned} \left[\hat{\mathcal{A}}^{12}(\mathbf{k}, \tilde{\omega}_n) \right]_{11} &= \left(i\tilde{\omega}_n + \tilde{\xi}_1 \right) \Delta_{12} \Delta_{22}^* \\ &\quad + \Delta_{11} \Delta_{12}^* \left(i\tilde{\omega}_n + \tilde{\xi}_2 \right), \end{aligned} \quad (2.52c)$$

$$\begin{aligned} \left[\hat{\mathcal{A}}^{12}(\mathbf{k}, \tilde{\omega}_n) \right]_{12} &= - \left[\left(i\tilde{\omega}_n + \tilde{\xi}_1 \right) \left(i\tilde{\omega}_n - \tilde{\xi}_2 \right) - |\Delta_{12}|^2 \right] \Delta_{12} \\ &\quad - \Delta_{11} \Delta_{12}^* \Delta_{22}, \end{aligned} \quad (2.52d)$$

$$\left[\hat{\mathcal{A}}^{21}(\mathbf{k}, \tilde{\omega}_n) \right]_{11} = \left[\hat{\mathcal{A}}^{12}(\mathbf{k}, -\tilde{\omega}_n^*) \right]_{11}^*, \quad (2.52e)$$

$$\left[\hat{A}^{21}(\mathbf{k}, \tilde{\omega}_n) \right]_{12} = \left[\hat{A}^{12}(\mathbf{k}, -\tilde{\omega}_n) \right]_{12}, \quad (2.52f)$$

$$\left[\hat{A}^{\alpha\beta}(\mathbf{k}, \tilde{\omega}_n) \right]_{22} = - \left[\hat{A}^{\alpha\beta}(\mathbf{k}, -\tilde{\omega}_n) \right]_{11}, \quad (2.52g)$$

$$\left[\hat{A}^{\alpha\beta}(\mathbf{k}, \tilde{\omega}_n) \right]_{21} = \left[\hat{A}^{\alpha\beta}(\mathbf{k}, \tilde{\omega}_n^*) \right]_{12}^*. \quad (2.52h)$$

where $\tilde{E}_\alpha = \sqrt{\tilde{\xi}_\alpha^2 + |\Delta_{\alpha\alpha}|^2}$, $\alpha = 1, 2$, with $\tilde{\xi}_1 = \xi_{\mathbf{k}}^{(1)} - E_c$, $\tilde{\xi}_2 = \xi_{\mathbf{k}}^{(2)} + E_c$.

The elements of $\hat{A}^{22}(\mathbf{k}, \omega_n)$ are obtained by exchanging the indices 1 and 2 in the expressions for the elements of $\hat{A}^{11}(\mathbf{k}, \omega_n)$. The inter- and intra-band normal and anomalous Green's functions are given by:

$$G^{\alpha\beta}(\mathbf{k}, \tilde{\omega}_n) = \frac{\left[\hat{A}^{\alpha\beta}(\mathbf{k}, \tilde{\omega}_n) \right]_{11}}{(\tilde{\omega}_n^2 + E_+^2)(\tilde{\omega}_n^2 + E_-^2)}, \quad (2.53a)$$

$$F^{\alpha\beta}(\mathbf{k}, \tilde{\omega}_n) = \frac{\left[\hat{A}^{\alpha\beta}(\mathbf{k}, \tilde{\omega}_n) \right]_{12}}{(\tilde{\omega}_n^2 + E_+^2)(\tilde{\omega}_n^2 + E_-^2)}. \quad (2.53b)$$

2.3.5 Gap equation for the interband order parameter

We derive the gap equation in the case of purely interband coupling, *i.e.* Cooper pairs formed exclusively by electrons in different bands. To do so we consider the following form of the coupling matrix:

$$g_{\alpha\alpha'\beta\beta'} = \begin{cases} g^{\text{inter}}, & \text{if } \alpha \neq \alpha', \beta \neq \beta' \\ 0, & \text{otherwise.} \end{cases} \quad (2.54)$$

Inserting this in Eq. (2.48) we obtain the following gap equation:

$$\Delta_{12} = \frac{g^{\text{inter}T}}{V} \sum_{\mathbf{k}\omega_n} [F^{12}(\mathbf{k}, \omega_n - ih) + F^{21}(\mathbf{k}, \omega_n - ih)]. \quad (2.55)$$

Setting $\Delta_{11} = \Delta_{22} = 0$ in Eq. (2.51) we get:

$$E_{\pm} = \frac{\tilde{\xi}_1 - \tilde{\xi}_2}{2} \pm E_{12}, \quad (2.56)$$

with $E_{12} = \sqrt{(\tilde{\xi}_1 + \tilde{\xi}_2)^2/4 + |\Delta_{12}|^2}$. Using the relation, defined in the main text, between the two bands $\xi_{\mathbf{k}}^{(2)} = \gamma \xi_{\mathbf{k}}^{(1)} + (\gamma - 1)\mu$, we can write:

$$E_{\pm} = \frac{(\xi_{\mathbf{k}}^{(1)} + \mu)(1 - \gamma)}{2} - E_c \pm E_{12}, \quad (2.57a)$$

$$E_{12} = \sqrt{\left(\frac{\xi_{\mathbf{k}}^{(1)}(1 + \gamma) - \mu(1 - \gamma)}{2}\right)^2 + |\Delta_{12}|^2}. \quad (2.57b)$$

The expression of the anomalous Green's function is:

$$F^{12}(\mathbf{k}, \omega_n - ih) = -\frac{(i\tilde{\omega}_n + \tilde{\xi}_1 + h)(i\tilde{\omega}_n - \tilde{\xi}_2 + h) - |\Delta_{12}|^2}{[(\omega_n - ih)^2 + E_+^2][(\omega_n - ih)^2 + E_-^2]} \Delta_{12}. \quad (2.58)$$

After summing over the Matsubara frequency the gap equation Eq. (2.55) takes the following form:

$$\begin{aligned} \frac{1}{g_{\text{inter}}} &= -\frac{1}{V} \sum_{\mathbf{k}} \sum_{s=\pm} \frac{s}{2E_{12}} [n_F(E_s - h) - n_F(-E_s - h)] \\ &= \frac{1}{V} \sum_{\mathbf{k}} \sum_{s=\pm} \frac{s}{4E_{12}} \left\{ \tanh \left[\frac{\beta}{2} (E_s + h) \right] + \tanh \left[\frac{\beta}{2} (E_s - h) \right] \right\}, \end{aligned} \quad (2.59)$$

where $n_F(\varepsilon) = (e^{\beta\varepsilon} + 1)^{-1}$ is the Fermi function and we have used:

$$\begin{aligned} n_F(E_{\pm} - h) - n_F(-E_{\pm} - h) &= -\frac{\sinh \beta E_{\pm}}{\cosh \beta E_{\pm} + \cosh \beta h} \\ &= -\frac{1}{2} \left\{ \tanh \left[\frac{\beta}{2} (E_{\pm} + h) \right] + \tanh \left[\frac{\beta}{2} (E_{\pm} - h) \right] \right\}. \end{aligned} \quad (2.60)$$

We now switch from the summation over momenta to integral over the energy: $V^{-1} \sum_{\mathbf{k}} (\cdot) = \int d\xi_1 N_1(\xi_1) (\cdot)$, where $N_1(\xi_1)$ is the density of state of band 1. We then approximate the density of state with its value at the Fermi level $N_1(\xi_1) \simeq N_1(0)$ and, defining the dimensionless superconducting coupling constant as done in the main text, we obtain the final expression for the interband gap equation:

$$\frac{1}{\lambda_{\text{inter}}} = \int_{-\omega_c}^{\omega_c} d\xi \sum_{s=\pm} \frac{s}{4E_{12}(\xi)} \left\{ \tanh \left[\frac{\beta}{2} (E_s(\xi) + h) \right] + \tanh \left[\frac{\beta}{2} (E_s(\xi) - h) \right] \right\}. \quad (2.61)$$

To obtain critical temperature and critical field, we linearize Eq. (2.61) with respect to Δ_{12} . The equation then takes the following simple form:

$$\frac{1}{\lambda^{\text{inter}}} = \int_{-\omega_c}^{\omega_c} \frac{d\xi}{2(\tilde{\xi}_1 + \tilde{\xi}_2)} \sum_{\alpha=1,2} \left\{ \tanh \left[\frac{\beta_c}{2} (\tilde{\xi}_\alpha + h_c) \right] + \tanh \left[\frac{\beta_c}{2} (\tilde{\xi}_\alpha - h_c) \right] \right\}. \quad (2.62)$$

We note that by setting $E_c = 0$ and $\gamma = 1$, we get $\tilde{\xi}_1 = \tilde{\xi}_2 = \xi$, the system reduces to a single band superconductor. Therefore, Eq. (2.62) takes the usual form for a single band spin-split superconductor:

$$\frac{1}{\lambda} = \int_{-\omega_c}^{\omega_c} \frac{d\xi}{2\xi} \left\{ \tanh \left[\frac{\beta_c}{2} (\xi + h_c) \right] + \tanh \left[\frac{\beta_c}{2} (\xi - h_c) \right] \right\}. \quad (2.63)$$

2.3.6 Gap equation for the intraband order parameters

In order to consider purely intraband coupling we take the following form of the coupling matrix:

$$g_{\alpha\alpha'\beta\beta'} = \begin{cases} g_{\alpha\beta}^{\text{intra}}, & \text{if } \alpha = \alpha', \beta = \beta' \\ 0, & \text{otherwise} \end{cases} \quad (2.64)$$

Using this expression in Eq. (2.48) we get the following coupled gap equations:

$$\Delta_{11} = \frac{g_{11}^{\text{intra}} T}{V} \sum_{\mathbf{k}\omega_n} F^{11}(\mathbf{k}, \omega_n - ih) + \frac{g_{12}^{\text{intra}} T}{V} \sum_{\mathbf{k}\omega_n} F^{22}(\mathbf{k}, \omega_n - ih), \quad (2.65a)$$

$$\Delta_{22} = \frac{g_{21}^{\text{intra}} T}{V} \sum_{\mathbf{k}\omega_n} F^{11}(\mathbf{k}, \omega_n - ih) + \frac{g_{22}^{\text{intra}} T}{V} \sum_{\mathbf{k}\omega_n} F^{22}(\mathbf{k}, \omega_n - ih). \quad (2.65b)$$

The two branches of the BCS quasiparticle spectrum are simply $E_+ = E_{11}$ and $E_- = E_{22}$ and we get the following expression for the anomalous Green's function:

$$F^{\alpha\alpha}(\mathbf{k}, \omega_n - ih) = \frac{\Delta_{\alpha\alpha}}{(i\omega_n + E_{\alpha\alpha} + h)(i\omega_n - E_{\alpha\alpha} + h)}. \quad (2.66)$$

Following the same steps as in the previous section we finally get the following:

$$\Delta_{\alpha\alpha} = \sum_{\beta=1,2} \lambda_{\alpha\beta} \Delta_{\beta\beta} \int_{-\omega_n}^{\omega_n} \frac{d\xi_\beta}{4E_{\beta\beta}} \left(\tanh \frac{E_{\beta\beta} + h}{2T} + \tanh \frac{E_{\beta\beta} - h}{2T} \right). \quad (2.67)$$

Linearizing Eq. (2.67) with respect to the order parameters, again allows to obtain the superconducting critical temperature and critical field. We set $\Delta_{\alpha\alpha} = \epsilon\delta_\alpha$, where $\epsilon(T = T_c) = 0$, and obtain the following system:

$$\begin{pmatrix} \delta_1 \\ \delta_2 \end{pmatrix} \begin{pmatrix} \lambda_{11}I_1(T_c, h_c) - 1 & \lambda_{12}I_2(T_c, h_c) \\ \lambda_{21}I_1(T_c, h_c) & \lambda_{22}I_2(T_c, h_c) - 1 \end{pmatrix} = 0, \quad (2.68)$$

where

$$I_\alpha(T, h) = \int_{-\omega_c}^{\omega_c} \frac{d\xi}{4\tilde{\xi}_\alpha} \left\{ \tanh \left[\frac{\beta}{2} (\tilde{\xi}_\alpha + h) \right] + \tanh \left[\frac{\beta}{2} (\tilde{\xi}_\alpha - h) \right] \right\}, \quad (2.69)$$

with $\alpha = 1, 2$. The critical parameters are found by setting to zero the determinant of the matrix in Eq. (2.68).

2.3.7 Linearized gap equation for coupled interband and intraband order parameters

When including the superconducting coupling constants representing scattering processes connecting interband to intraband Cooper pairs, the gap equations for the interband and intraband order parameters become coupled. In this case the linearized gap equation yields the following system:

$$\begin{pmatrix} \delta_1 \\ \delta_2 \\ \delta_3 \end{pmatrix} \begin{pmatrix} \lambda_{11}I_1(T_c, h_c) - 1 & \lambda_{12}I_2(T_c, h_c) & \lambda_{13}I_3(T_c, h_c) \\ \lambda_{21}I_1(T_c, h_c) & \lambda_{22}I_2(T_c, h_c) - 1 & \lambda_{23}I_3(T_c, h_c) \\ \lambda_{31}I_1(T_c, h_c) & \lambda_{32}I_2(T_c, h_c) & \lambda_{33}I_3(T_c, h_c) - 1 \end{pmatrix} = 0, \quad (2.70)$$

where the constants $\lambda_{\alpha 3}$ and $\lambda_{3\alpha}$, with $\alpha = 1, 2$, represent the scattering processes connecting interband to intraband Cooper pairs, and λ_{33} corresponds to λ^{inter} in the main text. The terms I_α , $\alpha = 1, 2$ are given in Eq. (2.69), while I_3 corresponds to the energy integral in Eq. (2.62). Again, the critical parameters are found by setting to zero the determinant of the matrix in Eq. (2.70).

2.3.8 Results for a Two-Band Superconductor

We presented the linearized equations Eqs. (2.62) and (2.68) allowing to obtain the curve $h_c(T)$, for the interband and intraband domains, respectively. A remark here is needed, as shown below for the interband curves, to each temperature (except the maximum one), correspond two solutions for h . This is a problem for the numerical solver. To address this, first we find the value of the critical field corresponding to the maximum temperature of the superconducting curve. This can be done through

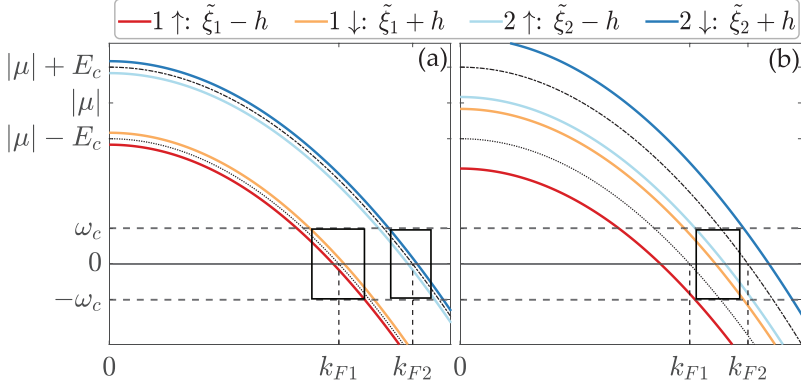


Figure 2.3: Band structure of the system in the presence of an exchange field, for (a) small and (b) large values of the field and generic values of E_c , γ , ω_c , μ . The rectangles indicate the regions where Cooper pair formation can occur.

analytical considerations as explained below. Having obtained this value we can then find separately a solution for the critical field higher and lower than this value, as a function of the temperature.

We consider a two bands system with spin-split hole-like parabolic bands: $\xi_{\mathbf{k}}^{(\alpha)} = -k^2/(2m_\alpha) - \mu$ with m_α the effective mass of the band α and μ the chemical potential. Defining the ratio between the two band masses as $\gamma = m_1/m_2$ we can write $\xi_{\mathbf{k}}^{(2)} = \gamma\xi_{\mathbf{k}}^{(1)} + (\gamma - 1)\mu$. The band structure of the system for generic values of E_c , γ , μ and two different limits of h is represented in Fig. 2.3, where we also show the energy cutoff of the effective attractive interaction ω_c . By examining the case of small spin-splitting represented in Fig. 2.3(a), we note that intraband pairing is favored, since bands with the same band index and opposite spin are close to each other. On the other hand, the presence of a large spin-splitting field can bring two bands with different band and spin indices closer to each other, favoring an interband pairing mechanism, as shown in Fig. 2.3(b).

To simplify the problem, we neglect those scattering processes connecting interband to intraband Cooper pairs and vice versa, *i.e.* we set $g_{\alpha\alpha,\alpha\beta} = g_{\alpha\beta,\alpha\alpha} = 0$ with $\alpha \neq \beta$. With these simplifications, from Eq. (2.48), the gap equation for the intraband and interband order parameters are decoupled and we can solve them separately. We set the chemical potential μ as the energy scale and choose the energy cutoff for the effective attractive interaction and the band separation to be $\omega_c = 0.2|\mu|$ and $E_c = 0.05|\mu|$, respectively. Furthermore, we consider dimensionless superconducting coupling constants: $\lambda_{\alpha\beta}^{\text{intra}} = N_\alpha(0)g_{\alpha\alpha,\beta\beta}$ and $\lambda^{\text{inter}} = N_1(0)g_{\alpha\beta,\alpha\beta}$, ($\alpha \neq \beta$), where $N_\alpha(0)$ is the density of states at the Fermi energy for the band α . Their values are chosen to be $\lambda_{11}^{\text{intra}} = 0.3$, $\lambda^{\text{inter}} = \lambda_{22}^{\text{intra}} = 2\lambda_{12}^{\text{intra}} = 0.2$. We assume that λ^{inter} can be taken to be larger than some $\lambda_{\alpha\beta}^{\text{intra}}$

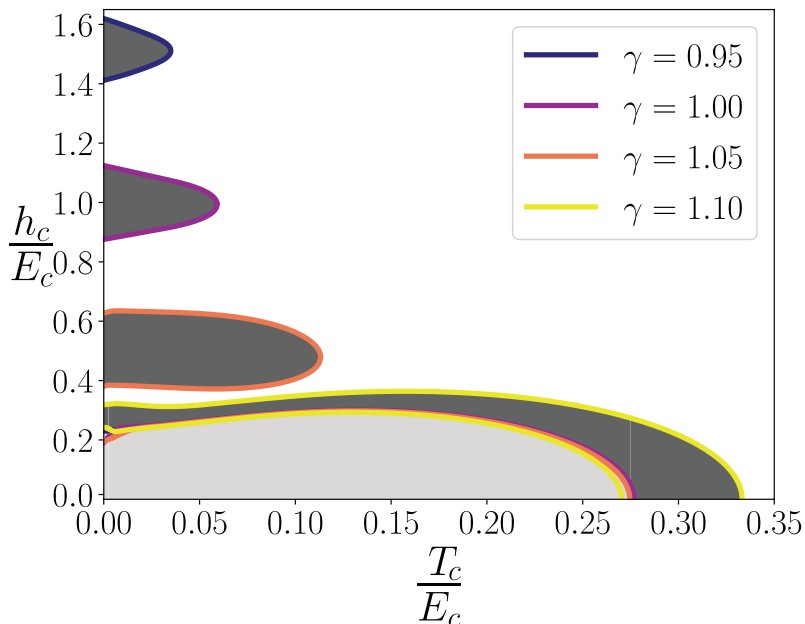


Figure 2.4: Critical field h_c as a function of temperature T for different values of the band mass ratio γ , for $E_c = 0.05 |\mu|$, $\lambda_{11}^{\text{intra}} = 0.3$, $\lambda^{\text{inter}} = \lambda_{22}^{\text{intra}} = 2\lambda_{12}^{\text{intra}} = 0.2$, and $\omega_c = 0.2 |\mu|$. The dark (light) gray areas represent the region of interband (intraband) superconducting coupling. Except for the case $\gamma = 1.1$, we note a reentrant superconductivity, with the two disconnected intra- and interband superconducting domains.

because of the external magnetic field, which may bring two different bands with opposite spin very close to each other in energy, see *e.g.* Fig. 2.3(b).

We determine the critical values of temperature T_c and exchange field h_c of our system for different values of the effective mass ratio γ by linearizing Eq. (2.48) with respect to $\Delta_{\alpha\alpha'}$, separately for interband ($\alpha \neq \alpha'$) and intraband ($\alpha = \alpha'$) superconducting pairing. The linearized gap equation in the interband case is given by Eq. (2.62) and the interband critical parameters are the values satisfying the equation. In the intraband case, instead we have the system given by Eqs. (2.68) and (2.69) and the intraband critical parameters are found by setting to zero the determinant of the matrix in Eq. (2.68)⁴.

The results are shown in Fig. 2.4, displaying reentrant superconductivity, *i.e.* the superconducting state present at zero magnetic field is first progressively destroyed and then recovered at a finite value of the magnetic field. The figure shows the inter- and intraband superconducting domains, delimited by the $h_c(T)$ curves, for

⁴Following publication it was confirmed that the solutions for the order parameter reported here minimize the free energy of the system.

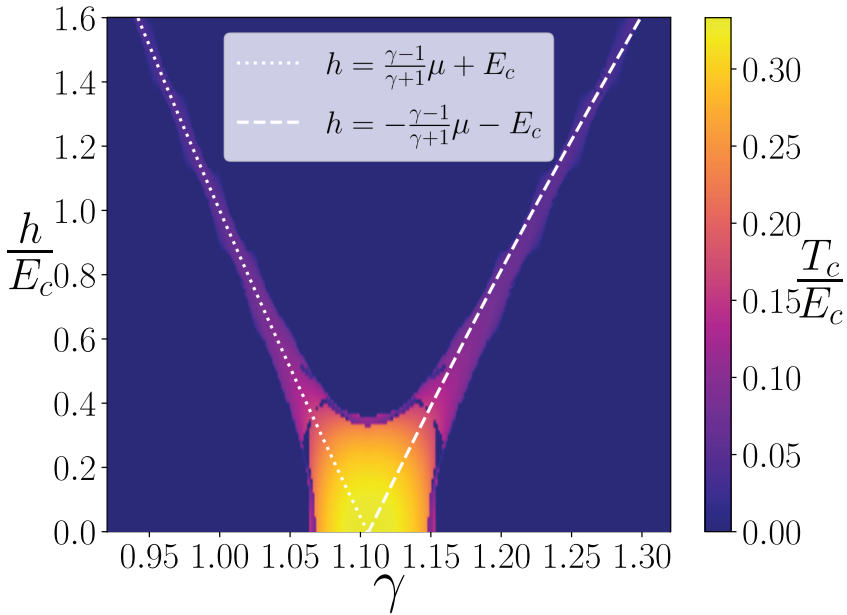


Figure 2.5: Critical temperature of the interband superconducting domains as a function of γ and h , for $E_c = 0.05 |\mu|$, $\lambda^{\text{inter}} = 0.2$, and $\omega_c = 0.2 |\mu|$.

different values of γ , the lines correspond to the critical values of temperature and exchange field, while the colored area identifies the superconducting region, with dark gray color identifying the interband regions and light gray the intraband. From Fig. 2.4, we immediately note that intraband regions develop around $h = 0$ for all the values of γ , while the interband regions, except for the case $\gamma = 1.1$, they are centered around a certain finite value of h .

Given these results, we can investigate how the band mass ratio γ influences the value of the exchange field at which the interband superconducting domains are centered. Cooper pairs are formed by electrons with opposite momenta close to the Fermi momentum, and energies in a “shell” of width ω_c around the Fermi energy. Therefore, only electrons meeting these two criteria can form Cooper pairs. In a multiband system with spin-split bands, each band will have its own intervals of energies and momenta where this can be realized. When the intervals of two different bands overlap, Cooper pair formation among them is feasible. These overlap regions are represented by the rectangles in Fig. 2.3.

Qualitatively, the maximum in the size of the overlap, and thus in the superconducting critical temperature, occurs when the Fermi momenta of the two bands involved are equal to each other. For Cooper pairs formed by one electron in band $1 \downarrow$ and the other in $2 \uparrow$, we have the equality for:

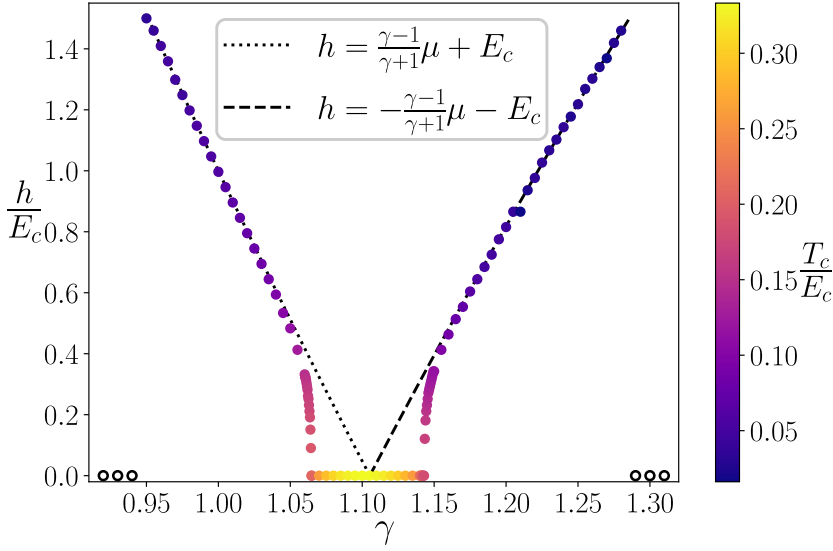


Figure 2.6: Scatter plot of the exchange field value corresponding to maximum T_c of the interband superconducting domains as a function of γ , for the same parameters as in Fig. 2.5. The color of dots corresponds to the value of T_c . Empty dots stand for values which do not present superconductivity.

$$h = \frac{\gamma - 1}{\gamma + 1} \mu + E_c. \quad (2.71)$$

While in the case of Cooper pairs formed by one electron in band 1 \uparrow and the other in band 2 \downarrow :

$$h = -\frac{\gamma - 1}{\gamma + 1} \mu - E_c. \quad (2.72)$$

Having determined the value of h which produces a maximum of the overlap in the different cases, with our choice of parameters we calculate numerically the critical temperature of the interband domains as a function of γ and h . The numerical results are plotted in Figs. 2.5 and 2.6 together with the theoretical prediction given by Eqs. (2.71) and (2.72).

Observing Fig. 2.5, we can see that peaks in T_c can be found for rather high values of the exchange field, up to $h \simeq 1.6E_c$. Therefore, when the system has both intraband and interband superconducting pairing, it can present two disconnected superconducting domains, one for low magnetic field due to the intraband pairing, and one for high magnetic field coming exclusively from interband pairing.

Finally, it is worth noting that the case of two electron-like bands yields qualitatively similar results. The difference is in the value of the band mass ratio γ at

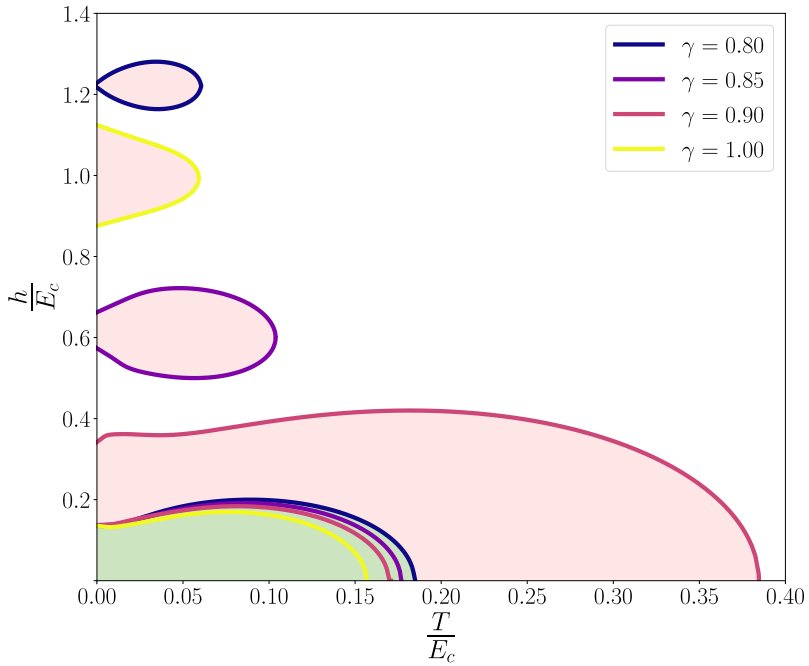


Figure 2.7: electron-like bands: critical field h_c as a function of temperature T for different values of the band mass ratio γ , for same values as in Fig. 2.4. The pink (green) areas represent the regions of interband (intraband) superconducting coupling.

which the band overlap occurs as can be seen in Fig. 2.7. The case where there is a coupling between an electron-like and a hole-like band is more complicated and would require a separate study.

Chapter 3

Fabrication Techniques for Curved Nanostructures

In this chapter we will present some of the recent advances in the fabrication of curved nanostructures¹.

3.1 Standard Fabrication Techniques

Conventional electronics and spintronics devices are manufactured with standard thin-film deposition, lithography and chemical etching techniques. A typical technique for the realization of thin-films is sputtering, a physical vapour deposition technique where the target material or cathode, is bombarded in a vacuum chamber by ions in order to vaporise (or sputter) atoms or molecules from it. The sputtered particles are then gradually deposited on a substrate or anode.

On the other hand, lithography in combination with etching can be used for patterning of thin films, and the realization of nanowires, arrays of nanowires and other structures. Some of the most common techniques are photolithography (or optical lithography), electron-beam (e-beam) lithography, focused ion-beam (FIO) lithography and dip-pen nanolithography (DPN). In photolithography, UV light is used to pattern a material in a desired shape: the film is exposed to the radiation and then the exposed or unexposed areas are removed. This is done with typical resolutions of 100nm, which can be pushed down to 15nm by means of surface plasmon interference [146]. In e-beam and FIO lithography the same is done through a focused beam of electrons or ions, respectively. The resolution of e-beam lithography can be as down as 1nm [147], while for FIO it is ~ 5 nm [148].

¹The following sections are not meant to be a complete review of fabrication methods for curved systems. For further details, see the reviews [142–145].

While all these techniques are negative lithography, since they remove parts of the material, DPN, first introduced by Mirkin and coworkers [149], can be considered as a positive technique, since it uses an atomic force microscope tip to deposit molecules of a substance on top of a substrate by capillary action, with resolutions lower than 50nm. These lithography methods are often coupled to chemical etching, also known as chemical milling, a technique where layers of a material are removed using etching chemicals. The use of masks to protect certain areas of the material allow to realize the desired structure.

Over the past twenty years, significant progress has been made in the manufacturing of geometrically curved nanostructures. The first breakthrough came with the realization of nanotubes by rolling up thin films through use of chemical etching: the films were deposited on top of an etchant-sensitive material, which was then selectively etched away, causing the film to wrap up and fold back [150, 151]. This has been followed by the development of novel processes and techniques for bending, wrinkling and buckling nanostructures. These techniques provide additional freedom for the design of new spintronics devices. For instance, independent control of spin and charge resistances has been achieved in a curved nanochannel realized through direct growth on curved templates [152].

3.2 Lithography Techniques

Generally, geometrically curved systems can be fabricated using techniques based on thin film deposition and lithography, similarly to their straight counterparts. For instance, e-beam lithography has been used to realize curved magnetic nanowires [153, 159–161] (see Fig. 3.1(a)), nanorings [162–165] and spirals [166]. Another common method is two-photon (TP) lithography, a technique similar to photolithography, in which patterning is achieved through two-photon absorption. TP lithography has been used to realize cylindrical nanowires [167], tetrapod structures and their lattice [156, 168, 169] (see Fig. 3.1(d)).

Combination of lithography and strain engineering techniques allows to realize complex 3D nanostructures. Strain engineering refers to the tuning of a material's properties through the modification of its structural or mechanical properties. This can be achieved in different ways, such as lattice mismatch between a material and its substrate, intrinsic and extrinsic defects, and mechanically shifting the atomic structure by changing bond length and angle. For instance, these techniques have been used for strain-induced bending of bilayers to realize nanotubes with diameters ranging from $\approx 4\mu\text{m}$ to 4nm, and nanohelices with minimum diameter of 7nm and their arrays [150, 151]. Additionally, photolithography combined with sputter deposition and strain application allowed to realize wrinkled membranes with thicknesses $< 2\mu\text{m}$ and bending radii $< 3\mu\text{m}$ [170–173]. Other structures

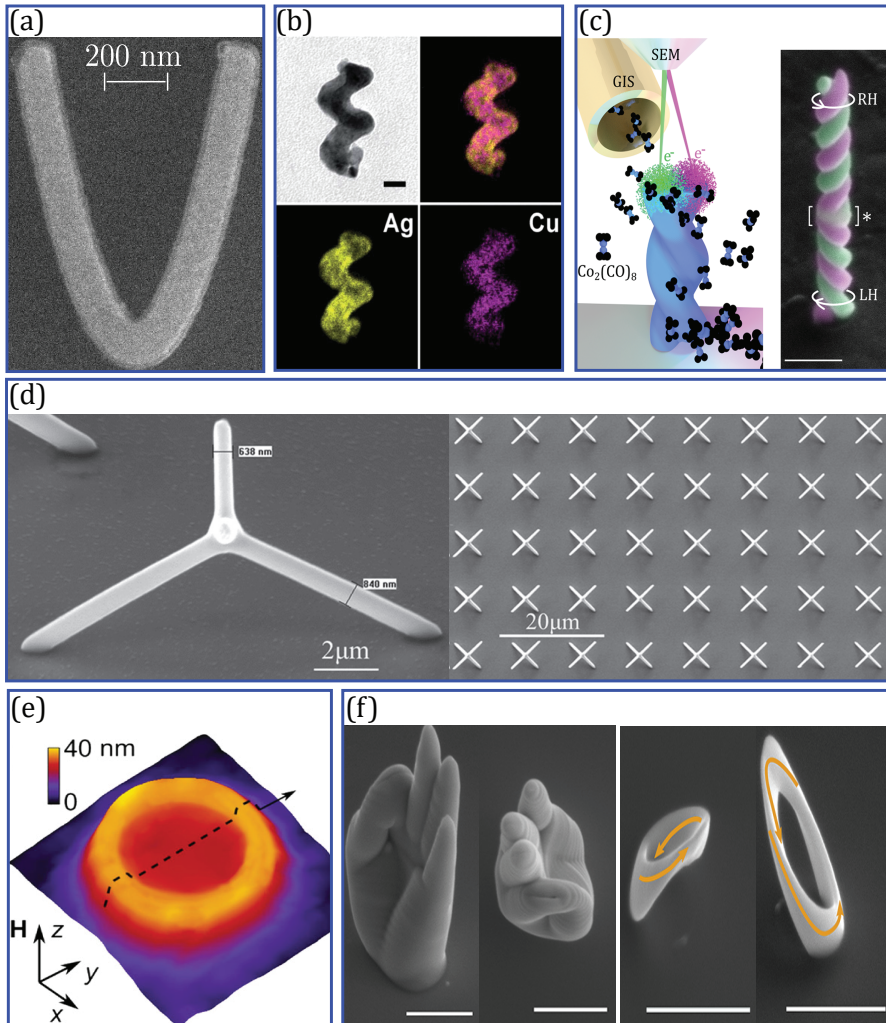


Figure 3.1: Fabrication of curved structures. (a) Parabolic stripe, patterned with electron beam lithography and ion beam etching [153]. (b) Two-turns Ag-Cu alloy nanohelix realized through Glancing Angle Deposition (GLAD), and energy-filtered TEM chemical mapping, the scale bar is 20nm [154]. (c) 3D printing of a cobalt double nanohelix through focused electron-beam induced deposition (FEBID) and its colored scanning electron microscope image, the scale bar is 250nm [155]. (d) Single tetrapod (left) and array of tetrapod structures (right), fabricated through two-photon lithography and electrodeposition [156]. (e) Nanovolcano realized through FEBID, with outer diameter of 300nm and crater diameter of 200nm [157]. (f) Side and top view of a nanoscale replica of a human hand (left) and Möbius nanoring (right) fabricated by FEBID, scalebars are $1\mu\text{m}$ [158]. Image permissions listed in footnote².

realized with similar methods are microhelix coils [174], Swiss-rolls, *i.e.* rolled-up nanomembranes, with diameters on the micrometer range [175–180], microscale polyhedral [181, 182] and more complex micro-origami structures [183–185].

Additionally, electrochemical synthesis techniques, such as coaxial lithography (COAL) and atomic layer deposition (ALD) have also been implemented to realize different curved nanostructures. COAL is a method involving sequential electrodeposition of conductive materials with different mechanical and chemical stabilities within anodic aluminum oxide templates, and it has been used to realize core/shell nanowires with diameters ranging from 20nm to 400nm and length from 8nm to few micrometers [186, 187]. ALD involves growth of films by exposing the surface of a template to different gaseous reactants, and it has been employed to realize multi-layered nanotubes with diameters of ~ 100 nm [188, 189].

These techniques allow in many cases to realize curved structures at the nanoscale when considering simple geometries. However, when dealing with more complex geometries they seem to be restricted to the microscale.

3.3 Glancing Angle Deposition

Alternatives to lithography are represented by Glancing Angle Deposition (GLAD) techniques [190]. GLAD is an extension of the oblique angle deposition (OAD) growth method where physical vapor is deposited at an oblique angle on a substrate. As evaporated single atoms or molecules reach the substrate nuclei are formed. Due to the oblique angle there is a shadowing effect where other incoming particles are prevented to condense in areas situated behind the previously formed nuclei. This means that particles are incorporated in the structure at the point of impact, thereby forming tilted columns. In addition to OAD, the substrate in GLAD can be rotated in the polar and azimuthal directions, allowing to control the columnar shape and therefore realize various different nanostructure designs, such as nanorods and nanohelices.

One of the limitation of GLAD is that it is often difficult to achieve a uniform thickness of the structure, since some columns will grow faster than other

²(a) Reproduced with permission from [153] Copyright 2019, American Physical Society. (b) Reproduced with permission from [154] Copyright 2014, Royal Society of Chemistry. (c) Reproduced under the terms of the ACS Author Choice with CC-BY license (https://pubs.acs.org/page/policy/authorchoice_ccby_termsofuse.html) from [155] Copyright 2020, American Chemical Society. (d) Reproduced under the terms of the CC-BY 3.0 license (<https://creativecommons.org/licenses/by/3.0/>) from [156] Copyright 2018 Authors, published by Royal Society of Chemistry. (e) Reproduced under the terms of the CC-BY 4.0 (<https://creativecommons.org/licenses/by/4.0/>) from [157] Copyright 2021 AIP Publishing. (f) Reproduced under the terms of the ACS Author Choice with CC-BY license (https://pubs.acs.org/page/policy/authorchoice_ccby_termsofuse.html) from [158] Copyright 2020, American Chemical Society.

columns, with a consequent shadowing of the slower growing columns. Moreover, a broadening increasing with the height of the structure is generally observed in GLAD.

GLAD has been used for the fabrication of nanohelices with a minimum length of $\sim 50\text{nm}$ and pitch $\sim 20\text{nm}$ [154, 191] (see Fig. 3.1(b)), nano-columns with various shapes [192] and arrays of posts, chevrons and helices, with single elements of nanoscale sizes [193–196].

3.4 Focused Electron Beam Induced Deposition

Recent advances in material science allow to overcome geometry-specific limitations through 3D nanoprinting methods, which include multiple techniques of beam and optical deposition. One of the most popular among these is focused electron-beam induced deposition (FEBID) [197, 198], a direct write method with resolution comparable to that of advanced e-beam lithography and to characteristic magnetic length scales, additionally allowing to realize arbitrarily complex structures.

In FEBID, a scanning electron microscope (SEM) generates a focused electron beam, which is then directed towards a precursor gas near the substrate. The interaction between the high-energy electrons and the precursor gas molecules results in the dissociation of the precursor and deposition on the substrate surface. The deposited material can be a metal, semiconductor, or insulator, depending on the precursor. Parameters such as electron beam intensity, precursor gas flow rate, and scan speed allow the control of composition and morphology of the deposited structures. FEBID allows for the fabrication of three-dimensional structures with dimensions below 10nm , with the world record pattern resolution of 1nm sized dots [199]. Moreover, FEBID can be performed under ambient conditions, eliminating the need for a high-vacuum environment. However, FEBID has a relatively low growth rate compared to other nanofabrication techniques, and the deposited structures may exhibit higher levels of contamination and impurities. Furthermore, a lateral broadening is observed: the lateral size of the grown structure is considerably larger than the electron beam probe size.

FEBID has been used to fabricate nanohelices with $4 - 12\mu\text{m}$ length and wire diameters of $\sim 100\text{nm}$ [200], and with lengths of $2 \sim \mu\text{m}$, wire diameters of $\sim 65 \sim \text{nm}$ and pitch of $\sim 2\mu\text{m}$ [201]. Moreover, double helices with length of 880nm , wire diameter of 68nm and pitch of 250nm have been realized [155] (see Fig. 3.1(c)). More complex structures have also been realized, such as nanocubes and nanotrees [202, 203], nanovolcanoes with outer diameter of 300nm and crater diameter of 200nm [157] (see Fig. 3.1(e)), Möbius nanorings and nanoscale replicas of human hands [158] (see Fig. 3.1(f)).

Given all these techniques, it is clear that there are plenty of possibilities in terms

of shapes of geometrically curved materials. This in turns allows for a multitude of device designs, which can be exploited for novel systems and applications.

Chapter 4

Curvature-Induced Effects and Theory of Curved Nanostructures

In this chapter we will discuss the main effects and interesting phenomena arising when geometric curvature is introduced in such systems. We will start by presenting the general theoretical framework for the study of geometric curvature in nanostructure, and then we will give a review on the literature studying the effects in curved nanostructures¹.

4.1 Theoretical Framework for Curved Nanostructures

When studying geometrically curved systems it is convenient to switch from Cartesian to orthonormal curvilinear coordinates. The approach presented below allows to study any arbitrarily curved nanostructures in 2D and 3D space. We will use the following approach for a general structure curved in 3D space, described through its curvature and torsion.

4.1.1 Frenet-Serret frame

As a start, we parametrize the 3D space as

$$\mathbf{R}(s, n, b) = \mathbf{r}(s) + n\hat{\mathcal{N}}(s) + b\hat{\mathcal{B}}(s). \quad (4.1)$$

Here $\mathbf{r}(s)$ is the parametrization of the curve in the plane of the curvature and s , n and b are the arclength, normal and binormal coordinates respectively, as it can be seen in Fig. 4.1. The geometry of the space can therefore be determined

¹For a broader review and further details on curvature induced effects in nanostructures, see [142–145, 204, 205].

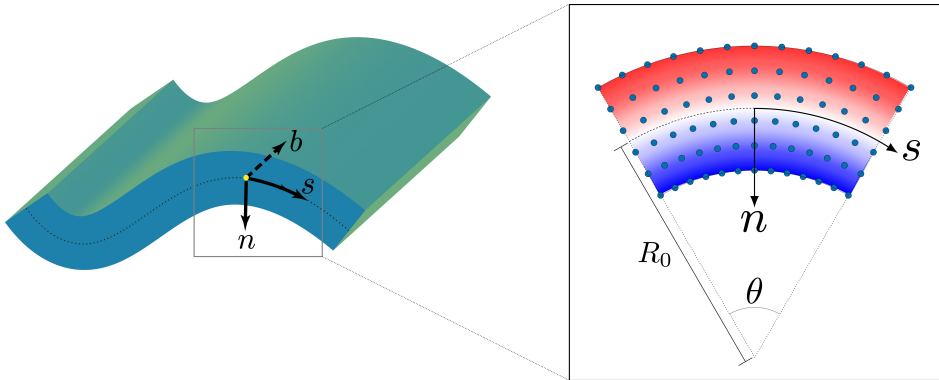


Figure 4.1: The figure shows the local coordinate system of a curved material, illustrating the tangential, normal and binormal directions. The finite curvature $\kappa = 1/R_0$ leads to regions with both tensile ($n < 0$) and compressive ($n > 0$) strain in the material [206, 207].

from the set of three orthonormal unit vectors: $\hat{\mathcal{T}}(s) = \partial_s \mathbf{r}(s) / |\partial_s \mathbf{r}(s)|$, $\hat{\mathcal{N}}(s) = \partial_s \hat{\mathcal{T}}(s) / |\partial_s \hat{\mathcal{T}}(s)|$ and $\hat{\mathcal{B}}(s) = \hat{\mathcal{T}}(s) \times \hat{\mathcal{N}}(s)$, representing the tangential, normal and binormal curvilinear directions respectively. These obey the following Frenet-Serret-type equation of motion:

$$\begin{pmatrix} \partial_s \hat{\mathcal{T}}(s) \\ \partial_s \hat{\mathcal{N}}(s) \\ \partial_s \hat{\mathcal{B}}(s) \end{pmatrix} = \begin{pmatrix} 0 & \kappa(s) & 0 \\ -\kappa(s) & 0 & \tau(s) \\ 0 & -\tau(s) & 0 \end{pmatrix} \begin{pmatrix} \hat{\mathcal{T}}(s) \\ \hat{\mathcal{N}}(s) \\ \hat{\mathcal{B}}(s) \end{pmatrix}, \quad (4.2)$$

where $\kappa(s) = |\partial_s \hat{\mathcal{T}}(s)|$ and $\tau(s) = |\partial_s \hat{\mathcal{B}}(s)|$ identify the curvature and torsion of the structure. By defining

$$u = \begin{pmatrix} \hat{\mathcal{T}}(s) \\ \hat{\mathcal{N}}(s) \\ \hat{\mathcal{B}}(s) \end{pmatrix}, \quad (4.3)$$

it is possible to rewrite Eq. (4.2) in a compact form:

$$\partial_s u_\alpha = F_{\alpha\beta} u_\beta. \quad (4.4)$$

By comparison with Eq. (4.2) the Frenet tensor $F_{\alpha\beta}$ is given by:

$$F_{\alpha\beta} = \begin{pmatrix} 0 & \kappa(s) & 0 \\ -\kappa(s) & 0 & \tau(s) \\ 0 & -\tau(s) & 0 \end{pmatrix}. \quad (4.5)$$

The covariant basis vectors are defined by:

$$\mathbf{e}_\alpha = \partial_\alpha \mathbf{R}(s, n, b), \quad (4.6)$$

where $\alpha = \{t, n, b\}$ and we use the subscript t, n, b for the tangential, normal and binormal components, respectively. In general the basis vectors are not orthogonal, and both the length and direction can vary in space [208]. The metric tensor is defined as

$$\mathcal{G}_{\alpha\beta} = \mathbf{e}_\alpha \cdot \mathbf{e}_\beta, \quad (4.7)$$

meaning the unit basis vectors are given by $\hat{e}_\alpha = \mathbf{e}_\alpha / \sqrt{\mathcal{G}_{\alpha\alpha}}$. The contravariant basis vectors \mathbf{e}^α are related to the covariant basis vectors by $\mathbf{e}_\alpha \cdot \mathbf{e}^\beta = \delta_\alpha^\beta$.

From Eq. (4.6), using Eqs. (4.1) and (4.2), we get the following form for the covariant basis vectors:

$$\mathbf{e}_t = \partial_s \mathbf{R} = \eta(s, n) \hat{\mathcal{T}} - b\tau(s) \hat{\mathcal{N}} + n\tau(s) \hat{\mathcal{B}}, \quad (4.8a)$$

$$\mathbf{e}_n = \partial_n \mathbf{R} = \hat{\mathcal{N}}, \quad (4.8b)$$

$$\mathbf{e}_b = \partial_b \mathbf{R} = \hat{\mathcal{B}}, \quad (4.8c)$$

where we have defined $\eta(s, n) = 1 - n\kappa(s)$. Using Eq. (4.7) and the above basis vectors, we get the following metric tensor:

$$\mathcal{G}_{\alpha\beta} = \begin{pmatrix} \eta(s, n)^2 + \zeta(s, n, b)^2 & -b\tau(s) & n\tau(s) \\ -b\tau(s) & 1 & 0 \\ n\tau(s) & 0 & 1 \end{pmatrix}, \quad (4.9)$$

where $\zeta(s, n, b) = \tau(s) \sqrt{n^2 + b^2}$.

Considering a general contravariant vector $\mathbf{v} = v^\beta \mathbf{e}_\beta$, we can write its gradient as:

$$\nabla \mathbf{v} = \mathbf{e}^\alpha \partial_\alpha v^\beta \mathbf{e}_\beta = \mathbf{e}^\alpha \left[(\partial_\alpha v^\beta) + v^\beta (\partial_\alpha \mathbf{e}_\beta) \right]. \quad (4.10)$$

We now define the Christoffel symbols of the second kind [208, 209]:

$$\Gamma_{\alpha\beta}^\gamma \mathbf{e}_\gamma = \partial_\beta \mathbf{e}_\alpha, \quad (4.11)$$

and obtain the following expression for the space covariant derivative of a contravariant vector:

$$\mathcal{D}_\alpha v^\beta = \partial_\alpha v^\beta + v^\gamma \Gamma_{\gamma\alpha}^\beta. \quad (4.12)$$

From this expression it is clear that, in general, in a curvilinear coordinate system the derivative of a vector contains additional terms with respect to Cartesian coordinate system, due to its basis vectors varying in space.

Using the relation between covariant and contravariant basis vectors provided above, we can relate the derivative of a contravariant basis vector to the Christoffel symbols: $\partial_\gamma \mathbf{e}^\beta = -\Gamma_{\alpha\gamma}^\beta \mathbf{e}^\alpha$. Therefore, we can write the space covariant derivative of a covariant vector as:

$$\mathcal{D}_\alpha v_\beta = \partial_\alpha v_\beta - v_\gamma \Gamma_{\alpha\beta}^\gamma. \quad (4.13)$$

It can be shown [208, 209] that the Christoffel symbols are related to the metric of the systems through the following expression:

$$\Gamma_{\alpha\beta}^\gamma = \frac{1}{2} \mathcal{G}^{\gamma\lambda} [\partial_\beta \mathcal{G}_{\alpha\lambda} + \partial_\alpha \mathcal{G}_{\lambda\beta} - \partial_\lambda \mathcal{G}_{\alpha\beta}], \quad (4.14)$$

where $\mathcal{G}^{\gamma\lambda}$ is the inverse of the metric tensor of Eq. (4.9), given by:

$$\mathcal{G}^{\alpha\beta} = \frac{1}{\eta(s, n)^2} \begin{pmatrix} 1 & b\tau(s) & -n\tau(s) \\ b\tau(s) & \eta(s, n)^2 + b^2\tau(s)^2 & -nb\tau(s)^2 \\ -n\tau(s) & -nb\tau(s)^2 & \eta(s, n)^2 + n^2\tau(s)^2 \end{pmatrix}. \quad (4.15)$$

From Eq. (4.14) we see that $\Gamma_{\alpha\beta}^\gamma$ is invariant under the exchange of the lower indices $\alpha \leftrightarrow \beta$. From Eq. (4.14), with the use of Eqs. (4.9) and (4.15), the Christoffel symbols take the following form

$$\Gamma_{\alpha\beta}^s = \frac{1}{\eta(s, n)} \begin{pmatrix} \partial_s \eta(s, n) + b\kappa(s)\tau(s) & -\kappa(s) & 0 \\ -\kappa(s) & 0 & 0 \\ 0 & 0 & 0 \end{pmatrix}, \quad (4.16a)$$

$$\Gamma_{\alpha\beta}^n = \frac{1}{\eta(s, n)} \begin{pmatrix} -\eta(s, n)^2 \partial_n \eta(s, n) + b \partial_s [\eta(s, n) \tau(s)] & -b\kappa(s)\tau(s) & -\tau(s) \\ +\kappa(s)\zeta(s, n, b)^2 - n\tau(s)^2 & 0 & 0 \\ -b\kappa(s)\tau(s) & 0 & 0 \\ -\tau(s) & 0 & 0 \end{pmatrix}, \quad (4.16b)$$

$$\Gamma_{\alpha\beta}^b = \frac{1}{\eta(s, n)} \begin{pmatrix} n[\partial_s(\eta(s, n))\tau(s) - \eta(s, n)\partial_s\tau(s)] - b\tau(s)^2 & \tau(s) & 0 \\ \tau(s) & 0 & 0 \\ 0 & 0 & 0 \end{pmatrix}. \quad (4.16c)$$

It is important to note that, due to the space dependence of the length of the basis vectors, the components v_α of a vector, can generally have incorrect physical dimensions. To solve this we introduce the physical components of a vector as:

$$v_{\langle\alpha\rangle} = \hat{e}_\alpha \cdot \mathbf{v} = \frac{v_\alpha}{\sqrt{\hat{G}_{\alpha\alpha}}}. \quad (4.17)$$

In Cartesian coordinates the metric is the identity matrix, and therefore the notion of physical vector components is not necessary.

4.1.2 Curvature Induced Spin-Orbit Coupling

When a material with initially regular atomic lattice is induced to bend, the inter-atomic distances become non-uniform, leading to tensile and compressive strains in the material, see Fig. 4.1. The strain is directly related to the change in length of the different coordinate axes when deforming the line segment [210], which for the tangential component (see Eq. (4.8a)) results in a strain [206, 207, 211]:

$$\epsilon_{tt} = -\kappa(s)n. \quad (4.18)$$

The deformation leads to an additional potential in the material, which for small strains is assumed to be linear in strain [212, 213],

$$V = -\Lambda\kappa(s)n, \quad (4.19)$$

where Λ is the deformation potential constant. This approximation should be applicable when the thickness of the material is much smaller than the local radius of curvature. The potential in turn leads to an electric field:

$$\mathbf{E} = -\nabla V = \frac{\hat{e}^\alpha}{\sqrt{\hat{G}_{\alpha\alpha}}} \partial_\alpha V = \frac{\Lambda n}{\sqrt{\eta(s, n)^2 + \zeta(s, n, b)^2}} [\partial_s \kappa(s)] \hat{\mathcal{T}} + \Lambda \kappa(s) \hat{\mathcal{N}}, \quad (4.20)$$

which when averaged over a volume with infinitesimal thickness ds in the tangential direction results in an electric field pointing along the normal direction [206, 207],

$$\langle \mathbf{E} \rangle = \Lambda \kappa(s) \hat{\mathcal{N}}. \quad (4.21)$$

In the rest frame of an electron moving with momentum $\mathbf{p} = \hbar \mathbf{k}$, this translates to a magnetic field $\mathbf{B} \sim \mathbf{p} \times \mathbf{E}$ [214] which couples to the electron's spin via the Zeeman coupling, leading to an effective spin-orbit coupling

$$H_N = \frac{\alpha_N}{m^*} \hat{\mathcal{N}} \cdot [\boldsymbol{\sigma} \times \boldsymbol{p}], \quad (4.22)$$

due to the asymmetry in the normal direction. Here we have defined the curvature-dependent spin-orbit constant $\alpha_N = \hbar \Lambda g |e| \kappa(s) / 4m^* c^2$ [1], where g is the g -factor that characterizes the magnetic moment and angular momentum, e the electron mass, and c is the speed of light.

4.2 Curvature-Induced Effects

In this section we will review some theoretical works in geometrically curved systems, treating magnetic and non-magnetic systems separately. Here we will not consider curved superconductors, for which fabrication methods and theoretical studies are still in their infancy². Later in this thesis we will focus on curved structures proximity-coupled to bulk superconductors.

4.2.1 Non-magnetic Systems

For curved non-magnetic systems, theoretical investigations have been using mainly a ballistic quantum motion approach. A fundamental tool for the study of curved structures is the thin-wall quantization procedure [216, 217], where the quantum motion of a particle in a 2D torsion-less curved surface is treated as equivalent to the motion in a 3D space with the addition of lateral quantum confinement. The effects of curvature are then included in a curvature-induced quantum geometric potential (QGP). With this procedure, the energy of excitations in the normal direction results far above the energy of the excitations in the tangential direction. This allows to integrate out the motion in the normal direction and derive an effective 1D Hamiltonian [206]. More recently this approach has been generalized to include torsion [218], showing the appearance of an equivalent torsion-induced QGP, which allows to apply the same procedure for the binormal direction.

Within this framework geometric curvature introduces two main effects: the QGP, producing many interesting phenomena at the nanoscale [219–222] and a strain field leading to a curvature-induced Rashba spin-orbit coupling (SOC) [206, 223, 224] (see Section 4.1.2). In addition, intrinsic SOC, which may or may not be present in some materials, is governed by the geometry of the system [206, 218, 225]. Studies have focused on new properties appearing as a consequence of these effects in different classes of materials, *e.g.* semiconductors [226–231] and superconductors [232–235]. For instance, it was shown that geometric curvature

²For reviews on curved superconductors, see *e.g.* [145, 215].

can promote topological surface states in deformed wires [219], edge states in bent quantum wires with Rashba SOC [227], bound states in toroidal surfaces [221] and in rolled-up nanotubes [222], as well as topological superconductivity in superconducting Rashba nanowires [233] and in curved 2D topological insulators [235]. Moreover, various studies have shown the possibility of geometric control of the spin phase of the electrons during their dynamics in curved circuits [226, 236–238], potentially driving topological transitions [239–242].

Aside from the quantum confinement effects due to curvature, curved nanostructures exhibit also classical geometry-induced effects. These effects have been recently analyzed in Ref.[205], where they have been categorized as falling into three broad areas: curved spintronics, geometric nonlinear Hall effect and directional-dependent magnetotransport. Curved spintronics comprises all those effects resulting from the geometry of curved channels, which, for instance can allow independent control of charge and spin transport properties [152]. A nonlinear, geometric Hall effect, in absence of any externally applied magnetic field, has been demonstrated in a semicircular curved wire [243]. Finally, considering directional-dependent magnetotransport, a quadratic longitudinal magnetoresistance has been experimentally observed in graphite nanotubules [244] and in a single multiwalled carbon nanotube [245], and later demonstrated theoretically [230]. Moreover, the oscillations of the effective magnetic field experienced by electrons in carbon nanotubes cause the appearance of classical snake orbits [230]. These trajectories have an impact on the magnetotransport properties of tubular nanostructures [205, 230, 246–248].

4.2.2 Micromagnetic Theory for Ferromagnetic Systems

One general theoretical description of curvature-induced effects in curved ferromagnets is based on micromagnetic frameworks. The first studies developed theories based on specific geometries, to study the influence of the geometry of the systems on magnetism in *e.g.* cylinders [249–251], necks and circular cones [251–253], nanorings [254], nanotubes [255], toruses [256, 257], curved wires [258, 259] and spherical shells [260, 261]. Later, Gaididei *et al.* [262] developed a framework for generic curved geometries, showing that the effect of curvature can be treated as the appearance of an effective magnetic field. More recently, Sheka *et al.* [263] generalized this framework to include non-local magnetostatic interactions, leading to a chiral interaction whose effect is to introduce handedness in intrinsically achiral materials, potentially producing ferrotoroidic order and magnetoelectric response.

A micromagnetic framework for an uniaxial ferromagnet is formulated through its energy density:

$$\mathcal{E} = \mathcal{E}_x + \mathcal{E}_A + \mathcal{E}_{\text{DM}} + \mathcal{E}_{\text{MS}}, \quad (4.23)$$

where \mathcal{E}_x is the exchange energy density, \mathcal{E}_A is the anisotropy energy density, \mathcal{E}_{DM} is the Dzyaloshinskii–Moriya interaction (DMI) energy density and \mathcal{E}_{MS} is the magnetostatic energy density. These contributions can be written in terms of the normalized magnetization \mathbf{m} in the following way:

$$\mathcal{E}_x = -A\mathbf{m} \cdot \nabla^2 \mathbf{m}, \quad (4.24a)$$

$$\mathcal{E}_A = \frac{K}{2}(\mathbf{m} \cdot \hat{\mathbf{e}}_a)^2, \quad (4.24b)$$

$$\mathcal{E}_{\text{DM}} = D \sum_{ijk} (m_i \partial_k m_j - m_j \partial_k m_i), \quad (4.24c)$$

$$\mathcal{E}_{\text{MS}} = \frac{1}{2} M_s^2 \int d\mathbf{r}' \frac{[\mathbf{m}(\mathbf{r}) \cdot \nabla_{\mathbf{r}}] [\mathbf{m}(\mathbf{r}') \cdot \nabla_{\mathbf{r}'}]}{|\mathbf{r} - \mathbf{r}'|}, \quad (4.24d)$$

where A is the exchange constant, K and $\hat{\mathbf{e}}_a$ are the anisotropy constant and anisotropy axis, respectively, D is the DMI constant and M_s is the saturation magnetization.

In order to obtain curvature-induced effects, the system is then described in a curvilinear reference frame, in which all the terms containing spatial derivatives are consequently reshaped. One can group together all the terms according to their spatial symmetry and rewrite the energy density of Eq. (4.23) as [263]:

$$\mathcal{E} = \mathcal{E}_0 + \tilde{\mathcal{E}}_A + \tilde{\mathcal{E}}_{\text{DM}} + \tilde{\mathcal{E}}_{\text{MS}}, \quad (4.25)$$

where the first term in the right hand side contains all the terms that do not explicitly depend on the curvature. The second term $\tilde{\mathcal{E}}_A$, is the effective anisotropy and contains the intrinsic anisotropy \mathcal{E}_A and an extrinsic curvature-induced contribution. The extrinsic term in turn contains two contributions: one is driven by the exchange interaction and the other is driven by DMI. Similarly, the effective DMI term $\tilde{\mathcal{E}}_{\text{DM}}$, includes an intrinsic DMI written in the curvilinear framework and a curvature-induced, extrinsic exchange-driven contribution. The last term $\tilde{\mathcal{E}}_{\text{MS}}$ represents the magnetostatic interaction. It is usually expressed by decomposing the volume and surface magnetostatic charges in three components [263]: a surface charge σ obtained from the normal component of the magnetization, a tangential charge ρ from the tangential component and a geometrical charge g , representing the coupling between the geometric curvature and the magnetization texture. The magnetostatic interaction is then expressed as a sum of terms representing different pair interactions between these three charges.

Table 4.1: Table showing approximate exchange and anisotropy constants, and the resulting maximum curvature κ_c [204] for a few ferromagnetic materials at low temperatures.

Material	A (J/m)	$ K $ (J/m ³)	κ_c (nm ⁻¹)
Cobalt	$\sim 2 \times 10^{-11}$ [271]	$\sim 8 \times 10^5$ [272]	~ 0.1
Iron	$\sim 2 \times 10^{-11}$ [273, 274]	$\sim 5 \times 10^4$ [274, 275]	~ 0.03
Nickel	$\sim 1 \times 10^{-11}$ [274]	$\sim 1 \times 10^5$ [274, 276]	~ 0.07

Curvature-induced anisotropy and extrinsic DMI have been shown to be the source of an effective curvature-induced magnetic field [204, 262]. These terms generally influence ground state magnetization and spin-wave dynamics. For instance, in an helical wire with easy-tangential anisotropy the ground state magnetization is tilted, resulting in a quasi-tangential state, and mirror symmetry is broken in the spin-wave spectrum [264]. Curvature also produces a gap in the magnon spectrum of nanotubes [265].

Another intriguing curvature-induced effect is the interplay between local and global geometric aspects, supported by nonlocal magnetic interactions. This interplay manifests in the appearance of topologically protected magnetization textures in topologically non-trivial curved geometries [144]. Some examples are the formation of vortex and transverse domain walls in nanotubes [266], skyrmion and vortex textures in hyperboloids [267], transversal and longitudinal domain walls across and along Möbius rings [268], whirligig and 3D onion states in spherical shells [269] and toroidal and poloidal vortices in toroidal nanoshells [270]. These findings are interesting in the context of our study, since we will consider curved ferromagnetic wires coupled to bulk superconductors. We will show that the interplay between curvature and proximity induced superconductivity in the ferromagnetic wire generates magnetization components in different directions with respect to the exchange field.

From all this it is clear that the curvature influences the magnetic state, inducing more complicated magnetization textures than a purely tangential exchange field, which we will assume later in this thesis. However, Sheka *et al.* [204] showed theoretically for Heisenberg magnets that in a curved ferromagnetic wire with tangential uniaxial anisotropy, the magnetic ground state remained oriented in the tangential direction as long as the curvature was lower than a critical curvature $\kappa_c \approx 0.657\sqrt{|K|/A}$, where A and K are the exchange and anisotropy constants respectively. The critical curvature is therefore inversely proportional to the domain wall length [277]. Assuming that a similar analysis is applicable also to metallic

ferromagnets, one should use materials with strong uniaxial anisotropy to ensure a tangential exchange field. The critical curvatures, according to the results in Ref. [204], for a few ferromagnetic materials relevant for spintronics systems are given in Table 4.1.

Finally we conclude by mentioning a recent interesting effect which has been observed experimentally, that is the appearance of superconducting triplet rim currents in a spin-textured ferromagnetic disk coupled to a superconducting disk [278]. From the analysis performed in this study the curved surfaces appear to be central to obtain rim supercurrents, but their observation is not yet fully understood from a theoretical perspective.

4.2.3 Antiferromagnetic Systems

While for curved ferromagnets there has been plenty of experimental and theoretical investigations, for curvilinear antiferromagnets the field is still in its infancy. To the best of our knowledge, only a few studies have been carried out so far for antiferromagnetic chains [279–282]. In the following we will summarize the theoretical description of a curvilinear antiferromagnetic chain presented in Refs[145, 280], highlighting some of their findings, useful for the analysis presented later in this thesis.

A general Hamiltonian for a lattice of classical magnetic moments, valid both in the straight and curvilinear case, can be written as [145, 280]:

$$\mathcal{H} = S^2 \sum_{\langle ij \rangle} J_{ij} \mathbf{m}_i \cdot \mathbf{m}_j + S^2 \sum_i K_i (\mathbf{m}_i \cdot \hat{\mathbf{e}}_A)^2 - \mu \sum_i \mathbf{m}_i \cdot \mathbf{H}_i^d. \quad (4.26)$$

The first term in Eq. (4.26) represents the exchange interaction, where \mathbf{m}_i is the unit magnetic moment of site i , J_{ij} is the exchange integral between sites i and j and S is the spin length. The second term represents the anisotropy, with K_i anisotropy constant of site i and $\hat{\mathbf{e}}_A$ anisotropy axis. The last term is the dipolar interaction, where $\mu = g\mu_B S$ with g Landé factor and μ_B Bohr magneton. The dipolar field of site i is given by:

$$\mathbf{H}_i^d = -\mu \sum_{j \neq i} \frac{\mathbf{m}_j r_{ij}^2 - 3\mathbf{r}_{ij} (\mathbf{m}_j \cdot \mathbf{r}_{ij})}{r_{ij}^5}, \quad (4.27)$$

where $\mathbf{r}_{ij} = \mathbf{r}_i - \mathbf{r}_j$. To study a curvilinear antiferromagnet, it is assumed that the system is described by a parametrization $\mathbf{r}(s)$ having curvature $\kappa(s)$ and torsion $\tau(s)$, where s is the arclength coordinate, defined in Section 4.1.1 and Fig. 3.1. The next step is to switch to a continuum model and define two vector fields from the magnetization of the two sublattices \mathbf{m}_1 and \mathbf{m}_2 , the total magnetization

$\mathbf{m}(s) = (\mathbf{m}_1 + \mathbf{m}_2)/2$ and the Néel vector $\mathbf{n}(s) = (\mathbf{m}_1 - \mathbf{m}_2)/2$. The Lagrangian of the system is given by:

$$L = -\frac{2M_s}{\gamma_0} \int ds \left[\mathbf{m} \cdot \left(\mathbf{n} \times \frac{\partial \mathbf{n}}{\partial t} \right) - \mathcal{E} \right], \quad (4.28)$$

where M_s is the saturation magnetization of one sublattice and γ_0 is the gyromagnetic ratio. The energy density \mathcal{E} is derived from the Hamiltonian of Eq. (4.26).

The model presented above, has been developed and applied in Ref.[280] in the case of an antiferromagnetic helix chain, using the same method derived for curvilinear ferromagnets to obtain the effective energy density of the antiferromagnet in a curvilinear reference frame.

If the total magnetization and its derivatives are small, then $|\mathbf{m}|, |\mathbf{m}'|, |\mathbf{m}''| \ll |\mathbf{n}|$ and the effective energy density reads [280]:

$$\mathcal{E} = \mathcal{E}_x + \mathcal{E}_A + \mathcal{E}_{\text{DM}} + K n_T^2, \quad (4.29)$$

where \mathcal{E}_x is the exchange contribution, and \mathcal{E}_A and \mathcal{E}_{DM} are curvature-induced anisotropy and DMI, respectively. These contributions read:

$$\mathcal{E}_x = A \partial_s n_\alpha \partial_s n_\alpha, \quad (4.30a)$$

$$\mathcal{E}_A = A K_{\alpha\beta} n_\alpha n_\beta, \quad (4.30b)$$

$$\mathcal{E}_{\text{DM}} = A F_{\alpha\beta} (n_\alpha \partial_s n_\beta - n_\beta \partial_s n_\alpha), \quad (4.30c)$$

where A is the exchange stiffness, $F_{\alpha\beta}$ is the Frenet tensor defined in Eq. (4.5), and $K_{\alpha\beta} = F_{\alpha\gamma} F_{\beta\gamma}$ is the curvature-induced exchange driven anisotropy tensor. The DM contribution is linear in curvature and torsion, while the anisotropy term is quadratic. The last term in Eq. (4.29), is an effective hard axis anisotropy with axis along the tangential direction, resulting from the dipolar interaction in the absence of other anisotropy contributions [280].

The Néel vector orientation of the equilibrium state in the curvilinear coordinate system can either be homogeneous, *i.e.* constant orientation with respect to the curved reference frame, or periodic, *i.e.* varying as a function of the arclength coordinate along the geometry of the structure, depending on the strength of the DMI. We identify the direction of the Néel vector in the curvilinear coordinate system with $\mathbf{n} = \cos \theta \hat{\mathbf{T}} + \sin \theta \cos \phi \hat{\mathbf{N}} + \sin \theta \sin \phi \hat{\mathbf{B}}$. The homogeneous state is realized for $\tau < \tau_b(\kappa) \approx 0.85\kappa$ and the orientation of the Néel vector is given by $\theta = \pi/2 - \psi$ and $\phi = \pi/2$, with $\psi \approx \kappa\tau L^2$, L being the length of the chain. Thus the Néel vector lies in the TB plane. Conversely, the periodic state is realized for $\tau > \tau_b(\kappa)$ and the orientation of the Néel vector in this configuration is approximately uniform in the plane perpendicular to the helix axis. For $\kappa \ll \tau$,

the orientation of the Néel vector is given by $\theta = \pi/2$ and $\phi = -\tau s$, where s is the arclength coordinate.

This analysis shows that a curvilinear antiferromagnetic helix has a chiral behavior and that geometric curvature and torsion control the strength of the DMI and the orientation of the Néel vector, realizing a homogeneous or periodic state [280]. Later on we will make use of these findings in the context of a diffusive treatment of proximity coupled superconductor-antiferromagnetic helix hybrid structures, assuming the antiferromagnet to be in the homogeneous state.

Chapter 5

Diffusive Theory of Superconductivity

In this chapter we will derive a transport equation for the quasiclassical Green's function in the diffusive limit at equilibrium. This transport equation, with suitable boundary conditions allows to study the proximity effect in superconductor-ferromagnet hybrid structures. Finally, we will show how the equation is modified in the context of curvilinear geometries.

5.1 Usadel Equation

The quasiclassical framework describes electronic transport in materials with high number of impurities. It allows to define a system of second-order partial differential equations for the Green's functions of the systems. In this section we will first define the Green's function in the Keldysh formalism, and show how the quasiclassical transport equations can be derived in the diffusive regime. We will then discuss how these equations can be used to study different materials. Throughout this section we will set $\hbar = 1$.

5.1.1 Green's function in the Keldysh formalism

In quantum field theory, Green's functions are defined in various ways, with slight variations among them, generally including the expectation value of a product of creation and annihilation operators. Here we define the single particle Green's function (see [94]) as:

$$\mathcal{G}_{\sigma\sigma'}(\mathbf{r}, t; \mathbf{r}', t') = -i \left\langle \text{T} \psi_{\sigma}(\mathbf{r}, t) \psi_{\sigma'}^{\dagger}(\mathbf{r}', t') \right\rangle, \quad (5.1)$$

where T is the time-ordered product, the field operator $\psi_{\sigma'}^{\dagger}(\mathbf{r}', t')$ creates a particle with spin σ' , in position \mathbf{r}' , at time t' , while $\psi_{\sigma}(\mathbf{r}, t)$ annihilates a particle with spin σ , in position \mathbf{r} and time t . If we assume $t > t'$, the Green's function can be regarded as the probability amplitude for a particle to propagate from \mathbf{r}' , at time t' , to position \mathbf{r} , at time t . Therefore, Green's functions are often referred to as propagators.

In the Keldysh formalism [283–285], one defines the following three Green's functions

$$G_{\sigma\sigma'}^R(\mathbf{r}, t; \mathbf{r}', t') = -i \left\langle \left\{ \psi_{\sigma}(\mathbf{r}, t), \psi_{\sigma'}^{\dagger}(\mathbf{r}', t') \right\} \right\rangle \theta(t - t'), \quad (5.2)$$

$$G_{\sigma\sigma'}^A(\mathbf{r}, t; \mathbf{r}', t') = +i \left\langle \left\{ \psi_{\sigma}(\mathbf{r}, t), \psi_{\sigma'}^{\dagger}(\mathbf{r}', t') \right\} \right\rangle \theta(t' - t), \quad (5.3)$$

$$G_{\sigma\sigma'}^K(\mathbf{r}, t; \mathbf{r}', t') = -i \left\langle \left[\psi_{\sigma}(\mathbf{r}, t), \psi_{\sigma'}^{\dagger}(\mathbf{r}', t') \right] \right\rangle, \quad (5.4)$$

where $G^{R, A, K}$ are the *retarded*, *advanced*, and *Keldysh* Green's functions, respectively. In the context of superconductivity, we need to describe the Cooper pairs. This is done by defining the following anomalous components:

$$F_{\sigma\sigma'}^R(\mathbf{r}, t; \mathbf{r}', t') = -i \left\langle \left\{ \psi_{\sigma}(\mathbf{r}, t), \psi^{\sigma'}(\mathbf{r}', t') \right\} \right\rangle \theta(t - t'), \quad (5.5)$$

$$F_{\sigma\sigma'}^A(\mathbf{r}, t; \mathbf{r}', t') = +i \left\langle \left\{ \psi_{\sigma}(\mathbf{r}, t), \psi^{\sigma'}(\mathbf{r}', t') \right\} \right\rangle \theta(t' - t), \quad (5.6)$$

$$F_{\sigma\sigma'}^K(\mathbf{r}, t; \mathbf{r}', t') = -i \left\langle \left[\psi_{\sigma}(\mathbf{r}, t), \psi^{\sigma'}(\mathbf{r}', t') \right] \right\rangle. \quad (5.7)$$

Throughout this work, we will study proximity effects between superconducting and magnetic materials. In this context, it is useful to introduce the following basis, in the Nambu \otimes spin space, describing particle and holes both with spin-up and spin-down:

$$\Psi^{\dagger}(\mathbf{r}, t) = \left(\psi_{\uparrow}^{\dagger}(\mathbf{r}, t), \psi_{\downarrow}^{\dagger}(\mathbf{r}, t), \psi_{\downarrow}(\mathbf{r}, t), \psi_{\uparrow}(\mathbf{r}, t) \right). \quad (5.8)$$

In this basis, one can group together the normal and anomalous Green's function in Eqs. (5.4) and (5.7) in the following 4×4 form:

$$\hat{G}^R(\mathbf{r}, t; \mathbf{r}', t') = -i\hat{\tau}_3 \left\langle \left\{ \Psi(\mathbf{r}, t), \Psi^{\dagger}(\mathbf{r}', t') \right\} \right\rangle \theta(t - t'), \quad (5.9)$$

$$\hat{G}^A(\mathbf{r}, t; \mathbf{r}', t') = +i\hat{\tau}_3 \left\langle \left\{ \Psi(\mathbf{r}, t), \Psi^{\dagger}(\mathbf{r}', t') \right\} \right\rangle \theta(t' - t), \quad (5.10)$$

$$\hat{G}^K(\mathbf{r}, t; \mathbf{r}', t') = -i\hat{\tau}_3 \left\langle \left[\Psi(\mathbf{r}, t), \Psi^{\dagger}(\mathbf{r}', t') \right] \right\rangle, \quad (5.11)$$

where $\hat{\tau}_3 = \text{diag}(1, 1, -1, -1)$. It is useful to express these in a single 8×8 matrix:

$$\check{G}(\mathbf{r}, t; \mathbf{r}', t') = \begin{pmatrix} \hat{G}^R(\mathbf{r}, t; \mathbf{r}', t') & \hat{G}^K(\mathbf{r}, t; \mathbf{r}', t') \\ 0 & \hat{G}^A(\mathbf{r}, t; \mathbf{r}', t') \end{pmatrix}. \quad (5.12)$$

Many useful observables in superconducting hybrid structures can be expressed as functions of the Green's function of Eq. (5.12). In and out of equilibrium, we have the following relation between retarded and advanced Green's function:

$$\hat{G}^A = -\hat{\tau}_3 \left(\hat{G}^R \right)^\dagger \hat{\tau}_3. \quad (5.13)$$

5.1.2 Quasiclassical Approximation

To obtain the Green's function of a system, an equation of motion is needed. Typically, for superconducting hybrid systems, one can derive the Gor'kov equations [86] for the Green's function. However, for most of the systems, a series of approximations must be introduced [284–286]. First, one performs a transformation to center of mass (\mathbf{r}, T) and relative (\mathbf{s}, t) space and time coordinates. Since in this work we will focus on stationary problems, we can discard the variable T . As first realized by Eilenberger [287] and Larkin and Ovchinnikov [288], the Green's function oscillates rapidly as a function of the relative coordinate, on a scale of the Fermi wavelength λ_F . We are interested in variations of the order of the superconducting coherence length, much larger than λ_F , therefore, we can ignore the short range variations by averaging over the relative space coordinate. To do this, we Fourier transform the relative space and time coordinate \mathbf{s} and t , resulting in the Green's function $\check{G}(\mathbf{p}, \mathbf{r}, \varepsilon)$, function of the center of mass space coordinate \mathbf{r} and quasiparticle momentum and energy \mathbf{p} and ε . These coordinates are also known as Wigner coordinates. After Fourier transforming the relative space coordinate, the Green's function will be strongly peaked at the Fermi momentum $|\mathbf{p}_F| = p_F$. However, one has to pay attention to the dependence on the direction of the Fermi momentum $\hat{\mathbf{p}}_F$, which identifies the transport direction. This is done by writing the Green's function as $\check{G}(\xi_p, \hat{\mathbf{p}}_F, \mathbf{r}, \varepsilon)$, where $\xi_p = p^2/(2m) - \varepsilon_F$ is the kinetic energy relative to the Fermi energy ε_F , depending on the magnitude of the momentum. This allows to define the quasiclassical Green's function as

$$\check{g}(\mathbf{r}, \hat{\mathbf{p}}_F, \varepsilon) = \frac{i}{\pi} \int d\xi_p \check{G}(\xi_p, \hat{\mathbf{p}}_F, \mathbf{r}, \varepsilon). \quad (5.14)$$

From the Gorkov equation it is possible to derive the Eilenberger equation of motion for the quasiclassical Green's function:

$$v_F \hat{\mathbf{p}}_F \cdot \nabla \check{g}(\mathbf{r}, \hat{\mathbf{p}}_F, \varepsilon) = i \left[\varepsilon \check{\tau}_3 - \check{\Sigma}(\mathbf{r}) - \check{\Sigma}_{\text{imp}}(\mathbf{r}, \mathbf{p}_F), \check{g}(\mathbf{r}, \hat{\mathbf{p}}_F) \right], \quad (5.15)$$

where $\tilde{\tau}_3 = \text{diag}(\hat{\tau}_3, \hat{\tau}_3)$, $\tilde{\Sigma}$ is the self-energy of the system, describing, *e.g.* superconductivity, ferromagnetism etc, and $\tilde{\Sigma}_{\text{imp}}$ is the impurity self-energy, describing impurity scattering.

It can be shown that the quasiclassical Green's function is normalized:

$$\check{g}\check{g} = \check{\tau}_0, \quad (5.16)$$

where $\check{\tau}_0$ is the 8×8 identity matrix.

5.1.3 The Dirty Limit

In the limit of high impurity density, the scattering of particles with impurities is so frequent that their momentum is randomly oriented in any direction. This means that it is possible to expand the quasiclassical Green's function to first order in momentum, writing it in terms of an isotropic, s-wave component, \check{g}_s and an anisotropic, p-wave component, \check{g}_p , with $\check{g}_p \ll \check{g}_s$:

$$\check{g} = \check{g}_p + \hat{\mathbf{p}}_F \cdot \check{g}_p. \quad (5.17)$$

Inserting this expansion in Eq. (5.16) we get the following two conditions:

$$\check{g}_s \check{g}_s = \check{\tau}_0, \quad (5.18)$$

$$\{\check{g}_s, \check{g}_p\} = 0. \quad (5.19)$$

The impurity self-energy can be expressed in terms of \check{g}_s as:

$$\tilde{\Sigma}_{\text{imp}} = -\frac{i}{2\tau_{\text{imp}}} \check{g}_s. \quad (5.20)$$

Substituting Eqs. (5.17) and (5.20) in Eq. (5.15), we get:

$$v_F \hat{\mathbf{p}}_F \cdot \nabla \check{g}_s + v_F \hat{\mathbf{p}}_F^2 \nabla \cdot \check{g}_p = i [\varepsilon \tilde{\tau}_3 - \tilde{\Sigma}, \check{g}_s] + i \hat{\mathbf{p}}_F \cdot [\varepsilon \tilde{\tau}_3 - \tilde{\Sigma}, \check{g}_p] - \frac{1}{\tau_{\text{imp}}} \check{g}_s \hat{\mathbf{p}}_F \cdot \check{g}_p, \quad (5.21)$$

where we made use of Eq. (5.19). Averaging Eq. (5.21) over the Fermi surface, the odd terms in $\hat{\mathbf{p}}_F$ disappear and we are left with:

$$\frac{v_F}{3} \nabla \cdot \check{g}_p = i [\varepsilon \tilde{\tau}_3 - \tilde{\Sigma}, \check{g}_s]. \quad (5.22)$$

On the other hand, if we first multiply by $\hat{\mathbf{p}}_F$ and then take the average, we get:

$$v_F \nabla \check{g}_s = -\frac{1}{\tau_{\text{imp}}} \check{g}_s \check{g}_p, \quad (5.23)$$

where we have assumed that the equation is dominated by the impurity scattering. Multiplying Eq. (5.23) from the left by \check{g}_s we obtain $\check{g}_p = -\tau_{\text{imp}}v_F\check{g}_s\nabla\check{g}_s$. Substituting this in Eq. (5.22) we finally obtain the Usadel equation [289]:

$$D\nabla(\check{g}_s\nabla\check{g}_s) = -i[\varepsilon\check{\tau}_3 - \check{\Sigma}, \check{g}_s]. \quad (5.24)$$

The quasiclassical Green's function \check{g} has the same structure as the full Green's function given in Eq. (5.12), and again, in and out of equilibrium, we have the following relation between retarded and advanced components:

$$\hat{g}^A = -\hat{\tau}_3(\hat{g}^R)^\dagger\hat{\tau}_3. \quad (5.25)$$

Additionally, the Keldysh component is given by:

$$\hat{g}^K = \hat{g}^R\hat{h} - \hat{h}\hat{g}^A, \quad (5.26)$$

where the matrix \hat{h} contains the distribution functions. At equilibrium we simply have

$$\hat{h} = \tanh(\beta\varepsilon/2), \quad (5.27)$$

with $\beta = 1/k_B T$. Therefore, at equilibrium it is sufficient to solve the Usadel equation for the retarded Green's function only.

The general form of the Usadel equation of Eq. (5.24) allows to consider different materials, one only has to chose the appropriate form for the self energy $\check{\Sigma}$. For a diffusive bulk normal metal, we simply have $\check{\Sigma} = 0$, and the solution for the retarded Green's function is $\hat{g}^R = \hat{\tau}_3$, which gives $\hat{g}^A = -\hat{\tau}_3$ and $\hat{g}^K = 2\hat{\tau}_3 \tanh(\beta\varepsilon/2)$.

If the considered material presents spin-orbit coupling described by an SU(2) spin-orbit field \mathbf{A} , this can be included through the gauge covariant derivative:

$$\nabla(\cdot) \rightarrow \tilde{\nabla}(\cdot) = \nabla(\cdot) - i[\tilde{\mathbf{A}}, \cdot], \quad (5.28)$$

where:

$$\tilde{\mathbf{A}} = \text{diag}(\hat{\mathbf{A}}, \hat{\mathbf{A}}), \quad \hat{\mathbf{A}} = \text{diag}(\mathbf{A}, -\mathbf{A}^*). \quad (5.29)$$

When considering a conventional superconductor, we have:

$$\check{\Sigma} = \text{diag}(\hat{\Delta}, \hat{\Delta}), \quad \hat{\Delta} = \text{antidiag}(\Delta, -\Delta, \Delta^*, -\Delta^*), \quad (5.30)$$

where Δ is the order paramater describing the superconducting correlations.

Finally, in the case of a ferromagnetic metal the self-energy is:

$$\tilde{\Sigma} = \text{diag}(\hat{M}, \hat{M}). \quad \hat{M} = \mathbf{h} \cdot \hat{\boldsymbol{\sigma}}, \quad (5.31)$$

where \mathbf{h} is the exchange field describing spin-splitting in the ferromagnet, and $\hat{\boldsymbol{\sigma}} = \text{diag}(\boldsymbol{\sigma}, \boldsymbol{\sigma}^*)$, with $\boldsymbol{\sigma}$ Pauli vector.

5.1.4 Boundary Conditions

In order to solve the Usadel equation either analytically or numerically for superconducting hybrid systems, boundary conditions are needed. In this work we will mainly employ the Kupryianov-Lukichev boundary conditions [290], which ensure the continuity of the current flow through the interface:

$$L_j \zeta_j \check{g}_j \tilde{\nabla}_I \check{g}_j = [\check{g}_L, \check{g}_R]. \quad (5.32)$$

Here $\tilde{\nabla}_I$ is the gauge covariant derivative at the interface, j refers to the different materials comprising the hybrid system, with $j = L, R$ denoting the materials on the left and right side of the relevant interface, L_j represents the length of the material and $\zeta_j = R_B/R_j$ is the interface parameter given by the ratio between the barrier resistance R_B and its bulk resistance R_j .

When considering magnetic interfaces, the boundary conditions take a rather more complicated form. The magnetic interfaces lead to a spin-dependent conductance, described through average transmission probability \mathcal{T}_n and spin-polarization \mathcal{P}_n for each conduction channel n , and to spin-dependent phase shift for the reflection of quasiparticles. The boundary conditions can be derived through a scattering description of the interface where one defines a scattering matrix for each conduction channel. Up to the first order in transmission probabilities and spin-dependent phase shifts the boundary conditions take the following form [291]¹:

$$2G_L L_L \check{g}_j \tilde{\nabla}_I \check{g}_L = G_q \sum_n \left[\hat{T}_n^{LR} \check{g}_L (\hat{T}_n^{LR})^\dagger - i \delta \phi_n^L (\mathbf{m} \cdot \hat{\boldsymbol{\sigma}}), \check{g}_R \right], \quad (5.33)$$

where $\hat{T}^{LR} = t_{n0} + t_{n1}(\mathbf{m}\hat{\boldsymbol{\sigma}})$ is the transmission matrix for channel n , with coefficients $t_{n0} = (t_{n\uparrow} + t_{n\downarrow})/2$ and $t_{n1} = (t_{n\uparrow} - t_{n\downarrow})/2$ defined from the spin-dependent transmission coefficients $t_{n\sigma}$. The term $\delta \phi_n^L = \phi_{\uparrow}^L - \phi_{\downarrow}^L$ is the spin-dependent phase shift between reflection of spin-up and spin-down quasiparticles in channel n at the left interface, the unit vector \mathbf{m} identifies the direction of the interface magnetization and $G_q = 2e^2/h$ is the conductance quantum. The average transmission probability and spin-polarization can be written in terms

¹For simplicity we only write the equation at the left interface. The corresponding equation for the right interface is obtained simply by substituting $L \leftrightarrow R$.

of the transmission coefficients of the channel, $\mathcal{T}_n = (t_{n\uparrow}^2 + t_{n\downarrow}^2)/2$ and $\mathcal{P}_n = (t_{n\uparrow}^2 - t_{n\downarrow}^2)/(t_{n\uparrow}^2 + t_{n\downarrow}^2)$.

It is possible to rewrite Eq. (5.33) in a more useful form for numerical calculations:

$$2G_j L_j \check{g}_j \tilde{\nabla}_I \check{g}_j = G^0 [\check{g}_R, \check{g}_L] + G^1 [\mathbf{m} \cdot \hat{\sigma} \check{g}_R \mathbf{m} \cdot \hat{\sigma}, \check{g}_L] + G^{MR} [\{\mathbf{m} \cdot \hat{\sigma}, \check{g}_R\}, \check{g}_L] - iG^\phi [\mathbf{m} \cdot \hat{\sigma}, \check{g}_L], \quad (5.34)$$

where we have defined

$$G^0 = G_q \sum_n \mathcal{T}_n \left(1 + \sqrt{1 - \mathcal{P}_n^2}\right), \quad (5.35a)$$

$$G^1 = G_q \sum_n \mathcal{T}_n \left(1 - \sqrt{1 - \mathcal{P}_n^2}\right), \quad (5.35b)$$

$$G^{MR} = G_q \sum_n \mathcal{T}_n \mathcal{P}_n, \quad (5.35c)$$

$$G^\phi = 2G_q \sum_n \delta\phi_n^L. \quad (5.35d)$$

5.1.5 Riccati Parametrization

To solve numerically Eq. (5.24) it is useful to introduce a parametrization for the quasiclassical Green's function.

The components of the 4×4 quasiclassical retarded Green's function \hat{g}_R are not independent and can be written as:

$$\hat{g}_R(s, \varepsilon) = \begin{pmatrix} g(s, \varepsilon) & f(s, \varepsilon) \\ -f^*(s, -\varepsilon) & -g^*(s, \varepsilon) \end{pmatrix}, \quad (5.36)$$

where g and f are the 2×2 quasiclassical normal and anomalous Green's function, respectively. Furthermore, making use of the normalization condition $\hat{g}_R^2 = 1$, we obtain an additional constraint on \hat{g}_R , relating its normal and anomalous components:

$$g(s, \varepsilon)g(s, \varepsilon) - f(s, \varepsilon)f^*(s, -\varepsilon) = 1, \quad (5.37a)$$

$$g(s, \varepsilon)f(s, \varepsilon) - f(s, \varepsilon)g^*(s, -\varepsilon) = 0. \quad (5.37b)$$

We can now define the Riccati parametrization [79, 292], which satisfies the above constraints, by expressing the retarded Green's function as:

$$\hat{g}_R = \begin{pmatrix} N(1 + \gamma\tilde{\gamma}) & 2N\gamma \\ -2\tilde{N}\tilde{\gamma} & -\tilde{N}(1 + \tilde{\gamma}\gamma) \end{pmatrix}, \quad (5.38)$$

with $N = (1 - \gamma\tilde{\gamma})^{-1}$ and $\tilde{N} = (1 - \tilde{\gamma}\gamma)^{-1}$ and the tilde conjugation denotes the operation $\tilde{\gamma}(s, \varepsilon) = \gamma^*(s, -\varepsilon)$. Therefore, with the use of this parametrization we can reduce the Usadel equation and Kupriyanov-Lukichev boundary conditions for the 4×4 matrix \hat{g}_R to equations for the 2×2 matrix γ .

A detailed derivation of Usadel equation and Kupriyanov-Lukichev boundary conditions in an SF bilayer in the presence of SOC in the F is provided in [79]. Considering transport along the z direction the Usadel equation in the ferromagnet reads:

$$\begin{aligned} D_F \left\{ \partial_z^2 \gamma + 2(\partial_z \gamma) \tilde{N} \tilde{\gamma} (\partial_z \gamma) \right\} &= -2i\varepsilon\gamma - i(\mathbf{h} \cdot \boldsymbol{\sigma} \gamma - \gamma \mathbf{h} \cdot \boldsymbol{\sigma}^*) \\ &+ D_F \left[\mathbf{A}^2 \gamma - \gamma \mathbf{A}^{*2} + 2(A_j \gamma + \gamma A_j^*) \tilde{N} (A_j^* + \tilde{\gamma} A_j \gamma) \right] \\ &+ 2i D_F \left[(A_T + \gamma A_z^* \tilde{\gamma}) N (\partial_z \gamma) + (\partial_z \gamma) \tilde{N} (A_z^* + \tilde{\gamma} A_z \gamma) \right]. \end{aligned} \quad (5.39)$$

While in the superconductor we have:

$$D_S \left\{ \partial_z^2 \gamma + 2(\partial_z \gamma) \tilde{N} \tilde{\gamma} (\partial_z \gamma) \right\} = -2i\varepsilon\gamma - \Delta \sigma_2 + \gamma \Delta^* \sigma_2 \gamma, \quad (5.40)$$

where $\sigma_2 = \text{antidiag}(-i, i)$ is the second Pauli matrix. The equations for the boundary conditions at the superconductor-ferromagnet interface instead are:

$$\nabla_I \gamma_S = \frac{1}{L_S \zeta_S} (1 - \gamma_S \tilde{\gamma}_F) N_F (\gamma_F - \gamma_S) + i A_z \gamma_S + i \gamma_S A_z^*, \quad (5.41a)$$

$$\nabla_I \gamma_F = \frac{1}{L_F \zeta_F} (1 - \gamma_F \tilde{\gamma}_S) N_S (\gamma_F - \gamma_S) + i A_z \gamma_F + i \gamma_F A_z^*. \quad (5.41b)$$

The corresponding equations for $\tilde{\gamma}$ are simply obtained by tilde conjugation of Eqs. (5.39) to (5.41b).

5.1.6 Weak Proximity Effect

The Usadel equation is usually expressed in a quite complicated form. It is therefore useful to introduce the weak proximity effect, an approximation which allows to get more simple and easily interpretable equations. In this limit $|\gamma_{ij}| \ll 1$ and $N \sim 1$, so that $\gamma = f/2$, where $f = (f_0 + \mathbf{d} \cdot \boldsymbol{\sigma}) i \sigma_2$. Here f is the anomalous Green's function, the off-diagonal block matrix in \hat{g}_R , and is defined in terms of the scalar function f_0 and the d-vector $\mathbf{d} = (d_x, d_y, d_z)$ representing the condensate functions

for the singlet and triplet components, respectively. This gives the following form for the Riccati matrix

$$\gamma = \frac{1}{2} \begin{pmatrix} id_y - d_x & d_z + f_0 \\ d_z - f_0 & id_y + d_x \end{pmatrix}. \quad (5.42)$$

Expressions for the weak proximity equations in a ferromagnet in the presence of SOC are provided in [79, 83]. Here we report the weak proximity equations for singlet f_0 and triplet components, defining short range triplets as $\mathbf{d}_{\parallel} \equiv \mathbf{d} \cdot \mathbf{h} / |\mathbf{h}|$ and long range triplets as $\mathbf{d}_{\perp} \equiv \mathbf{d} \times \mathbf{h} / |\mathbf{h}|$. In a ferromagnetic wire having axis along z , exchange field lying in the xy plane $\mathbf{h} = h_0(\cos \theta, \sin \theta, 0)$, and SOC field $\mathbf{A} = (A_x, A_y, A_z)$ with $A_x = 0$, $A_y = 0$ and $A_z = \alpha(\sigma_x - \sigma_y)$, the equations read:

$$D_F \partial_z^2 f_0 = -2i(\varepsilon f_0 + h_0 d_{\parallel}), \quad (5.43a)$$

$$D_F \partial_z^2 d_{\parallel} = -2i\varepsilon d_{\parallel} - 2ih_0 f_0 + 4D_F \alpha^2 [1 - i \cos(2\theta)] d_{\parallel} + 4iD_F \alpha^2 \sin(2\theta) d_{\perp} + 4D_F \alpha (\cos \theta + \sin \theta) \partial_z d_z, \quad (5.43b)$$

$$D_F \partial_z^2 d_{\perp} = -2i\varepsilon d_{\perp} + 4D_F \alpha^2 [1 + i \cos(2\theta)] d_{\perp} + 4iD_F \alpha^2 \sin(2\theta) d_{\parallel} - 4D_F \alpha (\cos \theta + \sin \theta) \partial_z d_z, \quad (5.43c)$$

$$D_F \partial_z^2 d_z = -2i\varepsilon d_z + 8D_F \alpha^2 - 4D_F \alpha \partial_z (d_x + d_y). \quad (5.43d)$$

From these equations it is clear that the SOC introduces a coupling between all the triplet components, and depending on the orientation of the exchange field it is possible to achieve LRT generation. The singlet component acts as a source for the SRT component d_{\parallel} , which in turn, if $\theta \neq 0$ is converted into the LRT component d_{\perp} with a term proportional to α and with maximum conversion being achieved for $\theta = \pi/4$. It can also be noted that SOC adds an imaginary energy contribution, which corresponds to a damping term, proportional to α^2 . Therefore, SOC facilitates LRT generation for low values (with respect to the relevant scales) and contributes to a decay in the triplet components for high values.

5.2 Observables

Here we provide the expressions, in the quasiclassical approximation, of some observables which we will use to analyze our systems in the following of this work.

5.2.1 Density of States

The density of states $N(\varepsilon)$ can be expressed in terms of the Riccati matrices as [79]:

$$N(\varepsilon) = \frac{1}{2} \text{Tr} \{N(1 + \gamma\tilde{\gamma})\}. \quad (5.44)$$

In the weak proximity limit the zero energy term $N(0)$ can be written in terms of singlet and triplet components by using Eq. (5.42)

$$N(0) = 1 - \frac{|f_0|^2}{2} + \frac{1}{2} \sum_i |d_i|^2, \quad (5.45)$$

showing that singlets contribute to lower the density of states at zero energy, while triplets contribute to increase it. Therefore the appearance of a gap in $N(0)$ is a signature of a singlet-dominated regime and a zero energy peak is a signature of triplet-dominated regime [79, 293].

5.2.2 Proximity-Induced Magnetization

To calculate the proximity contribution to the magnetization we consider the spin density expressed in terms of the field operators:

$$\mathbf{s}(\mathbf{r}) = \frac{\hbar}{2} \sum_{\sigma\sigma'} \psi_{\sigma}^{\dagger}(\mathbf{r}) \boldsymbol{\sigma}_{\sigma\sigma'} \psi_{\sigma'}(\mathbf{r}). \quad (5.46)$$

This allows to define the magnetization as:

$$\mathbf{M}(\mathbf{r}) = -\frac{g\mu_B}{\hbar} \langle \mathbf{s}(\mathbf{r}) \rangle, \quad (5.47)$$

which in terms of the Green's function in the Wigner representation is [294]:

$$\mathbf{M}(\mathbf{r}) = i \frac{g\mu_B}{8} \int \frac{d\mathbf{p}}{(2\pi)^3} \int_{-\infty}^{\infty} \frac{d\varepsilon}{2\pi} \text{Tr} \left\{ \hat{\boldsymbol{\sigma}} \hat{G}^K(\mathbf{p}, \mathbf{r}, \varepsilon) \right\}. \quad (5.48)$$

Finally, introducing the quasiclassical approximation, we find the proximity contribution to the magnetization in terms of the quasiclassical Green's function:

$$\mathbf{M}(\mathbf{r}) = \frac{g\mu_B N(0)}{16} \int_{-\infty}^{\infty} d\varepsilon \text{Tr} \left\{ \hat{\boldsymbol{\sigma}} \hat{g}^K(\mathbf{r}, \varepsilon) \right\}. \quad (5.49)$$

With the use of Eqs. (5.26), (5.27) and (5.38) and the weak proximity expression of the γ matrix of Eq. (5.42), we find the following expression for the magnetization in the limit of weak proximity effect:

$$\mathbf{M}(\mathbf{r}) = -\frac{g\mu_B N(0)}{8} \int_{-\infty}^{\infty} d\varepsilon \text{Re} [f_0(\mathbf{r}, \varepsilon) \mathbf{d}(\mathbf{r}, \varepsilon)] \tanh(\beta\varepsilon/2). \quad (5.50)$$

This expression states that the magnetization depends on the product of the singlet and triplet condensate functions. Therefore, the magnetization in a certain direction is a signature of the presence of triplet correlations with spins polarized in that particular direction.

5.2.3 Charge Current Density

To calculate the charge current we consider the continuity equation for the current density \mathbf{J}_Q :

$$\frac{\partial}{\partial t}\rho + \nabla \cdot \mathbf{J}_Q = 0, \quad (5.51)$$

where $\rho = e \langle \psi_\sigma^\dagger(\mathbf{r})\psi_\sigma(\mathbf{r}) \rangle$ is the charge density. The time derivative of the charge density can be expressed as [294]:

$$\frac{\partial}{\partial t}\rho = \frac{e\hbar}{4m}\nabla \cdot \left[\lim_{\mathbf{r}_1 \rightarrow \mathbf{r}_2} (\nabla_1 - \nabla_2)\hat{G}_{\sigma\sigma}^K(\mathbf{r}_1, \mathbf{r}_2) \right]. \quad (5.52)$$

This expression allows to obtain the current density, which once generalized to the Nambu \otimes spin spaces takes the following form:

$$\mathbf{J}_Q = -\frac{e\hbar}{8m} \lim_{\mathbf{r}_1 \rightarrow \mathbf{r}_2} (\nabla_1 - \nabla_2)\text{Tr} \left\{ \hat{\tau}_3 \hat{G}_{\sigma\sigma}^K(\mathbf{r}_1, \mathbf{r}_2) \right\}. \quad (5.53)$$

Writing the Green's function in the Wigner representation, and then considering the quasiclassical approximation and the diffusive limit we get the final expression for the charge current density [294]:

$$\mathbf{J}_Q = \frac{eN(0)D}{16} \int_{-\infty}^{\infty} d\varepsilon \text{Tr} \left\{ \hat{\tau}_3 (\check{g}\nabla\check{g})^K \right\}. \quad (5.54)$$

Again we can derive a weak proximity expression for the current density, which allows to separate it in singlet and triplet contributions $\mathbf{J}_Q = \mathbf{J}_0 + \mathbf{J}_t$, where $\mathbf{J}_t = \mathbf{J}_x + \mathbf{J}_y + \mathbf{J}_z$ and

$$\mathbf{J}_0 = -\frac{eN(0)D}{2} \int_{-\infty}^{\infty} d\varepsilon \text{Re} \left[\tilde{f}_0 \nabla f_0 - f_0 \nabla \tilde{f}_0 \right] \tanh(\beta\varepsilon/2), \quad (5.55a)$$

$$\mathbf{J}_j = -\frac{eN(0)D}{2} \int_{-\infty}^{\infty} d\varepsilon \text{Re} \left[\tilde{d}_j \nabla d_j - d_j \nabla \tilde{d}_j \right] \tanh(\beta\varepsilon/2), \quad (5.55b)$$

with $j = (x, y, z)$. This expression allows to analyze separately the weight of singlets and triplets on the charge current, giving a useful tool for determining whether the system is singlet or triplet dominated.

5.2.4 Spin Current Density

Similarly to the charge current density, the spin current density is derived starting from the continuity equation in terms of the spin density $\rho_s(\mathbf{r}) = \langle \mathbf{s}(\mathbf{r}) \rangle$:

$$\rho_s^j + \nabla \cdot \mathbf{J}_s^j = 0, \quad (5.56)$$

where \mathbf{J}_s^j is the spin current density for spin pointing along $j = \{x, y, z\}$. With the same steps as the charge current density, the spin current density can be written as:

$$\mathbf{J}_s^j = \frac{\hbar N(0)D}{32} \int_{-\infty}^{\infty} d\varepsilon \text{Tr} \{ \hat{\sigma}_j \hat{\tau}_3 (\hat{g} \nabla \hat{g})^K \}. \quad (5.57)$$

Once more we can write a weak proximity expression for the spin density for spins polarized in different directions:

$$\mathbf{J}_s^x = \frac{\hbar N(0)D}{4} \int_{-\infty}^{\infty} d\varepsilon \text{Im} \left[d_y \nabla \tilde{d}_z - \tilde{d}_z \nabla d_y + \text{t.c.} \right] \tanh(\beta\varepsilon/2), \quad (5.58a)$$

$$\mathbf{J}_s^y = \frac{\hbar N(0)D}{4} \int_{-\infty}^{\infty} d\varepsilon \text{Im} \left[d_z \nabla \tilde{d}_x - \tilde{d}_x \nabla d_z + \text{t.c.} \right] \tanh(\beta\varepsilon/2), \quad (5.58b)$$

$$\mathbf{J}_s^z = \frac{\hbar N(0)D}{4} \int_{-\infty}^{\infty} d\varepsilon \text{Im} \left[d_x \nabla \tilde{d}_y - \tilde{d}_y \nabla d_x + \text{t.c.} \right] \tanh(\beta\varepsilon/2), \quad (5.58c)$$

where t.c. stands for the tilde conjugate of the preceding terms in the brackets. From these expression we can see that the spin current density for spin polarized in a certain direction depends on the triplet correlations with spin polarized in the corresponding perpendicular directions. This is a hallmark of how the spins are converted through spin precession.

5.3 Diffusion Equation in Curved Systems

In this section we will show how to modify the diffusion equation to include geometric curvature. We will present a space covariant formulation of the Hamiltonian and then we will do the same for the Usadel equation. The boundary value defined by the Usadel equation for curved system and the appropriate boundary conditions has been solved numerically to obtain the results presented in the next chapter. Numerical simulations have been performed in MATLAB through the `bvp6c` solver on the SAGA supercomputer provided by UNINETT Sigma2 - the National Infrastructure for High Performance Computing and Data Storage in Norway. The code used in this work is inspired by the the set of numerical programs GENEUS openly accessible on GitHub [295]. This code is modified to include geometric curvature and is available upon reasonable request.

5.3.1 Covariant Hamiltonian for Curved Geometries

The starting point is the the following Hamiltonian describing the motion of electrons in the presence of spin-orbit coupling:

$$H = \frac{\hbar^2 \mathbf{k}^2}{2m^*} - \hbar \boldsymbol{\alpha} \cdot \frac{\boldsymbol{\sigma} \times \mathbf{k}}{m^*}, \quad (5.59)$$

where $\mathbf{k} = -i\nabla$, m^* is the electron effective mass and $\boldsymbol{\sigma}$ is the Pauli vector. The components of the vector $\boldsymbol{\alpha}$ give the strength of the spin-orbit coupling due to asymmetric confinement in the different directions. When dealing with a geometrically curved system, the Hamiltonian of Eq. (5.59) can be written in a general covariant form:

$$H = -\frac{\hbar^2 \mathcal{G}^{\lambda\mu}}{2m^*} \mathcal{D}_\lambda \mathcal{D}_\mu + \frac{i\hbar}{m^*} \frac{\epsilon^{\lambda\mu\nu}}{\sqrt{G}} \alpha_\lambda \sigma_\mu \mathcal{D}_\nu, \quad (5.60)$$

where we used the Einstein summation rule, with the Greek indices running over the components t, n, b in the covariant basis defined in Section 4.1.1. The terms $\mathcal{G}^{\lambda\mu}$ and G are the inverse and the determinant of the metric tensor respectively, and $\epsilon^{\lambda\mu\nu}$ is the Levi-Civita symbol. The space covariant derivatives are defined through Eqs. (4.12) and (4.13), and the Christoffel symbols are given by Eq. (4.14).

To further simplify the derivation we exploit the last term in Eq. (5.60) to define a (contravariant) spin-orbit field as:

$$A^\nu = \epsilon^{\lambda\mu\nu} \alpha_\lambda \sigma_\mu / \sqrt{G} = \mathcal{G}^{\nu\mu} A_\mu. \quad (5.61)$$

With the assumption of weak spin-orbit coupling, the Hamiltonian of Eq. (5.60) can be written in a form manifestly showing a local SU(2) gauge invariance [296, 297]:

$$H = -\frac{\hbar^2 \mathcal{G}^{\lambda\mu}}{2m^*} (\mathcal{D}_\lambda - iA_\lambda) (\mathcal{D}_\mu - iA_\mu). \quad (5.62)$$

Therefore the SOC enters the Hamiltonian with the usual form of a 2×2 matrix-valued SU(2) vector field [72, 73]. The values of the components A_μ depend on the physical system at hand, *e.g.* the intrinsic types of SOC in the system, and the curvature-induced SOC discussed in the previous subsection.

5.3.2 Effective Hamiltonian for Curved Nanowire

In order to derive an effective Hamiltonian for a curved nanowire one can apply a thin-wall quantization procedure [216, 217] to the Hamiltonian of Eq. (5.60), additionally taking into account the effect of the constraining potential in the normal

and binormal directions. These allow to expand the Hamiltonian in powers of n and b , taking the zeroth order terms, and employ an adiabatic approximation to separate the relevant degree of freedom s . This procedure has been performed in [206] for a planarly curved wire, *i.e.* zero torsion, and in [218] with the addition of torsion. Considering curvature-induced and intrinsic spin-orbit interaction, α_N and α_B respectively, when both $\kappa(s)$ and $\tau(s)$ are non-zero, one gets [206, 218]:

$$H = -\frac{\hbar^2}{2m^*}\partial_s^2 - \frac{\hbar^2}{8m^*}\kappa(s)^2 - \frac{\hbar^2}{4m^*}\tau(s)^2 - \frac{i\hbar}{m^*}\alpha_N \left(\sigma_B \partial_s - \frac{\tau(s)}{2} \sigma_N \right) + \frac{i\hbar}{m^*}\alpha_B \left(\sigma_N \partial_s - \frac{\kappa(s)}{2} \sigma_T + \frac{\tau(s)}{2} \sigma_B \right). \quad (5.63)$$

The second and third terms in the right hand side are the quantum geometric potentials due to curvature and torsion respectively. These terms will be neglected in the following as they lead to an overall energy shift.

With the use of Eq. (4.2) it is possible to reorganize the terms in the second line of Eq. (5.63) and incorporate them in the following SU(2) spin-orbit field:

$$\mathbf{A} = (\alpha_N \sigma_B - \alpha_B \sigma_N, 0, 0), \quad (5.64)$$

having a vector structure in the geometric space and a 2×2 matrix structure in spin space.

5.3.3 Usadel equation for curved nanowires

We will make use of Green's functions in the diffusive limit and study the dynamics through the second order partial differential Usadel equation [289] derived in Section 5.1

The Hamiltonian of Eq. (5.62) allows us to define the Usadel equation in a covariant form and, with the right boundary conditions, describe the diffusion of superconducting correlations in an SF hybrid structure with geometric curvature.

We restrict ourselves to the case of diffusive equilibrium, allowing us to consider just the retarded component \hat{g}_R of the quasiclassical Green's function to describe the system [286]. The Usadel equation of Eq. (5.24), defined from the Hamiltonian of Eq. (5.62) is generalized to:

$$D_F \mathcal{G}^{\lambda\mu} \tilde{\mathcal{D}}_\lambda (\hat{g}_R \tilde{\mathcal{D}}_\mu \hat{g}_R) + i \left[\varepsilon \hat{\tau}_3 + \hat{\Delta} + \hat{M}, \hat{g}_R \right] = 0, \quad (5.65)$$

where $\hat{\Delta}$ and $\hat{M} = h^\mu \text{diag}(\sigma_\mu, \sigma_\mu^*)$ are defined in Eqs. (5.30) and (5.31), respectively, with the difference that the exchange field and Pauli vector components

in the magnetization are now defined in the curvilinear coordinate system, with $\mu = \{T, N, B\}$. Here we have set $\hbar = 1$, and we have defined the space-gauge covariant derivative as:

$$\tilde{D}_\lambda v_\mu = \tilde{\partial}_\lambda v_\mu - \Gamma_{\lambda\mu}^\nu v_\nu, \quad (5.66)$$

where $\tilde{\partial}_\lambda v_\mu = \partial_\lambda v_\mu - i[\hat{A}_\lambda, v_\mu]$ is the gauge-only covariant derivative, with $\hat{A}_\lambda = \text{diag}(A_\lambda, -A_\lambda^*)$.

We now wish to evaluate the first term in Eq. (5.65), by using the expression of Eq. (5.66) for the space-gauge covariant derivative we can write:

$$D_F \mathcal{G}^{\lambda\mu} \tilde{D}_\lambda (\hat{g}_R \tilde{D}_\mu \hat{g}_R) = D_F \mathcal{G}^{\lambda\mu} \tilde{\partial}_\lambda (\hat{g}_R \tilde{\partial}_\mu \hat{g}_R) - D_F \mathcal{G}^{\lambda\mu} \Gamma_{\lambda\mu}^\nu (\hat{g}_R \tilde{\partial}_\nu \hat{g}_R). \quad (5.67)$$

With the use of Eqs. (4.15) and (4.16c), we can write the terms in Eq. (5.67) respectively as:

$$\begin{aligned} D_F \mathcal{G}^{\lambda\mu} \tilde{\partial}_\lambda (\hat{g}_R \tilde{\partial}_\mu \hat{g}_R) &= \frac{1}{\eta(s, n)^2} \left\{ \tilde{\partial}_s (\hat{g}_R \tilde{\partial}_s \hat{g}_R) + (\eta(s, n)^2 + b^2 \tau(s)^2) \tilde{\partial}_n (\hat{g}_R \tilde{\partial}_n \hat{g}_R) \right. \\ &+ (\eta(s, n)^2 + n^2 \tau(s)^2) \tilde{\partial}_b (\hat{g}_R \tilde{\partial}_b \hat{g}_R) + b\tau(s) \left[\tilde{\partial}_s (\hat{g}_R \tilde{\partial}_n \hat{g}_R) + \tilde{\partial}_n (\hat{g}_R \tilde{\partial}_s \hat{g}_R) \right] \\ &\left. - n\tau(s) \left[\tilde{\partial}_s (\hat{g}_R \tilde{\partial}_b \hat{g}_R) + \tilde{\partial}_b (\hat{g}_R \tilde{\partial}_s \hat{g}_R) \right] - nb\tau(s)^2 \left[\tilde{\partial}_n (\hat{g}_R \tilde{\partial}_b \hat{g}_R) + \tilde{\partial}_b (\hat{g}_R \tilde{\partial}_n \hat{g}_R) \right] \right\}, \end{aligned} \quad (5.68a)$$

$$\begin{aligned} D_F \mathcal{G}^{\lambda\mu} \Gamma_{\lambda\mu}^\nu (\hat{g}_R \tilde{\partial}_\nu \hat{g}_R) &= \frac{1}{\eta(s, n)^3} \left\{ [\partial_s \eta(s, n) - b\kappa(s)\tau(s)] \hat{g}_R \tilde{\partial}_s \hat{g}_R \right. \\ &+ [\eta(s, n)^2 \partial_n \eta(s, n) + b\partial_s (\eta(s, n)\tau(s)) + (n^2 - b^2)\kappa(s)\tau(s)^2 + n\tau(s)^2] \hat{g}_R \tilde{\partial}_n \hat{g}_R \\ &\left. + [n(\partial_s (\eta(s, n))\tau(s) - \eta(s, n)\partial_s \tau(s)) + b\tau(s)^2] \hat{g}_R \tilde{\partial}_b \hat{g}_R \right\}. \end{aligned} \quad (5.68b)$$

In this work we will only consider nanowires, allowing us to ignore the dependence of \hat{g}_R on n and b and take the limit $n, b \rightarrow 0$. Therefore the Usadel equation takes the form:

$$D_F \tilde{\partial}_s (\hat{g}_R \tilde{\partial}_s \hat{g}_R) + i \left[\varepsilon \hat{\rho}_3 + \hat{\Delta} + \hat{M}, \hat{g}_R \right] = 0, \quad (5.69)$$

where the effects of the curvature enter the equation through the Pauli matrices contained in the spin-orbit field and the magnetization.

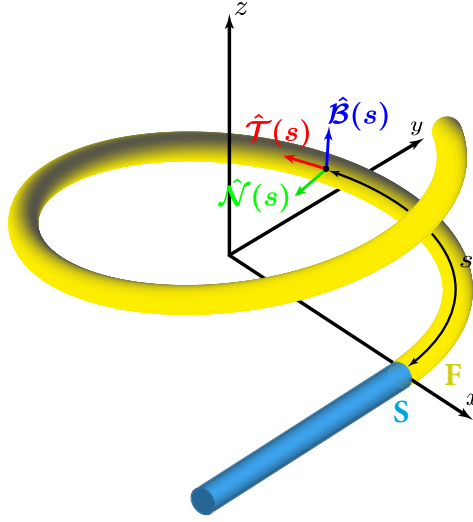


Figure 5.1: Superconductor-ferromagnet hybrid nanowire with a ferromagnet with constant curvature $\kappa = |\partial_s \hat{T}|$ and torsion $\tau = |\partial_s \hat{B}|$. The orthonormal unit vectors $\hat{T}, \hat{N}, \hat{B}$ identifying the curvilinear coordinates and the arclength coordinate s are also shown.

5.3.4 Riccati parametrization

To study a superconductor-ferromagnet hybrid system like the one depicted in Fig. 5.1, we define the Usadel equation separately for a curved ferromagnet with spin-orbit coupling, and a straight s-wave superconductor, using the Riccati parametrization.

Substituting Eq. (5.38) into Eq. (5.69) we get the Usadel equation for the ferromagnet:

$$\begin{aligned}
 D_F \left\{ \partial_s^2 \gamma + 2(\partial_s \gamma) \tilde{N} \tilde{\gamma} (\partial_s \gamma) \right\} &= -2i\varepsilon \gamma \\
 -i(\mathbf{h} \cdot \boldsymbol{\sigma} \gamma - \gamma \mathbf{h} \cdot \boldsymbol{\sigma}^*) - iD_F [(\partial_s A_T) \gamma + \gamma (\partial_s A_T^*)] & \\
 + D_F [A^2 \gamma - \gamma A^{*2} + 2(A_j \gamma + \gamma A_j^*) \tilde{N} (A_j^* + \tilde{\gamma} A_j \gamma)] & \\
 + 2iD_F [(A_T + \gamma A_T^* \tilde{\gamma}) N (\partial_s \gamma) + (\partial_s \gamma) \tilde{N} (A_T^* + \tilde{\gamma} A_T \gamma)], &
 \end{aligned} \tag{5.70}$$

and the superconductor:

$$D_F \left\{ \partial_y^2 \gamma + 2(\partial_y \gamma) \tilde{N} \tilde{\gamma} (\partial_y \gamma) \right\} = -2i\varepsilon \gamma - \Delta \sigma_2 + \gamma \Delta^* \sigma_2 \gamma, \tag{5.71}$$

where the index j runs over the physical components T, N, B of the SOC field and $\sigma_2 = \text{antidiag}(-i, i)$. In Eq. (5.70) both the exchange field vector $\mathbf{h} =$

(h_T, h_N, h_B) and the Pauli vector $\boldsymbol{\sigma} = (\sigma_T, \sigma_N, \sigma_B)$ are expressed in curvilinear components.

We note that the result obtained here for the Riccati parametrization of the Usadel equation is the same as in [79] (see Eqs. (5.39) and (5.40)) with the addition of the last term in the second line of Eq. (5.70) due to the spatial dependence of the spin-orbit field.

Upon substitution of Eq. (5.38) in Eq. (5.32) we get the following form for the boundary conditions at the superconductor-ferromagnet interface:

$$\partial_I \gamma_S = \frac{1}{L_S \zeta_S} (1 - \gamma_S \tilde{\gamma}_F) N_F (\gamma_F - \gamma_S) + i A_T \gamma_S + i \gamma_S A_T^*, \quad (5.72a)$$

$$\partial_I \gamma_F = \frac{1}{L_F \zeta_F} (1 - \gamma_F \tilde{\gamma}_S) N_S (\gamma_F - \gamma_S) + i A_T \gamma_F + i \gamma_F A_T^*. \quad (5.72b)$$

The corresponding equations for $\tilde{\gamma}$ are simply obtained by tilde conjugation of Eqs. (5.70) to (5.72b).

5.3.5 Weak proximity effect equations

To interpret the effects of the geometrical curvature and spin-orbit coupling components in our system, we will now study a ferromagnetic helix with constant curvature and torsion in the limit of weak proximity effect. As in Section 5.1.6, we can write the Riccati matrix as $\gamma = (f_0 + \mathbf{d} \cdot \boldsymbol{\sigma}) i \sigma_2 / 2$, again defined in terms of the scalar function f_0 and the d-vector $\mathbf{d} = (d_T, d_N, d_B)$ representing the condensate functions for the singlet and triplet components in the curvilinear framework, respectively.

An helical nanowire like the one depicted in Fig. 5.1, having radius R and $2c\pi$ pitch, i.e. the height of a complete helix turn, can be defined in cylindrical coordinates as:

$$x = R \cos \phi \quad (5.73a)$$

$$y = R \sin \phi \quad (5.73b)$$

$$z = c\phi \quad (5.73c)$$

with $\phi = [0, 2n\pi]$, and n defining the number of turns. The value of c determines how much the nanowire is tilted out of plane. Curvature and torsion are respectively given by $\kappa = R / (R^2 + c^2)$ and $\tau = c / (R^2 + c^2)$. The arclength coordinate $s = \phi \sqrt{R^2 + c^2}$. The components $\sigma_{T,N,B}(s)$ in the ferromagnet are obtained from the following set of three unit vectors:

$$\hat{T}(\phi) = -\cos\alpha \sin\phi \hat{x} + \cos\alpha \cos\phi \hat{y} + \sin\alpha \hat{z}, \quad (5.74a)$$

$$\hat{N}(\phi) = -\cos\phi \hat{x} - \sin\phi \hat{y}, \quad (5.74b)$$

$$\hat{B}(\phi) = \sin\alpha \sin\phi \hat{x} - \sin\alpha \cos\phi \hat{y} + \cos\alpha \hat{z}, \quad (5.74c)$$

with $\alpha = \text{atan}(\tau/\kappa)$. Consequently, we get the following form for the γ matrix:

$$\gamma = \frac{1}{2} \begin{pmatrix} (id_T \cos\alpha + d_N - id_B \sin\alpha) e^{-i\phi} & d_T \sin\alpha + d_B \cos\alpha + f_0 \\ d_T \sin\alpha + d_B \cos\alpha - f_0 & (id_T \cos\alpha - d_N - id_B \sin\alpha) e^{i\phi} \end{pmatrix}. \quad (5.75)$$

In this limit it becomes straightforward to identify the SRT $\mathbf{d}_{\parallel} = \mathbf{d} \cdot \mathbf{h} / |\mathbf{h}|$ and LRT $\mathbf{d}_{\perp} = \mathbf{d} \times \mathbf{h} / |\mathbf{h}|$ components. For instance, if the exchange field \mathbf{h} is directed along the \hat{T} direction the SRT can be identified with d_T , while d_N and d_B represent the LRTs. The weak proximity limit allows us to consider only the terms linear in γ both in the Usadel equation and in the Kupriyanov-Lukichev boundary conditions. The linearized Usadel equation Eq. (5.70) in the ferromagnet can be written as:

$$\begin{aligned} D_F \partial_s^2 \gamma &= -2i\varepsilon\gamma - i(\mathbf{h} \cdot \boldsymbol{\sigma} \gamma - \gamma \mathbf{h} \cdot \boldsymbol{\sigma}^*) + iD_F[(\partial_s A_T)\gamma + \gamma(\partial_s A_T^*)] \\ &+ D_F(A^2 \gamma + \gamma A^{*2} + 2A_j \gamma A_j^*) + 2iD_F[A_T(\partial_s \gamma) + (\partial_s \gamma)A_T^*]. \end{aligned} \quad (5.76)$$

With the spin-orbit field given by Eq. (5.64) and the form of γ from Eq. (5.75), after some calculations we obtain the following differential equations for the d-vector and singlet components:

$$\begin{aligned} \frac{iD_F}{2} \partial_s^2 d_T - iD_F(\kappa + 2\alpha_N) \partial_s d_N - 2iD_F \alpha_B \partial_s d_B &= f_0 h_T \\ &+ \left\{ \varepsilon + \frac{iD_F}{2} [(\kappa + 2\alpha_N)^2 + 4\alpha_B^2] \right\} d_T + iD_F \alpha_B \tau d_N - \frac{iD_F}{2} (\kappa + 2\alpha_N) \tau d_B, \end{aligned} \quad (5.77a)$$

$$\begin{aligned} \frac{iD_F}{2} \partial_s^2 d_N + iD_F(\kappa + 2\alpha_N) \partial_s d_T - iD_F \tau \partial_s d_B &= f_0 h_N \\ &+ \left\{ \varepsilon + \frac{iD_F}{2} (\kappa + 2\alpha_N)^2 \right\} d_N + iD_F \tau \alpha_B d_T + iD_F \alpha_B (\kappa + 2\alpha_N) d_B, \end{aligned} \quad (5.77b)$$

$$\begin{aligned} \frac{iD_F}{2} \partial_s^2 d_B + 2iD_F \alpha_B \partial_s d_T - iD_F \tau \partial_s d_N &= f_0 h_B \\ &+ \left\{ \varepsilon + \frac{iD_F}{2} (\tau^2 + 4\alpha_B^2) \right\} d_B - \frac{iD_F}{2} (\kappa + 2\alpha_N) \tau d_T + iD_F (\kappa + 2\alpha_N) \alpha_B d_N, \end{aligned} \quad (5.77c)$$

$$\frac{iD_F}{2} \partial_s^2 f_0 = \varepsilon f_0 + \mathbf{h} \cdot \mathbf{d}. \quad (5.77d)$$

By inspecting these equations it is possible to understand how the mechanism for singlet-triplet conversion works in the ferromagnet. Let us consider an exchange field along the \hat{T} direction: at the SF interface on the ferromagnet side, due to the proximity effect, singlets are present, which are partially converted into the SRT component d_T by the exchange field. The presence of any among geometric curvature, torsion and spin-orbit coupling results then in the generation of LRT components d_N, d_B .

The effect of κ, τ, α_N and α_B in Eqs. (5.77a) to (5.77c) is twofold: the triplets undergo spin-precession and spin-relaxation. The former can be identified with the terms having a first derivative of a triplet component and describes the rotation of the spin of superconducting triplet correlations while moving along the ferromagnet. The latter appears as an additional imaginary component of the triplet energy and represents a loss of spin information due to frequent impurity scattering. Consequently, curvature, torsion and spin-orbit coupling, all independently provide a pathway for LRT generation. At the same time, if their value becomes too large, they become detrimental for the triplets, as they would cause decoherence. For instance, in the case of zero torsion and spin-orbit coupling, an estimate of the value for the crossover between the two regimes can be provided by comparison of the spin-precession prefactor $\epsilon_p \sim D_F \kappa / L_F$ and the spin-relaxation prefactor $\epsilon_r \sim D_F \kappa^2 / 2$, where we for simplicity consider geometric curvature only. Therefore, a transition from spin-precession dominated to spin-relaxation dominated regimes occurs when $\epsilon_p \sim \epsilon_r$, i.e. when $\kappa L_F \sim 2$ or $\kappa L_F / \pi \sim 0.6$. The inclusion of torsion and SOC terms will shift the transition towards 0².

Finally, we note that in Eqs. (5.77a) to (5.77c) κ and α_N always appear together in the same form, highlighting that they have the same effect on the d-vector components. It is therefore possible to define an "effective" curvature $\tilde{\kappa} = \kappa + 2\alpha_N$ and consider α_N as a factor which boosts the effects of the geometrical curvature.

5.3.6 Diffusion Equation in Nonequilibrium

As we mentioned in Section 5.1.3, at equilibrium it is sufficient to solve the Usadel equation for the retarded Green's function only. However, in the presence of an external voltage bias we need to define the quantum kinetic equations allowing to calculate the distribution matrix \hat{h} , and consequently the Keldysh Green's function $\hat{g}^K = \hat{g}^R \hat{h} - \hat{h} \hat{g}^A$. Once the quantum kinetic equations are defined, we would have all the tools to investigate hybrid structures of superconductors and curved ferromagnets in the diffusive regime outside of equilibrium.

²For a finite α_N we have the condition $(\kappa + 2\alpha_N)L_F \sim 2$.

The equation for the distribution matrix is found by taking the Keldysh component of Eq. (5.24). The equation in a curved ferromagnet with SOC reads:

$$\begin{aligned}
& D_F \left\{ \partial_s^2 \hat{h} - \hat{g}^R (\partial_s^2 \hat{h}) \hat{g}^A + (\hat{g}^R \partial_s \hat{g}^R) (\partial_s \hat{h}) - (\partial_s \hat{h}) (\hat{g}^A \partial_s \hat{g}^A) - (\partial_s \hat{g}^R) (\partial_s \hat{h}) \hat{g}^A \right. \\
& \left. - \hat{g}^R (\partial_s \hat{h}) (\partial_s \hat{g}^A) + [(\partial_s \hat{g}^R)^2 + \hat{g}^R (\partial_s^2 \hat{g}^R)] \hat{h} - \hat{h} [(\partial_s \hat{g}^A)^2 - (\partial_s^2 \hat{g}^A)] \right\} \\
& = i [\hat{g}^K, \varepsilon \hat{\tau}_3 + \hat{M}] + i D_F \left\{ \partial_s \hat{g}^R [\hat{A}_T, \hat{g}^K] + \partial_s \hat{g}^K [\hat{A}_T, \hat{g}^A] \right. \\
& \left. - (\hat{g}^R \hat{A}_T + \hat{A}_T \hat{g}^R) \partial_s \hat{g}^K + (\hat{g}^K \hat{A}_T + \hat{A}_T \hat{g}^K) \partial_s \hat{g}^A - 2 (\hat{g}^R \partial_s \hat{g}^K + \hat{g}^K \partial_s \hat{g}^A) \hat{A}_T \right. \\
& \left. + \hat{g}^R [\partial_s \hat{A}_T, \hat{g}^K] + \hat{g}^K [\partial_s \hat{A}_T, \hat{g}^A] + [\hat{A}_T, \hat{g}^R \hat{A}_T \hat{g}^K + \hat{g}^K \hat{A}_T \hat{g}^A] \right\}.
\end{aligned} \tag{5.78}$$

Similarly the Kupryianov-Lukichev boundary conditions are:

$$\begin{aligned}
& 2L_j \zeta_j \left[\partial_I \hat{h}_j - \hat{g}_j^R (\partial_I \hat{h}_j) \hat{g}_j^A + \hat{g}_j^R (\partial_I \hat{g}_j^R) \hat{h}_j + \hat{h}_j \hat{g}_j^A (\partial_I \hat{g}_j^A) \right] \\
& = [\check{g}_L, \check{g}_R]^K + 2iL_j \zeta_j \left(\hat{g}_j^R \hat{A}_T^I \hat{g}_j^R \hat{h}_j - \hat{h}_j \hat{g}_j^A \hat{A}_T^I \hat{g}_j^A + \hat{g}_j^R \hat{h}_j \hat{A}_T^I \hat{g}_j^A - \hat{g}_j^R \hat{A}_T^I \hat{h}_j \hat{g}_j^A \right).
\end{aligned} \tag{5.79}$$

with $j = \{L, R\}$, indicating the material at the left or right of the interface, and ∂_I and \hat{A}_T^I are the values of the derivative and the SO field at the interface.

The form in which Eqs. (5.78) and (5.79) are expressed is not suitable for numerical calculations. In order to obtain a suitable form of these equations, it is useful to introduce a decomposition of the distribution matrix \hat{h} as done in Ref.[125]. It is possible to decompose \hat{h} as follows:

$$\hat{h} = h_n \hat{\rho}_n, \tag{5.80}$$

where the coefficients h_m are defined as:

$$h_n = \frac{1}{4} \text{Tr} \left\{ \hat{h} \hat{\rho}_n \right\}. \tag{5.81}$$

The set of basis matrices $\hat{\rho}_n$ represents the block diagonal spin \otimes Nambu space and has the following elements:

$$\begin{aligned}
\hat{\rho}_0 &= \hat{\tau}_0 \hat{\sigma}_0, & \hat{\rho}_1 &= \hat{\tau}_0 \hat{\sigma}_1, & \hat{\rho}_2 &= \hat{\tau}_0 \hat{\sigma}_2, & \hat{\rho}_3 &= \hat{\tau}_0 \hat{\sigma}_3, \\
\hat{\rho}_4 &= \hat{\tau}_3 \hat{\sigma}_0, & \hat{\rho}_5 &= \hat{\tau}_3 \hat{\sigma}_1, & \hat{\rho}_6 &= \hat{\tau}_3 \hat{\sigma}_2, & \hat{\rho}_7 &= \hat{\tau}_3 \hat{\sigma}_3.
\end{aligned} \tag{5.82}$$

Substituting Eq. (5.80) in Eq. (5.78), multiplying from the left by $\hat{\rho}_m/4$ and then taking the trace we can rewrite the kinetic equations as:

$$M_{mn}\partial_s^2 h_n = -(\partial_s M_{mn} + Q_{mn} + A_{mn})\partial_s h_n - (\partial_s Q_{mn} + A_{mn}^d + A_{mn}^q + V_{mn})h_n, \quad (5.83)$$

where we have defined the following matrices:

$$M_{mn} = \frac{1}{4}\text{Tr} \{ \hat{\rho}_m (\hat{\rho}_n - \hat{g}^R \hat{\rho}_n \hat{g}^A) \}, \quad (5.84a)$$

$$Q_{mn} = \frac{1}{4}\text{Tr} \{ \hat{\rho}_m (\hat{g}^R \partial_s \hat{g}^R \hat{\rho}_n - \hat{\rho}_n \hat{g}^A \partial_s \hat{g}^A) \}, \quad (5.84b)$$

$$A_{mn} = \frac{i}{4}\text{Tr} \left\{ \hat{\rho}_m \left(\hat{g}^R \hat{\rho}_n \hat{g}^A \hat{A}_T - \hat{A}_T \hat{g}^R \hat{\rho}_n \hat{g}^A + \hat{g}^R \hat{A}_T \hat{g}_m^K + \hat{g}_m^K \hat{A}_T \hat{g}^A \right) \right\}, \quad (5.84c)$$

$$\begin{aligned} A_{mn}^d = \frac{i}{4}\text{Tr} \left\{ \hat{\rho}_m \left(\partial_s \hat{g}^R \left(\hat{A}_T \hat{g}_n^K - \hat{g}_n^K \hat{A}_T \right) + \left(\hat{A}_T \hat{g}_n^K + \hat{g}_n^K \hat{A}_T \right) \partial_s \hat{g}^A \right) \right. \\ \left. + \left(\hat{g}^R \hat{A}_T + \hat{A}_T \hat{g}^R \right) \partial_s \hat{g}_n^K + \partial_s \hat{g}_n^K \left(\hat{A}_T \hat{g}^A - \hat{g}^A \hat{A}_T \right) \right. \\ \left. - 2 \left(\hat{g}^R \partial_s \hat{g}_n^K + \hat{g}_n^K \partial_s \hat{g}^A \right) + \hat{g}_n^K \partial_s \hat{A}_T \hat{g}^A - \hat{g}^R \partial_s \hat{A}_T \hat{g}_n^K \right\}, \end{aligned} \quad (5.84d)$$

$$A_{mn}^q = \frac{i}{4}\text{Tr} \left\{ \hat{\rho}_m \hat{g}^R \hat{A}_T \hat{g}_n^K \hat{A}_T \right\}, \quad (5.84e)$$

$$V_{mn} = \frac{i}{4}\text{Tr} \left\{ \left[\hat{\rho}_m, \varepsilon \hat{\tau}_3 + \hat{M} \right] \left(\hat{g}^R \hat{\rho}_n - \hat{\rho}_n \hat{g}^A \right) \right\}, \quad (5.84f)$$

where $\hat{g}_n^K = \hat{g}^R \hat{\rho}_n - \hat{\rho}_n \hat{g}^A$. With the same approach the boundary conditions of Eq. (5.79) become:

$$M_{mn}^j \partial_I h_n^j = \frac{1}{2L_j \zeta_j} (C_{mn}^{LR} h_n^R - C_{mn}^{RL} h_n^L) - (D_{mn}^j + A_{mn}^j) h_m^j, \quad (5.85)$$

with:

$$M_{mn}^j = \frac{1}{4}\text{Tr} \left\{ \hat{\rho}_m (\hat{\rho}_n - \hat{g}_j^R \hat{\rho}_n \hat{g}_j^A) \right\}, \quad (5.86a)$$

$$C_{mn}^{ij} = \frac{1}{4}\text{Tr} \left\{ \hat{\rho}_m (\hat{g}_i^R \hat{g}_j^R \hat{\rho}_n + \hat{\rho}_n \hat{g}_j^A \hat{g}_i^A - \hat{g}_i^R \hat{\rho}_n \hat{g}_j^A - \hat{g}_j^R \hat{\rho}_n \hat{g}_i^A) \right\}, \quad (5.86b)$$

$$D_{mn}^j = \frac{1}{4}\text{Tr} \left\{ \hat{\rho}_m (\hat{g}_j^R \partial_I \hat{g}_j^R \hat{\rho}_n - \hat{\rho}_n \hat{g}_j^A \partial_I \hat{g}_j^A) \right\}, \quad (5.86c)$$

$$A_{mn}^j = -\frac{i}{4}\text{Tr} \left\{ \hat{\rho}_m \left(\hat{g}_j^R \hat{A}_T^I \hat{g}_j^R \hat{\rho}_n - \hat{\rho}_n \hat{g}_j^A \hat{A}_T^I \hat{g}_j^A + \hat{g}_j^R \hat{\rho}_n \hat{A}_T^I \hat{g}_j^A - \hat{g}_j^R \hat{A}_T^I \hat{\rho}_n \hat{g}_j^A \right) \right\}. \quad (5.86d)$$

The boundary conditions can then be used to include a voltage bias in the desired system by placing at its interface a bulk material or reservoir. It is then required to know the expression of the bulk distribution matrix in the reservoir, at equilibrium we simply have $\hat{h} = \tanh(\beta\varepsilon/2)\hat{\rho}_0$. When a voltage V is introduced the distribution matrix becomes:

$$\hat{h} = \begin{pmatrix} \tanh[\beta(\varepsilon + eV)/2] \sigma_0 & 0 \\ 0 & \tanh[\beta(\varepsilon - eV)/2] \sigma_0 \end{pmatrix}. \quad (5.87)$$

More generally, it is possible to have a spin reservoir, which would allow to inject a spin-polarized current. Such a reservoir can be described by introducing two voltages for particles with different spins, V_\uparrow and V_\downarrow . We then define $V = (V_\uparrow + V_\downarrow)/2$ and $V_s = (V_\uparrow - V_\downarrow)/2$ and an arbitrary spin quantization axis $\mathbf{s} = (s_x, s_y, s_z)$. Then the distribution matrix \hat{h} can be written in terms of its component h_n defined in Eq. (5.81):

$$h_0 = h_{++} + h_{+-} + h_{-+} + h_{--}, \quad (5.88a)$$

$$h_1 = (h_{++} - h_{+-} + h_{-+} - h_{--})s_x, \quad (5.88b)$$

$$h_2 = (h_{++} - h_{+-} + h_{-+} - h_{--})s_y, \quad (5.88c)$$

$$h_3 = (h_{++} - h_{+-} + h_{-+} - h_{--})s_z, \quad (5.88d)$$

$$h_4 = h_{++} + h_{+-} - h_{-+} - h_{--}, \quad (5.88e)$$

$$h_5 = (h_{++} - h_{+-} - h_{-+} + h_{--})s_x, \quad (5.88f)$$

$$h_6 = (h_{++} - h_{+-} - h_{-+} + h_{--})s_y, \quad (5.88g)$$

$$h_7 = (h_{++} - h_{+-} - h_{-+} + h_{--})s_z. \quad (5.88h)$$

$$(5.88i)$$

The formalism presented thus allows the study of superconducting hybrid structures with a voltage bias. The bias is applied through the inclusion of a bulk normal metal in the hybrid structure, and it will be considered in the study of a NFS structure with a curved ferromagnet³.

³Related work has been carried out in collaboration with Alv J. Skarpeid, who considered similar systems in his master thesis [298].

Chapter 6

Curvature Effects in Superconductor-Ferromagnet Hybrid Structures

In this chapter we will present some curvature induced effects in SF hybrid structures. Firstly, we will study an SFS junction with a planarly curved ferromagnet, showing that the curvature induces a $0 - \pi$ transition in the current flowing through the junction. Moreover, we will analyze how curvature produces long-range triplets in the system. Then we will consider an SF hybrid nanowire with a planarly curved ferromagnet, demonstrating the existence of a spin-valve effect controlled by the curvature. We will also consider an SFS junction with a ferromagnetic helix instead of a planarly curved ferromagnet, and describe it through some observables like magnetization, charge current and spin current. Finally, we will consider an NFS hybrid structure with a planarly curved F, and a voltage bias introduced through the normal metal N. Throughout this chapter, unless stated, we set $\hbar = 1$.

6.1 Diffusive SFS Josephson Junctions with Curved Ferromagnetic Weak Link

Josephson junctions containing a ferromagnetic weak link can exhibit a ground state with a π phase difference between the superconducting contacts (π -state), for some thicknesses and exchange field values of the weak link [58, 299, 300]. Junctions in such a state, named π -junctions, have been realized experimentally for the first time in 2001 [301, 302], and they have been attracting much interest for their potential applications in solid state quantum computing [303–306].

Tuning the transition between the 0 and π states, where the current flows in

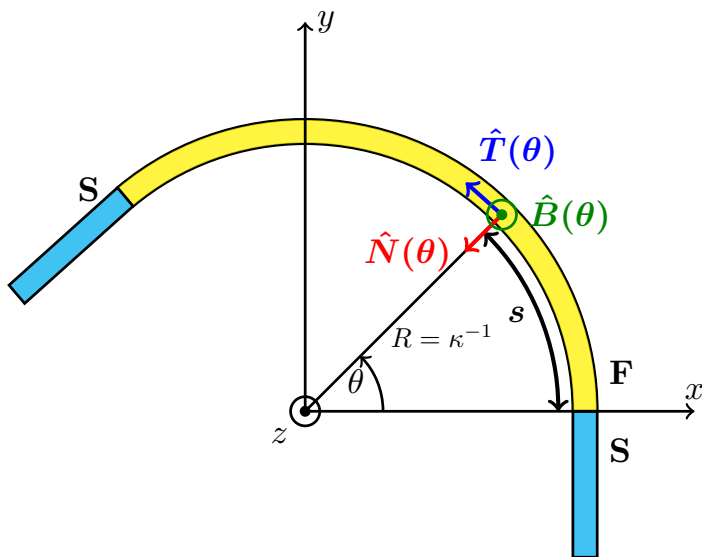


Figure 6.1: Model system. SFS junction having a ferromagnet with constant curvature as weak link. The three orthonormal unit vectors $\hat{T}(\theta)$, $\hat{N}(\theta)$ and $\hat{B}(\theta)$ identifying the curvilinear coordinates are also shown.

opposite directions through the junction, has direct applications for the realization of Josephson MRAM devices for superconducting computers [307]. As mentioned above the transition can be governed by altering the length of the ferromagnetic weak link. However, this is not practicable to do in-situ and must be done by preparing multiple samples of different lengths. However, in 2016 it has been shown experimentally that it is possible to control the $0 - \pi$ transition in a Josephson junction containing a ferromagnetic spin valve [308]. Moreover, it has recently been predicted that the $0 - \pi$ transition can be realized by altering the strength of the SOC via voltage gating [309]. In this section and in Paper I [1], we show that dynamically changing the curvature of the magnet via in-situ strain manipulation, for example via photostriction, piezoelectrics or thermoelectric effects [310, 311], allows for a single-sample $0 - \pi$ transition in the diffusive regime, without the need to apply a varying voltage. Moreover, we show that curvature can yield long-ranged Josephson currents without any magnetic inhomogeneities or intrinsic SOC.

6.1.1 Diffusive equations

We consider the SFS junction with a planarly curved ferromagnet depicted in Fig. 6.1, in absence of any intrinsic SOC. As discussed in Section 5.3.5 the curvature κ and the curvature-induced SOC α_N enter in the weak proximity equations in the

same way, so that it is reasonable to ignore the curvature-induced SOC. Furthermore, we assume BCS bulk superconductors at the two interfaces with the ferromagnet, so that we do not need to solve self-consistently the Usadel equation in the whole system.

The Riccati parametrized Usadel equation of Eq. (5.70) for the ferromagnet thus becomes:

$$D_F \left\{ \partial_s^2 \gamma + 2(\partial_s \gamma) \tilde{N} \tilde{\gamma} (\partial_s \gamma) \right\} = -2i\varepsilon\gamma - i\mathbf{h} \cdot (\boldsymbol{\sigma}(s)\gamma - \gamma\boldsymbol{\sigma}^*(s)), \quad (6.1)$$

where the dependence on the curvature is implicitly contained in the Pauli matrices $\sigma_{T,N,B}(s)$. Superconductivity is introduced in the system through the Kupryianov-Lukichev boundary conditions from Eq. (5.72b)

$$\partial_I \gamma_F = \frac{1}{L_F \zeta_F} (1 - \gamma_F \tilde{\gamma}_{S_1}) N_{S_1} (\gamma_F - \gamma_{S_1}), \quad (6.2a)$$

$$\partial_I \gamma_F = \frac{1}{L_F \zeta_F} (1 - \gamma_F \tilde{\gamma}_{S_2}) N_{S_2} (\gamma_{S_2} - \gamma_F). \quad (6.2b)$$

$$(6.2c)$$

We will consider our one-dimensional curved wire to be lying in the xy plane as represented in Fig. 6.1, so that the set of three unit vectors is:

$$\hat{T}(s) = -\sin \theta(s) \hat{x} + \cos \theta(s) \hat{y}, \quad (6.3a)$$

$$\hat{N}(s) = -\cos \theta(s) \hat{x} - \sin \theta(s) \hat{y}, \quad (6.3b)$$

$$\hat{B}(s) \equiv \hat{z}, \quad (6.3c)$$

with $\theta(s) = \kappa s$.

6.1.2 Dynamic $0 - \pi$ transition and long-ranged currents

Solving the Usadel equation, and therefore finding the quasiclassical Green function of the system, allows us to calculate many interesting quantities. We will focus on the charge current given by:

$$\frac{I_Q}{I_{Q0}} = \int_{-\infty}^{+\infty} d\varepsilon \text{Tr} \left\{ \hat{\tau}_3 (\hat{g}_R \partial_s \hat{g}_R - \hat{g}_A \partial_s \hat{g}_A) \right\} \tanh(\beta\varepsilon/2). \quad (6.4)$$

Here $I_{Q0} = N_0 e D_F A \Delta_0 / 4L_F$, where N_0 is the density of states at the Fermi energy, A the interfacial contact area and Δ_0 the bulk gap of the two superconductors. Lengths and energies have been normalized to L_F (which in turn is scaled

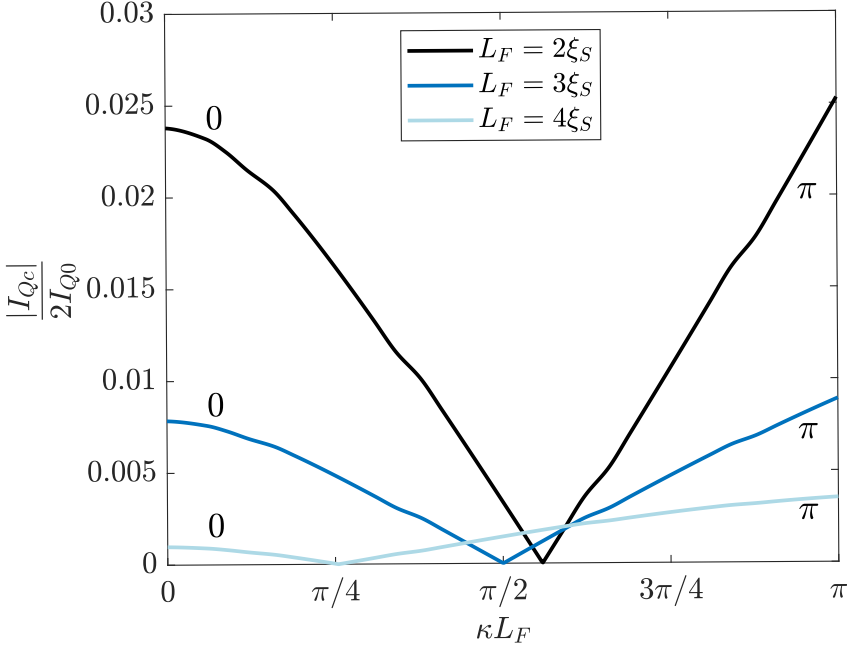


Figure 6.2: Magnitude of the critical current as a function of the curvature for different lengths L_F of the ferromagnet, with $T = 0.005T_c$, $\vec{h} = \Delta_0 \hat{T}$, $\zeta = 3$. A $0 - \pi$ transition occurs when changing the curvature of the wire.

with the superconducting coherence length ξ_S) and superconducting bulk gap Δ_0 respectively, so that the integral on the right side of Eq. (6.4) is dimensionless.

We investigate the system portrayed in Fig. 6.1 by solving numerically the boundary value problem defined by Eqs. (6.1), (6.2a) and (6.2b) for various lengths L_F of the ferromagnet and multiple curvatures κ for each length. We set the interface parameter with both superconductors to be $\zeta = 3$ and the temperature to $T = 0.005T_c$. We consider the exchange field inside the curved ferromagnet to be tangential to its curvature profile at each point, $\mathbf{h}(s) \parallel \hat{T}(s)$. This assumption is justified by the considerations of Section 4.2.2.

In Fig. 6.2 we plot the absolute value of the critical current as given by Eq. (6.4) as a function of the curvature κ of the ferromagnet across the junction for different lengths L_F . From the figure we see that starting in the 0 state with a straight wire, increasing the curvature results in a decreasing magnitude of the critical current. For a certain κ , the current is completely suppressed, and further increasing the curvature produces a revival of the critical current, which then flows in the opposite direction with respect to the initial case, indicating the $0 - \pi$ transition. Similar behaviors are observed for all the length shown in Fig. 6.2.

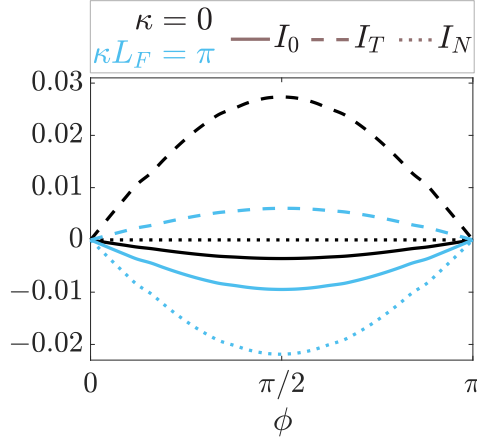


Figure 6.3: Charge current as a function of the phase difference ϕ , showing separately the singlet (solid lines) and triplet (dashed lines) contributions with $T = 0.005T_c$, $\hbar = \Delta_0\hat{T}$, $\zeta = 3$, and $L_F = 2\xi_S$, for a straight ($\kappa = 0$) and semi-circular ($\kappa L_F = \pi$) ferromagnetic wire. Increasing the curvature causes the triplet contribution to change sign.

It is useful to split the charge current into singlet and triplet contributions, I_0 and I_t respectively. This will help us explain how the $0 - \pi$ transition appears, and to show that the role of the triplets is crucial in tuning it. It can be shown that the charge current given by Eq. (6.4) only depends on the anomalous quasiclassical Green's function f . As usual f_0 represents the singlet contribution and $\mathbf{d} = (d_T, d_N, d_z)$ the d-vector represents the triplet contribution. The charge current can be written as $I_Q/I_{Q0} = I_0 + I_t$, where $I_t = I_T + I_N + I_z + I_\kappa$ and:

$$I_0 = -8 \int_0^\infty d\varepsilon \operatorname{Re} \left\{ \tilde{f}_0 \partial_s f_0 - f_0 \partial_s \tilde{f}_0 \right\} \tanh(\beta\varepsilon/2), \quad (6.5a)$$

$$I_j = 8 \int_0^\infty d\varepsilon \operatorname{Re} \left\{ \tilde{d}_j \partial_s d_j - d_j \partial_s \tilde{d}_j \right\} \tanh(\beta\varepsilon/2), \quad (6.5b)$$

$$I_\kappa = 16\kappa \int_0^\infty d\varepsilon \operatorname{Re} \left\{ \tilde{d}_N d_T - \tilde{d}_T d_N \right\} \tanh(\beta\varepsilon/2), \quad (6.5c)$$

with $j = (T, N, z)$. The terms I_0 and I_j represent the contribution coming from the singlet and triplets with spin aligned in the j direction respectively. The last term I_κ instead defines an inverse Edelstein term due to the curvature. This kind of contribution appears whenever the d-vector undergoes a rotation and is therefore non zero only in the presence of finite curvature and/or spin-orbit coupling [312].

In Fig. 6.3 we plot these different contributions to the charge current for two different values of κ and $L_F = 2\xi_S$. It can be seen that for $\kappa = 0$ triplets and singlet charge currents have opposite sign, with the triplets contribution, which comes only

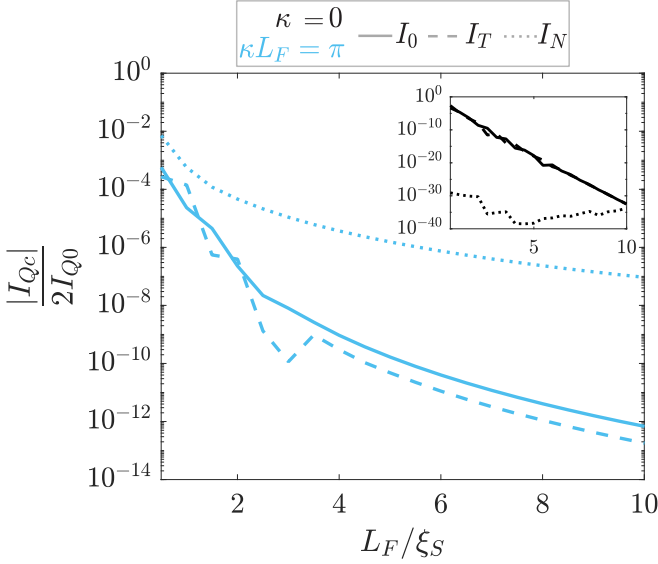


Figure 6.4: Singlet (solid line), short-range (dashed line) and long-range (dotted line) triplets contributions to the critical current as a function of L_F , with $T = 0.005T_c$, $|\mathbf{h}| = 50\Delta_0$, for $\kappa L_F = \pi$ and $\kappa = 0$ (inset).

from the short-range component I_T , being generally bigger than the singlet one. Interestingly however, when increasing the curvature the triplet current changes sign, i.e. starts flowing in the opposite direction, because of the appearance of the long-range component I_N , while the singlet contribution does not. Hence, the $0 - \pi$ transition is tuned by the curvature through its effect on the triplets. Furthermore, in the π -phase for $\kappa = \pi/L_F$ the singlet and triplet currents have the same sign and thus flow in the same direction. Consequently, the two contributions add up, resulting in a larger critical current in the π -phase at $\kappa = \pi/L_F$ compared to the 0 -phase at $\kappa = 0$.

To highlight that the triplets generate a long range Josephson effect, we analyze Fig. 6.4, where we plot the singlet and triplets contributions to the critical current as a function of L_F for a strong exchange field $|\mathbf{h}| = 50\Delta_0$. While for $\kappa = 0$, in the inset of the figure, there is no long-range component, the case $\kappa L_F = \pi$ shows the long-range component I_N decaying with a much larger decay length than the singlet contribution I_0 and the short-range triplet contribution I_T .

It is useful to consider the limit of weak proximity effect. Setting $\tau = \alpha_N = \alpha_B = 0$ in Eqs. (5.77a) to (5.77d), we get the following equations for the singlet and triplet components:

$$\frac{D_F}{2} \partial_s^2 f_0 = -i\varepsilon f_0 - i\mathbf{h} \cdot \mathbf{d}, \quad (6.6a)$$

$$\frac{D_F}{2} (\partial_s^2 d_T - 2\kappa \partial_s d_N) = \left(-i\varepsilon + \frac{D_F \kappa^2}{2}\right) d_T - i f_0 h_T, \quad (6.6b)$$

$$\frac{D_F}{2} (\partial_s^2 d_N + 2\kappa \partial_s d_T) = \left(-i\varepsilon + \frac{D_F \kappa^2}{2}\right) d_N - i f_0 h_N, \quad (6.6c)$$

$$\frac{D_F}{2} \partial_s^2 d_z = -i\varepsilon d_z - i f_0 h_z. \quad (6.6d)$$

As already highlighted in Section 5.3.5, by inspecting the linearized Usadel equation for the triplet components, we see that the curvature produces Dyakonov-Perel terms, describing the spin-relaxation due to precession around the exchange field. A curvature of $\kappa L_F = \pi$ gives a strong spin-relaxation term which causes a fast decay even for the LRT component. From a qualitative perspective we can see that, since the exchange field varies with the position, a LRT component flowing through the wire will acquire an increasing component parallel to \mathbf{h} , i.e. a quickly decaying short-range component. The SRT component likewise acquires a LRT, but the conversion region is restricted to the typical decay of the SRT $\sim 1/\sqrt{\hbar}$. In order to maximise the LRT generation from the SRT, one should therefore have a region of high curvature over the spatial decay of the SRT near the superconducting interface, and then minimal or zero curvature beyond.

Finally, we propose a possible device design for the realization of the $0 - \pi$ transition discussed here. It is generally not practical in experiments to have a full variation from straight wire to semicircular ring, since the structure the nanowire would experience high amount of strain and potentially break. However, if one would manufacture the ferromagnetic weak link with curvature at the value where no current flow is observed, then increasing or decreasing the curvature by minimal amounts, would allow to the achieve control of the direction of the current.

6.2 Diffusive SF hybrid nanowires with curvature

The critical temperature T_c of superconducting hybrid structures can be influenced and controlled through the magnetic properties of ferromagnets, allowing in some cases to realize so-called superconducting spin-valves. Such devices were proposed in the form of SF₁F₂ [313] and of F₁SF₂ [314, 315] structures: for both it was shown that the critical temperature of the system is sensitive to the relative orientation of the magnetizations of the two ferromagnets. Furthermore, experiments studying CuNi/Nb/CuNi trilayers demonstrated that it is possible to control the critical temperature of the structure by switching between parallel and antiparallel

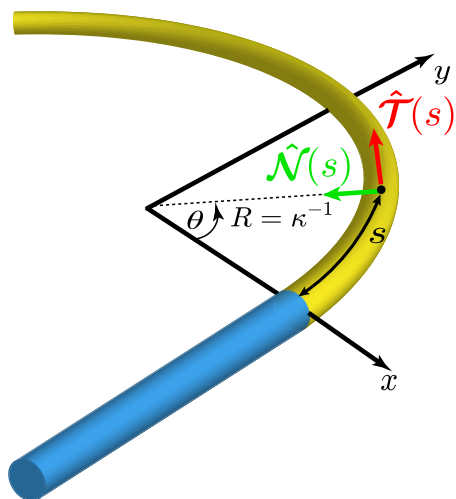


Figure 6.5: Superconductor-ferromagnet hybrid nanowire with a ferromagnet with constant curvature. The orthonormal unit vectors \hat{T} , \hat{N} identifying the curvilinear coordinates are also shown.

orientation of the magnetization in the CuNi layers [316, 317]. Control of the critical temperature can not be achieved in an SF system with a single ferromagnet, since the critical temperature is not sensitive to the orientation of the magnetization of the single F layer. However, the presence of spin-orbit coupling changes this picture as was shown in Ref.[79] for an SF bilayer, where control of the critical temperature was provided by the presence of Rashba and Dresselhaus SOC in the ferromagnet. This was confirmed experimentally in a system where Nb was proximity coupled to an asymmetric Pt/Co/Pt trilayer [80].

Here and in Paper II [2] we show that geometric curvature alone allows for control of the superconducting critical temperature of an SF structure with a curved ferromagnet, thereby realizing a superconducting spin-valve effect. We also show that the inclusion of SOC can increase the magnitude of this effect.

6.2.1 Diffusive Equations and Weak Proximity Effect

We consider the system depicted in Fig. 6.5, a hybrid SF nanowire with a planarly curved ferromagnet. Here we allow for the presence of both curvature-induced and intrinsic SOC. Since the aim is to calculate the critical temperature of the hybrid structure, we can no longer assume a bulk solution for the superconductor. Therefore, we need to find a self-consistent solution for the quasiclassical Green's function of the hybrid system, which we will then use to compute the critical temperature of the system.

The Usadel equations in the S and F and the boundary conditions defining the boundary value problem are given in Eqs. (5.70), (5.71), (5.72a) and (5.72b). For the sake of convenience we rewrite these equations. The Usadel equation in the ferromagnet and in the superconductor are respectively:

$$\begin{aligned}
 D_F \left\{ \partial_s^2 \gamma + 2(\partial_s \gamma) \tilde{N} \tilde{\gamma} (\partial_s \gamma) \right\} &= -2i\varepsilon \gamma \\
 &- i(\mathbf{h} \cdot \boldsymbol{\sigma} \gamma - \gamma \mathbf{h} \cdot \boldsymbol{\sigma}^*) - iD_F [(\partial_s A_T) \gamma + \gamma (\partial_s A_T^*)] \\
 &+ D_F [A^2 \gamma - \gamma A^{*2} + 2(A_j \gamma + \gamma A_j^*) \tilde{N} (A_j^* + \tilde{\gamma} A_j \gamma)] \\
 &+ 2iD_F [(A_T + \gamma A_T^* \tilde{\gamma}) N (\partial_s \gamma) + (\partial_s \gamma) \tilde{N} (A_T^* + \tilde{\gamma} A_T \gamma)], \quad (6.7a)
 \end{aligned}$$

$$D_F \left\{ \partial_y^2 \gamma + 2(\partial_y \gamma) \tilde{N} \tilde{\gamma} (\partial_y \gamma) \right\} = -2i\varepsilon \gamma - \Delta \sigma_2 + \gamma \Delta^* \sigma_2 \gamma, \quad (6.7b)$$

where the SU(2) SO field is $\mathbf{A} = (\alpha_N \sigma_B - \alpha_B \sigma_N, 0, 0)$. The boundary conditions at the SF interface are:

$$\partial_I \gamma_S = \frac{1}{L_S \zeta_S} (1 - \gamma_S \tilde{\gamma}_F) N_F (\gamma_F - \gamma_S) + iA_T \gamma_S + i\gamma_S A_T^*, \quad (6.8a)$$

$$\partial_I \gamma_F = \frac{1}{L_F \zeta_F} (1 - \gamma_F \tilde{\gamma}_S) N_S (\gamma_F - \gamma_S) + iA_T \gamma_F + i\gamma_F A_T^*. \quad (6.8b)$$

It is useful to consider the weak proximity equations in the ferromagnet. The equations for the triplets components are obtained by setting $\tau = 0$ in Eqs. (5.77a) to (5.77c), while the singlet one remains unchanged. These equations read:

$$\begin{aligned}
 \frac{iD_F}{2} \partial_s^2 d_T - iD_F (\kappa + 2\alpha_N) \partial_s d_N - 2iD_F \alpha_B \partial_s d_z &= f_0 h_T \\
 + \left\{ \varepsilon + \frac{iD_F}{2} [(\kappa + 2\alpha_N)^2 + 4\alpha_B^2] \right\} d_T, \quad (6.9a)
 \end{aligned}$$

$$\begin{aligned}
 \frac{iD_F}{2} \partial_s^2 d_N + iD_F (\kappa + 2\alpha_N) \partial_s d_T &= f_0 h_N \\
 + \left\{ \varepsilon + \frac{iD_F}{2} (\kappa + 2\alpha_N)^2 \right\} d_N + iD_F \alpha_B (\kappa + 2\alpha_N) d_z, \quad (6.9b)
 \end{aligned}$$

$$\begin{aligned}
 \frac{iD_F}{2} \partial_s^2 d_z + 2iD_F \alpha_B \partial_s d_T &= f_0 h_z \\
 + \left\{ \varepsilon + 2iD_F \alpha_B^2 \right\} d_z - iD_F \alpha_B (\kappa + 2\alpha_N) d_N, \quad (6.9c)
 \end{aligned}$$

$$\frac{iD_F}{2} \partial_s^2 f_0 = \varepsilon f_0 + \mathbf{h} \cdot \mathbf{d}. \quad (6.9d)$$

As specified in Section 5.3.5, κ , α_N and α_B induce both spin-precession, which provides LRT generation, and spin-relaxation, which causes a decay in all triplet components. We already provided an estimate of the value for the crossover between the regime of LRT generation and triplet decay by comparing the spin-precession prefactor. Considering geometric curvature only the crossover occurs when $\kappa L_F/\pi \sim 0.6$. The inclusion of SOC terms will shift the transition towards 0. This effect is crucial to understand how curvature and spin-orbit coupling influence the critical temperature of the system.

6.2.2 Triplet spin-valve effect controlled by curvature

In order to obtain numerical results for the hybrid system of Fig. 6.5, we look for a self-consistent solution to the Usadel equation given by Eqs. (6.7a) and (6.7b), with the boundary conditions of Eqs. (6.8a) and (6.8b), and the following gap equation [79]:

$$\Delta(s) = N_0\lambda \int_0^{\Delta_0 \cosh(1/N_0\lambda)} d\varepsilon \operatorname{Re} \{f_0(\varepsilon, s)\} \times \tanh\left(\frac{\pi}{2e^\gamma} \frac{\varepsilon/\Delta_0}{T/T_{c0}}\right), \quad (6.10)$$

where λ is the coupling constant between electrons, N_0 is the density of states at the Fermi level, $\gamma \simeq 0.577$ is the Euler-Mascheroni constant, and T is the temperature. Δ_0 and T_{c0} are the superconducting gap and critical temperature of the bulk superconductor, respectively.

To calculate the critical temperature numerically we make use of a binary search algorithm. With this, after calculating $\Delta(s, T)$ for N different values of T , we obtain the critical temperature with a precision of $T_{c0}/2^{N+1}$. The binary search algorithm is presented in [318] and can be found as part of the set of numerical programs GENEUS openly accessible on GitHub [295].

Once a self-consistent solution is found, we can extract the critical temperature of the system for different values of the geometrical curvature κ , the intrinsic and extrinsic (curvature-induced) spin-orbit coupling constants α_B and α_N , and ferromagnet and superconductor lengths L_F and L_S . Again, we consider the exchange field of the ferromagnet to be along the tangential direction and the interface parameter to be $\zeta = 3$. Similarly to the previous section energies are renormalized to the bulk gap of the superconductor at zero temperature Δ_0 , and lengths to its (diffusive) coherence length ξ_0 . Furthermore, we consider a conventional s-wave superconductor with the material parameter $N_0\lambda = 0.2$.

We note that the critical temperature of the hybrid system will always be smaller than the bulk critical temperature of the superconductor. This is due to the

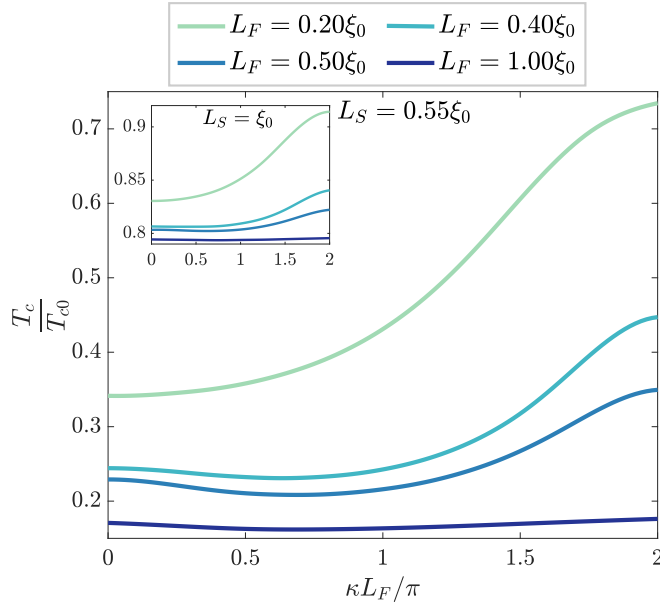


Figure 6.6: Critical temperature of the system T_c divided by the critical temperature of the isolated superconductor T_{c0} as a function of curvature of the ferromagnet κ , for $L_S = 0.55\xi_0$ and $L_S = \xi_0$ (inset) and different lengths of the ferromagnet L_F , with $\hbar = 10\Delta_0\tilde{\tau}$ and zero spin-orbit coupling.

proximity effect, where singlet correlations leak into the ferromagnet. As is clear from Eq. (6.10) a decrease in singlets in the superconductor directly corresponds to a reduction of the singlet order parameter and consequently of the critical temperature.

Analyzing the curvature dependence of the critical temperature of the hybrid system, a range of parameters gives a significant variation with respect to the bulk critical temperature, suggesting a superconducting triplet spin-valve effect tunable via the geometrical curvature. To understand how this effect works we consider again the weak proximity effect limit.

To study this spin-valve effect, we start by considering the case of zero spin-orbit coupling. We consider two different lengths of the superconductor: $L_S = 0.55\xi_0$ and $L_S = \xi_0$. In Fig. 6.6 we plot the behavior of the critical temperature as a function of $\kappa L_F / \pi$, for $L_S = 0.55\xi_0$ and different lengths of the ferromagnet L_F . For a very short ferromagnetic wire, $L_F = 0.20\xi_0$, the critical temperature T_c of the SF structure undergoes a variation of $\sim 40\%$ of the value of the bulk critical temperature of the superconductor T_{c0} , thus giving a very good spin-valve effect. For such a short ferromagnet to be realizable, one would require a large coherence length ξ_0 . For $L_F = 0.40\xi_0$ and $L_F = 0.50\xi_0$ there is still a significant variation of T_c : $\sim 20\%$ and $\sim 15\%$ of the value of T_{c0} , respectively. Interestingly, for $L_S = 0.55\xi_0$ and $L_F \neq 0.20\xi_0$ we note a non-monotonic behavior of T_c : at

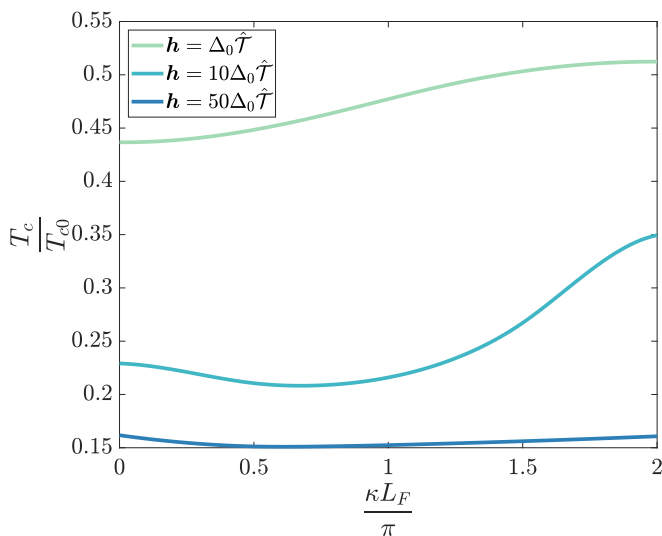


Figure 6.7: Critical temperature of the system T_c divided by the critical temperature of the isolated superconductor T_{c0} as a function of curvature of the ferromagnet κ , for different values of the exchange field \mathbf{h} , with $L_S = 0.55\xi_0$, $L_F = 0.50\xi_0$ and zero spin-orbit coupling.

small values of κ , T_c decreases and then starts to increase again, due to the interplay of spin-precession and relaxation mechanisms. There is no decrease in T_c at small κ for $L_S = 0.55\xi_0$ and $L_F = 0.2\xi_0$ because in this case the length of the ferromagnet is too small for the spin-precession to contribute significantly. In the inset of Fig. 6.6, on the other hand, we plot the case $L_S = \xi_0$ and we note two differences: (i) the critical temperature of the hybrid system is much closer to that of the bulk superconductor and (ii) its variation when changing the curvature is substantially reduced. This is not surprising since we expect the superconductivity to be more robust with respect to proximity effects when increasing the length of the superconductor. Therefore, in order to have a stronger spin-valve effect, we will from now on consider the case $L_S = 0.55\xi_0$.

We also analyze the effect of varying the magnitude of the exchange field \mathbf{h} in the curved ferromagnet. In Fig. 6.7 we plot the ratio T_c/T_{c0} as a function of the curvature κ for three values of the magnitude of the exchange field $|\mathbf{h}| = (\Delta_0, 10\Delta_0, 50\Delta_0)$ with $L_S = 0.55\xi_0$, $L_F = 0.50\xi_0$ and zero spin-orbit coupling. Increasing the magnitude of the exchange field reduces T_c due to the inverse proximity effect. The higher the value of the magnetization the more the singlet correlations are suppressed inside the superconductor, reducing the critical temperature of the system.

We now consider the presence of curvature-induced spin-orbit coupling α_N . As we discussed in Section 4.1.2, α_N is proportional to the curvature, so that we

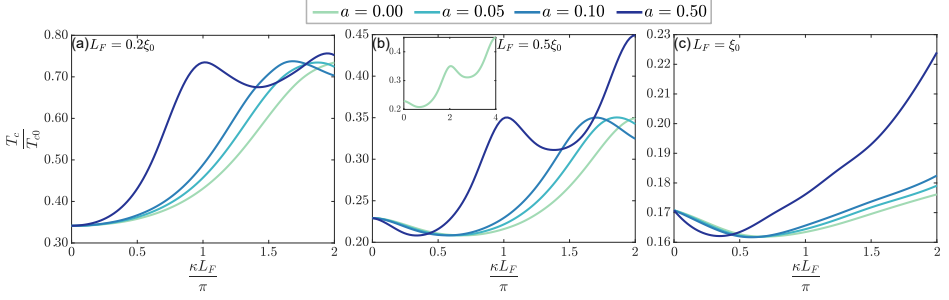


Figure 6.8: Critical temperature of the system T_c divided by the critical temperature of the isolated superconductor T_{c0} as a function of curvature of the ferromagnet κ , for: (a) $L_F = 0.2\xi_0$, (b) $L_F = 0.5\xi_0$, (c) $L_F = \xi_0$ and different values of the curvature-induced spin-orbit proportionality constant a , with $L_S = 0.55\xi_0$, $L_F = 0.50\xi_0$, $\hbar = 10\Delta_0\hat{\mathcal{T}}$ and $\alpha_B = 0$. The inset of (b) shows T_c/T_{c0} as a function of the curvature for $\kappa L_F/\pi$ values up to 4, for $\alpha_N = 0$.

can define it to be $\alpha_N = a\kappa$, with $a = \hbar\Delta g|e|/4mc^2$. In Fig. 6.8 we plot T_c/T_{c0} as a function of κ for different lengths of the ferromagnet and four different values of the curvature-induced SOC proportionality constant a each, with $L_S = 0.55\xi_0$, $\hbar = 10\Delta_0\hat{\mathcal{T}}$. The introduction of a finite a results in a rescaling of the $a = 0$ curves. As was noted in Section 5.3.5, in Eqs. (6.9a) to (6.9c) κ and α_N always appear together in a way that allows us to introduce an effective curvature $\tilde{\kappa} = \kappa + 2\alpha_N = \kappa(1 + 2a)$. Therefore, the case of finite α_N can be considered as equivalent to the $a = 0$ case extended to higher curvatures. To make this more clear, in the inset of Fig. 6.8(b) we plot T_c/T_{c0} as a function of the curvature for κL_F ranging from 0 to 4π , for $L_S = 0.55\xi_0$, $L_F = 0.50\xi_0$, $\hbar = 10\Delta_0\hat{\mathcal{T}}$ and $a = 0$. Comparing in Fig. 6.8(b) the $a = 0.5$ curve with the inset, we note that the two curves look equivalent, showing the effect quantitatively. This equivalency also shows that the weak proximity effect limit is a very good approximation to the full Usadel equation in this case.

Again, we can provide a suggestion which could facilitate the realization of devices to exploit the superconducting spin-valve effect in SF hybrid nanowires with curvature. To circumvent the problem of achieving large curvature variation in the curved ferromagnet, one could fabricate the device with the value of curvature corresponding to where our results suggest a steep variation of the critical temperature, *e.g.* see the dark blue curve in Fig. 6.8(a). Consequently, slightly varying the curvature from that value would allow to achieve a considerable change in the critical temperature.

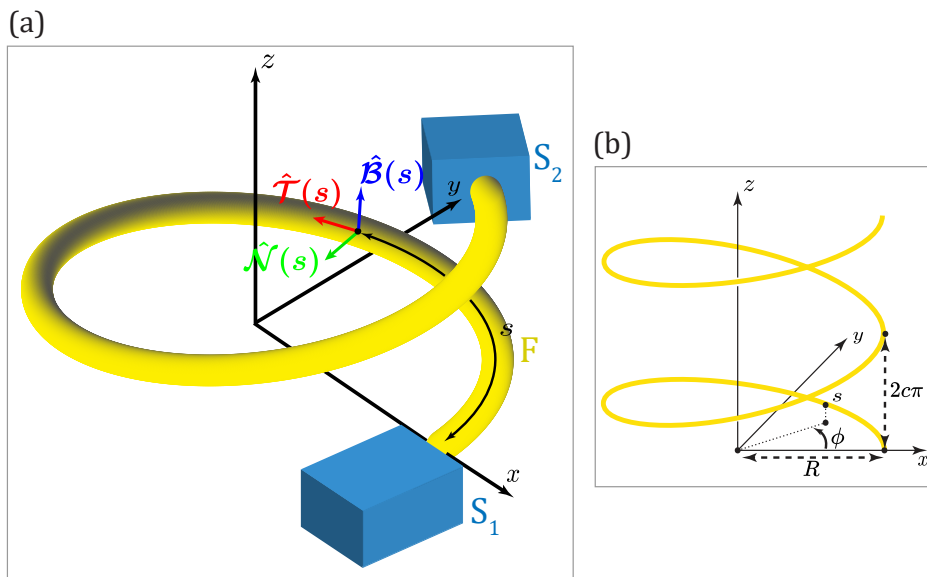


Figure 6.9: (a) Illustration of an SFS junction with right-handed (helicity $\varepsilon = \pm 1$) ferromagnetic helix with constant curvature and torsion, showing the unit vectors $\hat{T}(s)$, $\hat{N}(s)$ and $\hat{B}(s)$ identifying the curvilinear coordinates. (b) Illustration of the parameters used to define the helix in cylindrical coordinates.

6.3 Diffusive SFS Josephson Junctions with Ferromagnetic Helix

Here we will consider an SFS junction with a ferromagnetic helix in the absence of intrinsic SOC. We will analyze the effect of the inclusion of torsion in the system, as well as the handedness of the helix. Again we will assume a bulk solution for the superconductors and consider the exchange field to be in the tangential direction.

A helical nanowire, having radius R , $2c\pi$ pitch, *i.e.* the height of a complete helix turn, can be defined in cylindrical coordinates as:

$$x = R \cos \phi, \quad (6.11a)$$

$$y = \varepsilon R \sin \phi, \quad (6.11b)$$

$$z = c\phi, \quad (6.11c)$$

where $\phi = [0, 2n\pi]$, n defines the number of turns, and $\varepsilon = \pm 1$ is the helicity, *i.e.* $\varepsilon = 1$ identifies a right-handed helix and $\varepsilon = -1$ identifies a left-handed helix. The value of c determines how much the nanowire is tilted out of plane. Curvature and torsion are respectively given by $\kappa = R/(R^2 + c^2)$ and $\tau = c/(R^2 + c^2)$.

The arclength coordinate is $s = \phi\sqrt{R^2 + c^2}$. The helix can be parametrized through the function $\mathbf{r}(\phi) = R \cos \phi \hat{x} + R \sin \phi \hat{y} + c\phi \hat{z}$, which, with the usual definitions $\hat{\mathcal{T}}(\phi) = \partial_\phi \mathbf{r}(\phi) / |\partial_s \mathbf{r}(\phi)|$, $\hat{\mathcal{N}}(\phi) = \partial_\phi \hat{\mathcal{T}}(\phi) / \left| \partial_\phi \hat{\mathcal{T}}(\phi) \right|$ and $\hat{\mathcal{B}}(\phi) = \hat{\mathcal{T}}(\phi) \times \hat{\mathcal{N}}(\phi)$, allows to get:

$$\hat{\mathcal{T}}(\phi) = -\cos \alpha \sin \phi \hat{x} + \varepsilon \cos \alpha \cos \phi \hat{y} + \sin \alpha \hat{z}, \quad (6.12a)$$

$$\hat{\mathcal{N}}(\phi) = -\cos \phi \hat{x} - \varepsilon \sin \phi \hat{y}, \quad (6.12b)$$

$$\hat{\mathcal{B}}(\phi) = \varepsilon \sin \alpha \sin \phi \hat{x} - \sin \alpha \cos \phi \hat{y} + \varepsilon \cos \alpha \hat{z}, \quad (6.12c)$$

where we have defined $\alpha = \text{atan}(\tau/\kappa)$. The components $\sigma_{T,N,B}(s)$ in the ferromagnet are obtained from this set of three unit vectors.

6.3.1 Current-Phase Relation

First of all we analyze the current phase relation of the system by calculating the charge current as given by Eq. (6.4). We note that the charge current I_Q is not sensitive to the helicity of the helix.

It is worth noting that, in order to analyze results for a fixed helix length when varying κ and τ , we need to establish a relationship between curvature and torsion. The length of the helix for a given number of turns of the helix n is given by $L = 2n\pi\sqrt{R^2 + c^2} = 2n\pi/\sqrt{\kappa^2 + \tau^2}$, which provides us of the relationship needed.

In Fig. 6.10 we report the current-phase relation of the junction for $L_F = 2\xi_0$, $T = 0.005T_c$, $|\mathbf{h}| = \Delta_0$ and zero SOC, and number of turns of the helix ranging from 0.5 to 3. An interesting effect of the inclusion of torsion is that the current phase relation acquires a 2ϕ behavior for some κ and τ pairs, rather than the usual $\sin \phi$. This is observed for any number of turns.

Similar higher harmonics contributions have been predicted in $\text{SF}_1\text{F}_2\text{S}$ with noncollinear magnetization [319], as well as in SFS junctions in the clean and diffusive limits [320–323]. They have also been predicted and observed in d-wave superconductors [324, 325]. The appearance of the higher harmonic contributions is generally attributed to the coexistence of stable and metastable 0 and π states [320].

The ferromagnetic helix is a limiting case of multiple noncollinear layers, where the curvature to torsion ratio governs the relative rates and angle of spin precession and relaxation, which in turn govern the 0 – π crossover, as shown previously in this chapter and in Paper I [1]. Therefore, it is reasonable to assume a similar mechanism for the appearance of the higher harmonic contributions also in this

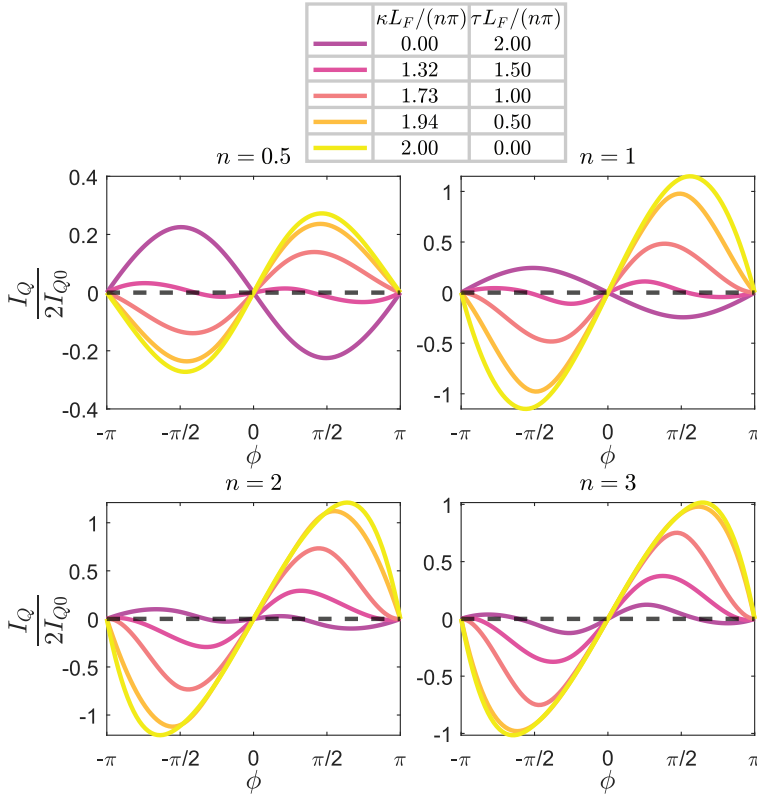


Figure 6.10: Current phase relation for an SFS junction with ferromagnetic helix as weak link for different values of n , with $L_F = 2\xi_0$, $T = 0.005T_c$, $\mathbf{h} = \Delta_0 \hat{\mathcal{T}}$ and zero SOC.

case, due to the influence of κ and τ on singlet and triplet components of the charge current.

6.3.2 Magnetization

Here we discuss the proximity induced magnetization in the ferromagnet as a function of the position at zero phase difference between the superconductors, in right-handed and left-handed helices. The handedness of the helix is introduced by choosing the value of the helicity ε in the parametrization Eqs. (6.12a) to (6.12c), used for the numerical calculations. The magnetization is obtained through Eq. (5.49). The results are reported in Fig. 6.11 for the magnetization in the different directions. It is possible to note the influence of the handedness of the helix, comparing the right-handed helix of Fig. 6.11(a) with the left-handed helix of Fig. 6.11(b). We can see that, while the magnetization in the tangential and

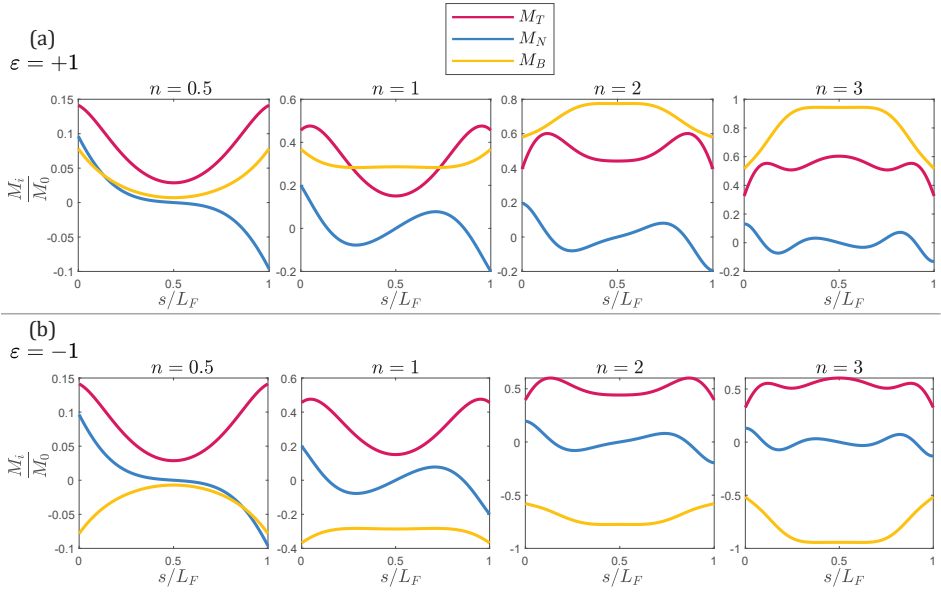


Figure 6.11: Magnetization for the different spin directions T, N, B , in (a) $\varepsilon = +1$ right-handed ferromagnetic helix and (b) $\varepsilon = -1$ left-handed helix as a function of the position, for different values of n , with $L_F = 2\xi_0$, $T = 0.005T_c$, $\mathbf{h} = \Delta_0\hat{\mathcal{T}}$ and zero SOC.

normal direction coincide for the two helicities, the magnetization in the binormal direction has opposite sign between right-handed and left-handed helix. It is also interesting to note that the magnetization in the tangential and binormal direction are symmetric throughout the helix, while the magnetization in the normal direction is asymmetric. Moreover, we highlight the plateau in the binormal magnetization, realized for $n \neq 0.5$, which produces a constant component for a good portion of the helix, see *e.g.* the case $n = 1$.

6.3.3 Spin Current

Finally we calculate the spin current in the ferromagnet as a function of the position at zero phase difference, comparing right-handed and left-handed helices. The formula for the spin current flowing in the wire is obtained from spin current density of Eq. (5.57):

$$I_S^\mu(s) = I_{S0} \int_{-\infty}^{\infty} d\varepsilon j_S^\mu(s, \varepsilon), \quad (6.13)$$

where $\mu = \{T, N, B\}$, $I_{S0} = \hbar N(0)D/32L$ and we have defined the spectral spin current $j_S^\mu = \text{Tr} \{ \hat{\sigma}_\mu \hat{\tau}_3 (\hat{g} \partial_s \hat{g})^K \}$. We report the results in Fig. 6.12. Again we can

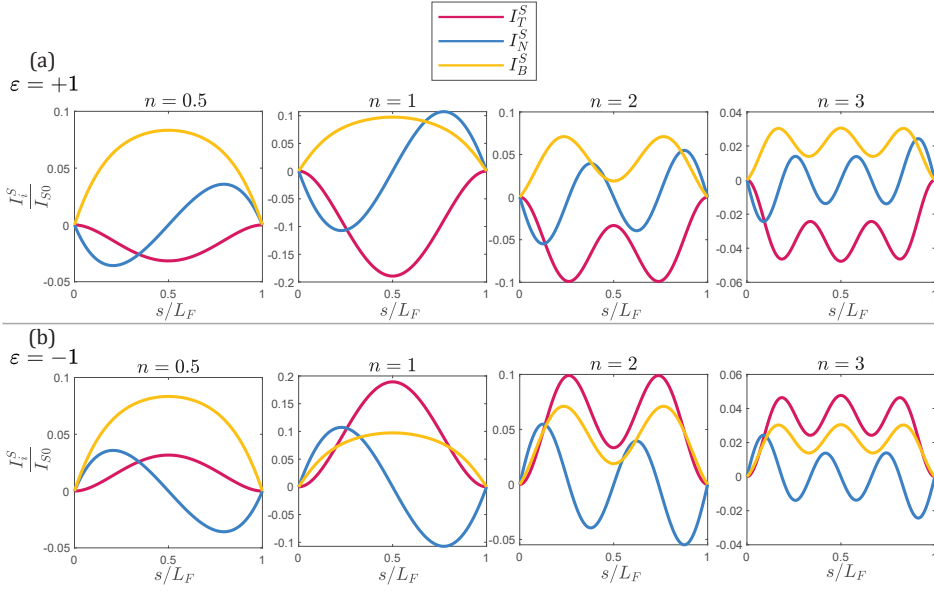


Figure 6.12: Spin currents with spins pointing in the T, N, B directions, in (a) $\varepsilon = +1$ right-handed ferromagnetic helix and (b) $\varepsilon = -1$ left-handed helix as a function of the position, for different values of n , with $L_F = 2\xi_0$, $T = 0.005T_c$, $\mathbf{h} = \Delta_0\hat{\tau}$ and zero SOC.

note the differences occurring between the right-handed helix of Fig. 6.12(a) and the left-handed helix of Fig. 6.12(b). Differently from the magnetization, the spin current with spin directed along the tangential and normal directions have opposite sign for the two helicities, while the spin current with spin along the binormal direction coincides. Again, tangential and binormal components are symmetric while the normal components is asymmetric. We also observe oscillations in all the components of the spin currents, with the number of oscillations increasing with the number of turns n .

We note that the spin current does not present a conserved component as a consequence of the geometry dependent exchange field, differently from what is observed in superconducting hybrid structures with a straight ferromagnet with constant exchange field [81, 326]. Nonetheless, it is possible to define a conserved quantity through analytical considerations. Using the Frenet-Serret formulas of Eq. (4.2) we can define the following constant spin current component:

$$\frac{\bar{I}_S(s)}{I_{S0}} = \int_{-\infty}^{\infty} d\varepsilon \left\{ j_S^{\parallel}(s, \varepsilon) - \int_0^s ds' [h_N (-\kappa j_S^T(s') + \tau j_S^B(s')) + (\kappa h_T - \tau h_B) j_S^N(s')] \right\}, \quad (6.14)$$

where $j_S^{\parallel} = \text{Tr} \{ (\hat{\sigma} \cdot \mathbf{h}) \hat{\tau}_3 (\check{g} \partial_s \check{g})^K \}$ is the spectral spin current with spin parallel to

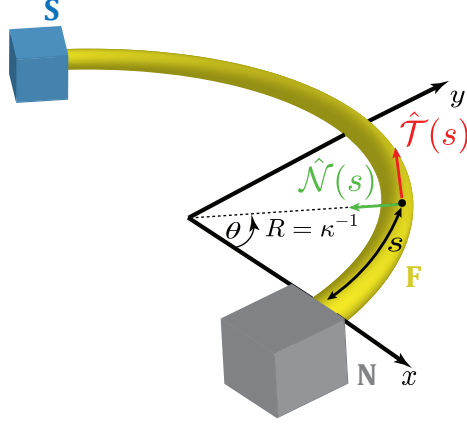


Figure 6.13: Normal metal-superconductor-ferromagnet hybrid nanowire with a ferromagnet with constant curvature. The orthonormal unit vectors \hat{T}, \hat{N} identifying the curvilinear coordinates are also shown.

the exchange field and h_T, h_N, h_B are the components of the exchange field along the $\hat{T}, \hat{N}, \hat{B}$ directions. When the exchange field is directed along the tangential direction Eq. (6.14) reduces to:

$$\frac{\bar{I}_S(s)}{I_{S0}} = \int_{-\infty}^{\infty} d\varepsilon \left\{ j_S^T(s, \varepsilon) - \kappa h_T \int_0^s ds' j_S^N(s') \right\}. \quad (6.15)$$

Despite being mathematically conserved along the helix structure, this spin component does not constitute a realistic observable on its own.

6.4 Non Equilibrium Spin Currents in Diffusive NFS hybrid structure with curved ferromagnet

To conclude this chapter we consider a normal metal-ferromagnet-superconductor hybrid nanowire with a curved ferromagnet, where we assume bulk solutions both for the normal metal and the superconductor. The normal metal is used to apply a voltage bias to the nanostructure. In this case together with the Usadel equation Eq. (6.1) we need to solve the kinetic equation for the distribution matrix \hat{h} Eq. (5.78). As usual, the exchange field in the ferromagnet is chosen in the tangential direction: $\vec{h} = \Delta_0 \hat{T}$, and we set the interface parameters at the NF interface $\zeta_1 = 15$ and at the FS interface $\zeta_2 = 3$. We consider a situation where a spin current is injected through the normal metal, by applying voltages for the two spin directions $V_{\uparrow} = 0.25\Delta_0/e$ and $V_{\downarrow} = -0.25\Delta_0/e$, and we solve the equations

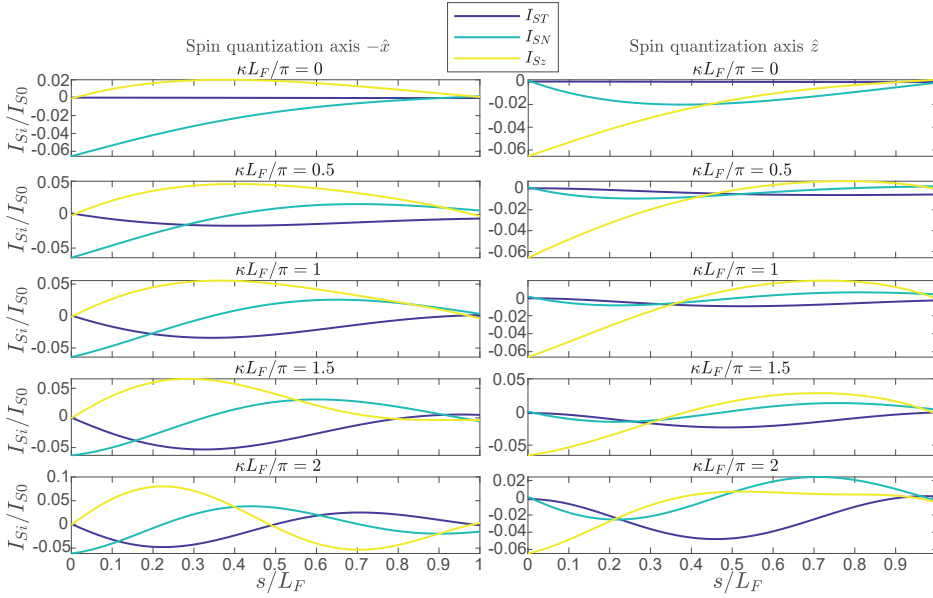


Figure 6.14: Spin current components inside the ferromagnet as a function of the position, for an injected spin currents with spin quantization axis at the NF interface along $-\hat{x}$ (left column) and \hat{z} (right column) through the voltages $V_{\uparrow} = 0.25\Delta_0/e$ and $V_{\downarrow} = -0.25\Delta_0/e$, and different values of the curvature κ of the ferromagnet, with length $L_F = 2\xi_S$, $\vec{h} = \Delta_0\hat{T}$, $\zeta_1 = 15$ and $\zeta_2 = 3$.

for the retarded Green's function and the distribution matrix. With the solutions we can calculate the spin current flowing in the ferromagnet through

$$I_S^\mu(s) = I_{S_0} \int_{-\infty}^{\infty} d\varepsilon \text{Tr} \{ \hat{\sigma}_\mu \hat{\tau}_3 (\hat{g}^R \partial_s \hat{g}^K + \hat{g}^K \partial_s \hat{g}^A) \}, \quad (6.16)$$

where $\hat{g}^K = (\hat{g}^R \hat{h} - \hat{h} \hat{g}^A)$ and $\mu = \{T, N, z\}$.

The results for a ferromagnet of length $L_F = 2\xi_S$ are shown in Fig. 6.14, where we plot the spin current components inside the ferromagnet as a function of the position, for two different directions of the spin quantization axis of the injected spin current at the NF interface and different values of the curvature of the ferromagnet. We compare the injection of a spin current with spin along $-\hat{x}$ and with spin along \hat{z} at the NF interface $s/L_F = 0$. In both cases the spin direction of the injected spin current is rotated due to precession around the exchange field in the ferromagnet, resulting in a conversion to other components with different spins. We observe that the various components of the spin current do not decay completely through the ferromagnet, and residual values are found at the FS interface $s/L_F = 1$. These values are quite small compared to the magnitude of the injected spin current, as an effect of the process of spin relaxation given the large length of the ferromagnet.

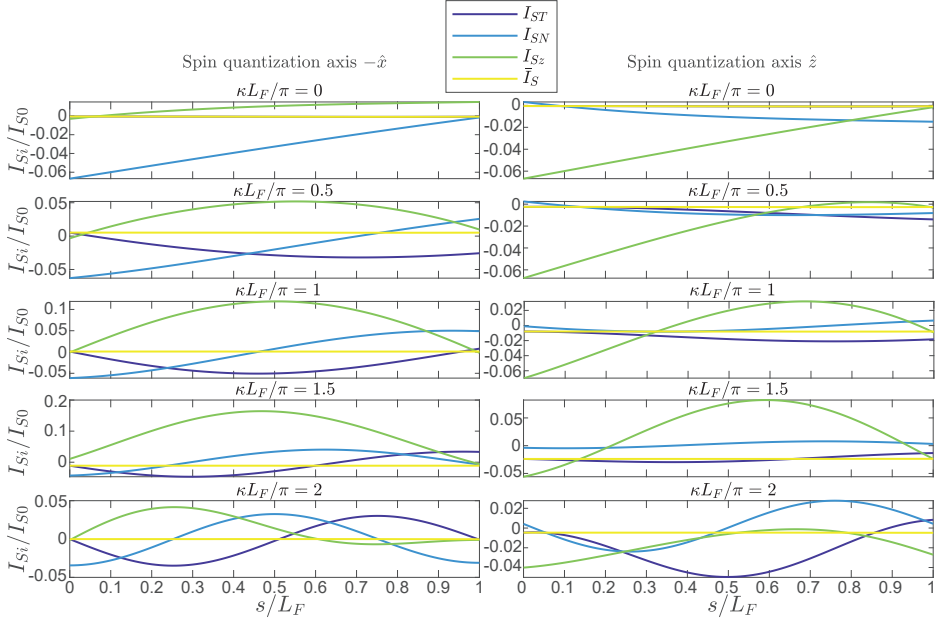


Figure 6.15: Spin current components inside the ferromagnet as a function of the position, for an injected spin currents with spin quantization axis at the NF interface along $-\hat{x}$ (left column) and \hat{z} (right column) through the voltages $V_{\uparrow} = 0.25\Delta_0/e$ and $V_{\downarrow} = -0.25\Delta_0/e$, and different values of the curvature κ of the ferromagnet, with length $L_F = 0.8\xi_S$, $\hbar = \Delta_0\hat{T}$, $\zeta_1 = 15$ and $\zeta_2 = 3$.

In Fig. 6.15 we plot again the spin current components for a shorter ferromagnet with $L_F = 0.8\xi_S$, again for an injected spin current with two different spin quantization axis. We note that in this case, higher values of the spin currents are obtained at the FS interface since the spin relaxation has less impact in this shorter system, see *e.g.* the case $\kappa L_F/\pi = 2$. Moreover, in Fig. 6.15 we plot with a yellow line \bar{I}_S defined in Eq. (6.15). This component is conserved, confirming our analytical predictions, and appears to have a maximum achieved $\kappa L_F/\pi = 1.5$, as it can be seen in Fig. 6.15.

Chapter 7

Curvature Effects in Superconductor-Antiferromagnet Hybrid Structures

In this chapter we present a formulation of the quasiclassical theory for diffusive curvilinear antiferromagnets. First, we provide details on the newly developed quasiclassical theory of antiferromagnetic metals in the dirty limit and the corresponding Usadel equation and boundary conditions [327]. Then we generalize the theory to include geometric curvature in the antiferromagnet and derive a new form of the Usadel equation. We conclude by applying these equations to a superconducting-antiferromagnetic helix hybrid structure¹.

7.1 Diffusive Theory of Curved Antiferromagnetic Metals

The approach used so far to derive the quasiclassical theory in normal metals, superconductors and ferromagnetic metals needs to be modified when treating antiferromagnetic metals (AFMs), owing to their alternating magnetization on the two different sublattices. Recently, a quasiclassical theory for superconductors and AFMs has been developed in Ref.[327]. This theory has been applied to the study of the proximity effect in a S/AFM hybrid structure, showing the appearance of LRTs [34]. We note that a quasiclassical theory for AF insulators with superconductivity has also been developed in Ref.[329]. This shows a growing interest in the study of potential applications of AF within superconducting spintronics. At the same time, as outlined in Chapter 4, the study of curvilinear antiferromagnetism is also

¹This project has been carried out in collaboration with Magnus S. Skjærpe for the realization of his master thesis [328].

experiencing significant advances. Therefore, it seems natural, in the context of this work, to incorporate geometric curvature in the newly developed quasiclassical theory of AFMs, in order to investigate new effects for superconducting spintronics applications.

In this section we will summarize the quasiclassical theory of AFMs developed in Ref. [327], and will discuss how it can be modified to include geometric curvature. The result is a quasiclassical equation of motion for two sub-lattice AFMs with the presence of superconductivity, impurities, spin-orbit coupling and external fields. Moreover, Ref.[327] provides also spin-active boundary conditions for compensated and uncompensated interfaces.

An important difference in the derivation of the equation of motion for AF is the presence of two sub-lattices. This means that the system presents an additional degree of freedom with respect to what we have presented so far. However, Ref. [327] presents a way to circumvent this: the sub-lattice degree of freedom is eliminated by deriving equations for the Green's function of the conduction band crossing the Fermi level. This is possible because only states close to the Fermi level contribute to the quasiclassical Green's function.

7.1.1 Tight Binding Hamiltonian

The Hamiltonian of an AFM within a tight binding model, ignoring any time dependence, can be expressed as:

$$\mathcal{H} = \sum_{n,m \in \mathcal{A}} \psi_n^\dagger (H_0 + V)_{nm} \psi_m, \quad (7.1)$$

where \mathcal{A} is the set of unit cells in the material. Each unit cell n contains one orbital of sublattice A at position \mathbf{r}_n and one orbital of sublattice B at position $\mathbf{r}_n + \boldsymbol{\delta}$. The basis ψ_n^\dagger is defined as:

$$\psi_n^\dagger = \left(c_{nA\uparrow}^\dagger, c_{nA\downarrow}^\dagger, c_{nB\uparrow}^\dagger, c_{nB\downarrow}^\dagger, c_{nA\downarrow}, -c_{nA\uparrow}, c_{nB\downarrow}, -c_{nB\uparrow} \right), \quad (7.2)$$

where the operators $c_{nA\sigma}^\dagger, c_{nB\sigma}^\dagger$ ($c_{nA\sigma}, c_{nB\sigma}$) create (annihilate) an electron with spin σ in unit cell n at sublattice A and B respectively. The non-interacting part of the Hamiltonian of Eq. (7.1) is:

$$(H_0)_{nm} = -\frac{t}{4} [(\rho_x + i\rho_y)\tau_z\chi(\mathbf{r}_n - \mathbf{r}_m - \boldsymbol{\delta}) + (\rho_x - i\rho_y)\tau_z\chi(\mathbf{r}_n - \mathbf{r}_m + \boldsymbol{\delta})] - \frac{1}{2}\delta_{nm} \left\{ \mu\tau_z - J\rho_z\boldsymbol{\sigma} \cdot \left[\frac{1+\rho_z}{2}\mathbf{n}(\mathbf{r}_n) + \frac{1-\rho_z}{2}\mathbf{n}(\mathbf{r}_n + \boldsymbol{\delta}) \right] \right\}, \quad (7.3)$$

where the parameter t is the nearest neighbor hopping, assumed to occur only within different sublattices, J is the exchange energy between conducting electrons and localized spins, μ is the chemical potential and $\chi(\mathbf{r})$ is a nearest neighbor characteristic function, which equals 1 if \mathbf{r} is a nearest neighbor vector and 0 otherwise. The vectors $\boldsymbol{\sigma}$, $\boldsymbol{\tau}$ and $\boldsymbol{\rho}$ have as elements the Pauli matrices in the spin, Nambu and sublattice spaces. The unit vector $\mathbf{n} = (\sin \theta \cos \phi, \sin \theta \sin \phi, \cos \theta)$, with θ and ϕ azimuthal and polar angles respectively, identifies the direction of the Néel vector.

The term V in Eq. (7.1) contains additional effects which may be present in the system, like superconductivity, spin-splitting or spin-orbit coupling.

The next step taken in Ref.[327] to simplify the Hamiltonian is to rotate the spin space in order to have the Néel vector always oriented along the z axis. This is done through the following rotation matrix:

$$R(\mathbf{r}) = \exp \left\{ -i \frac{\theta}{2 \sin \theta} [\mathbf{n}(\mathbf{r}) \times e_z] \cdot \boldsymbol{\sigma} \right\}. \quad (7.4)$$

With this it is possible to write the new basis vector as:

$$\tilde{\psi}_n = \left[\frac{1 + \rho_z}{2} R^\dagger(\mathbf{r}_n) + \frac{1 - \rho_z}{2} R^\dagger(\mathbf{r}_n + \boldsymbol{\delta}) \right] \psi_n. \quad (7.5)$$

The Hamiltonian can now be written as

$$\mathcal{H} = \sum_{n,m \in \mathcal{A}} \tilde{\psi}_n^\dagger \left(\tilde{H}_0 + \tilde{V} \right)_{nm} \tilde{\psi}_m, \quad (7.6)$$

with

$$\begin{aligned} (\tilde{H}_0)_{nm} = & -\frac{1}{2} \delta_{nm} (J \rho_z \sigma_z + \mu \tau_z) + \frac{1}{2} K_{nm} \tau_z \\ & - \frac{\tau_z}{2} \{ (\mathbf{r}_n - \mathbf{r}_m) K_{nm} + [\rho_B \boldsymbol{\delta}, K_{nm}] \} \cdot \left(R^\dagger \nabla R \right) (\mathbf{r}), \end{aligned} \quad (7.7)$$

where $\rho_B = (1 - \rho_z)/2$ is the projection operator on the B sublattice and

$$K_{nm} = \frac{t}{2} [(\rho_x + i \rho_y) \tau_z \chi(\mathbf{r}_n - \mathbf{r}_m - \boldsymbol{\delta}) + (\rho_x - i \rho_y) \tau_z \chi(\mathbf{r}_n - \mathbf{r}_m + \boldsymbol{\delta})]. \quad (7.8)$$

With this Hamiltonian, the next step is to define the Green's functions in the Keldysh formalism, similarly to Section 5.1.1, with the additional sub-lattice degree of freedom, and then derive the Gor'kov equations. As presented in Section 5.1.2, the problem is simplified by switching to center of mass and relative coordinates

and then perform a Fourier transformation of the relative coordinates, so as to obtain the Green's functions as function of the Wigner coordinates. Differently from the approach presented previously, before defining the quasiclassical Green's function and the Eilenberger equation, it is necessary to extract the relevant conduction band. This is done by diagonalizing the Hamiltonian of the system and redefining the Green's function in the new basis. From this new Green's function, it is then possible to identify the component associated with the energy band crossing the Fermi level and continue the derivation only for this component.

7.1.2 Usadel Equation

Having taken the Green's function of the conduction band crossing the Fermi level, the dimensionality is then reduced by a factor of two, and we are back to a Green's function with the same dimensions as in the conventional case. From this component it is possible to define the quasiclassical Green's function like in Eq. (5.14). A requirement for the quasiclassical theory to be valid in this context is that, defining ΔE as the smallest energy difference between the Fermi level and the edges of the conduction band, ΔE must be much larger than any other energy scale of the system, with the exception of the exchange energy J . After some simplifications it is possible to obtain an Eilenberger equation similar to Eq. (5.15), with the difference that the gradient operator ∇ is replaced by a discrete finite difference operator, since the Green's function was defined from a lattice model. However, the distance between neighboring points is short compared to the center of mass characteristic length scale, so that the quasiclassical Green's function can be approximated as a continuous function and the discrete finite difference operator can be replaced with the gradient operator ∇ .

Following similar steps to those presented in Section 5.1.3 it is possible to derive the equation of motion in the dirty limit for diffusive systems, *i.e.* the Usadel equation. The Usadel equation for the quasiclassical Green's function \check{g} is [327]:

$$i\nabla \cdot \check{\mathbf{j}} + \left[\tau_z \epsilon - \check{\Sigma} + i \frac{J^2}{2\tau_{\text{imp}}\eta^2} \sigma_z \tau_z \check{g} \sigma_z \tau_z, \check{g} \right] = 0, \quad (7.9)$$

where $\check{\mathbf{j}}$ is the matrix current, τ_{imp} is the elastic impurity scattering time and $\eta = \sqrt{J^2 + K^2}$, with K kinetic energy. Again, like in Eq. (5.24), $\check{\Sigma}$ contains appropriate additional terms which may be present in the material under consideration. The antiferromagnetic ordering modifies the expression of the matrix current which is given by:

$$\check{\mathbf{j}} = -D\check{g}\nabla\check{g} - \frac{J^2}{2\eta^2}\check{g} [\sigma_z\tau_z\check{g}\sigma_z\tau_z, \check{\mathbf{j}}], \quad (7.10)$$

where D is the diffusion constant. Another modification to the Usadel equation due to antiferromagnetic ordering is represented by the last term in the commutator of Eq. (7.9), which represents effective magnetic impurities with scattering time $\tau_{\text{imp}}\eta^2/J^2$ [327]. Taking advantage of the fact that by definition $J^2/\eta^2 < 1$ it is possible to solve for $\check{\mathbf{j}}$ by iteratively inserting it in the right hand side of Eq. (7.10), and consequently rewrite the equation as:

$$\check{\mathbf{j}} = -\frac{1}{1 + (J/\mu)^2} \left\{ D\check{g}\nabla\check{g} + \frac{J^2}{2\eta^2}\check{g} [\sigma_z\tau_z [\check{g}, \sigma_z\tau_z], \check{\mathbf{j}}] \right\}. \quad (7.11)$$

This expression is particularly useful to get a series expansion with a fast convergence rate. In the limit of small J/η or vanishing $[\check{g}, \sigma_z\tau_z]$, the matrix current becomes:

$$\check{\mathbf{j}} \approx -\frac{1}{1 + (J/\eta)^2} D\check{g}\nabla\check{g}, \quad (7.12)$$

which is equivalent to have a renormalized diffusion constant $D \rightarrow [1 + (J/\eta)^2]^{-1}D$ and greatly simplifies the solution of the Usadel equation.

To summarize, the Usadel equation for AFMs has three main modifications. Firstly, because of the procedure of extraction of the conduction band, all the quantities involved, *e.g.* the self-energy, must be projected into the conduction band according to the matrix of the change of basis. Secondly, the coupling between spin and sublattice degrees of freedom resulting from this procedure produces effective magnetic impurities. Lastly, this magnetic impurities modify the expression for the matrix current which in the conventional case is simply $\check{\mathbf{j}} = -D\check{g}\nabla\check{g}$.

7.1.3 Boundary Conditions

To include AFMs in hybrid structures suitable boundary conditions are needed. These are also derived in the diffusive regime in Ref.[327], for a superconductor (S)-antiferromagnet (A) interface. The boundary condition for the matrix current going from material $a = \{S, A\}$ to material $b = \{S, A\}$ is [34, 327]:

$$\mathbf{e}_n \cdot \check{\mathbf{j}}_a = [\hat{T}_{ab}\check{g}_b\hat{T}_{ba} + i\hat{R}_a, \check{g}_a], \quad (7.13)$$

where \mathbf{e}_n is the outward unit vector normal to the interface, \hat{T}_{ab} is the tunneling matrix and \hat{R}_a is the reflection matrix. This equation coincides with the generalization of the Kupryianov-Lukichev boundary conditions for spin-active interfaces.

In the case of compensated interfaces $\hat{T}_{ab} = t$ and \hat{R}_a are scalars and the boundary conditions of Eq. (7.13) reduce to the usual Kupryianov-Lukichev boundary

conditions. For compensated interfaces, assuming that the tunneling occurs between the superconductor and the A sublattice, the tunneling matrix is [34]:

$$\hat{T}_{SA} = \frac{1}{2} (t_0 + t_1 \mathbf{m} \cdot \hat{\boldsymbol{\sigma}}), \quad (7.14)$$

where $t_0 = t(\sqrt{\eta} + \sqrt{1 - J/\eta})$ and $t_1 = t(\sqrt{\eta} - \sqrt{1 - J/\eta})$. The unit vector \mathbf{m} identifies the direction of the interface magnetization. The reflection matrix can be set equal at both sides of the interface, and taking the value [34] $\hat{R}_S = \hat{R}_A = r\mathbf{m} \cdot \hat{\boldsymbol{\sigma}}$.

7.2 Usadel Equation for Curved Antiferromagnets

We now consider a curvilinear antiferromagnetic helix with constant curvature and torsion, and consider the antiferromagnet to be in the homogeneous state. As specified in Section 4.2.3, in this case the Néel vector lies in the TB plane, and its orientation is given by $\mathbf{n} = \sin \psi \hat{T} + \cos \psi \hat{B}$, with $\psi \approx \kappa \tau L^2$, L being the length of the antiferromagnet.

In the limit of small J/η , the matrix current is given by Eq. (7.12), we follow the same steps of Section 5.3.3 to introduce the space-gauge covariant derivative. The Usadel equation of Eq. (7.9) for the retarded component of the quasiclassical Green's function takes the following form:

$$-i \frac{D}{1+(J/\eta)^2} \tilde{\partial}_s (\hat{g}_R \tilde{\partial}_s \hat{g}_R) + \left[\tau_z \epsilon - \check{\Sigma} + i \frac{J^2}{2\tau_{\text{imp}} \mu^2} (\mathbf{n} \cdot \hat{\boldsymbol{\sigma}}) \tau_z \hat{g}_R (\mathbf{n} \cdot \hat{\boldsymbol{\sigma}}) \tau_z, \hat{g}_R \right] = 0, \quad (7.15)$$

where $\hat{\boldsymbol{\sigma}} = \text{diag}(\boldsymbol{\sigma}, \boldsymbol{\sigma}^*)$ and the Pauli vector is expressed in curvilinear coordinates $\boldsymbol{\sigma} = (\sigma_T, \sigma_N, \sigma_B)$.

7.2.1 Riccati Parametrization

We now introduce the Riccati parametrization for Eq. (7.15) as done in Section 5.3.4. We obtain the following equation for the AFM in the absence of spin-orbit coupling:

$$\begin{aligned} \frac{D}{1+(J/\eta)^2} \left\{ \partial_s^2 \gamma + 2(\partial_s \gamma) \tilde{N} \tilde{\gamma} (\partial_s \gamma) \right\} = & -2i\epsilon \gamma + \frac{J^2}{\tau_{\text{imp}} \eta^2} [(\mathbf{n} \cdot \boldsymbol{\sigma}) N (\mathbf{n} \cdot \boldsymbol{\sigma}) \gamma \\ & + \gamma (\mathbf{n} \cdot \boldsymbol{\sigma})^* \tilde{N} (\mathbf{n} \cdot \boldsymbol{\sigma})^* + (\mathbf{n} \cdot \boldsymbol{\sigma}) N \gamma (\mathbf{n} \cdot \boldsymbol{\sigma})^* + \gamma (\mathbf{n} \cdot \boldsymbol{\sigma})^* \tilde{N} \tilde{\gamma} (\mathbf{n} \cdot \boldsymbol{\sigma}) \gamma - \gamma]. \end{aligned} \quad (7.16)$$

The equation in the S is given by Eq. (5.71).

Regarding the boundary conditions, to solve numerically in the case of compensated interfaces we can use similar equations as those given in Eqs. (5.72a) and (5.72b). In the case of uncompensated interfaces the expression for the boundary condition becomes more complicated, as we need to use the spin-active boundary conditions of Eq. (7.13). The equation for the AFM side of the interface can be written as:

$$\frac{1}{1 + (J/\eta)^2} \partial_I \gamma_{AF} = \frac{t}{4} (1 - \gamma_{AF} \tilde{\gamma}_{AF}) (I_1 \gamma_{AF} + I_2), \quad (7.17)$$

where the terms I_1 and I_2 are:

$$\begin{aligned} I_1 = & - (g_{AF} g_S - f_{AF} \tilde{f}_S) (t_0^2 + t_0 t_1 \mathbf{m} \cdot \boldsymbol{\sigma}) \\ & + (t_0^2 + t_0 t_1 \mathbf{m} \cdot \boldsymbol{\sigma}) (g_S g_{AF} - f_S \tilde{f}_{AF}) \\ & - (g_{AF} \mathbf{m} \cdot \boldsymbol{\sigma} g_S - f_{AF} \mathbf{m} \cdot \boldsymbol{\sigma}^* \tilde{f}_S) (t_0 t_1 + t_1^2 \mathbf{m} \cdot \mathbf{s}) \\ & + (t_0 t_1 + t_1^2 \mathbf{m} \cdot \boldsymbol{\sigma}) (g_S \mathbf{m} \cdot \boldsymbol{\sigma} g_{AF} - f_S \mathbf{m} \cdot \boldsymbol{\sigma}^* \tilde{f}_{AF}) \\ & + i r (\mathbf{m} \cdot \boldsymbol{\sigma} g_{AF} - g_{AF} \mathbf{m} \cdot \boldsymbol{\sigma}), \end{aligned} \quad (7.18a)$$

$$\begin{aligned} I_2 = & - (g_{AF} f_S - f_{AF} \tilde{g}_S) (t_0^2 + t_0 t_1 \mathbf{m} \cdot \boldsymbol{\sigma}^*) \\ & + (t_0^2 + t_0 t_1 \mathbf{m} \cdot \boldsymbol{\sigma}) (g_S f_{AF} - f_S \tilde{g}_{AF}) \\ & - (g_{AF} \mathbf{m} \cdot \mathbf{s} f_S - f_{AF} \mathbf{m} \cdot \boldsymbol{\sigma}^* \tilde{g}_S) (t_0 t_1 + t_1^2 \mathbf{m} \cdot \mathbf{s}^*) \\ & + (t_0^2 + t_0 t_1 \mathbf{m} \cdot \boldsymbol{\sigma}) (g_S \mathbf{m} \cdot \boldsymbol{\sigma} f_{AF} - f_S \mathbf{m} \cdot \boldsymbol{\sigma}^* \tilde{g}_{AF}) \\ & + i r (f_{AF} \mathbf{m} \cdot \boldsymbol{\sigma}^* - \mathbf{m} \cdot \boldsymbol{\sigma} f_{AF}), \end{aligned} \quad (7.18b)$$

and $g_a = 2N_a - 1$, $f_a = 2N_a \gamma_a$ are the 2×2 normal and anomalous Green's functions. A similar equation to Eq. (7.17) holds for the S side of the interface.

7.2.2 Weak Proximity Effect

We will now consider the limit of weak proximity effect with the three unit vectors given by Eqs. (5.74a) to (5.74c) and the expression of the γ matrix of Eq. (5.75). For simplicity we consider the Néel vector to be along the binormal direction ($\psi = 0$), and we get the following equations for the d-vector and singlet components:

$$\begin{aligned} & \frac{iD}{2(1+J^2/\eta^2)} (\partial_s^2 d_T - iD\kappa \partial_s d_N) \\ & = \left(\varepsilon - \frac{J^2}{\tau_{\text{imp}} \eta^2} + \frac{iD_F}{2(1+J^2/\eta^2)} \kappa^2 \right) d_T - \frac{iD_F}{2(1+J^2/\eta^2)} \kappa \tau d_B, \end{aligned} \quad (7.19a)$$

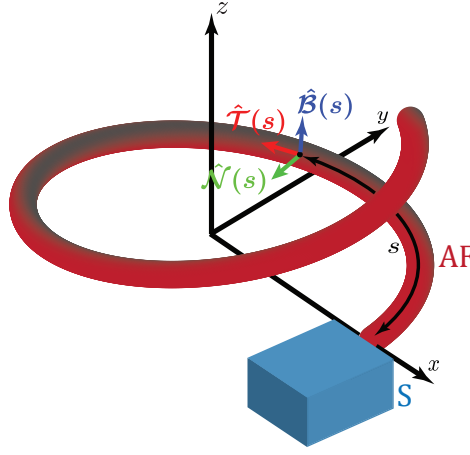


Figure 7.1: Superconductor-antiferromagnet hybrid nanowire with an antiferromagnetic helix. The orthonormal unit vectors \hat{T} , \hat{N} identifying the curvilinear coordinates are also shown.

$$\begin{aligned} & \frac{iD}{2(1+J^2/\eta^2)} (\partial_s^2 d_N + iD\kappa\partial_s d_T - iD_F\tau\partial_s d_B) \\ &= \left(\varepsilon - \frac{J^2}{\tau_{\text{imp}}\eta^2} + \frac{iD}{2(1+J^2/\eta^2)} \kappa^2 \right) d_N, \end{aligned} \quad (7.19b)$$

$$\begin{aligned} & \frac{iD}{2(1+J^2/\eta^2)} (\partial_s^2 d_B - iD\tau\partial_s d_N) \\ &= \left(\varepsilon + \frac{iD}{2(1+J^2/\eta^2)} \tau^2 \right) d_B - \frac{iD_F}{2(1+J^2/\eta^2)} \kappa\tau d_T, \end{aligned} \quad (7.19c)$$

$$\frac{iD}{2(1+J^2/\eta^2)} \partial_s^2 f_0 = \varepsilon f_0. \quad (7.19d)$$

From these equations we note that no conversion to triplets occurs if they are not already present in the system, motivating the need of spin-active boundary conditions. Considering the boundary with a superconductor, the magnetization at the interface will convert singlet correlations in triplets with spin parallel to it. Once triplets are generated at the interface, curvature and torsion govern the conversion between the different components. We also note that the antiferromagnetic exchange J/η introduces a shift in the energy of the triplets d_T and d_N .

7.3 Diffusive Superconducting-Antiferromagnetic Helix Hybrid Nanowire

Here we consider a superconducting-antiferromagnetic helix hybrid nanowire, solving the Usadel equation Eq. (7.15) in the antiferromagnet using a bulk solution for the superconductor. We employ the spin-active boundary conditions of Eq. (7.17) with interface magnetization parallel to the tangential direction. We will assume the Néel vector to be oriented along the binormal direction, we choose the elastic impurity scattering time $\tau\Delta_0 = 0.01$ with Δ_0 bulk gap of the superconductor, the interface parameters $t/\sqrt{\Delta_0\xi_S} = 2$ and $r/\Delta_0\xi_S = 1$. In the following we will present results for the density of states and magnetization in the antiferromagnet.

7.3.1 Density of States

In Fig. 7.2, we plot the density of states as a function of the energy in the center of the antiferromagnetic helix with multiple curvature and torsion pairs, for $n = 1$ number of turns, different values of the antiferromagnetic exchange J and two lengths of the helix L_{AF} . As we discussed in Section 5.2.1, if the density of states at zero energy is suppressed, the system is singlet dominated, while if it presents a peak the system is instead triplet dominated. In Fig. 7.2(a) we plot the results for $L_{AF} = 0.8\xi_S$ and we immediately note that to achieve triplet conversion is necessary to have finite J and τ . When $J = 0$ the system presents an essentially featureless density of states for any value of κ and τ , while when $J \neq 0$ the system is gapped whenever $\tau = 0$. Progressively increasing the torsion causes the appearance of a peak in the density of states. This increase in the density of states at zero energy for increasing torsion is monotonic for $J^2/\eta^2 = 0.01$ with a maximum achieved for $\kappa = 0$. On the other hand, for $J^2/\eta^2 = 0.04$ the maximum peak is achieved for a finite $\kappa < \tau$, increasing the torsion and reducing the curvature from that value causes a decrease in the peak. The case $J^2/\eta^2 = 0.05$ also presents a non monotonic behavior but the maximum in the density of states at zero energy is achieved for $\kappa = 0$.

Analyzing the case of a longer antiferromagnet with length $L_{AF} = 2\xi_S$, shown in Fig. 7.2(b), we note a similar behavior. However, it is worth noting some interesting differences. Firstly, the gap in the density of states is reduced due to the longer length of the helix which causes more suppression of the singlets. Secondly, when the density of states features peaks, these are sharper than those for $L_{AF} = 0.8\xi_S$, signaling the presence of long range triplets which survive for longer distances compared to singlets and short range triplets. Finally, we note again a monotonic behavior of the density of states at zero energy for $J^2/\eta^2 = 0.01$ and a non monotonic behavior for $J^2/\eta^2 = 0.04$ and $J^2/\eta^2 = 0.05$. Again a maximum

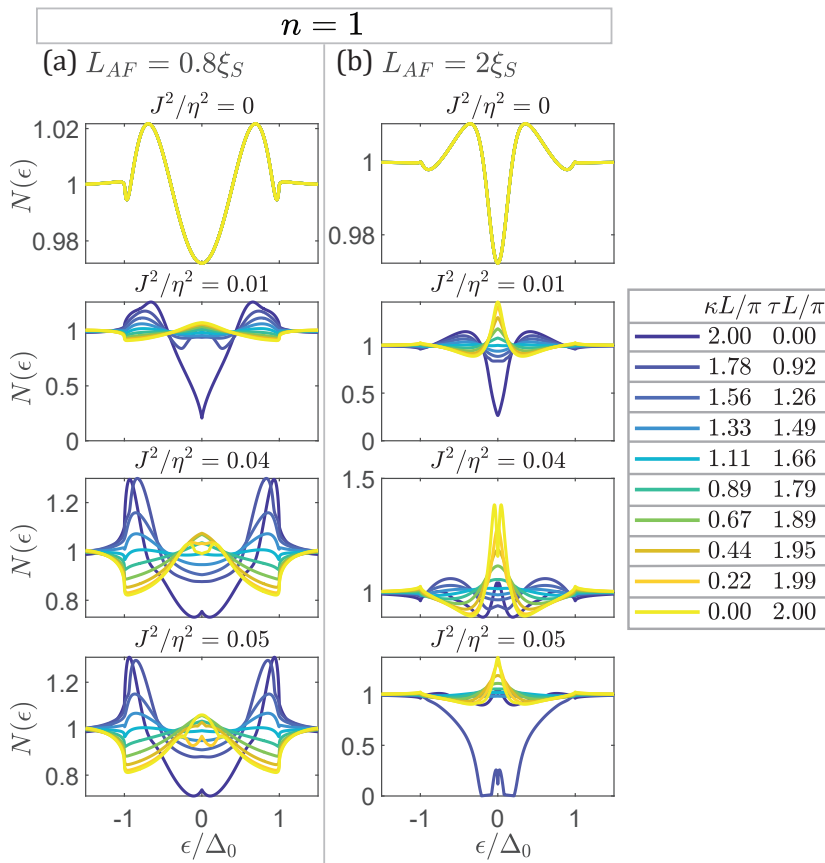


Figure 7.2: Density of states as a function of the energy in the center of an antiferromagnetic helix with $n = 1$ number of turns for (a) $L_{AF} = 0.8\xi_S$ and (b) $L_{AF} = 2\xi_S$, for different values of the antiferromagnetic exchange J and curvature and torsion pairs, with $\tau\Delta_0 = 0.01$ and interface parameters $t/\sqrt{\Delta_0}\xi_S = 2$, $r/\Delta_0\xi_S = 1$.

peak is achieved for $J^2/\eta^2 = 0.04$ for a finite $\kappa < \tau$, however a reduction in the curvature and increase in the torsion from the maximum peak causes the appearance of two peaks shifted from $\varepsilon = 0$, which can be noted observing the $\kappa = 0$ and $J^2/\eta^2 = 0.04$ yellow line in Fig. 7.2(b).

In Fig. 7.3 we show the density of states for $n = 2$ turns and $L_{AF} = 2\xi_S$. Similarly to the case $n = 1$ and $L_{AF} = 2\xi_S$, for $J^2/\eta^2 = 0.01$ the density of states at zero energy presents a monotonic increase for increasing torsion, while $J^2/\eta^2 = 0.04$ and $J^2/\eta^2 = 0.05$ show a non monotonic behavior. Again we note the appearance of two peaks slightly shifted from $\varepsilon = 0$ when $\kappa = 0$ and $J^2/\eta^2 = 0.04$. Differently from the case $n = 1$ and $L_{AF} = 2\xi_S$, the two shifted

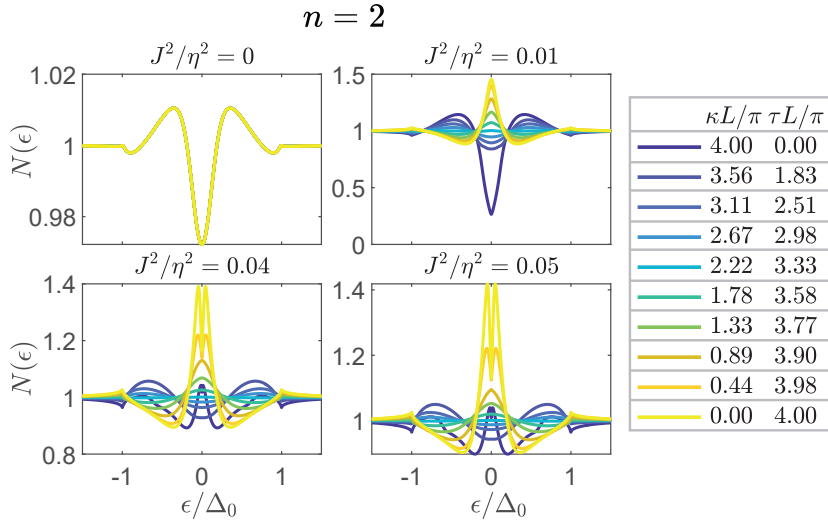


Figure 7.3: Density of states as a function of the energy in the center of an antiferromagnetic helix with $n = 2$ number of turns for different curvature and torsion pairs, with $L_{AF} = 2\xi_S$, $\tau\Delta_0 = 0.01$ and interface parameters $t/\sqrt{\Delta_0\xi_S} = 2$, $r/\Delta_0\xi_S = 1$.

peaks are also observed for a slightly smaller torsion and for $J^2/\eta^2 = 0.05$.

7.3.2 Magnetization

In Fig. 7.4 we plot the magnetization in the antiferromagnetic helix as a function of the position for $L_{AF} = 2\xi_S$, $J/\eta^2 = 0.01$ comparing $n = 1$ (Fig. 7.4(a)) with $n = 2$ number of turns (Fig. 7.4(b)). Consistently with what we observed for the density of states we note a robust presence of triplets in the system, given the finite magnetization components. The magnetization is finite even for $\tau = 0$, but given what we saw for the density of states the singlets are still dominating over the triplets. Introducing a finite torsion substantially increases the order of magnitude of the magnetization along the binormal direction at the interface with the superconductor (see plots with $\kappa L_{AF}/\pi = 1.78$ for $n = 1$ in Fig. 7.4(a), and with $\kappa L_{AF}/\pi = 3.56$ for $n = 2$ in Fig. 7.4(b)).

We note oscillations in the magnetization components as an effect of the conversion happening from one component to the other. For $\tau = 0$ we observe oscillations only in the tangential and normal \hat{z} , while the binormal, *i.e.* along \hat{z} , is simply decaying, meaning that the conversion happens only between M_T and M_N due to the curvature. Conversely, when $\kappa = 0$ only the normal and binormal components oscillate, with conversion happening due to the torsion. The amplitude of the oscillations of the magnetization along the binormal direction observed for

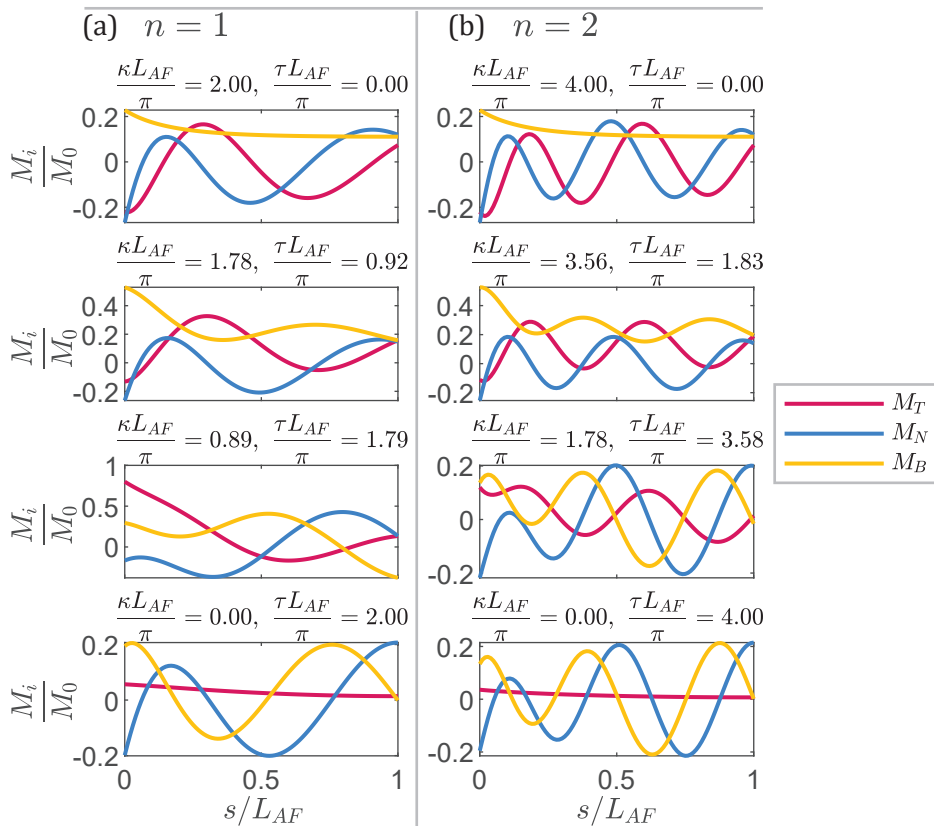


Figure 7.4: Magnetization as a function of the position in the antiferromagnetic helix with $L_{AF} = 2\xi_S$, $J/\eta^2 = 0.01$ and (a) $n = 1$ and (b) $n = 2$ number of turns, for $\tau\Delta_0 = 0.01$ and interface parameters $t/\sqrt{\Delta_0\xi_S} = 2$, $r/\Delta_0\xi_S = 1$.

$\tau \neq 0$ increases with increasing torsion and decreasing curvature. The opposite is observed for the amplitude of the tangential component. Comparing Fig. 7.4(a) with Fig. 7.4(b) we note that the frequency of the oscillations increases with the number of turns of the antiferromagnetic helix. We also note that going from the planarly curved wire ($\tau = 0$) to the fully twisted wire ($\kappa = 0$) the magnetization in the tangential direction is suppressed, and no oscillations are observed for $\kappa = 0$.

To conclude, we note that for high torsion and small curvature the magnetization along the normal and binormal directions appear to oscillate without decaying. This absence of decay is rather surprising given the high length of the helix, and further analysis would be needed to fully understand this behavior².

²More investigations are being carried out in a manuscript in preparation.

Chapter 8

Outlook

In this work we have investigated new avenues for the field of superconducting spintronics. We focused particularly on curved magnetic nanostructures, studying their properties and how they can provide novel effects and flexibility when incorporated in hybrid structures with superconductors. We demonstrated how a curved ferromagnetic weak link in a Josephson junction provides long range triplet generation and a dynamically tunable $0 - \pi$ transition where the direction of the current can be inverted by changing the curvature of the weak link. The transition can be realized in a single sample without application of an external voltage bias, and can therefore potentially improve existing devices and provide more freedom for the realization of new ones. In Section 6.1, we proposed that such new devices can be designed by realizing a junction at the value of the curvature of the ferromagnetic weak link where there is no current flow. Thus, increasing or decreasing the curvature by small amounts, for example via strain, would produce a current switching in the desired direction.

Moreover, we showed that tuning geometric curvature in a ferromagnetic wire proximity coupled to a superconductor, controls the critical temperature of the hybrid structure through its effect on the superconducting triplet correlations in the system. This effect permits the realization of a very efficient superconducting spin-valve, a device of extreme importance for superconducting spintronics applications. Again in Section 6.2, we suggested a promising design for new superconducting spin-valve devices. One could fabricate an hybrid superconducting-curved ferromagnetic nanowire, with the curvature of the ferromagnet close to the point of steepest variation of the critical temperature suggested by our results. Slightly varying the curvature from this point would result in substantial changes in the critical temperature T_c of the structure. Doing this at a fixed temperature $T \gtrsim T_c$, an increase of the curvature would then make T_c higher than T . Therefore, increasing and decreasing the curvature allows to switch on and off superconductivity realizing

a superconducting spin-valve.

Besides the curvature effects, we discussed a new mechanism for achieving high magnetic field superconductivity in a multiband superconductor, beyond the conventional limits. The coexistence between superconductivity and magnetism is of paramount interest for superconducting spintronics. Therefore, the effect we investigated can prove to be a new way of operating superconductors with higher magnetic fields, still preserving the superconducting properties. In this context it is worth noting that geometric curvature and torsion have also an effect on the band structure of materials due to strain¹. Analysis of the effect of strain suggests that the bands would be separated in energy by curvature, while the opposite is true when torsion is included. Furthermore, it has been shown that geometry can control topological transitions in electron spin transport [239–242]. This may reveal promising directions for geometric manipulation of energy bands in the future, potentially providing new avenues for the realization of systems with flat bands and topological materials².

Overall in this thesis we gave an overview of some of the phenomena that can be achieved by including curvature in the magnetic elements of superconducting heterostructures. There are multiple possible directions for extending these investigations. For instance, throughout this thesis we considered the case of a constant curvature, but situations of non constant curvature [298], which is being explored in a manuscript under preparation, can definitely provide further advances. Another possibility is to extend the existing 2D Usadel framework, which uses the finite element method [294], to the curvilinear case. This framework has already been applied to the study of disk-shaped planar Josephson junctions [332], and could allow the investigation of topological effects such as skyrmions in curved surfaces [232].

Additional fascinating prospects could involve applying geometric curvature directly to superconductors and study the system in the diffusive regime. Various theoretical studies have already shown the appearance of interesting physics and the experimental realization of curved superconductors is attracting increasing interest³. However, an extensive diffusive proximity theory of curved superconductors is still missing, and its development could unveil further interesting phenomena, such as a possible influence of geometric curvature in the realization of chiral and topological states in curved superconductors⁴.

With the technological advances we are currently witnessing, there are plenty of possibilities in terms of shapes of geometrically curved materials, and even more

¹For strain effects on the band structure of semiconductors see the review [330].

²For a review on topological materials see [331].

³See the reviews [145, 215] and references therein.

⁴For reviews on chiral and topological superconductors see [333–335].

are surely going to appear in the future. As we showed in this thesis, even simply curving a structure in-plane, allows to achieve effects which usually need extremely complex and marginal device designs, realizable only in limited scales. Moreover, geometric manipulation allows for designable, variable and controllable effective SOC throughout the structure. This possibility has been lacking in the past and could reveal extremely useful for a whole range of applications. Consequently, more complex geometries could provide even more interesting and novel effects. It is therefore clear that we should not limit ourselves to the conventional and rigid device design we have inherited from the past, and we should rather exploit the freedom provided by geometric curvature. After all, the DNA, a vital component for all living species, has a helical shape, and similar geometries could prove to be similarly pivotal for the next generation of nanodevices.

Nowadays, superconductors have already found many widespread applications, however, as we showed in this thesis with the inclusion of geometrically curved magnetic materials in superconducting heterostructures, there is still plenty of potential for the development of novel devices which could revolutionise their applications in superconducting spintronics. This abundance of possibilities is probably the most intriguing aspect of superconducting systems and why we should keep pursuing the effects of geometry in superconductors and their heterostructures to unlock their full potential.

Bibliography

- [1] T. Salamone, M. B. M. Svendsen, M. Amundsen, and S. Jacobsen, [Physical Review B **104**, L060505 \(2021\)](#).
- [2] T. Salamone, H. G. Hugdal, M. Amundsen, and S. H. Jacobsen, “Curvature control of the superconducting proximity effect in diffusive ferromagnetic nanowires”, [Phys. Rev. B **105**, 134511 \(2022\)](#).
- [3] T. Salamone, H. G. Hugdal, S. H. Jacobsen, and M. Amundsen, “High magnetic field superconductivity in a two-band superconductor”, [Phys. Rev. B **107**, 174516 \(2023\)](#).
- [4] A. Hirohata and K. Takanashi, “Future perspectives for spintronic devices”, [Journal of Physics D: Applied Physics **47**, 193001 \(2014\)](#).
- [5] M. Julliere, “Tunneling between ferromagnetic films”, [Physics Letters A **54**, 225–226 \(1975\)](#).
- [6] M. N. Baibich, J. M. Broto, A. Fert, F. N. Van Dau, F. Petroff, P. Etienne, G. Creuzet, A. Friederich, and J. Chazelas, “Giant Magnetoresistance of (001)Fe/(001)Cr Magnetic Superlattices”, [Phys. Rev. Lett. **61**, 2472–2475 \(1988\)](#).
- [7] G. Binasch, P. Grünberg, F. Saurenbach, and W. Zinn, “Enhanced magnetoresistance in layered magnetic structures with antiferromagnetic interlayer exchange”, [Phys. Rev. B **39**, 4828–4830 \(1989\)](#).
- [8] T. Miyazaki and N. Tezuka, “Giant magnetic tunneling effect in Fe/Al₂O₃/Fe junction”, [Journal of Magnetism and Magnetic Materials **139**, L231–L234 \(1995\)](#).
- [9] J. S. Moodera, L. R. Kinder, T. M. Wong, and R. Meservey, “Large Magnetoresistance at Room Temperature in Ferromagnetic Thin Film Tunnel Junctions”, [Phys. Rev. Lett. **74**, 3273–3276 \(1995\)](#).
- [10] S. Yuasa, T. Nagahama, A. Fukushima, Y. Suzuki, and K. Ando, “Giant room-temperature magnetoresistance in single-crystal Fe/MgO/Fe magnetic tunnel junctions”, [Nature Materials **3**, 868–871 \(2004\)](#).

- [11] S. S. P. Parkin, C. Kaiser, A. Panchula, P. M. Rice, B. Hughes, M. Samant, and S.-H. Yang, “Giant tunnelling magnetoresistance at room temperature with MgO (100) tunnel barriers”, *Nature Materials* **3**, 862–867 (2004).
- [12] S. Ikeda, J. Hayakawa, Y. Ashizawa, Y. M. Lee, K. Miura, H. Hasegawa, M. Tsunoda, F. Matsukura, and H. Ohno, “Tunnel magnetoresistance of 604% at 300K by suppression of Ta diffusion in CoFeB/MgO/CoFeB pseudo-spin-valves annealed at high temperature”, *Applied Physics Letters* **93**, 082508, 10.1063/1.2976435 (2008).
- [13] S. S. P. Parkin, Z. G. Li, and D. J. Smith, “Giant magnetoresistance in antiferromagnetic Co/Cu multilayers”, *Applied Physics Letters* **58**, 2710–2712 (1991).
- [14] A. Hirohata, K. Yamada, Y. Nakatani, I.-L. Prejbeanu, B. Diény, P. Pirro, and B. Hillebrands, “Review on spintronics: Principles and device applications”, *Journal of Magnetism and Magnetic Materials* **509**, 166711 (2020).
- [15] D. Apalkov, B. Dieny, and J. M. Slaughter, “Magnetoresistive Random Access Memory”, *Proceedings of the IEEE* **104**, 1796–1830 (2016).
- [16] T. Jungwirth, X. Marti, P. Wadley, and J. Wunderlich, “Antiferromagnetic spintronics”, *Nature Nanotechnology* **11**, 231–241 (2016).
- [17] V. Baltz, A. Manchon, M. Tsoi, T. Moriyama, T. Ono, and Y. Tserkovnyak, “Antiferromagnetic spintronics”, *Rev. Mod. Phys.* **90**, 015005 (2018).
- [18] D. Xiong, Y. Jiang, K. Shi, A. Du, Y. Yao, Z. Guo, D. Zhu, K. Cao, S. Peng, W. Cai, D. Zhu, and W. Zhao, “Antiferromagnetic spintronics: An overview and outlook”, *Fundamental Research* **2**, 522–534 (2022).
- [19] A. S. Núñez, R. A. Duine, P. Haney, and A. H. MacDonald, “Theory of spin torques and giant magnetoresistance in antiferromagnetic metals”, *Phys. Rev. B* **73**, 214426 (2006).
- [20] P. Merodio, A. Kalitsov, H. Béa, V. Baltz, and M. Chshiev, “Spin-dependent transport in antiferromagnetic tunnel junctions”, *Applied Physics Letters* **105**, 122403, 10.1063/1.4896291 (2014).
- [21] B. G. Park, J. Wunderlich, X. Martí, V. Holý, Y. Kurosaki, M. Yamada, H. Yamamoto, A. Nishide, J. Hayakawa, H. Takahashi, A. B. Shick, and T. Jungwirth, “A spin-valve-like magnetoresistance of an antiferromagnet-based tunnel junction”, *Nature Materials* **10**, 347–351 (2011).
- [22] S. Loth, S. Baumann, C. P. Lutz, D. M. Eigler, and A. J. Heinrich, “Bistability in Atomic-Scale Antiferromagnets”, *Science* **335**, 196–199 (2012).

- [23] X. Marti, I. Fina, C. Frontera, J. Liu, P. Wadley, Q. He, R. J. Paull, J. D. Clarkson, J. Kudrnovský, I. Turek, J. Kuneš, D. Yi, J.-H. Chu, C. T. Nelson, L. You, E. Arenholz, S. Salahuddin, J. Fontcuberta, T. Jungwirth, and R. Ramesh, “Room-temperature antiferromagnetic memory resistor”, *Nature Materials* **13**, 367–374 (2014).
- [24] P. Wadley, B. Howells, J. Železný, C. Andrews, V. Hills, R. P. Campion, V. Novák, K. Olejník, F. Maccherozzi, S. S. Dhesi, S. Y. Martin, T. Wagner, J. Wunderlich, F. Freimuth, Y. Mokrousov, J. Kuneš, J. S. Chauhan, M. J. Grzybowski, A. W. Rushforth, K. W. Edmonds, B. L. Gallagher, and T. Jungwirth, “Electrical switching of an antiferromagnet”, *Science* **351**, 587–590 (2016).
- [25] P.-H. Lin, B.-Y. Yang, M.-H. Tsai, P.-C. Chen, K.-F. Huang, H.-H. Lin, and C.-H. Lai, “Manipulating exchange bias by spin–orbit torque”, *Nature Materials* **18**, 335–341 (2019).
- [26] X. H. Liu, K. W. Edmonds, Z. P. Zhou, and K. Y. Wang, “Tuning Interfacial Spins in Antiferromagnetic–Ferromagnetic–Heavy-Metal Heterostructures via Spin-Orbit Torque”, *Phys. Rev. Appl.* **13**, 014059 (2020).
- [27] E. Z. Zhang, Y. C. Deng, X. H. Liu, X. Z. Zhan, T. Zhu, and K. Y. Wang, “Manipulating antiferromagnetic interfacial states by spin-orbit torques”, *Phys. Rev. B* **104**, 134408 (2021).
- [28] B. M. Andersen, I. V. Bobkova, P. J. Hirschfeld, and Y. S. Barash, “Bound states at the interface between antiferromagnets and superconductors”, *Phys. Rev. B* **72**, 184510 (2005).
- [29] E. Erlandsen, A. Kamra, A. Brataas, and A. Sudbø, “Enhancement of superconductivity mediated by antiferromagnetic squeezed magnons”, *Phys. Rev. B* **100**, 100503 (2019).
- [30] E. Erlandsen, A. Brataas, and A. Sudbø, “Magnon-mediated superconductivity on the surface of a topological insulator”, *Phys. Rev. B* **101**, 094503 (2020).
- [31] E. Thingstad, E. Erlandsen, and A. Sudbø, “Eliashberg study of superconductivity induced by interfacial coupling to antiferromagnets”, *Phys. Rev. B* **104**, 014508 (2021).
- [32] G. A. Bobkov, I. V. Bobkova, A. M. Bobkov, and A. Kamra, “Thermally induced spin torque and domain-wall motion in superconductor/antiferromagnetic-insulator bilayers”, *Phys. Rev. B* **103**, 094506 (2021).

- [33] L. G. Johnsen, S. H. Jacobsen, and J. Linder, “[Magnetic control of superconducting heterostructures using compensated antiferromagnets](#)”, *Phys. Rev. B* **103**, L060505 (2021).
- [34] E. H. Fyhn, A. Brataas, A. Qaiumzadeh, and J. Linder, “[Superconducting proximity effect and long-ranged triplets in dirty metallic antiferromagnets](#)”, arXiv:2210.09325, 2023.
- [35] K. Olejník, T. Seifert, Z. Kašpar, V. Novák, P. Wadley, R. P. Campion, M. Baumgartner, P. Gambardella, P. Němec, J. Wunderlich, J. Sinova, P. Kužel, M. Müller, T. Kampfrath, and T. Jungwirth, “[Terahertz electrical writing speed in an antiferromagnetic memory](#)”, *Science Advances* **4**, eaar3566 (2018).
- [36] E. A. Mashkovich, K. A. Grishunin, R. M. Dubrovin, A. K. Zvezdin, R. V. Pisarev, and A. V. Kimel, “[Terahertz light-driven coupling of antiferromagnetic spins to lattice](#)”, *Science* **374**, 1608–1611 (2021).
- [37] E. Rongione, O. Gueckstock, M. Mattern, O. Gomonay, H. Meer, C. Schmitt, R. Ramos, T. Kikkawa, M. Mičica, E. Saitoh, J. Sinova, H. Jaffrès, J. Mangeney, S. T. B. Goennenwein, S. Geprägs, T. Kampfrath, M. Kläui, M. Bargheer, T. S. Seifert, S. Dhillon, and R. Lebrun, “[Emission of coherent THz magnons in an antiferromagnetic insulator triggered by ultrafast spin-phonon interactions](#)”, *Nature Communications* **14**, 1818 (2023).
- [38] H. K. Onnes, “The superconductivity of Mercury”, *Comm. Phys. Lab. Univ. Leiden* **122**, 122–124 (1911).
- [39] W. Meissner and R. Ochsenfeld, “[Ein neuer Effekt bei Eintritt der Supraleitfähigkeit](#)”, *Naturwissenschaften* **21**, 787–788 (1933).
- [40] F. London, H. London, and F. A. Lindemann, “[The electromagnetic equations of the supraconductor](#)”, *Proceedings of the Royal Society of London. Series A - Mathematical and Physical Sciences* **149**, 71–88 (1935).
- [41] M. Tinkham, *Introduction to superconductivity*, Second Edition (Dover Books on Physics, 2004).
- [42] J. Bardeen, L. N. Cooper, and J. R. Schrieffer, “[Microscopic Theory of Superconductivity](#)”, *Phys. Rev.* **106**, 162–164 (1957).
- [43] J. Nagamatsu, N. Nakagawa, T. Muranaka, Y. Zenitani, and J. Akimitsu, “[Superconductivity at 39 K in magnesium diboride](#)”, *Nature* **410**, 63–64 (2001).

- [44] N. Dasenbrock-Gammon, E. Snider, R. McBride, H. Pasan, D. Durkee, N. Khalvashi-Sutter, S. Munasinghe, S. E. Dissanayake, K. V. Lawler, A. Salamat, and R. P. Dias, “Evidence of near-ambient superconductivity in a N-doped lutetium hydride”, *Nature* **615**, 244–250 (2023).
- [45] C. W. Chu, P. H. Hor, R. L. Meng, L. Gao, Z. J. Huang, Wang, and Y. Q., “Evidence for superconductivity above 40 K in the La-Ba-Cu-O compound system”, *Phys. Rev. Lett.* **58**, 405–407 (1987).
- [46] G. Sun, K. Wong, B. Xu, Y. Xin, and D. Lu, “Tc enhancement of $\text{HgBa}_2\text{Ca}_2\text{Cu}_3\text{O}_{8+\delta}$ by Tl substitution”, *Physics Letters A* **192**, 122–124 (1994).
- [47] L. Gao, Y. Y. Xue, F. Chen, Q. Xiong, R. L. Meng, D. Ramirez, C. W. Chu, J. H. Eggert, and H. K. Mao, “Superconductivity up to 164 K in $\text{HgBa}_2\text{Ca}_{m-1}\text{Cu}_m\text{O}_{2m+2+\delta}$ ($m=1, 2, \text{ and } 3$) under quasihydrostatic pressures”, *Phys. Rev. B* **50**, 4260–4263 (1994).
- [48] J.-F. Ge, Z.-L. Liu, C. Liu, C.-L. Gao, D. Qian, Q.-K. Xue, Y. Liu, and J.-F. Jia, “Superconductivity above 100 K in single-layer FeSe films on doped SrTiO_3 ”, *Nature Materials* **14**, 285–289 (2015).
- [49] A. P. Drozdov, M. I. Erements, I. A. Troyan, V. Ksenofontov, and S. I. Shylin, “Conventional superconductivity at 203 kelvin at high pressures in the sulfur hydride system”, *Nature* **525**, 73–76 (2015).
- [50] A. P. Drozdov, P. P. Kong, V. S. Minkov, S. P. Besedin, M. A. Kuzovnikov, S. Mozaffari, L. Balicas, F. F. Balakirev, D. E. Graf, V. B. Prakapenka, E. Greenberg, D. A. Knyazev, M. Tkacz, and M. I. Erements, “Superconductivity at 250 K in lanthanum hydride under high pressures”, *Nature* **569**, 528–531 (2019).
- [51] X. Ming, Y.-J. Zhang, X. Zhu, Q. Li, C. He, Y. Liu, T. Huang, G. Liu, B. Zheng, H. Yang, J. Sun, X. Xi, and H.-H. Wen, “Absence of near-ambient superconductivity in $\text{LuH}_{2\pm x}\text{Ny}$ ”, *Nature, Accelerated Article Preview* (2023).
- [52] S. Hahn, K. Kim, K. Kim, X. Hu, T. Painter, I. Dixon, S. Kim, K. R. Bhattarai, S. Noguchi, J. Jaroszynski, and D. C. Larbalestier, “45.5-tesla direct-current magnetic field generated with a high-temperature superconducting magnet”, *Nature* **570**, 496–499 (2019).
- [53] D. Nakamura, A. Ikeda, H. Sawabe, Y. H. Matsuda, and S. Takeyama, “Record indoor magnetic field of 1200 T generated by electromagnetic flux-compression”, *Review of Scientific Instruments* **89**, 095106 (2018).
- [54] J. Linder and A. V. Balatsky, “Odd-frequency superconductivity”, *Rev. Mod. Phys.* **91**, 045005 (2019).

- [55] J. Linder and J. W. A. Robinson, “Superconducting spintronics”, *Nature Physics* **11**, 307–315 (2015).
- [56] M. Eschrig, “Spin-polarized supercurrents for spintronics”, *Physics Today* **64**, 43–49 (2011).
- [57] F. S. Bergeret, A. F. Volkov, and K. B. Efetov, “Odd triplet superconductivity and related phenomena in superconductor-ferromagnet structures”, *Rev. Mod. Phys.* **77**, 1321–1373 (2005).
- [58] A. I. Buzdin, “Proximity effects in superconductor-ferromagnet heterostructures”, *Rev. Mod. Phys.* **77**, 935–976 (2005).
- [59] I. F. Lyuksyutov and V. L. Pokrovsky, “Ferromagnet–superconductor hybrids”, *Advances in Physics* **54**, 67–136 (2005).
- [60] F. S. Bergeret, A. F. Volkov, and K. B. Efetov, “Long-Range Proximity Effects in Superconductor-Ferromagnet Structures”, *Phys. Rev. Lett.* **86**, 4096–4099 (2001).
- [61] A. Kadigrobov, R. I. Shekhter, and M. Jonson, “Quantum spin fluctuations as a source of long-range proximity effects in diffusive ferromagnet-superconductor structures”, *Europhysics Letters* **54**, 394 (2001).
- [62] M. Eschrig, J. Kopu, J. C. Cuevas, and G. Schön, “Theory of Half-Metal/Superconductor Heterostructures”, *Phys. Rev. Lett.* **90**, 137003 (2003).
- [63] T. S. Khaire, M. A. Khasawneh, W. P. Pratt, and N. O. Birge, “Observation of Spin-Triplet Superconductivity in Co-Based Josephson Junctions”, *Phys. Rev. Lett.* **104**, 137002 (2010).
- [64] J. W. A. Robinson, J. D. S. Witt, and M. G. Blamire, “Controlled Injection of Spin-Triplet Supercurrents into a Strong Ferromagnet”, *Science* **329**, 59–61 (2010).
- [65] R. S. Keizer, S. T. B. Goennenwein, T. M. Klapwijk, G. Miao, G. Xiao, and A. Gupta, “A spin triplet supercurrent through the half-metallic ferromagnet CrO₂”, *Nature* **439**, 825–827 (2006).
- [66] M. S. Anwar, F. Czeschka, M. Hesselberth, M. Porcu, and J. Aarts, “Long-range supercurrents through half-metallic ferromagnetic CrO₂”, *Phys. Rev. B* **82**, 100501 (2010).
- [67] D. Sprungmann, K. Westerholt, H. Zabel, M. Weides, and H. Kohlstedt, “Evidence for triplet superconductivity in Josephson junctions with barriers of the ferromagnetic Heusler alloy Cu₂MnAl”, *Phys. Rev. B* **82**, 060505 (2010).

-
- [68] J. Y. Gu, J. Kusnadi, and C.-Y. You, “Proximity effect in a superconductor/exchange-spring-magnet hybrid system”, *Phys. Rev. B* **81**, 214435 (2010).
- [69] J. Wang, M. Singh, M. Tian, N. Kumar, B. Liu, C. Shi, J. K. Jain, N. Samarth, T. E. Mallouk, and M. H. W. Chan, “Interplay between superconductivity and ferromagnetism in crystalline nanowires”, *Nature Physics* **6**, 389–394 (2010).
- [70] N. Satchell and N. O. Birge, “Supercurrent in ferromagnetic Josephson junctions with heavy metal interlayers”, *Phys. Rev. B* **97**, 214509 (2018).
- [71] N. Satchell, R. Loloee, and N. O. Birge, “Supercurrent in ferromagnetic Josephson junctions with heavy-metal interlayers. II. Canted magnetization”, *Phys. Rev. B* **99**, 174519 (2019).
- [72] F. S. Bergeret and I. V. Tokatly, “Singlet-Triplet Conversion and the Long-Range Proximity Effect in Superconductor-Ferromagnet Structures with Generic Spin Dependent Fields”, *Phys. Rev. Lett.* **110**, 117003 (2013).
- [73] F. S. Bergeret and I. V. Tokatly, *Physical Review B* **89**, 134517 (2014).
- [74] G. Dresselhaus, “Spin-Orbit Coupling Effects in Zinc Blende Structures”, *Phys. Rev.* **100**, 580–586 (1955).
- [75] E. Rashba, “Properties of semiconductors with an extremum loop. 1. Cyclotron and combinational resonance in a magnetic field perpendicular to the plane of the loop”, *Sov. Phys. Solid State* **2**, 1109–1122 (1960).
- [76] F. Konschelle, I. V. Tokatly, and F. S. Bergeret, “Theory of the spin-galvanic effect and the anomalous phase shift φ_0 in superconductors and Josephson junctions with intrinsic spin-orbit coupling”, *Phys. Rev. B* **92**, 125443 (2015).
- [77] S. Vélez, V. N. Golovach, A. Bedoya-Pinto, M. Isasa, E. Sagasta, M. Abadia, C. Rogero, L. E. Hueso, F. S. Bergeret, and F. Casanova, “Hanle Magnetoresistance in Thin Metal Films with Strong Spin-Orbit Coupling”, *Phys. Rev. Lett.* **116**, 016603 (2016).
- [78] E. Strambini, A. Iorio, O. Durante, R. Citro, C. Sanz-Fernández, C. Guarcello, I. V. Tokatly, A. Braggio, M. Rocci, N. Ligato, V. Zannier, L. Sorba, F. S. Bergeret, and F. Giazotto, “A Josephson phase battery”, *Nature Nanotechnology* **15**, 656–660 (2020).
- [79] S. H. Jacobsen, J. A. Ouassou, and J. Linder, “Critical Temperature and Tunneling Spectroscopy of Superconductor-Ferromagnet Hybrids with Intrinsic Rashba–Dresselhaus Spin-Orbit Coupling”, *Physical Review B* **92**, 024510 (2015).

- [80] N. Banerjee, J. A. Ouassou, Y. Zhu, N. A. Stelmashenko, J. Linder, and M. G. Blamire, “Controlling the superconducting transition by spin-orbit coupling”, *Phys. Rev. B* **97**, 184521 (2018).
- [81] S. H. Jacobsen, I. Kulagina, and J. Linder, “Controlling superconducting spin flow with spin-flip immunity using a single homogeneous ferromagnet”, *Scientific reports* **6**, 1–9 (2016).
- [82] S. H. Jacobsen and J. Linder, “Giant triplet proximity effect in π -biased Josephson junctions with spin-orbit coupling”, *Phys. Rev. B* **92**, 024501 (2015).
- [83] S. H. Jacobsen and J. Linder, “Quantum kinetic equations and anomalous nonequilibrium Cooper-pair spin accumulation in Rashba wires with Zeeman splitting”, *Phys. Rev. B* **96**, 134513 (2017).
- [84] G. R. Stewart, “Unconventional superconductivity”, *Advances in Physics* **66**, 75–196 (2017).
- [85] L. D. Landau and V. L. Ginzburg, “On the theory of superconductivity”, *Zh. Eksp. Teor. Fiz.* **20**, 1064 (1950).
- [86] L. P. Gor’kov, “Microscopic derivation of the Ginzburg-Landau equations in the theory of superconductivity”, *Sov. Phys. JETP* **9**, 1364–1367 (1959).
- [87] K. Fossheim and A. Sudbø, *Superconductivity: physics and applications* (John Wiley & Sons, 2004).
- [88] H. G. Hugdal, “A study of proximity-induced and magnon-mediated superconductivity on the surface of topological insulators”, PhD thesis (Norwegian University of Science and Technology (NTNU), 2021).
- [89] A. A. Abrikosov, “On the Magnetic properties of superconductors of the second group”, *Sov. Phys. JETP* **5**, 1174–1182 (1957).
- [90] L. N. Cooper, “Bound Electron Pairs in a Degenerate Fermi Gas”, *Phys. Rev.* **104**, 1189–1190 (1956).
- [91] P. G. De Gennes, *Superconductivity of Metals and Alloys*, en, 1st ed. (CRC Press, Mar. 2018).
- [92] W. Kohn and J. M. Luttinger, “New Mechanism for Superconductivity”, *Phys. Rev. Lett.* **15**, 524–526 (1965).
- [93] A. A. Abrikosov, L. P. Gorkov, and I. E. Dzyaloshinski, *Methods of quantum field theory in statistical physics* (Prentice Hall, 1963).
- [94] A. L. Fetter and J. D. Walecka, *Quantum Theory of Many-Particle Systems* (McGraw-Hill, 1971).

-
- [95] G. Blumberg, A. Mialitsin, B. S. Dennis, M. V. Klein, N. D. Zhigadlo, and J. Karpinski, “Observation of Leggett’s Collective Mode in a Multiband MgB_2 Superconductor”, *Phys. Rev. Lett.* **99**, 227002 (2007).
- [96] F. Giorgianni, T. Cea, C. Vicario, C. P. Hauri, W. K. Withanage, X. Xi, and L. Benfatto, “Leggett Mode Controlled by Light Pulses”, *Nature Physics* **15**, 341–346 (2019).
- [97] S. K. Ghosh, M. Smidman, T. Shang, J. F. Annett, A. D. Hillier, J. Quintanilla, and H. Yuan, “Recent progress on superconductors with time-reversal symmetry breaking”, *Journal of Physics: Condensed Matter* **33**, 033001 (2020).
- [98] H. Suhl, B. T. Matthias, and L. R. Walker, “Bardeen-Cooper-Schrieffer Theory of Superconductivity in the Case of Overlapping Bands”, *Phys. Rev. Lett.* **3**, 552–554 (1959).
- [99] V. A. Moskalenko, “Superconductivity in metals with overlapping energy bands”, *Fiz. Metal. i Metalloved* **8** (1959).
- [100] M. Iskin and C. A. R. Sá de Melo, “BCS-BEC crossover of collective excitations in two-band superfluids”, *Phys. Rev. B* **72**, 024512 (2005).
- [101] M. Iskin and C. A. R. Sá de Melo, “Two-band superfluidity from the BCS to the BEC limit”, *Phys. Rev. B* **74**, 144517 (2006).
- [102] Y. Yerin, H. Tajima, P. Pieri, and A. Perali, “Coexistence of giant Cooper pairs with a bosonic condensate and anomalous behavior of energy gaps in the BCS-BEC crossover of a two-band superfluid Fermi gas”, *Phys. Rev. B* **100**, 104528 (2019).
- [103] A. M. Black-Schaffer and A. V. Balatsky, “Odd-frequency superconducting pairing in multiband superconductors”, *Phys. Rev. B* **88**, 104514 (2013).
- [104] F. Korchorbé and M. Palistrant, “Superconductivity in a two-band system with low carrier density”, *Zh. Eksp. Teor. Fiz* **104**, 442 (1993).
- [105] J. Tahir-Kheli, “Interband pairing theory of superconductivity”, *Phys. Rev. B* **58**, 12307–12322 (1998).
- [106] L. Komendová, A. V. Balatsky, and A. M. Black-Schaffer, “Experimentally observable signatures of odd-frequency pairing in multiband superconductors”, *Phys. Rev. B* **92**, 094517 (2015).
- [107] E. Taylor and C. Kallin, “Intrinsic Hall Effect in a Multiband Chiral Superconductor in the Absence of an External Magnetic Field”, *Phys. Rev. Lett.* **108**, 157001 (2012).

- [108] A. A. Vargas-Paredes, A. A. Shanenkov, A. Vagov, M. V. Milošević, and A. Perali, “Crossband versus intraband pairing in superconductors: Signatures and consequences of the interplay”, *Phys. Rev. B* **101**, 094516 (2020).
- [109] G. N. Bremm, M. A. Continentino, and T. Micklitz, “BCS-BEC crossover in a two-band superconductor with odd-parity hybridization”, *Phys. Rev. B* **104**, 094514 (2021).
- [110] R. Zhi-An, L. Wei, Y. Jie, Y. Wei, S. Xiao-Li, Zheng-Cai, C. Guang-Can, D. Xiao-Li, S. Li-Ling, Z. Fang, and Z. Zhong-Xian, “Superconductivity at 55 K in Iron-Based F-Doped Layered Quaternary Compound $\text{Sm}[\text{O}_{1-x}\text{F}_x]\text{FeAs}$ ”, *Chinese Physics Letters* **25**, 2215–2216 (2008).
- [111] Q.-Y. Wang, Z. Li, W.-H. Zhang, Z.-C. Zhang, J.-S. Zhang, W. Li, H. Ding, Y.-B. Ou, P. Deng, K. Chang, J. Wen, C.-L. Song, K. He, J.-F. Jia, S.-H. Ji, Y.-Y. Wang, L.-L. Wang, X. Chen, X.-C. Ma, and Q.-K. Xue, “Interface-Induced High-Temperature Superconductivity in Single Unit-Cell FeSe Films on SrTiO_3 ”, *Chinese Physics Letters* **29**, 037402 (2012).
- [112] M. Xu, H. Kitazawa, Y. Takano, J. Ye, K. Nishida, H. Abe, A. Matsushita, N. Tsujii, and G. Kido, “Anisotropy of superconductivity from MgB_2 single crystals”, *Applied Physics Letters* **79**, 2779–2781 (2001).
- [113] V. Braccini, A. Gurevich, J. E. Giencke, M. C. Jewell, C. B. Eom, D. C. Larbalestier, A. Pogrebnyakov, Y. Cui, B. T. Liu, Y. F. Hu, J. M. Redwing, Q. Li, X. X. Xi, R. K. Singh, R. Gandikota, J. Kim, B. Wilkens, N. Newman, J. Rowell, B. Moeckly, V. Ferrando, C. Tarantini, D. Marré, M. Putti, C. Ferdeghini, R. Vaglio, and E. Haanappel, “High-field superconductivity in alloyed MgB_2 thin films”, *Phys. Rev. B* **71**, 012504 (2005).
- [114] A. S. Sefat, M. A. McGuire, B. C. Sales, R. Jin, J. Y. Howe, and D. Mandrus, “Electronic correlations in the superconductor $\text{LaFeAsO}_{0.89}\text{F}_{0.11}$ with low carrier density”, *Phys. Rev. B* **77**, 174503 (2008).
- [115] G. F. Chen, Z. Li, G. Li, J. Zhou, D. Wu, J. Dong, W. Z. Hu, P. Zheng, Z. J. Chen, H. Q. Yuan, J. Singleton, J. L. Luo, and N. L. Wang, “Superconducting Properties of the Fe-Based Layered Superconductor $\text{LaFeAsO}_{0.9}\text{F}_{0.1-\delta}$ ”, *Phys. Rev. Lett.* **101**, 057007 (2008).
- [116] Y. Jia, P. Cheng, L. Fang, H. Luo, H. Yang, C. Ren, L. Shan, C. Gu, and H.-H. Wen, “Critical fields and anisotropy of $\text{NdFeAsO}_{0.82}\text{F}_{0.18}$ single crystals”, *Applied Physics Letters* **93**, 032503 (2008).
- [117] M. M. Altarawneh, K. Collar, C. H. Mielke, N. Ni, S. L. Bud’ko, and P. C. Canfield, “Determination of anisotropic H_{c2} up to 60 T in $\text{Ba}_{0.55}\text{K}_{0.45}\text{Fe}_2\text{As}_2$ single crystals”, *Phys. Rev. B* **78**, 220505 (2008).

-
- [118] H. Q. Yuan, J. Singleton, F. F. Balakirev, S. A. Baily, G. F. Chen, J. L. Luo, and N. L. Wang, “Nearly isotropic superconductivity in $(\text{Ba,K})\text{Fe}_2\text{As}_2$ ”, *Nature* **457**, 565–568 (2009).
- [119] M. P. Smylie, A. E. Koshelev, K. Willa, R. Willa, W.-K. Kwok, J.-K. Bao, D. Y. Chung, M. G. Kanatzidis, J. Singleton, F. F. Balakirev, H. Hebbeker, P. Niraula, E. Bokari, A. Kayani, and U. Welp, “Anisotropic upper critical field of pristine and proton-irradiated single crystals of the magnetically ordered superconductor $\text{RbEuFe}_4\text{As}_4$ ”, *Phys. Rev. B* **100**, 054507 (2019).
- [120] A. M. Clogston, “Upper Limit for the Critical Field in Hard Superconductors”, *Phys. Rev. Lett.* **9**, 266–267 (1962).
- [121] B. S. Chandrasekhar, “A Note On The Maximum Critical Field Of High-field Superconductors”, *Applied Physics Letters* **1**, 7–8 (1962).
- [122] A. Gurevich, “Enhancement of the upper critical field by nonmagnetic impurities in dirty two-gap superconductors”, *Phys. Rev. B* **67**, 184515 (2003).
- [123] A. Gurevich, “Limits of the upper critical field in dirty two-gap superconductors”, *Physica C: Superconductivity* **456**, Recent Advances in MgB_2 Research, 160–169 (2007).
- [124] I. V. Bobkova and A. M. Bobkov, “Recovering the superconducting state via spin accumulation above the pair-breaking magnetic field of superconductor/ferromagnet multilayers”, *Phys. Rev. B* **84**, 140508 (2011).
- [125] J. A. Ouassou, T. D. Vethaak, and J. Linder, “Voltage-induced thin-film superconductivity in high magnetic fields”, *Phys. Rev. B* **98**, 144509 (2018).
- [126] S. V. Shulga, S.-L. Drechsler, G. Fuchs, K.-H. Müller, K. Winzer, M. Heinicke, and K. Krug, “Upper Critical Field Peculiarities of Superconducting $\text{YNi}_2\text{B}_2\text{C}$ and $\text{LuNi}_2\text{B}_2\text{C}$ ”, *Phys. Rev. Lett.* **80**, 1730–1733 (1998).
- [127] A. Ghanbari, E. Erlandsen, A. Sudbø, and J. Linder, “Going beyond the Chandrasekhar-Clogston limit in a flatband superconductor”, *Phys. Rev. B* **105**, L060501 (2022).
- [128] S. Hörhold, J. Graf, M. Marganska, and M. Grifoni, “Two-bands Ising superconductivity from Coulomb interactions in monolayer”, *2D Materials* **10**, 025008 (2023).
- [129] Y. Yerin, S.-L. Drechsler, and G. Fuchs, “Ginzburg-Landau Analysis of the Critical Temperature and the Upper Critical Field for Three-Band Superconductors”, *Journal of Low Temperature Physics* **173**, 247–263 (2013).

- [130] A. M. Marques, R. G. Dias, M. A. N. Araújo, and F. D. R. Santos, “In-plane magnetic field versus temperature phase diagram of a quasi-2D frustrated multiband superconductor”, *Superconductor Science and Technology* **28**, 045021 (2015).
- [131] X. Xi, Z. Wang, W. Zhao, J.-H. Park, K. T. Law, H. Berger, L. Forró, J. Shan, and K. F. Mak, “Ising pairing in superconducting NbSe₂ atomic layers”, *Nature Physics* **12**, 139–143 (2016).
- [132] M. Kuzmanović, T. Dvir, D. LeBoeuf, S. Ilić, M. Haim, D. Möckli, S. Kramer, M. Khodas, M. Houzet, J. S. Meyer, M. Aprili, H. Steinberg, and C. H. L. Quay, “Tunneling spectroscopy of few-monolayer NbSe₂ in high magnetic fields: Triplet superconductivity and Ising protection”, *Phys. Rev. B* **106**, 184514 (2022).
- [133] S. Ghannadzadeh, J. D. Wright, F. R. Foronda, S. J. Blundell, S. J. Clarke, and P. A. Goddard, “Upper critical field of NaFe_{1-x}Co_xAs superconductors”, *Phys. Rev. B* **89**, 054502 (2014).
- [134] X. Xing, W. Zhou, J. Wang, Z. Zhu, Y. Zhang, N. Zhou, B. Qian, X. Xu, and Z. Shi, “Two-band and pauli-limiting effects on the upper critical field of 112-type iron pnictide superconductors”, *Scientific Reports* **7**, 45943 (2017).
- [135] L. E. Chow, K. Y. Yip, M. Pierre, S. W. Zeng, Z. T. Zhang, T. Heil, J. Deuschle, P. Nandi, S. K. Sudheesh, Z. S. Lim, Z. Y. Luo, M. Nardone, A. Zitouni, P. A. van Aken, M. Goiran, S. K. Goh, W. Escoffier, and A. Ariando, “Pauli-limit violation in lanthanide infinite-layer nickelate superconductors”, [arXiv.2204.12606](https://arxiv.org/abs/2204.12606) (2022).
- [136] Y. Cao, J. M. Park, K. Watanabe, T. Taniguchi, and P. Jarillo-Herrero, “Pauli-limit violation and re-entrant superconductivity in moiré graphene”, *Nature* **595**, 526–531 (2021).
- [137] L. Balicas, J. S. Brooks, K. Storr, S. Uji, M. Tokumoto, H. Tanaka, H. Kobayashi, A. Kobayashi, V. Barzykin, and L. P. Gor’kov, “Superconductivity in an Organic Insulator at Very High Magnetic Fields”, *Phys. Rev. Lett.* **87**, 067002 (2001).
- [138] S. Uji, H. Shinagawa, T. Terashima, T. Yakabe, Y. Terai, M. Tokumoto, A. Kobayashi, H. Tanaka, and H. Kobayashi, “Magnetic-field-induced superconductivity in a two-dimensional organic conductor”, *Nature* **410**, 908–910 (2001).
- [139] H. W. Meul, C. Rossel, M. Decroux, Ø. Fischer, G. Remenyi, and A. Briggs, “Observation of Magnetic-Field-Induced Superconductivity”, *Phys. Rev. Lett.* **53**, 497–500 (1984).

- [140] F. Lévy, I. Sheikin, B. Grenier, and A. D. Huxley, “Magnetic Field-Induced Superconductivity in the Ferromagnet URhGe”, *Science* **309**, 1343–1346 (2005).
- [141] S. Ran, C. Eckberg, Q.-P. Ding, Y. Furukawa, T. Metz, S. R. Saha, I.-L. Liu, M. Zic, H. Kim, J. Paglione, and N. P. Butch, “Nearly ferromagnetic spin-triplet superconductivity”, *Science* **365**, 684–687 (2019).
- [142] R. Streubel, P. Fischer, F. Kronast, V. P. Kravchuk, D. D. Sheka, Y. Gaididei, O. G. Schmidt, and D. Makarov, “Magnetism in curved geometries”, *Journal of Physics D: Applied Physics* **49**, 363001 (2016).
- [143] R. Streubel, E. Y. Tsybal, and P. Fischer, “Magnetism in curved geometries”, *Journal of Applied Physics* **129**, 210902 (2021).
- [144] D. D. Sheka, “A perspective on curvilinear magnetism”, *Applied Physics Letters* **118**, 230502 (2021).
- [145] D. Makarov, O. M. Volkov, A. Kákay, O. V. Pylypovskiy, B. Budinská, and O. V. Dobrovolskiy, “New Dimension in Magnetism and Superconductivity: 3D and Curvilinear Nanoarchitectures”, *Advanced Materials* **34**, 2101758 (2022).
- [146] J. Dong, J. Liu, G. Kang, J. Xie, and Y. Wang, “Pushing the resolution of photolithography down to 15nm by surface plasmon interference”, *Scientific Reports* **4**, 5618 (2014).
- [147] O. Sahin, M. Ashokkumar, and P. M. Ajayan, “3 - Micro- and nanopatterning of biomaterial surfaces”, in *Fundamental Biomaterials: Metals*, edited by P. Balakrishnan, S. M S, and S. Thomas, Woodhead Publishing Series in Biomaterials (Woodhead Publishing, 2018), pp. 67–78.
- [148] C. Kong, S. Cheong, and R. D. Tilley, “2.15 - Recent Development in Focused Ion Beam Nanofabrication”, in *Comprehensive Nanoscience and Nanotechnology (Second Edition)*, edited by D. L. Andrews, R. H. Lipson, and T. Nann, Second Edition (Academic Press, Oxford, 2019), pp. 327–356.
- [149] R. D. Piner, J. Zhu, F. Xu, S. Hong, and C. A. Mirkin, ““Dip-Pen” Nanolithography”, *Science* **283**, 661–663 (1999).
- [150] V. Prinz, V. Seleznev, A. Gutakovskiy, A. Chehovskiy, V. Preobrazhenskii, M. Putyato, and T. Gavrilova, “Free-standing and overgrown InGaAs/GaAs nanotubes, nanohelices and their arrays”, *Physica E: Low-dimensional Systems and Nanostructures* **6**, 828–831 (2000).
- [151] O. G. Schmidt and K. Eberl, “Thin solid films roll up into nanotubes”, *Nature* **410**, 168–168 (2001).

- [152] K. S. Das, D. Makarov, P. Gentile, M. Cuoco, B. J. Van Wees, C. Ortix, and I. J. Vera-Marun, “[Independent geometrical control of spin and charge resistances in curved spintronics](#)”, *Nano letters* **19**, 6839–6844 (2019).
- [153] O. M. Volkov, A. Kákay, F. Kronast, I. Mönch, M.-A. Mawass, J. Fassbender, and D. Makarov, “[Experimental Observation of Exchange-Driven Chiral Effects in Curvilinear Magnetism](#)”, *Phys. Rev. Lett.* **123**, 077201 (2019).
- [154] J. G. Gibbs, A. G. Mark, T.-C. Lee, S. Eslami, D. Schamel, and P. Fischer, “[Nanohelices by shadow growth](#)”, *Nanoscale* **6**, 9457–9466 (2014).
- [155] D. Sanz-Hernández, A. Hierro-Rodriguez, C. Donnelly, J. Pablo-Navarro, A. Sorrentino, E. Pereiro, C. Magén, S. McVitie, J. M. de Teresa, S. Ferrer, P. Fischer, and A. Fernández-Pacheco, “[Artificial Double-Helix for Geometrical Control of Magnetic Chirality](#)”, *ACS Nano* **14**, 8084–8092 (2020).
- [156] S. Sahoo, S. Mondal, G. Williams, A. May, S. Ladak, and A. Barman, “[Ultrafast magnetization dynamics in a nanoscale three-dimensional cobalt tetrapod structure](#)”, *Nanoscale* **10**, 9981–9986 (2018).
- [157] O. V. Dobrovolskiy, N. R. Vovk, A. V. Bondarenko, S. A. Bunyayev, S. Lamb-Camarena, N. Zenbaa, R. Sachser, S. Barth, K. Y. Guslienko, A. V. Chumak, M. Huth, and G. N. Kakazei, “[Spin-wave eigenmodes in direct-write 3D nanovolcanoes](#)”, *Applied Physics Letters* **118**, 132405 (2021).
- [158] L. Skoric, D. Sanz-Hernández, F. Meng, C. Donnelly, S. Merino-Aceituno, and A. Fernández-Pacheco, “[Layer-by-Layer Growth of Complex-Shaped Three-Dimensional Nanostructures with Focused Electron Beams](#)”, *Nano Letters* **20**, 184–191 (2020).
- [159] F. J. Castaño, C. A. Ross, C. Frandsen, A. Eilez, D. Gil, H. I. Smith, M. Redjda, and F. B. Humphrey, “[Metastable states in magnetic nanorings](#)”, *Phys. Rev. B* **67**, 184425 (2003).
- [160] E. R. Lewis, D. Petit, L. Thevenard, A. V. Jausovec, L. O’Brien, D. E. Read, and R. P. Cowburn, “[Magnetic domain wall pinning by a curved conduit](#)”, *Applied Physics Letters* **95**, 152505 (2009).
- [161] D. M. Burn, M. Chadha, S. K. Walton, and W. R. Branford, “[Dynamic interaction between domain walls and nanowire vertices](#)”, *Phys. Rev. B* **90**, 144414 (2014).
- [162] Y. G. Yoo, M. Kläui, C. A. F. Vaz, L. J. Heyderman, and J. A. C. Bland, “[Switching field phase diagram of Co nanoring magnets](#)”, *Applied Physics Letters* **82**, 2470–2472 (2003).

- [163] M. Kläui, C. Vaz, L. Heyderman, U. Rüdiger, and J. Bland, “Spin switching phase diagram of mesoscopic ring magnets”, *Journal of Magnetism and Magnetic Materials* **290-291**, Proceedings of the Joint European Magnetic Symposia (JEMS’ 04), 61–67 (2005).
- [164] J.-S. Kim, M.-A. Mawass, A. Bisig, B. Krüger, R. M. Reeve, T. Schulz, F. Büttner, J. Yoon, C.-Y. You, M. Weigand, H. Stoll, G. Schütz, H. J. M. Swagten, B. Koopmans, S. Eisebitt, and M. Kläui, “Synchronous precessional motion of multiple domain walls in a ferromagnetic nanowire by perpendicular field pulses”, *Nature Communications* **5**, 3429 (2014).
- [165] K. Richter, A. Krone, M.-A. Mawass, B. Krüger, M. Weigand, H. Stoll, G. Schütz, and M. Kläui, “Localized domain wall nucleation dynamics in asymmetric ferromagnetic rings revealed by direct time-resolved magnetic imaging”, *Phys. Rev. B* **94**, 024435 (2016).
- [166] A. Westphalen, A. Remhof, and H. Zabel, “Magnetization reversal in nanowires with a spiral shape”, *Journal of Applied Physics* **104**, 013906 (2008).
- [167] J. Askey, M. O. Hunt, W. Langbein, and S. Ladak, “Use of Two-Photon Lithography with a Negative Resist and Processing to Realise Cylindrical Magnetic Nanowires”, *Nanomaterials* **10**, 429 (2020).
- [168] G. Williams, M. Hunt, B. Boehm, A. May, M. Taverne, D. Ho, S. Giblin, D. Read, J. Rarity, R. Allenspach, and S. Ladak, “Two-photon lithography for 3D magnetic nanostructure fabrication”, *Nano Research* **11**, 845–854 (2018).
- [169] A. May, M. Hunt, A. Van Den Berg, A. Hejazi, and S. Ladak, “Realisation of a frustrated 3D magnetic nanowire lattice”, *Communications Physics* **2**, 13 (2019).
- [170] M. Melzer, D. Makarov, A. Calvimontes, D. Karnaushenko, S. Baunack, R. Kaltofen, Y. Mei, and O. G. Schmidt, “Stretchable Magnetoelectronics”, *Nano Letters* **11**, 2522–2526 (2011).
- [171] M. Melzer, D. Karnaushenko, D. Makarov, L. Baraban, A. Calvimontes, I. Mönch, R. Kaltofen, Y. Mei, and O. G. Schmidt, “Elastic magnetic sensor with isotropic sensitivity for in-flow detection of magnetic objects”, *RSC Adv.* **2**, 2284–2288 (2012).
- [172] M. Melzer, M. Kaltenbrunner, D. Makarov, D. Karnaushenko, D. Karnaushenko, T. Sekitani, T. Someya, and O. G. Schmidt, “Imperceptible magnetoelectronics”, *Nature Communications* **6**, 6080 (2015).
- [173] D. Makarov, M. Melzer, D. Karnaushenko, and O. G. Schmidt, “Shapeable magnetoelectronics”, *Applied Physics Reviews* **3**, 011101 (2016).

- [174] E. J. Smith, D. Makarov, S. Sanchez, V. M. Fomin, and O. G. Schmidt, “Magnetic Microhelix Coil Structures”, *Phys. Rev. Lett.* **107**, 097204 (2011).
- [175] F. Balhorn, S. Mansfeld, A. Krohn, J. Topp, W. Hansen, D. Heitmann, and S. Mendach, “Spin-Wave Interference in Three-Dimensional Rolled-Up Ferromagnetic Microtubes”, *Phys. Rev. Lett.* **104**, 037205 (2010).
- [176] C. C. Bof Bufon, J. D. Cojal González, D. J. Thurmer, D. Grimm, M. Bauer, and O. G. Schmidt, “Self-Assembled Ultra-Compact Energy Storage Elements Based on Hybrid Nanomembranes”, *Nano Letters* **10**, 2506–2510 (2010).
- [177] D. Grimm, C. C. Bof Bufon, C. Deneke, P. Atkinson, D. J. Thurmer, F. Schäffel, S. Gorantla, A. Bachmatiuk, and O. G. Schmidt, “Rolled-up nanomembranes as compact 3D architectures for field effect transistors and fluidic sensing applications”, *Nano Letters* **13**, 213–218 (2013).
- [178] K. Torikai, R. Furlan de Oliveira, D. H. Starnini de Camargo, and C. C. Bof Bufon, “Low-Voltage, Flexible, and Self-Encapsulated Ultracompact Organic Thin-Film Transistors Based on Nanomembranes”, *Nano Letters* **18**, 5552–5561 (2018).
- [179] W. Huang, J. Zhou, P. J. Froeter, K. Walsh, S. Liu, M. D. Kraman, M. Li, J. A. Michaels, D. J. Sievers, S. Gong, and X. Li, “Three-dimensional radio-frequency transformers based on a self-rolled-up membrane platform”, *Nature Electronics* **1**, 305–313 (2018).
- [180] T. Deng, Z. Zhang, Y. Liu, Y. Wang, F. Su, S. Li, Y. Zhang, H. Li, H. Chen, Z. Zhao, Y. Li, and Z. Liu, “Three-Dimensional Graphene Field-Effect Transistors as High-Performance Photodetectors”, *Nano Letters* **19**, 1494–1503 (2019).
- [181] D. J. Filipiak, A. Azam, T. G. Leong, and D. H. Gracias, “Hierarchical self-assembly of complex polyhedral microcontainers”, *Journal of Micromechanics and Microengineering* **19**, 075012 (2009).
- [182] S. Felton, M. Tolley, E. Demaine, D. Rus, and R. Wood, “A method for building self-folding machines”, *Science* **345**, 644–646 (2014).
- [183] J.-H. Na, A. A. Evans, J. Bae, M. C. Chiappelli, C. D. Santangelo, R. J. Lang, T. C. Hull, and R. C. Hayward, “Programming Reversibly Self-Folding Origami with Micropatterned Photo-Crosslinkable Polymer Trilayers”, *Advanced Materials* **27**, 79–85 (2015).
- [184] C. Coullais, A. Sabbadini, F. Vink, and M. van Hecke, “Multi-step self-guided pathways for shape-changing metamaterials”, *Nature* **561**, 512–515 (2018).

- [185] F. Gabler, D. D. Karnaushenko, D. Karnaushenko, and O. G. Schmidt, “Magnetic origami creates high performance micro devices”, *Nature Communications* **10**, 3013 (2019).
- [186] T. Ozel, G. R. Bourret, and C. A. Mirkin, “Coaxial lithography”, *Nature Nanotechnology* **10**, 319–324 (2015).
- [187] T. Ozel, M. J. Ashley, G. R. Bourret, M. B. Ross, G. C. Schatz, and C. A. Mirkin, “Solution-Dispersible Metal Nanorings with Deliberately Controllable Compositions and Architectural Parameters for Tunable Plasmonic Response”, *Nano Letters* **15**, 5273–5278 (2015).
- [188] M. Rooth, A. Johansson, K. Kukli, J. Aarik, M. Boman, and A. Haarsta, “Atomic Layer Deposition of Iron Oxide Thin Films and Nanotubes using Ferrocene and Oxygen as Precursors”, *Chemical Vapor Deposition* **14**, 67–70 (2008).
- [189] R. Zierold, Z. Wu, J. Biskupek, U. Kaiser, J. Bachmann, C. E. Krill III, and K. Nielsch, “Magnetic, Multilayered Nanotubes of Low Aspect Ratios for Liquid Suspensions”, *Advanced Functional Materials* **21**, 226–232 (2011).
- [190] K. Robbie, J. C. Sit, and M. J. Brett, “Advanced techniques for glancing angle deposition”, *Journal of Vacuum Science & Technology B: Microelectronics and Nanometer Structures Processing, Measurement, and Phenomena* **16**, 1115–1122 (1998).
- [191] S. Eslami, J. G. Gibbs, Y. Rechkemmer, J. van Slageren, M. Alarcón-Correa, T.-C. Lee, A. G. Mark, G. L. J. A. Rikken, and P. Fischer, “Chiral Nanomagnets”, *ACS Photonics* **1**, 1231–1236 (2014).
- [192] Y.-P. Zhao, D.-X. Ye, G.-C. Wang, and T.-M. Lu, “Novel Nano-Column and Nano-Flower Arrays by Glancing Angle Deposition”, *Nano Letters* **2**, 351–354 (2002).
- [193] B. Dick, M. J. Brett, T. J. Smy, M. R. Freeman, M. Malac, and R. F. Egerton, “Periodic magnetic microstructures by glancing angle deposition”, *Journal of Vacuum Science & Technology A* **18**, 1838–1844 (2000).
- [194] B. Dick, M. J. Brett, and T. Smy, “Controlled growth of periodic pillars by glancing angle deposition”, *Journal of Vacuum Science & Technology B: Microelectronics and Nanometer Structures Processing, Measurement, and Phenomena* **21**, 23–28 (2002).
- [195] A. G. Mark, J. G. Gibbs, T.-C. Lee, and P. Fischer, “Hybrid nanocolloids with programmed three-dimensional shape and material composition”, *Nature Materials* **12**, 802–807 (2013).

- [196] C. Phatak, Y. Liu, E. B. Gulsoy, D. Schmidt, E. Franke-Schubert, and A. Petford-Long, “[Visualization of the Magnetic Structure of Sculpted Three-Dimensional Cobalt Nanospirals](#)”, *Nano Letters* **14**, 759–764 (2014).
- [197] M. Huth, F. Porrati, and O. Dobrovolskiy, “[Focused electron beam induced deposition meets materials science](#)”, *Microelectronic Engineering* **185-186**, 9–28 (2018).
- [198] A. Fernández-Pacheco, L. Skoric, J. M. De Teresa, J. Pablo-Navarro, M. Huth, and O. V. Dobrovolskiy, “[Writing 3D Nanomagnets Using Focused Electron Beams](#)”, *Materials* **13**, 3774 (2020).
- [199] W. F. van Dorp, B. van Someren, C. W. Hagen, P. Kruit, and P. A. Crozier, “[Approaching the Resolution Limit of Nanometer-Scale Electron Beam-Induced Deposition](#)”, *Nano Letters* **5**, 1303–1307 (2005).
- [200] A. Fernández-Pacheco, L. Serrano-Ramón, J. M. Michalik, M. R. Ibarra, J. M. De Teresa, L. O’Brien, D. Petit, J. Lee, and R. P. Cowburn, “[Three dimensional magnetic nanowires grown by focused electron-beam induced deposition](#)”, *Scientific Reports* **3**, 1492 (2013).
- [201] C. Phatak, C. S. Miller, Z. Thompson, E. B. Gulsoy, and A. K. Petford-Long, “[Curved Three-Dimensional Cobalt Nanohelices for Use in Domain Wall Device Applications](#)”, *ACS Applied Nano Materials* **3**, 6009–6016 (2020).
- [202] L. Keller, M. K. I. Al Mamoori, J. Pieper, C. Gspan, I. Stockem, C. Schröder, S. Barth, R. Winkler, H. Plank, M. Pohlitz, J. Müller, and M. Huth, “[Direct-write of free-form building blocks for artificial magnetic 3D lattices](#)”, *Scientific Reports* **8**, 6160 (2018).
- [203] M. K. I. Al Mamoori, L. Keller, J. Pieper, S. Barth, R. Winkler, H. Plank, J. Müller, and M. Huth, “[Magnetic Characterization of Direct-Write Free-Form Building Blocks for Artificial Magnetic 3D Lattices](#)”, *Materials* **11**, 289 (2018).
- [204] D. D. Sheka, V. P. Kravchuk, and Y. Gaididei, “[Curvature effects in statics and dynamics of low dimensional magnets](#)”, *Journal of Physics A: Mathematical and Theoretical* **48**, 125202 (2015).
- [205] P. Gentile, M. Cuoco, O. M. Volkov, Z.-J. Ying, I. J. Vera-Marun, D. Makarov, and C. Ortix, “[Electronic materials with nanoscale curved geometries](#)”, *Nature Electronics* **5**, 551–563 (2022).
- [206] P. Gentile, M. Cuoco, and C. Ortix, “[Curvature-induced rashba spin-orbit interaction in strain-driven nanostructures](#)”, *Spin* **3**, 1340002 (2013).

-
- [207] M. B. M. Svendsen, “Curvature in Superconductor-Ferromagnet Structures”, Master thesis (Norwegian University of Science and Technology (NTNU), 2021).
- [208] P. A. Kelly, “Vectors and Tensors”, in *Mechanics Lecture Notes Part III: Foundations of Continuum Mechanics* (University of Auckland, 2021) Chap. 1.
- [209] B. R. Kusse and E. A. Westwig, “Christoffel Symbols and Covariant derivatives”, in *Mathematical Physics: applied mathematics for scientists and engineers* (Wiley-VCH, 2006) Chap. F, pp. 655–659.
- [210] C. Kittel, Introduction to Solid State Physics, 8th ed. (Wiley, Hoboken, N.J., 2005).
- [211] C. Ortix, S. Kiravittaya, O. G. Schmidt, and J. van den Brink, “Curvature-induced geometric potential in strain-driven nanostructures”, *Physical Review B* **84**, 045438 (2011).
- [212] J. Bardeen and W. Shockley, “Deformation potentials and mobilities in non-polar crystals”, *Physical Review* **80**, 72–80 (1950).
- [213] C. G. Van de Walle, “Band lineups and deformation potentials in the model-solid theory”, *Physical Review B* **39**, 1871 (1989).
- [214] D. J. Griffiths, Introduction to Electrodynamics, 4th ed. (Pearson, 2013).
- [215] V. M. Fomin and O. V. Dobrovolskiy, “A Perspective on superconductivity in curved 3D nanoarchitectures”, *Applied Physics Letters* **120**, 090501 (2022).
- [216] H. Jensen and H. Koppe, “Quantum mechanics with constraints”, *Annals of Physics* **63**, 586–591 (1971).
- [217] R. C. T. da Costa, “Quantum mechanics of a constrained particle”, *Phys. Rev. A* **23**, 1982–1987 (1981).
- [218] C. Ortix, “Quantum mechanics of a spin-orbit coupled electron constrained to a space curve”, *Physical Review B* **91**, 245412 (2015).
- [219] G. Cantele, D. Ninno, and G. Iadonisi, “Topological surface states in deformed quantum wires”, *Phys. Rev. B* **61**, 13730–13736 (2000).
- [220] H. Aoki, M. Koshino, D. Takeda, H. Morise, and K. Kuroki, “Electronic structure of periodic curved surfaces: Topological band structure”, *Phys. Rev. B* **65**, 035102 (2001).
- [221] M. Encinosa and L. Mott, “Curvature-induced toroidal bound states”, *Phys. Rev. A* **68**, 014102 (2003).

- [222] C. Ortix and J. van den Brink, “Effect of curvature on the electronic structure and bound-state formation in rolled-up nanotubes”, *Phys. Rev. B* **81**, 165419 (2010).
- [223] J.-S. Jeong, J. Shin, and H.-W. Lee, “Curvature-induced spin-orbit coupling and spin relaxation in a chemically clean single-layer graphene”, *Phys. Rev. B* **84**, 195457 (2011).
- [224] Y.-L. Wang, H. Jiang, and H.-S. Zong, “Geometric influences of a particle confined to a curved surface embedded in three-dimensional Euclidean space”, *Phys. Rev. A* **96**, 022116 (2017).
- [225] D. Frustaglia and K. Richter, “Spin interference effects in ring conductors subject to Rashba coupling”, *Phys. Rev. B* **69**, 235310 (2004).
- [226] F. Nagasawa, D. Frustaglia, H. Saarikoski, K. Richter, and J. Nitta, “Control of the spin geometric phase in semiconductor quantum rings”, *Nature communications* **4**, 1–7 (2013).
- [227] P. Gentile, M. Cuoco, and C. Ortix, “Edge States and Topological Insulating Phases Generated by Curving a Nanowire with Rashba Spin-Orbit Coupling”, *Phys. Rev. Lett.* **115**, 256801 (2015).
- [228] Z.-J. Ying, P. Gentile, C. Ortix, and M. Cuoco, “Designing electron spin textures and spin interferometers by shape deformations”, *Phys. Rev. B* **94**, 081406(R) (2016).
- [229] Z.-J. Ying, M. Cuoco, C. Ortix, and P. Gentile, “Tuning pairing amplitude and spin-triplet texture by curving superconducting nanostructures”, *Phys. Rev. B* **96**, 100506(R) (2017).
- [230] C.-H. Chang and C. Ortix, “Theoretical prediction of a giant anisotropic magnetoresistance in carbon nanoscrolls”, *Nano letters* **17**, 3076–3080 (2017).
- [231] D. Bercioux, D. Frustaglia, and A. D. Martino, “Chiral spin channels in curved graphene *pn* junctions”, arXiv:2303.05833, 2023.
- [232] A. M. Turner, V. Vitelli, and D. R. Nelson, “Vortices on curved surfaces”, *Rev. Mod. Phys.* **82**, 1301–1348 (2010).
- [233] G. Francica, M. Cuoco, and P. Gentile, “Topological superconducting phases and Josephson effect in curved superconductors with time reversal invariance”, *Phys. Rev. B* **101**, 094504 (2020).
- [234] A. G. Kutlin and A. S. Mel’nikov, “Geometry-dependent effects in Majorana nanowires”, *Phys. Rev. B* **101**, 045418 (2020).
- [235] P.-H. Chou, C.-H. Chen, S.-W. Liu, C.-H. Chung, and C.-Y. Mou, “Geometry-induced topological superconductivity”, *Phys. Rev. B* **103**, 014508 (2021).

- [236] D. Frustaglia and J. Nitta, “Geometric spin phases in Aharonov-Casher interference”, *Solid State Communications* **311**, 113864 (2020).
- [237] Z.-J. Ying, P. Gentile, J. P. Baltanás, D. Frustaglia, C. Ortix, and M. Cuoco, “Geometric driving of two-level quantum systems”, *Phys. Rev. Res.* **2**, 023167 (2020).
- [238] E. J. Rodríguez and D. Frustaglia, “Nonmonotonic quantum phase gathering in curved spintronic circuits”, *Phys. Rev. B* **104**, 195308 (2021).
- [239] H. Saarikoski, J. E. Vázquez-Lozano, J. P. Baltanás, F. Nagasawa, J. Nitta, and D. Frustaglia, “Topological transitions in spin interferometers”, *Phys. Rev. B* **91**, 241406 (2015).
- [240] A. A. Reynoso, J. P. Baltanás, H. Saarikoski, J. E. Vázquez-Lozano, J. Nitta, and D. Frustaglia, “Spin resonance under topological driving fields”, *New Journal of Physics* **19**, 063010 (2017).
- [241] M. Wang, H. Saarikoski, A. A. Reynoso, J. P. Baltanás, D. Frustaglia, and J. Nitta, “Geometry-Assisted Topological Transitions in Spin Interferometry”, *Phys. Rev. Lett.* **123**, 266804 (2019).
- [242] A. Hijano, E. J. Rodríguez, D. Bercioux, and D. Frustaglia, “Spin-texture topology in curved circuits driven by spin-orbit interactions”, arXiv:2209.11653, 2023.
- [243] N. B. Schade, D. I. Schuster, and S. R. Nagel, “A nonlinear, geometric Hall effect without magnetic field”, *Proceedings of the National Academy of Sciences* **116**, 24475–24479 (2019).
- [244] S. N. Song, X. K. Wang, R. P. H. Chang, and J. B. Ketterson, “Electronic properties of graphite nanotubes from galvanomagnetic effects”, *Phys. Rev. Lett.* **72**, 697–700 (1994).
- [245] A. Y. Kasumov, I. I. Khodos, P. M. Ajayan, and C. Colliex, “Electrical resistance of a single carbon nanotube”, *Europhysics Letters* **34**, 429 (1996).
- [246] B. Zhao, Z. Wan, Y. Liu, J. Xu, X. Yang, D. Shen, Z. Zhang, C. Guo, Q. Qian, J. Li, R. Wu, Z. Lin, X. Yan, B. Li, Z. Zhang, H. Ma, B. Li, X. Chen, Y. Qiao, I. Shakir, Z. Almutairi, F. Wei, Y. Zhang, X. Pan, Y. Huang, Y. Ping, X. Duan, and X. Duan, “High-order superlattices by rolling up van der Waals heterostructures”, *Nature* **591**, 385–390 (2021).
- [247] L. M. Viculis, J. J. Mack, and R. B. Kaner, “A Chemical Route to Carbon Nanoscrolls”, *Science* **299**, 1361–1361 (2003).
- [248] X. Xie, L. Ju, X. Feng, Y. Sun, R. Zhou, K. Liu, S. Fan, Q. Li, and K. Jiang, “Controlled Fabrication of High-Quality Carbon Nanoscrolls from Monolayer Graphene”, *Nano Letters* **9**, 2565–2570 (2009).

- [249] R. Dandoloff, S. Villain-Guillot, A. Saxena, and A. R. Bishop, “Violation of Self-Duality for Topological Solitons due to Soliton-Soliton Interaction on a Cylindrical Geometry”, *Phys. Rev. Lett.* **74**, 813–815 (1995).
- [250] A. Saxena and R. Dandoloff, “Curvature-induced geometrical frustration in magnetic systems”, *Phys. Rev. B* **55**, 11049–11051 (1997).
- [251] R. Dandoloff and A. Saxena, “Heisenberg spins on a bilayer connected by a neck and other geometries with a characteristic length scale”, *Journal of Physics A: Mathematical and Theoretical* **44**, 045203 (2010).
- [252] W. A. Freitas, W. A. Moura-Melo, and A. Pereira, “Heisenberg spins on a cone: an interplay between geometry and magnetism”, *Physics Letters A* **336**, 412–422 (2005).
- [253] W. Moura-Melo, A. Pereira, L. Mól, and A. Pires, “Geometrical pinning of magnetic vortices induced by a deficit angle on a surface: Anisotropic spins on a conic space background”, *Physics Letters A* **360**, 472–480 (2007).
- [254] P. Landeros, J. Escrig, D. Altbir, M. Bahiana, and J. d’Albuquerque e Castro, “Stability of magnetic configurations in nanorings”, *Journal of Applied Physics* **100**, 044311 (2006).
- [255] P. Landeros, S. Allende, J. Escrig, E. Salcedo, D. Altbir, and E. E. Vogel, “Reversal modes in magnetic nanotubes”, *Applied Physics Letters* **90**, 102501 (2007).
- [256] V. L. Carvalho-Santos, A. R. Moura, W. A. Moura-Melo, and A. R. Pereira, “Topological spin excitations on a rigid torus”, *Phys. Rev. B* **77**, 134450 (2008).
- [257] V. L. Carvalho-Santos, W. A. Moura-Melo, and A. R. Pereira, “Miniaturization of vortex-comprising system using ferromagnetic nanotori”, *Journal of Applied Physics* **108**, 094310 (2010).
- [258] V. V. Slastikov and C. Sonnenberg, “Reduced models for ferromagnetic nanowires”, *IMA Journal of Applied Mathematics* **77**, 220–235 (2011).
- [259] V. S. Tkachenko, A. N. Kuchko, M. Dvornik, and V. V. Kruglyak, “Propagation and scattering of spin waves in curved magnonic waveguides”, *Applied Physics Letters* **101**, 152402 (2012).
- [260] V. Slastikov, “Micromagnetics of Thin Shells”, *Mathematical Models and Methods in Applied Sciences* **15**, 1469–1487 (2005).
- [261] V. P. Kravchuk, D. D. Sheka, R. Streubel, D. Makarov, O. G. Schmidt, and Y. Gaididei, “Out-of-surface vortices in spherical shells”, *Phys. Rev. B* **85**, 144433 (2012).

-
- [262] Y. Gaididei, V. P. Kravchuk, and D. D. Sheka, “Curvature Effects in Thin Magnetic Shells”, *Phys. Rev. Lett.* **112**, 257203 (2014).
- [263] D. D. Sheka, O. V. Pylypovskiy, P. Landeros, Y. Gaididei, A. Kákay, and D. Makarov, “Nonlocal chiral symmetry breaking in curvilinear magnetic shells”, *Communications Physics* **3**, 128 (2020).
- [264] D. D. Sheka, V. P. Kravchuk, K. V. Yershov, and Y. Gaididei, “Torsion-induced effects in magnetic nanowires”, *Phys. Rev. B* **92**, 054417 (2015).
- [265] A. González, P. Landeros, and Á. S. Núñez, “Spin wave spectrum of magnetic nanotubes”, *Journal of Magnetism and Magnetic Materials* **322**, 530–535 (2010).
- [266] J. López-López, D. Cortés-Ortuño, and P. Landeros, “Role of anisotropy on the domain wall properties of ferromagnetic nanotubes”, *Journal of Magnetism and Magnetic Materials* **324**, 2024–2029 (2012).
- [267] V. Carvalho-Santos, R. Elias, D. Altbir, and J. Fonseca, “Stability of skyrmions on curved surfaces in the presence of a magnetic field”, *Journal of Magnetism and Magnetic Materials* **391**, 179–183 (2015).
- [268] O. V. Pylypovskiy, V. P. Kravchuk, D. D. Sheka, D. Makarov, O. G. Schmidt, and Y. Gaididei, “Coupling of Chiralities in Spin and Physical Spaces: The Möbius Ring as a Case Study”, *Phys. Rev. Lett.* **114**, 197204 (2015).
- [269] M. I. Sloika, D. D. Sheka, V. P. Kravchuk, O. V. Pylypovskiy, and Y. Gaididei, “Geometry induced phase transitions in magnetic spherical shell”, *Journal of Magnetism and Magnetic Materials* **443**, 404–412 (2017).
- [270] A. Teixeira, S. Castillo-Sepúlveda, S. Vojkovic, J. Fonseca, D. Altbir, Á. Núñez, and V. Carvalho-Santos, “Analysis on the stability of in-surface magnetic configurations in toroidal nanoshells”, *Journal of Magnetism and Magnetic Materials* **478**, 253–259 (2019).
- [271] G. S. Abo, Y.-K. Hong, J. Park, J. Lee, W. Lee, and B.-C. Choi, “Definition of Magnetic Exchange Length”, *IEEE Transactions on Magnetics* **49**, 4937–4939 (2013).
- [272] D. M. Paige, B. Szpunar, and B. K. Tanner, “The magnetocrystalline anisotropy of cobalt”, *Journal of Magnetism and Magnetic Materials* **44**, 239–248 (1984).
- [273] P. Vavassori, D. Bisero, F. Carace, A. Di Bona, G. C. Gazzadi, M. Liberati, and S. Valeri, “Interplay between magnetocrystalline and configurational anisotropies in Fe(001) square nanostructures”, *Physical Review B* **72**, 054405 (2005).

- [274] K. Niitsu, “Temperature dependence of magnetic exchange stiffness in iron and nickel”, *Journal of Physics D: Applied Physics* **53**, 39LT01 (2020).
- [275] C. Graham Jr., “Magnetocrystalline Anisotropy Constants of Iron at Room Temperature and Below”, *Physical Review* **112**, 1117 (1958).
- [276] J. J. M. Franse and G. De Vries, “The magnetocrystalline anisotropy energy of nickel”, *Physica* **39**, 477–498 (1968).
- [277] M. E. Schabes and H. N. Bertram, “Magnetization processes in ferromagnetic cubes”, *Journal of Applied Physics* **64**, 1347 (1988).
- [278] R. Fermin, D. van Dinter, M. Hubert, B. Woltjes, M. Silaev, J. Aarts, and K. Lahabi, “Superconducting Triplet Rim Currents in a Spin-Textured Ferromagnetic Disk”, *Nano Letters* **22**, 2209–2216 (2022).
- [279] S. Castillo-Sepúlveda, R. A. Escobar, D. Altbir, M. Krizanac, and E. Y. Vedmedenko, “Magnetic Möbius stripe without frustration: Noncollinear metastable states”, *Phys. Rev. B* **96**, 024426 (2017).
- [280] O. V. Pylypovskyi, D. Y. Kononenko, K. V. Yershov, U. K. Röbber, A. V. Tomilo, J. Fassbender, J. van den Brink, D. Makarov, and D. D. Sheka, “Curvilinear One-Dimensional Antiferromagnets”, *Nano Letters* **20**, 8157–8162 (2020).
- [281] K. V. Yershov, “Dynamics of domain walls in curved antiferromagnetic wires”, *Phys. Rev. B* **105**, 064407 (2022).
- [282] Y. A. Borysenko, D. D. Sheka, J. Fassbender, J. van den Brink, D. Makarov, and O. V. Pylypovskyi, “Field-induced spin reorientation transitions in antiferromagnetic ring-shaped spin chains”, *Phys. Rev. B* **106**, 174426 (2022).
- [283] L. V. Keldysh et al., “Diagram technique for nonequilibrium processes”, *Sov. Phys. JETP* **20**, 1018–1026 (1965).
- [284] J. Rammer and H. Smith, “Quantum field-theoretical methods in transport theory of metals”, *Rev. Mod. Phys.* **58**, 323–359 (1986).
- [285] V. Chandrasekhar, “Proximity-Coupled Systems: Quasiclassical Theory of Superconductivity”, in *The Physics of Superconductors: Vol. II. Superconductivity in Nanostructures, High-Tc and Novel Superconductors, Organic Superconductors*, edited by K. H. Bennemann and J. B. Ketterson (Springer Berlin Heidelberg, Berlin, Heidelberg, 2004), pp. 55–110.
- [286] W. Belzig, F. K. Wilhelm, C. Bruder, G. Schön, and A. D. Zaikin, “Quasiclassical Green’s function approach to mesoscopic superconductivity”, *Superlattices and Microstructures* **25**, 1251–1288 (1999).

- [287] G. Eilenberger, “Transformation of Gorkov’s equation for type II superconductors into transport-like equations”, *Zeitschrift für Physik A Hadrons and nuclei* **214**, 195–213 (1968).
- [288] A. I. Larkin and Y. N. Ovchinnikov, “Quasiclassical method in the theory of superconductivity”, *Sov Phys JETP* **28**, 1200–1205 (1969).
- [289] K. D. Usadel, “Generalized Diffusion Equation for Superconducting Alloys”, *Phys. Rev. Lett.* **25**, 507–509 (1970).
- [290] M. Y. Kuprianov and V. Lukichev, “Influence of boundary transparency on the critical current of dirty SS’S structures”, *Zh. Eksp. Teor. Fiz* **94**, 149 (1988).
- [291] P. Machon, M. Eschrig, and W. Belzig, “Nonlocal Thermoelectric Effects and Nonlocal Onsager relations in a Three-Terminal Proximity-Coupled Superconductor-Ferromagnet Device”, *Phys. Rev. Lett.* **110**, 047002 (2013).
- [292] N. Schopohl and K. Maki, “Quasiparticle spectrum around a vortex line in a d-wave superconductor”, *Phys. Rev. B* **52**, 490–493 (1995).
- [293] Y. Tanaka and A. A. Golubov, “Theory of the Proximity Effect in Junctions with Unconventional Superconductors”, *Phys. Rev. Lett.* **98**, 037003 (2007).
- [294] M. Amundsen, “Proximity effects in superconducting hybrid structures with spin-dependent interactions”, PhD thesis (Norwegian University of Science and Technology (NTNU), 2020).
- [295] J. A. Ouassou, “GENEUS”, GitHub repository, 2018.
- [296] V. P. Mineev and G. E. Volovik, “Electric dipole moment and spin supercurrent in superfluid³He”, *Journal of Low Temperature Physics* **89**, 823–830 (1992).
- [297] J. Fröhlich and U. M. Studer, “Gauge invariance and current algebra in nonrelativistic many-body theory”, *Rev. Mod. Phys.* **65**, 733–802 (1993).
- [298] A. Skarpeid, “Diffusive Curved Superconductor-Ferromagnet Proximity Systems in and out of Equilibrium”, Master thesis (Norwegian University of Science and Technology (NTNU), 2022).
- [299] A. I. Buzdin, L. Bulaevskii, and S. Panyukov, “Critical-current oscillations as a function of the exchange field and thickness of the ferromagnetic metal (F) in an SFS Josephson junction”, *JETP lett* **35**, 147 (1982).
- [300] A. Buzdin and A. E. Koshelev, “Periodic alternating 0- and π -junction structures as realization of φ -Josephson junctions”, *Phys. Rev. B* **67**, 220504(R) (2003).

- [301] V. V. Ryazanov, V. A. Oboznov, A. Y. Rusanov, A. V. Veretennikov, A. A. Golubov, and J. Aarts, “Coupling of Two Superconductors through a Ferromagnet: Evidence for a π Junction”, *Phys. Rev. Lett.* **86**, 2427–2430 (2001).
- [302] T. Kontos, M. Aprili, J. Lesueur, F. Genêt, B. Stephanidis, and R. Boursier, “Josephson Junction through a Thin Ferromagnetic Layer: Negative Coupling”, *Phys. Rev. Lett.* **89**, 137007 (2002).
- [303] L. B. Ioffe, V. B. Geshkenbein, M. V. Feigel’man, A. L. Fauchère, and G. Blatter, “Environmentally decoupled sds -wave Josephson junctions for quantum computing”, *Nature* **398**, 679–681 (1999).
- [304] J. E. Mooij, T. P. Orlando, L. Levitov, L. Tian, C. H. van der Wal, and S. Lloyd, “Josephson Persistent-Current Qubit”, *Science* **285**, 1036–1039 (1999).
- [305] T. Yamashita, K. Tanikawa, S. Takahashi, and S. Maekawa, “Superconducting π Qubit with a Ferromagnetic Josephson Junction”, *Phys. Rev. Lett.* **95**, 097001 (2005).
- [306] A. K. Feofanov, V. A. Oboznov, V. V. Bol’ginov, J. Lisenfeld, S. Poletto, V. V. Ryazanov, A. N. Rossolenko, M. Khabipov, D. Balashov, A. B. Zorin, P. N. Dmitriev, V. P. Koshelets, and A. V. Ustinov, “Implementation of superconductor/ferromagnet/ superconductor π -shifters in superconducting digital and quantum circuits”, *Nature Physics* **6**, 593–597 (2010).
- [307] A. Y. Herr and Q. P. Herr, “Josephson magnetic random access memory system and method”, US Patent 8,270,209, 2012.
- [308] E. C. Gingrich, B. M. Niedzielski, J. A. Glick, Y. Wang, D. L. Miller, R. Loloee, W. P. Pratt Jr, and N. O. Birge, “Controllable $0-\pi$ Josephson junctions containing a ferromagnetic spin valve”, *Nature Physics* **12**, 564–567 (2016).
- [309] B. Bujnowski, R. Biele, and F. S. Bergeret, “Switchable Josephson current in junctions with spin-orbit coupling”, *Phys. Rev. B* **100**, 224518 (2019).
- [310] B. Kundys, “Photostrictive materials”, *Applied Physics Reviews* **2**, 011301 (2015).
- [311] S. Matzen, L. Guillemot, T. Maroutian, S. K. K. Patel, H. Wen, A. D. DiChiara, G. Agnus, O. G. Shpyrko, E. E. Fullerton, D. Ravelosona, P. Lecoeur, and R. Kukreja, “Tuning Ultrafast Photoinduced Strain in Ferroelectric-Based Devices”, *Advanced Electronic Materials* **5**, 1800709 (2019).
- [312] M. Amundsen and J. Linder, “Supercurrent vortex pinball via a triplet Cooper pair inverse Edelstein effect”, *Phys. Rev. B* **96**, 064508 (2017).

-
- [313] S. Oh, D. Youm, and M. R. Beasley, “A superconductive magnetoresistive memory element using controlled exchange interaction”, *Applied Physics Letters* **71**, 2376–2378 (1997).
- [314] L. R. Tagirov, “Low-Field Superconducting Spin Switch Based on a Superconductor /Ferromagnet Multilayer”, *Phys. Rev. Lett.* **83**, 2058–2061 (1999).
- [315] Buzdin, A. I., Vedyayev, A. V., and Ryzhanova, N. V., “Spin-orientation-dependent superconductivity in F/S/F structures”, *Europhys. Lett.* **48**, 686–691 (1999).
- [316] J. Y. Gu, C.-Y. You, J. S. Jiang, J. Pearson, Y. B. Bazaliy, and S. D. Bader, “Magnetization-Orientation Dependence of the Superconducting Transition Temperature in the Ferromagnet-Superconductor-Ferromagnet System: CuNi/Nb/CuNi”, *Phys. Rev. Lett.* **89**, 267001 (2002).
- [317] A. Potenza and C. H. Marrows, “Superconductor-ferromagnet CuNi/Nb/CuNi trilayers as superconducting spin-valve core structures”, *Phys. Rev. B* **71**, 180503(R) (2005).
- [318] J. A. Ouassou, A. Di Bernardo, J. W. A. Robinson, and J. Linder, “Electric control of superconducting transition through a spin-orbit coupled interface”, *Scientific Reports* **6**, 29312 (2016).
- [319] Z. Pajović, M. Božović, Z. Radović, J. Cayssol, and A. Buzdin, “Josephson coupling through ferromagnetic heterojunctions with noncollinear magnetizations”, *Phys. Rev. B* **74**, 184509 (2006).
- [320] Z. Radović, L. Dobrosavljević-Grujić, and B. Vujčić, “Coexistence of stable and metastable 0 and π states in Josephson junctions”, *Phys. Rev. B* **63**, 214512 (2001).
- [321] A. A. Golubov, M. Y. Kupriyanov, and Y. V. Fominov, “Nonsinusoidal current-phase relation in SFS Josephson junctions”, *Journal of Experimental and Theoretical Physics Letters* **75**, 588–592 (2002).
- [322] Z. Radović, N. Lazarides, and N. Flytzanis, “Josephson effect in double-barrier superconductor-ferromagnet junctions”, *Phys. Rev. B* **68**, 014501 (2003).
- [323] S. Djurdjević and Z. Popović, “Influence of d-wave superconductor orientation on Josephson current and phase difference in junctions with inhomogeneous ferromagnet”, *Progress of Theoretical and Experimental Physics* **2021**, 083I02, 10.1093/ptep/ptab077 (2021).
- [324] Z. Radović, L. Dobrosavljević-Grujić, and B. Vujčić, “Spontaneous currents in Josephson devices”, *Phys. Rev. B* **60**, 6844–6849 (1999).

- [325] E. Il'ichev, V. Zakosarenko, R. P. J. IJsselsteijn, H. E. Hoenig, V. Schultze, H.-G. Meyer, M. Grajcar, and R. Hlubina, “Anomalous periodicity of the current-phase relationship of grain-boundary Josephson junctions in high- T_c superconductors”, *Phys. Rev. B* **60**, 3096–3099 (1999).
- [326] J. A. Ouassou, S. H. Jacobsen, and J. Linder, “Conservation of spin supercurrents in superconductors”, *Phys. Rev. B* **96**, 094505 (2017).
- [327] E. H. Fyhn, A. Brataas, A. Qaiumzadeh, and J. Linder, “Quasiclassical theory for antiferromagnetic metals”, *Phys. Rev. B* **107**, 174503 (2023).
- [328] M. S. Skjærpe, “Superconducting Proximity Effects in Diffusive, Curved Antiferromagnets”, Master thesis (Norwegian University of Science and Technology (NTNU), 2023).
- [329] G. A. Bobkov, I. V. Bobkova, A. M. Bobkov, and A. Kamra, “Néel proximity effect at antiferromagnet/superconductor interfaces”, *Phys. Rev. B* **106**, 144512 (2022).
- [330] Z. Peng, X. Chen, Y. Fan, D. J. Srolovitz, and D. Lei, “Strain engineering of 2D semiconductors and graphene: from strain fields to band-structure tuning and photonic applications”, *Light: Science & Applications* **9**, 190 (2020).
- [331] P. Liu, J. R. Williams, and J. J. Cha, “Topological nanomaterials”, *Nature Reviews Materials* **4**, 479–496 (2019).
- [332] K. Lahabi, M. Amundsen, J. A. Ouassou, E. Beukers, M. Pleijster, J. Linder, P. Alkemade, and J. Aarts, “Controlling supercurrents and their spatial distribution in ferromagnets”, *Nature Communications* **8**, 2056 (2017).
- [333] C. Kallin and J. Berlinsky, “Chiral superconductors”, *Reports on Progress in Physics* **79**, 054502 (2016).
- [334] M. Sato and Y. Ando, “Topological superconductors: a review”, *Reports on Progress in Physics* **80**, 076501 (2017).
- [335] K. Flensberg, F. von Oppen, and A. Stern, “Engineered platforms for topological superconductivity and Majorana zero modes”, *Nature Reviews Materials* **6**, 944–958 (2021).

I

REFERENCE

T. Salamone, M. B. M. Svendsen, M. Amundsen, and S. H. Jacobsen,

Curvature-induced long-range supercurrents in diffusive superconductor-ferromagnet-superconductor Josephson junctions with a dynamic $0-\pi$ transition.

Physical Review B **104**, L060505 (2021)

CONTRIBUTIONS

SHJ initiated and supervised the project. TS performed analytical calculations and numerical simulations, prepared the figures and wrote the manuscript. MBMS contributed to analytical calculations and numerical simulations. MA and SHJ contributed to numerical simulations and identified the main results. All authors contributed to discussions and revisions of the manuscript.

Curvature-induced long-range supercurrents in diffusive superconductor-ferromagnet-superconductor Josephson junctions with a dynamic $0-\pi$ transition

Tancredi Salamone,^{1,*} Mathias B. M. Svendsen,¹ Morten Amundsen,² and Sol Jacobsen¹

¹Center for Quantum Spintronics, Department of Physics, NTNU Norwegian University of Science and Technology, NO-7491 Trondheim, Norway

²Nordita, KTH Royal Institute of Technology and Stockholm University, Hannes Alfvéns väg 12, SE-106 91 Stockholm, Sweden



(Received 27 May 2021; accepted 4 August 2021; published 17 August 2021)

We report that spin supercurrents can be induced in diffusive superconductor-ferromagnet-superconductor Josephson junctions without any magnetic misalignment or intrinsic spin-orbit coupling. Instead, the pathway to spin-triplet generation is provided via geometric curvature, and results in a long-range Josephson effect. In addition, the curvature is shown to induce a dynamically tunable $0-\pi$ transition in the junction. We provide the analytic framework and discuss potential experimental and innovation implications.

DOI: [10.1103/PhysRevB.104.L060505](https://doi.org/10.1103/PhysRevB.104.L060505)

Introduction. In the last two decades there have been substantial advances in the experimental realization of curved nanostructures. Since the realization of nanotubes by rolling up thin solid films [1], many new techniques of bending, wrinkling, and buckling nanostructures in up to three dimensions have been developed [2,3], as well as direct growth on curved templates [4], electron beam lithography [5–7], and many more (see, e.g., Ref. [8] and references therein). These techniques open a broad new range of spintronic device design, and have already been shown to enable independent control of spin and charge resistances [4].

Geometric curvature introduces two main effects: a quantum geometric potential, producing many interesting phenomena at the nanoscale [9–12], and a strain field leading to a curvature-induced Rashba spin-orbit coupling (SOC), with strength proportional to the curvature [13]. Several studies have investigated new properties triggered by curvature, e.g., in semiconductors [14–18], magnets [4,7,8], and superconductors [19–21]. Curved nanostructures with induced superconductivity can display geometric control of spin-triplet correlations in the clean limit [22], and proximitizing a superconductor with a curved semiconductor can result in topological edge states [15]. The curved topological superconductor/straight semiconductor Josephson junction counterpart has been predicted to display a $0-\pi$ transition and ϕ -junction behavior [20].

Hybrid structures of superconductors and ferromagnets are of great interest for the field of superconducting spintronics [23,24] since at the superconductor/ferromagnet (SF) interface the proximity effect allows the property of one material to “leak” into the other [25–27]. A coexistence of superconductivity and magnetism may therefore enable data processing, encoded in spin and charge degrees of freedom, to be performed without the heat loss associated with traditional electronics. In diffusive heterostructures, which cover

a range of commonly available materials that may have impurities or suboptimal interface transparencies, conventional s -wave superconducting correlations typically penetrate a ferromagnet for extremely short distances, proportional to $\sqrt{D_F/\hbar}$, with D_F the diffusion constant and \hbar the exchange field strength. Significant theoretical and experimental effort has focused on the conversion of singlet correlations into so-called long-range triplet correlations (LRTC), which penetrate for longer distances, on the order of $\sqrt{D_F/T}$, where T is the temperature. This conversion can take place in the presence of magnetic inhomogeneities [28–30] or due to intrinsic spin-orbit coupling either in the superconductor or in the ferromagnet [31,32]. The role of geometric curvature as a source of designable and dynamically alterable SOC in diffusive structures has not been investigated in this context, and we address this here. By considering a model superconductor-ferromagnet-superconductor (SFS) junction with constant curvature shown in Fig. 1, we show that the curvature alone can induce long-range supercurrents due to the generation of triplet correlations. Moreover, we show that these systems display a tunable $0-\pi$ transition.

The possibility of $0-\pi$ state switching has been of much interest, in part due to its potential role in solid state quantum computing [25,33–37]. Investigations have confirmed the transition can be governed by altering the length of the ferromagnetic weak link. However, this is not practicable to do *in situ* and must be done by preparing multiple samples of different lengths. It has recently been predicted that the $0-\pi$ transition can also be accessed out of equilibrium, by altering the strength of the SOC via voltage gating [38]. In this Letter, we show that dynamically changing the curvature of the magnet via *in situ* strain manipulation, for example via photostriction, piezoelectrics, or thermoelectric effects [39,40], allows for a single-sample $0-\pi$ transition in the diffusive regime, without the need to apply a varying voltage. Moreover, we show that curvature can yield long-range Josephson currents without any magnetic inhomogeneities or intrinsic SOC.

*Corresponding author: tancredi.salamone@ntnu.no

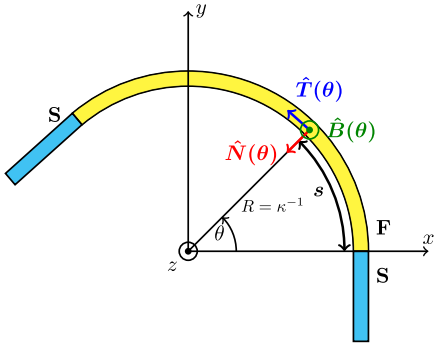


FIG. 1. Model system. SFS junction having a ferromagnet with constant curvature as a weak link. The three orthonormal unit vectors $\hat{T}(\theta)$, $\hat{N}(\theta)$, and $\hat{B}(\theta)$ identifying the curvilinear coordinates are also shown.

Theoretical framework. A fundamental tool for the study of curved structures is the thin-wall quantization procedure, where the quantum motion of a particle in a two-dimensional (2D) curved surface is treated as equivalent to the motion in a 3D space with the addition of lateral quantum confinement [41,42]. This procedure allows one to derive the Hamiltonian for the motion of electrons constrained to a curved planar one-dimensional structure [43,44].

When dealing with a ferromagnet, further effects of the curvature must be taken into account, namely in how it affects its exchange field. Recent studies have developed a fully 3D approach for thin magnetic shells of arbitrary shape and extended it to 2D shells and 1D wires [45,46]. This showed that curvature induces two effective magnetic interactions: an effective magnetic anisotropy and an effective Dzyaloshinskii-Moriya interaction (DMI). When dealing with a 1D curved wire below a certain critical curvature, the magnetic anisotropy and the DMI, which results in an effective Rashba SOC, both combine to give an effective field tangential to the wire. The geometrically defined SOC is therefore both designable and tunable, and gives greater freedom in the manipulation of superconducting proximity effects.

We parametrize the curve by its arc length s , and define a set of three orthonormal unit vectors $\hat{T}(s)$, $\hat{N}(s)$, $\hat{B}(s)$ representing the tangential, normal, and binormal curvilinear coordinates, respectively, as indicated in Fig. 1. These obey the following Frenet-Serret-type equation of motion,

$$\begin{pmatrix} \partial_s \hat{T}(s) \\ \partial_s \hat{N}(s) \\ \partial_s \hat{B}(s) \end{pmatrix} = \begin{pmatrix} 0 & \kappa(s) & 0 \\ -\kappa(s) & 0 & 0 \\ 0 & 0 & 0 \end{pmatrix} \begin{pmatrix} \hat{T}(s) \\ \hat{N}(s) \\ \hat{B}(s) \end{pmatrix}, \quad (1)$$

where $\kappa(s)$ is the curvature of the wire, whose role and effect will be discussed in detail below. Deriving the Hamiltonian for a wire, which may include intrinsic SOC in general, we find [44]

$$H = -\frac{\hbar^2}{2m} \partial_s^2 - \frac{\hbar^2}{8m} \kappa(s)^2 - i\hbar \alpha_N \sigma_B \partial_s + i\hbar \alpha_B \left(\sigma_N \partial_s - \frac{\kappa(s)}{2} \sigma_T \right). \quad (2)$$

The SOC constants $\alpha_{N,B}$ represent the spin-orbit field with axis along the normal and binormal direction, respectively, and $\sigma_{T,N,B}(s) = \boldsymbol{\sigma} \cdot \{\hat{T}, \hat{N}, \hat{B}\}(s)$ are the set of three Pauli matrices in curvilinear coordinates. By using Eqs. (1) we can incorporate the last three terms in Eq. (2) in a SU(2) spin-orbit field term,

$$A = (\alpha_N \sigma_B - \alpha_B \sigma_N, 0, 0), \quad (3)$$

which has a vector structure in the geometric space and a 2×2 matrix structure in spin space. It is worth distinguishing between the two terms entering the SU(2) field, namely α_B and α_N . The former represents the intrinsic, not induced by the curvature, SOC term which may or may not exist according to the material taken into consideration. The latter is curvature induced, and is proportional to the curvature strength. In natural units we have $\alpha_N = g\lambda\kappa(s)/(4m)$, where g is the g -factor and the parameter $\lambda > 0$ is a characteristic energy scale for the material. Inspection of the relevant diffusion equations for the system shows that α_N and $\kappa(s)$ appear together in such a way that the former always acts as a strengthening factor for the latter. Therefore, considering a material with no intrinsic term we can ignore spin-orbit coupling as a whole, and consider the $\kappa(s)$ term only.

Having set up the Hamiltonian, we employ Green's functions in the diffusive limit at equilibrium. Here, the dynamics are describable by the second-order partial differential Usadel equation [47], which, with suitable boundary conditions, describes the diffusion of superconducting correlations inside the ferromagnet. Treating the case of diffusive equilibrium, it is sufficient to consider just the retarded component \hat{g}_R of the quasiclassical Green's function to describe the system [48]. Using Eq. (2) the Usadel equation in a curved ferromagnet with constant curvature reads (from now on we set $\hbar = 1$)

$$D_F \partial_s (\hat{g}_R \partial_s \hat{g}_R) + i[\varepsilon \hat{\tau}_3 + \hat{M}, \hat{g}_R] = 0, \quad (4)$$

with $\hat{\tau}_3 = \text{diag}(1, 1, -1, -1)$, ε the quasiparticle energy, and magnetization $\hat{M} = \mathbf{h} \cdot \text{diag}(\boldsymbol{\sigma}, \boldsymbol{\sigma}^*)$. The components of both vectors $\mathbf{h} = (h_T, h_N, h_B)$ and $\boldsymbol{\sigma} = (\sigma_T, \sigma_N, \sigma_B)$ are expressed in curvilinear coordinates. To solve the Usadel equation we employ the Kuprianov-Lukichev boundary conditions [49],

$$L_j \zeta_j \hat{g}_{Rj} \nabla_I \hat{g}_{Rj} = [\hat{g}_{R1}, \hat{g}_{R2}]. \quad (5)$$

Here, ∇_I is the derivative at the interface, j refers to the various components of the hybrid system, with $j = 1, 2$ denoting the materials on the left and right side of the relevant interface, L_j represents the length of the material, and $\zeta_j = R_B/R_j$ is the interface parameter given by the ratio between the barrier resistance R_B and its bulk resistance R_j .

If desirable, the intrinsic SOC can be retained, in which case one also introduces the gauge covariant derivative [32],

$$\partial_s(\cdot) \rightarrow \tilde{\partial}_s(\cdot) \equiv \partial_s(\cdot) - i[\hat{A}_T, \cdot], \quad (6)$$

with $\hat{A}_T = \text{diag}(A_T, -A_T^*)$ and A_T is the tangential component of the SO field of Eq. (3).

To treat the system we will use the Riccati parametrization [50,51] for the quasiclassical Green's function,

$$\hat{g}_R = \begin{pmatrix} N(1 + \gamma \tilde{\gamma}) & 2N\gamma \\ -2\tilde{N}\tilde{\gamma} & -\tilde{N}(1 + \tilde{\gamma}\gamma) \end{pmatrix}, \quad (7)$$

where the normalization matrices are $N = (1 - \gamma\tilde{\gamma})^{-1}$ and $\tilde{N} = (1 - \tilde{\gamma}\gamma)^{-1}$ and the tilde operation denotes $\tilde{\gamma}(\varepsilon) = \gamma^*(-\varepsilon)$. The Usadel equation (4) thus becomes

$$D_F \left\{ \partial_s^2 \gamma + 2(\partial_s \gamma) \tilde{N} \tilde{\gamma} (\partial_s \gamma) \right\} = -2i\varepsilon\gamma - \mathbf{i}\mathbf{h} \cdot [\boldsymbol{\sigma}(s)\gamma - \gamma\boldsymbol{\sigma}^*(s)]. \quad (8)$$

Here, the dependence on the curvature is implicitly contained in the Pauli matrices $\sigma_{T,N,B}(s)$.

We will consider our one-dimensional curved wire to be lying in the xy plane as represented in Fig. 1, so that the set of three unit vectors is

$$\hat{T}(s) = -\sin\theta(s)\hat{x} + \cos\theta(s)\hat{y}, \quad (9a)$$

$$\hat{N}(s) = -\cos\theta(s)\hat{x} - \sin\theta(s)\hat{y}, \quad (9b)$$

$$\hat{B}(s) \equiv \hat{z}, \quad (9c)$$

with $\theta(s) = \kappa s$. It is useful to note that, when considering Eq. (8), the curved ferromagnet can be regarded as equivalent to a straight wire with a rotating exchange field, i.e., a tangential exchange field in a curved wire is equivalent to a position-dependent exchange field in a straight wire, varying as $\tilde{h}(s) = h_0[\sin\theta(s), -\cos\theta(s), 0]$, with $\theta(s) = \pi s/L_F$ and L_F being the length of the ferromagnet.

Results. Solving the Usadel equation, and therefore finding the quasiclassical Green's function of the system, allows us to calculate many interesting quantities. In this Letter we will focus mainly on the charge current, a quantity directly measurable in experiments, given by

$$\frac{I_Q}{I_{Q0}} = \int_{-\infty}^{+\infty} d\varepsilon \text{Tr} \{ \hat{t}_3 (\hat{g}_R \partial_s \hat{g}_R - \hat{g}_A \partial_s \hat{g}_A) \} \tanh(\beta\varepsilon/2). \quad (10)$$

Here, $\hat{g}_A = -\hat{t}_3 \hat{g}_R^\dagger \hat{t}_3$ is the advanced quasiclassical Green's function and $\beta = (k_B T)^{-1}$ is the inverse temperature, with k_B being the Boltzmann constant. Moreover, $I_{Q0} = N_0 e D_F A \Delta_0 / 4L_F$, where N_0 is the density of states at the Fermi energy, A the interfacial contact area, and Δ_0 the bulk gap of the two superconductors. Lengths and energies have been normalized to L_F (which in turn is scaled with the superconducting coherence length ξ_S) and superconducting bulk gap Δ_0 , respectively, so that the integral on the right-hand side of Eq. (10) is dimensionless.

We investigate the system portrayed in Fig. 1 by solving numerically Eq. (8) for various lengths L_F of the ferromagnet and multiple curvatures κ for each length. We set the interface parameter with both superconductors to be $\zeta = 3$ and the temperature to $T = 0.005T_c$. We consider the exchange field inside the curved ferromagnet to be tangential to its curvature profile at each point, $\mathbf{h}(s) \parallel \hat{T}(s)$, which we expect to be the case in 1D curved structures below a certain critical curvature [46].

Two interesting effects of the curvature appear immediately from our results. First, we show in Fig. 2 that it is possible to induce a $0-\pi$ transition in the junction by changing the curvature of the ferromagnetic wire while keeping its length fixed. Second, we will show in Fig. 3 that even for a long junction, where the singlet contribution to the supercurrent is negligible, a Josephson effect still appears for a nonzero κ due to the presence of long-range triplets.

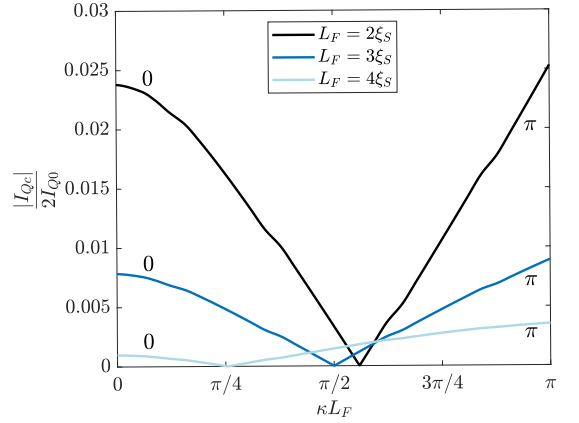


FIG. 2. Magnitude of the critical current as a function of the curvature for different lengths L_F of the ferromagnet, with $T = 0.005T_c$, $\tilde{h} = \Delta_0 \hat{T}$, $\zeta = 3$. A $0-\pi$ transition occurs when changing the curvature of the wire.

In Fig. 2 we plot the absolute value of the critical current as given by Eq. (10) as a function of the curvature κ of the ferromagnet across the junction for different lengths L_F . From the figure we see that starting in the 0 state with a straight wire, increasing the curvature results in a decreasing magnitude of the critical current, until it completely disappears for a certain κ , indicating a $0-\pi$ transition. A further increase in the curvature produces a revival of the critical current, which now flows in the opposite direction with respect to the straight case. We also note that increasing the length of the ferromagnet reduces not only the overall magnitude of the critical current but also the curvature at which the $0-\pi$ transition takes place.

In order to better understand how this $0-\pi$ transition appears, and to show that the role of the triplets is crucial in tuning it, we split the charge current into singlet and triplet contributions, I_0 and I_t , respectively. It can be shown that

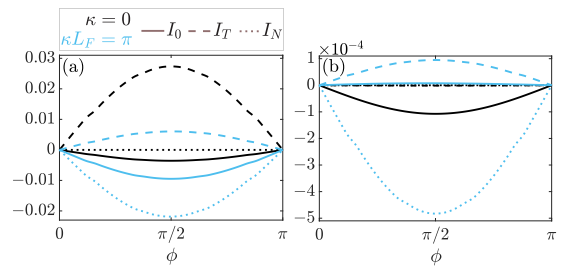


FIG. 3. Charge current as a function of the phase difference ϕ , showing separately the singlet (solid lines) and triplet (dashed lines) contributions with $T = 0.005T_c$, $\tilde{h} = \Delta_0 \hat{T}$, $\zeta = 3$, for a straight ($\kappa = 0$) and semicircular ($\kappa L_F = \pi$) ferromagnetic wire. (a) $L_F = 2\xi_S$: Increasing the curvature causes the triplet contribution to change sign. (b) $L_F = 6\xi_S$: Increasing the curvature causes the singlet contribution to be negligible with respect to the triplet one, signaling that the charge current is transported almost exclusively by the triplet correlations.

the charge current given by Eq. (10) only depends on the anomalous Green's function f which is the off-diagonal block matrix in the retarded Green's function. We define $f = (f_0 + \mathbf{d} \cdot \boldsymbol{\sigma})i\sigma_y$, with f_0 representing the singlet contribution and $\mathbf{d} = (d_T, d_N, d_z)$ the d vector representing the triplet contribution, and obtain that the charge current can be written as $I_Q/I_{Q0} = I_0 + I_t$, where $I_t = I_T + I_N + I_z + I_\kappa$ and

$$I_0 = -8 \int_0^\infty d\varepsilon \operatorname{Re}\{\tilde{f}_0 \partial_s f_0 - f_0 \partial_s \tilde{f}_0\} \tanh(\beta\varepsilon/2), \quad (11a)$$

$$I_j = 8 \int_0^\infty d\varepsilon \operatorname{Re}\{\tilde{d}_j \partial_s d_j - d_j \partial_s \tilde{d}_j\} \tanh(\beta\varepsilon/2), \quad (11b)$$

$$I_\kappa = 16\kappa \int_0^\infty d\varepsilon \operatorname{Re}\{\tilde{d}_N d_T - \tilde{d}_T d_N\} \tanh(\beta\varepsilon/2), \quad (11c)$$

with $j = (T, N, z)$. The terms I_0 and I_j represent the contribution coming from the singlet and triplets with spin aligned in the j direction, respectively. Equation (11c) describes instead an inverse Edelstein effect [52]. A nonzero I_κ requires that there be a nonzero, energy-dependent phase difference between d_T and d_N . Hence, this contribution only appears when the d vector undergoes a rotation. In our case, such a rotation is maintained by the presence of a finite curvature and/or spin-orbit coupling.

The short-range I_T and long-range I_N triplet contributions to the charge current are sufficient to demonstrate that the current system exhibits a $0-\pi$ transition and long-range Josephson effect, i.e., one has to show that the long-range term dominates over the short-range one, as shown in Fig. 3. As the other contributions to the charge current, the inverse Edelstein term I_κ has a conventional sinusoidal dependence on the phase difference ϕ across the junction in this case, but may deviate for other configurations.

In Fig. 3(a) we plot singlet and triplet contributions to the charge current for two different values of κ and $L_F = 2\xi_S$. It can be seen that for $\kappa = 0$ triplet and singlet charge currents have opposite sign, with the triplet contribution, which comes only from the short-range component I_T , being generally bigger than the singlet one. Interestingly however, when increasing the curvature the triplet current changes sign, i.e., starts flowing in the opposite direction, because of the appearance of the long-range component I_N , while the singlet contribution does not. Hence, the $0-\pi$ transition is tuned by the curvature through its effect on the triplets. Furthermore, we note from Fig. 3(a) that in the π phase for $\kappa = \pi/L_F$ the singlet and triplet currents have the same sign and thus flow in the same direction. Consequently, the two contributions add up, resulting in a larger critical current in the π phase at $\kappa = \pi/L_F$ compared to the 0 phase at $\kappa = 0$.

We point out that curvature also introduces a spin current to the system, which is absent in a straight nanowire. This *exchange* spin current, as it is known in the literature, is caused by the misalignment of the magnetization in the system and is nonzero even at phase differences of $\phi = 0$ and $\phi = \pi$, where there are no charge currents [53,54]. The magnitude of the spin current is affected by the curvature, thereby providing means by which it can be externally manipulated.

To highlight that the triplets generate a long-range Josephson effect, we consider a long junction, $L_F = 6\xi_S$, and plot in Fig. 3(b) separately singlet and triplet contributions for a straight ($\kappa = 0$) and semicircular ($\kappa L_F = \pi$) wire. We see that, while for $\kappa = 0$ the triplet term is essentially zero and the singlet term is finite, for $\kappa L_F = \pi$ the singlet contribution is negligible compared to the triplet one, which additionally presents a long-range component I_N dominating over the short-range one I_T . Going from a straight to a semicircular ferromagnet produces a significant singlet to triplet conversion, of which component in the normal direction is long ranged, i.e., $d_N = |\mathbf{d} \times \hat{\mathbf{h}}|$, since in the case considered the d_z component is zero. In the simple example of a long wire with constant curvature chosen here, the magnitude of this LRT component is quite small, but we explain how this can be increased and manipulated below.

To better understand the role played by the curvature, it is useful to consider the weak proximity effect, meaning that $|\gamma_{ij}| \ll 1$ and $N \simeq 1$. The γ matrix can be then expressed in terms of f : $\gamma = f/2$. We then obtain the following linearized version of the Usadel equation,

$$\frac{D_F}{2} \partial_s^2 f_0 = -i\varepsilon f_0 - i\mathbf{h} \cdot \mathbf{d}, \quad (12a)$$

$$\frac{D_F}{2} (\partial_s^2 d_T - 2\kappa \partial_s d_N) = \left(-i\varepsilon + \frac{D_F \kappa^2}{2}\right) d_T - i f_0 h_T, \quad (12b)$$

$$\frac{D_F}{2} (\partial_s^2 d_N + 2\kappa \partial_s d_T) = \left(-i\varepsilon + \frac{D_F \kappa^2}{2}\right) d_N - i f_0 h_N, \quad (12c)$$

$$\frac{D_F}{2} \partial_s^2 d_z = -i\varepsilon d_z - i f_0 h_z. \quad (12d)$$

By inspecting the linearized Usadel equation for the triplet components, given in (12a)–(12c), we see that the curvature produces a Dyakonov-Perel term, describing the spin relaxation due to precession around the exchange field. A curvature of $\kappa L_F = \pi$ gives a strong spin-relaxation term which causes a fast decay even for the LRT component. From a qualitative perspective we can see that, since the exchange field varies with the position, a LRT component flowing through the wire will acquire an increasing component parallel to \mathbf{h} , i.e., a quickly decaying short-range component. The short-range triplet (SRT) component likewise acquires a LRT, but the conversion region is restricted to the typical decay of the SRT $\sim 1/\sqrt{h}$. In order to maximize the LRT generation from the SRT, one should therefore have a region of high curvature over the spatial decay of the SRT near the superconducting interface, and then minimal or zero curvature beyond. Alternatively, one may start with an intrinsically triplet superconductor, or have a compensating spin-orbit field in the ferromagnet that can negate the effect of the curvature.

Concluding remarks. We have shown that curvature is a designable and tunable parameter that can generate and control long-range supercurrents in diffusive SFS Josephson junctions without any magnetic inhomogeneities or intrinsic SOC. The system displays a curvature-controlled $0-\pi$ transition, which can be manipulated dynamically *in situ* with a single sample. This can facilitate experimental

investigation of the transition, and improve our understanding of the coexistence of superconductivity and magnetism in different phases. In the longer term this opens a diverse toolkit for the design and control of diffusive superconducting spintronic systems, and may be a useful implementation in solid state quantum computing. Since this field is still in its infancy, with several exciting directions still to be explored, we anticipate that curvature in such systems will be integral to the new generation of spintronic designs.

Acknowledgments. We thank P. Gentile for useful discussions and H. G. Hugdal for his helpful insights. The computations have been performed on the SAGA supercomputer provided by UNINETT Sigma2 - the National Infrastructure for High Performance Computing and Data Storage in Norway. We acknowledge funding via the “Outstanding Academic Fellows” programme at NTNU, the Research Council of Norway Grant No. 302315, as well as through its Centres of Excellence funding scheme, Project No. 262633, “QuSpin.”

- [1] O. G. Schmidt and K. Eberl, *Nature (London)* **410**, 168 (2001).
- [2] P. Cendula, S. Kiravittaya, Y. F. Mei, C. Deneke, and O. G. Schmidt, *Phys. Rev. B* **79**, 085429 (2009).
- [3] S. Xu, Z. Yan, K.-I. Jang, W. Huang, H. Fu, J. Kim, Z. Wei, M. Flavin, J. McCracken, R. Wang, A. Badae, Y. Liu, D. Xiao, G. Zhou, J. Lee, H. U. Chung, H. Cheng, W. Ren, A. Banks, X. Li, U. Paik, R. G. Nuzzo, Y. Huang, Y. Zhang, and J. A. Rogers, *Science* **347**, 154 (2015).
- [4] K. S. Das, D. Makarov, P. Gentile, M. Cuoco, B. J. Van Wees, C. Ortix, and I. J. Vera-Marun, *Nano Lett.* **19**, 6839 (2019).
- [5] E. R. Lewis, D. Petit, L. Thevenard, A. V. Jausovec, L. O’Brien, D. E. Read, and R. P. Cowburn, *Appl. Phys. Lett.* **95**, 152505 (2009).
- [6] D. M. Burn, M. Chadha, S. K. Walton, and W. R. Branford, *Phys. Rev. B* **90**, 144414 (2014).
- [7] O. M. Volkov, A. Kákay, F. Kronast, I. Mönch, M.-A. Mawass, J. Fassbender, and D. Makarov, *Phys. Rev. Lett.* **123**, 077201 (2019).
- [8] R. Streubel, P. Fischer, F. Kronast, V. P. Kravchuk, D. D. Sheka, Y. Gaididei, O. G. Schmidt, and D. Makarov, *J. Phys. D* **49**, 363001 (2016).
- [9] G. Cantele, D. Ninno, and G. Iadonisi, *Phys. Rev. B* **61**, 13730 (2000).
- [10] H. Aoki, M. Koshino, D. Takeda, H. Morise, and K. Kuroki, *Phys. Rev. B* **65**, 035102 (2001).
- [11] M. Encinosa and L. Mott, *Phys. Rev. A* **68**, 014102 (2003).
- [12] C. Ortix and J. van den Brink, *Phys. Rev. B* **81**, 165419 (2010).
- [13] P. Gentile, M. Cuoco, and C. Ortix, *SPIN* **03**, 1340002 (2013).
- [14] F. Nagasawa, D. Frustaglia, H. Saarikoski, K. Richter, and J. Nitta, *Nat. Commun.* **4**, 2526 (2013).
- [15] P. Gentile, M. Cuoco, and C. Ortix, *Phys. Rev. Lett.* **115**, 256801 (2015).
- [16] Z.-J. Ying, P. Gentile, C. Ortix, and M. Cuoco, *Phys. Rev. B* **94**, 081406(R) (2016).
- [17] C.-H. Chang and C. Ortix, *Nano Lett.* **17**, 3076 (2017).
- [18] G. Francica, P. Gentile, and M. Cuoco, *Europhys. Lett.* **127**, 30001 (2019).
- [19] A. M. Turner, V. Vitelli, and D. R. Nelson, *Rev. Mod. Phys.* **82**, 1301 (2010).
- [20] G. Francica, M. Cuoco, and P. Gentile, *Phys. Rev. B* **101**, 094504 (2020).
- [21] P.-H. Chou, C.-H. Chen, S.-W. Liu, C.-H. Chung, and C.-Y. Mou, *Phys. Rev. B* **103**, 014508 (2021).
- [22] Z.-J. Ying, M. Cuoco, C. Ortix, and P. Gentile, *Phys. Rev. B* **96**, 100506(R) (2017).
- [23] J. Linder and J. W. Robinson, *Nat. Phys.* **11**, 307 (2015).
- [24] M. Eschrig, *Phys. Today* **64** (1), 43 (2011).
- [25] A. I. Buzdin, *Rev. Mod. Phys.* **77**, 935 (2005).
- [26] F. S. Bergeret, A. F. Volkov, and K. B. Efetov, *Rev. Mod. Phys.* **77**, 1321 (2005).
- [27] I. F. Lyuksyutov and V. L. Pokrovsky, *Adv. Phys.* **54**, 67 (2005).
- [28] F. S. Bergeret, A. F. Volkov, and K. B. Efetov, *Phys. Rev. Lett.* **86**, 4096 (2001).
- [29] T. S. Khaire, M. A. Khasawneh, W. P. Pratt, and N. O. Birge, *Phys. Rev. Lett.* **104**, 137002 (2010).
- [30] J. W. A. Robinson, J. D. S. Witt, and M. G. Blamire, *Science* **329**, 59 (2010).
- [31] F. S. Bergeret and I. V. Tokatly, *Phys. Rev. Lett.* **110**, 117003 (2013).
- [32] F. S. Bergeret and I. V. Tokatly, *Phys. Rev. B* **89**, 134517 (2014).
- [33] A. I. Buzdin, L. Bulaevskii, and S. Panyukov, *JETP Lett.* **35**, 147 (1982).
- [34] A. Buzdin and A. E. Koshelev, *Phys. Rev. B* **67**, 220504(R) (2003).
- [35] V. V. Ryazanov, V. A. Oboznov, A. Y. Rusanov, A. V. Veretennikov, A. A. Golubov, and J. Aarts, *Phys. Rev. Lett.* **86**, 2427 (2001).
- [36] T. Kontos, M. Aprili, J. Lesueur, F. Genêt, B. Stephanidis, and R. Boursier, *Phys. Rev. Lett.* **89**, 137007 (2002).
- [37] J. E. Mooij, T. P. Orlando, L. Levitov, L. Tian, C. H. van der Wal, and S. Lloyd, *Science* **285**, 1036 (1999).
- [38] B. Bujnowski, R. Biele, and F. S. Bergeret, *Phys. Rev. B* **100**, 224518 (2019).
- [39] B. Kundys, *Appl. Phys. Rev.* **2**, 011301 (2015).
- [40] S. Matzen, L. Guillemot, T. Maroutian, S. K. K. Patel, H. Wen, A. D. DiChiara, G. Agnus, O. G. Shpyrko, E. E. Fullerton, D. Ravelosona, P. Lecoeur, and R. Kukreja, *Adv. Electron. Mater.* **5**, 1800709 (2019).
- [41] H. Jensen and H. Koppe, *Ann. Phys.* **63**, 586 (1971).
- [42] R. C. T. da Costa, *Phys. Rev. A* **23**, 1982 (1981).
- [43] C. Ortix, S. Kiravittaya, O. G. Schmidt, and J. van den Brink, *Phys. Rev. B* **84**, 045438 (2011).
- [44] C. Ortix, *Phys. Rev. B* **91**, 245412 (2015).
- [45] Y. Gaididei, V. P. Kravchuk, and D. D. Sheka, *Phys. Rev. Lett.* **112**, 257203 (2014).
- [46] D. D. Sheka, V. P. Kravchuk, and Y. Gaididei, *J. Phys. A: Math. Theor.* **48**, 125202 (2015).

- [47] K. D. Usadel, *Phys. Rev. Lett.* **25**, 507 (1970).
- [48] W. Belzig, F. K. Wilhelm, C. Bruder, G. Schön, and A. D. Zaikin, *Superlattices Microstruct.* **25**, 1251 (1999).
- [49] M. Y. Kuprianov and V. Lukichev, *Zh. Eksp. Teor. Fiz.* **94**, 149 (1988) [*Sov. Phys. JETP* **67**, 1163 (1988)].
- [50] N. Schopohl and K. Maki, *Phys. Rev. B* **52**, 490 (1995).
- [51] S. H. Jacobsen, J. A. Ouassou, and J. Linder, *Phys. Rev. B* **92**, 024510 (2015).
- [52] M. Amundsen and J. Linder, *Phys. Rev. B* **96**, 064508 (2017).
- [53] S. H. Jacobsen, I. Kulagina, and J. Linder, *Sci. Rep.* **6**, 23926 (2016).
- [54] W. Chen, P. Horsch, and D. Manske, *Phys. Rev. B* **89**, 064427 (2014).

II

REFERENCE




T. Salamone, H. G. Hugdal, M. Amundsen, and S. H. Jacobsen,

Curvature control of the superconducting proximity effect in diffusive ferromagnetic nanowires.

Physical Review B **105**, 134511 (2022)

CONTRIBUTIONS

SHJ initiated and supervised the project. TS contributed to analytical calculations, to the writing of the manuscript and performed numerical simulations. HGH contributed to analytical calculations and to the writing of the manuscript. MA and SHJ contributed to analytical results and numerical simulations. All authors contributed to discussions and revisions of the manuscript.

Curvature control of the superconducting proximity effect in diffusive ferromagnetic nanowiresTancredi Salamone,¹ Henning G. Hugdal ¹, Morten Amundsen ² and Sol H. Jacobsen ¹¹*Center for Quantum Spintronics, Department of Physics, NTNU,**Norwegian University of Science and Technology, NO-7491 Trondheim, Norway*²*Nordita, KTH Royal Institute of Technology and Stockholm University, Hannes Alfvéns väg 12, SE-106 91 Stockholm, Sweden*

(Received 23 December 2021; revised 15 March 2022; accepted 1 April 2022; published 14 April 2022)

Coupling a conventional *s*-wave superconductor to a ferromagnet allows us, via the proximity effect, to generate superconducting triplet correlations. This feature can be employed to achieve a superconducting triplet spin-valve effect in superconductor-ferromagnet (SF) hybrid structures, for example by switching the magnetizations of the ferromagnets between parallel and antiparallel configurations in F_1SF_2 and SF_1F_2 trilayers, or in SF bilayers with both Rashba and Dresselhaus spin-orbit coupling (SOC). It was recently reported that geometric curvature can control the generation of long-ranged triplets. We use this property to show that the superconducting critical temperature of an SF hybrid nanowire can be tuned by varying the curvature of the ferromagnetic side alone, with no need of another ferromagnet or SOC. We show that the variation of the critical temperature as a function of the curvature can be exploited to obtain a robust, curvature-controlled, superconducting triplet spin-valve effect. Furthermore, we perform an analysis with the inclusion of spin-orbit coupling and explain how it modifies the spin-valve effect both quantitatively and qualitatively.

DOI: [10.1103/PhysRevB.105.134511](https://doi.org/10.1103/PhysRevB.105.134511)**I. INTRODUCTION**

In recent years, progress in the fabrication of nanostructures with curved geometries have opened new perspectives regarding their properties and applications. From etching [1,2] and compressive buckling [3], to electron beam lithography [4–6], two-photon lithography [7,8], and glancing angle deposition [9], to cite just some, the possibilities for the realization of different structures and shapes in up to three dimensions are manifold. Moreover, many processes, such as photostriction, piezoelectrics, thermoelectric effects, tuning of the surface chemistry, and more [10–12], allow one to dynamically change and control the strain and curvature of nanostructures. This gives good prospects for rapid, *in situ* manipulation of geometric curvature in spintronic devices in the future. The application of geometrical curvature to magnetic nanoarchitectures is seeing a rising interest, with the growing research area of curvilinear magnetism aiming to explain and characterize curvature-induced effects [13–15].

Micromagnetic studies show that geometric curvature in magnetic materials induces two main effects, an anisotropy term and a chiral or extrinsic Dzyaloshinskii-Moriya interaction (DMI) [16], source of an effective magnetic field [17], and many other peculiar features. The curvature-induced DMI causes, for instance, the appearance of chiral and topological spin textures of the effective magnetization in toroidal nanomagnets [18,19], bent nanotubes [20,21], curved surfaces [22], nanohelices [23,24], and spherical shells [17,25,26].

The effects of geometric curvature in nanostructures have been extensively studied in the ballistic framework. In these systems curvature has two main consequences: the appearance of a quantum geometric potential causing interesting

phenomena at the nanoscale [27–30] and of a strain field producing a curvature-induced Rashba-type spin-orbit coupling (SOC) [31–33]. Theoretical studies have focused on new properties appearing in semiconductors [34–38] as well as in superconductors [39–42]. For instance, it was shown that geometric curvature can promote topological edge states in bent quantum wire with Rashba SOC [35] and topological superconductivity in curved two-dimensional (2D) topological insulators [42].

Interestingly, it has been demonstrated that Rashba spin-orbit coupling in magnetic structure leads to DMI and magnetic anisotropy [43–45], highlighting the close relationship between the curvature-induced DMI and anisotropy term obtained in the micromagnetic framework, and the curvature-induced Rashba SOC from ballistic studies.

The fact that geometric curvature has nontrivial consequences on nanostructures suggests that the inclusion of geometrically curved materials, and in particular magnetic materials, could provide new prospects for the modeling of spintronic devices, as we already showed for a superconductor/ferromagnet/superconductor (SFS) Josephson junction in our previous work [46].

In the field of superconducting spintronics [47,48], hybrid structures of superconductors and ferromagnets play a crucial role, since at the SF interface the properties of one material can leak into the other due to the proximity effect [49–51]. Thus, the combination of magnetism with superconductivity permits all the operations typical of conventional spintronics with the advantage of no heat loss by virtue of the dissipationless currents provided by superconductors. Superconducting *s*-wave correlations in diffusive heterostructures typically penetrate only a short distance into a ferromagnet, proportional

to $\sqrt{D_F/\hbar}$, where D_F is the diffusion constant and \hbar is the magnitude of the exchange field of the ferromagnet. Extensive experimental and theoretical studies have been performed in order to achieve conversion of spin-singlet correlations into the so-called long-range triplet (LRT) correlations, penetrating for longer distances of order $\sqrt{D_F/T}$, where T is the temperature. It has been shown that this conversion can be accomplished by means of magnetic inhomogeneities [52–54], spin-orbit coupling [55,56], or geometric curvature [46] in the system.

The critical temperature T_c of superconducting hybrid structures can be influenced and controlled through the magnetic properties of ferromagnets, allowing us in some cases to realize so-called superconducting spin valves. Such devices were proposed in the form of SF_1F_2 [57] and of F_1SF_2 [58,59] structures: for both it was shown that the critical temperature of the system is sensitive to the relative orientation of the magnetizations of the two ferromagnets. Furthermore, experiments studying CuNi/Nb/CuNi trilayers demonstrated that it is possible to control the critical temperature of the structure by switching between parallel and antiparallel orientation of the magnetization in the CuNi layers [60,61]. Control of the critical temperature cannot be achieved in an SF system with a single ferromagnet, since the critical temperature is not sensitive to the orientation of the magnetization of the single F layer. However, the presence of spin-orbit coupling changes this picture as was shown in Ref. [62] for an SF bilayer, where control of the critical temperature was provided by the presence of Rashba and Dresselhaus SOC in the ferromagnet. This was confirmed experimentally in a system where Nb was proximity coupled to an asymmetric Pt/Co/Pt trilayer [63].

In this work we show that geometric curvature alone allows for control of the superconducting critical temperature of an SF structure with a curved ferromagnet, thereby realizing a superconducting spin-valve effect. We also show that the inclusion of SOC can increase the magnitude of this effect. The article is organized as follows: in Sec. II we introduce the relevant Hamiltonian and treat it within a covariant formulation for the introduction of geometric curvature. In Sec. III we extend the formalism to the Usadel equation, focusing on a curved nanowire. We then present our numerical results in Sec. IV, followed by a discussion and summary in Sec. V.

II. HAMILTONIAN FOR CURVED SYSTEMS

We will start by considering the following Hamiltonian describing the motion of electrons in the presence of spin-orbit coupling:

$$H = \frac{\hbar^2 \mathbf{k}^2}{2m^*} - \hbar \boldsymbol{\alpha} \cdot \frac{\boldsymbol{\sigma} \times \mathbf{k}}{m^*}, \quad (1)$$

where $\mathbf{k} = -i\nabla$, m^* is the electron effective mass, and $\boldsymbol{\sigma}$ is the Pauli vector. The components of the vector $\boldsymbol{\alpha}$ give the strength of the spin-orbit coupling due to asymmetric confinement in the different directions. In order to study how the Hamiltonian of Eq. (1) is modified when dealing with a curved system, in the following we will develop a covariant formulation.

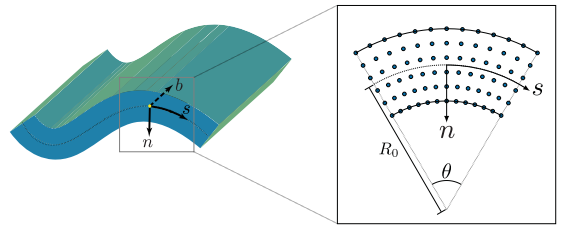


FIG. 1. The local coordinate system of a curved material, illustrating the tangential, normal, and binormal directions. The finite curvature $\kappa = 1/R_0$ leads to regions with both tensile ($n < 0$) and compressive ($n > 0$) strain in the material [32,64].

A. Frenet-Serret frame

As a start, we parametrize the three-dimensional (3D) space as $\mathbf{R}(s, n, b) = \mathbf{r}(s) + n\hat{\mathcal{N}}(s) + b\hat{\mathcal{B}}(s)$. Here $\mathbf{r}(s)$ is the parametrization of the curve in the plane of the curvature and s , n , and b are the arclength, normal, and binormal coordinates, respectively, as it can be seen in Fig. 1. The geometry of the space can therefore be determined from the set of three orthonormal unit vectors: $\hat{\mathcal{T}}(s) = \partial_s \mathbf{r}(s)$, $\hat{\mathcal{N}}(s) = \partial_s \hat{\mathcal{T}}(s)/\kappa(s)$, and $\hat{\mathcal{B}}(s) = \hat{\mathcal{T}}(s) \times \hat{\mathcal{N}}(s)$, representing the tangential, normal, and binormal curvilinear directions respectively. Here we have defined the curvature $\kappa(s) = |\partial_s \hat{\mathcal{T}}(s)|$. These obey the following Frenet-Serret-type equation of motion:

$$\begin{pmatrix} \partial_s \hat{\mathcal{T}}(s) \\ \partial_s \hat{\mathcal{N}}(s) \\ \partial_s \hat{\mathcal{B}}(s) \end{pmatrix} = \begin{pmatrix} 0 & \kappa(s) & 0 \\ -\kappa(s) & 0 & 0 \\ 0 & 0 & 0 \end{pmatrix} \begin{pmatrix} \hat{\mathcal{T}}(s) \\ \hat{\mathcal{N}}(s) \\ \hat{\mathcal{B}}(s) \end{pmatrix}. \quad (2)$$

With this, as shown in the Appendix, we obtain the following metric tensor:

$$\hat{G}_{\mu\nu} = \begin{pmatrix} \eta(s, n)^2 & 0 & 0 \\ 0 & 1 & 0 \\ 0 & 0 & 1 \end{pmatrix}, \quad (3)$$

where $\eta(s, n) = 1 - \kappa(s)n$.

B. Curvature-induced spin-orbit coupling

When a material with initially regular atomic lattice is induced to bend, the interatomic distances become nonuniform, leading to tensile and compressive strains in the material, see Fig. 1. The strain is directly related to the change in length of the different coordinate axes when deforming the line segment [65], which for the tangential component [see Eq. (A15a)] results in a strain [32,64,66]:

$$\epsilon_{tt} = -\kappa(s)n. \quad (4)$$

The deformation leads to an additional potential in the material, which for small strains is assumed to be linear in strain [67,68],

$$V = -\Lambda \kappa(s)n, \quad (5)$$

where Λ is the deformation potential constant. This approximation should be applicable when the thickness of the material is much smaller than the local radius of curvature.

The potential in turn leads to an electric field [see Eq. (A6)]

$$\mathbf{E} = -\nabla V = \frac{\Lambda n}{\eta(s, n)} [\partial_s \kappa(s)] \hat{T} + \Lambda \kappa(s) \hat{N}, \quad (6)$$

which when averaged over a volume with infinitesimal thickness ds in the tangential direction results in an electric field pointing along the normal direction [32,64],

$$\langle \mathbf{E} \rangle = \Lambda \kappa(s) \hat{N}. \quad (7)$$

In the rest frame of an electron moving with momentum $\mathbf{p} = \hbar \mathbf{k}$ this translates to a magnetic field $\mathbf{B} \sim \mathbf{p} \times \mathbf{E}$ [69] which couples to the electron's spin via the Zeeman coupling, leading to an effective spin-orbit coupling

$$H_N = \frac{\alpha_N}{m^*} \hat{N} \cdot [\boldsymbol{\sigma} \times \mathbf{p}] \quad (8)$$

due to the asymmetry in the normal direction. Here we have defined the curvature-dependent spin-orbit constant $\alpha_N = \hbar \Lambda g |e| \kappa(s) / 4m^* c^2$ [46], where g is the g factor, e is the electron mass, and c is the speed of light.

C. Covariant formulation of Hamiltonian

In order to derive the correct form of the Usadel equation for a general curved manifold we rewrite the Hamiltonian of Eq. (1) in a general covariant form:

$$H = -\frac{\hbar^2 \mathcal{G}^{\lambda\mu}}{2m^*} \mathcal{D}_\lambda \mathcal{D}_\mu + \frac{i\hbar}{m^*} \frac{\epsilon^{\lambda\mu\nu}}{\sqrt{G}} \alpha_\lambda \sigma_\mu \mathcal{D}_\nu, \quad (9)$$

where we used the Einstein summation rule, with the Greek indices running over the components t, n, b in the covariant basis defined in the Appendix. The terms $\mathcal{G}^{\lambda\mu}$ and G are the inverse and the determinant of the metric tensor, respectively, and $\epsilon^{\lambda\mu\nu}$ is the Levi-Civita symbol.

The (space) covariant derivatives are defined through their action on any general covariant vector v_μ as $\mathcal{D}_\lambda v_\mu = \partial_\lambda v_\mu - \Gamma_{\lambda\mu}^\nu v_\nu$, with $\Gamma_{\lambda\mu}^\nu$ representing the Christoffel symbols:

$$\Gamma_{\lambda\mu}^\nu = \frac{1}{2} \mathcal{G}^{\nu\gamma} (\partial_\lambda \mathcal{G}_{\gamma\lambda} + \partial_\lambda \mathcal{G}_{\gamma\mu} - \partial_\gamma \mathcal{G}_{\lambda\mu}). \quad (10)$$

To further simplify the derivation we exploit the last term in Eq. (9) to define a (contravariant) spin-orbit field as $A^\nu = \epsilon^{\lambda\mu\nu} \alpha_\lambda \sigma_\mu / \sqrt{G} = \mathcal{G}^{\nu\mu} A_\mu$.

With the assumption of weak spin-orbit coupling, the Hamiltonian of Eq. (9) can be written in a form manifestly showing a local SU(2) gauge invariance [70,71]:

$$H = -\frac{\hbar^2 \mathcal{G}^{\lambda\mu}}{2m^*} (\mathcal{D}_\lambda - iA_\lambda) (\mathcal{D}_\mu - iA_\mu). \quad (11)$$

Therefore, the SOC enters the Hamiltonian with the usual form of a 2×2 matrix-valued SU(2) vector field [55,56]. The values of the components A_μ depend on the physical system at hand, e.g., the intrinsic types of SOC in the system, and the curvature-induced SOC discussed in the previous subsection.

D. Effective Hamiltonian for a curved nanowire

In order to derive an effective Hamiltonian for a curved nanowire one can apply a thin-wall quantization procedure [72,73] to the Hamiltonian of Eq. (9), additionally taking into account the effect of the constraining potential in the normal and binormal directions. These allow us to expand

the Hamiltonian in powers of n and b , taking the zeroth order terms, and employ an adiabatic approximation to separate the relevant degree of freedom s . Considering curvature-induced and intrinsic spin-orbit interaction, α_N and α_B , respectively, one gets [32,74]

$$H = -\frac{\hbar^2}{2m^*} \partial_s^2 - \frac{\hbar^2}{8m^*} \kappa(s)^2 - \frac{i\hbar}{m^*} \alpha_N \sigma_B \partial_s + \frac{i\hbar}{m^*} \alpha_B \left(\sigma_N \partial_s - \frac{\kappa(s)}{2} \sigma_T \right). \quad (12)$$

The second term is the quantum geometric potential, which is neglected in the following as it only leads to an overall energy shift. With the use of Eq. (2) it is possible to reorganize the terms in the second line of Eq. (12) and incorporate them in the following SU(2) spin-orbit field:

$$\mathbf{A} = (\alpha_N \sigma_B - \alpha_B \sigma_N, 0, 0), \quad (13)$$

having a vector structure in the geometric space and a 2×2 matrix structure in spin space.

III. USADEL EQUATION FOR CURVED NANOWIRES

In this work we will make use of Green's functions in the diffusive limit and study the dynamics through the second order partial differential Usadel equation [75]. The Hamiltonian of Eq. (11) allows us to define the Usadel equation in a covariant form and, with the right boundary conditions, describe the diffusion of superconducting correlations in an SF hybrid structure with geometric curvature. We restrict ourselves to the case of diffusive equilibrium, allowing us to consider just the retarded component \hat{g}_R of the quasiclassical Green's function to describe the system [76]. The Usadel equation defined from the Hamiltonian of Eq. (11) reads

$$D_F \mathcal{G}^{\lambda\mu} \tilde{\mathcal{D}}_\lambda (\hat{g}_R \tilde{\mathcal{D}}_\mu \hat{g}_R) + i[\varepsilon \hat{\rho}_3 + \hat{\Delta} + \hat{M}, \hat{g}_R] = 0, \quad (14)$$

where $\hat{\rho}_3 = \text{diag}(1, 1, -1, -1)$, ε is the quasiparticle energy, and $\hat{\Delta} = \text{antidiag}(\Delta, -\Delta, \Delta^*, -\Delta^*)$ with Δ the superconducting order parameter and magnetization $\hat{M} = \hbar^\mu \text{diag}(\sigma_\mu, \sigma_\mu^*)$. Here we have set $\hbar = 1$. We have also defined the space-gauge covariant derivative as

$$\tilde{\mathcal{D}}_\lambda v_\mu = \tilde{\partial}_\lambda v_\mu - \Gamma_{\lambda\mu}^\nu v_\nu, \quad (15)$$

where we have defined the gauge-only covariant derivative $\tilde{\partial}_\lambda v_\mu = \partial_\lambda v_\mu - i[\hat{A}_\lambda, v_\mu]$, with $\hat{A}_\lambda = \text{diag}(A_\lambda, -A_\lambda^*)$.

We now rewrite the first term of Eq. (14) by inserting the expression for the covariant derivative of Eq. (15). With the use of Eqs. (3) and (10), we get

$$\begin{aligned} & D_F \mathcal{G}^{\lambda\mu} \tilde{\mathcal{D}}_\lambda (\hat{g}_R \tilde{\mathcal{D}}_\mu \hat{g}_R) \\ &= \frac{D_F}{\eta(s, n)} \{ [\tilde{\partial}_s (\eta(s, n))^{-1} \hat{g}_R \tilde{\partial}_s \hat{g}_R] + \tilde{\partial}_n (\eta(s, n)) \hat{g}_R \tilde{\partial}_n \hat{g}_R \} \\ & \quad + \tilde{\partial}_b (\eta(s, n)) \hat{g}_R \tilde{\partial}_b \hat{g}_R \}. \end{aligned} \quad (16)$$

For the case of a nanowire we can ignore the dependence of \hat{g}_R on n and b and take the limit $n, b \rightarrow 0$. Therefore, the Usadel equation takes the form

$$D_F \tilde{\partial}_s (\hat{g}_R \tilde{\partial}_s \hat{g}_R) + i[\varepsilon \hat{\rho}_3 + \hat{\Delta} + \hat{M}, \hat{g}_R] = 0, \quad (17)$$

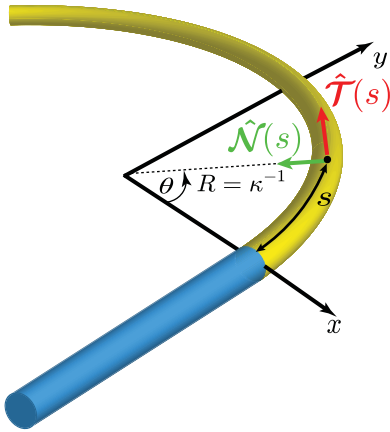


FIG. 2. Superconductor-ferromagnet hybrid nanowire with a ferromagnet with constant curvature. The orthonormal unit vectors \hat{T} , \hat{N} identifying the curvilinear coordinates are also shown.

where the effects of the curvature enter the equation through the Pauli matrices, contained in the spin-orbit field and the magnetization.

In order to solve the Usadel equation either analytically or numerically for superconducting hybrid systems, boundary conditions are needed. In this work we will employ the Kupriyanov-Lukichev boundary conditions [77], which

$$D_F \{ \partial_s^2 \gamma + 2(\partial_s \gamma) \tilde{N} \tilde{\gamma}(\partial_s \gamma) \} = -2i\varepsilon\gamma - i(\mathbf{h} \cdot \boldsymbol{\sigma}\gamma - \gamma \mathbf{h} \cdot \boldsymbol{\sigma}^*) - iD_F[(\partial_s A_T)\gamma + \gamma(\partial_s A_T^*)] \\ + D_F[A^2\gamma - \gamma A^{*2} + 2(A_j\gamma + \gamma A_j^*)\tilde{N}(A_j^* + \tilde{\gamma}A_j\gamma)] \\ + 2iD_F[(A_T + \gamma A_T^* \tilde{\gamma})N(\partial_s \gamma) + (\partial_s \gamma)\tilde{N}(A_T^* + \tilde{\gamma}A_T\gamma)], \quad (20a)$$

$$D_F \{ \partial_s^2 \tilde{\gamma} + 2(\partial_s \tilde{\gamma}) \tilde{N} \tilde{\gamma}(\partial_s \tilde{\gamma}) \} = -2i\varepsilon\tilde{\gamma} - \Delta\sigma_2 + \gamma\Delta^*\sigma_2\gamma, \quad (20b)$$

where the index j runs over the physical components [see Eq. (A17)] T, N, B of the SOC field and $\sigma_2 = \text{anti diag}(-i, i)$. In Eq. (20a) both the exchange field vector $\mathbf{h} = (h_T, h_N, h_B)$ and the Pauli vector $\boldsymbol{\sigma} = (\sigma_T, \sigma_N, \sigma_B)$ are expressed in curvilinear components.

We note that the result obtained here for the Riccati parametrization of the Usadel equation is the same as in [62] with the addition of the last term in the second line of Eq. (20a) due to the spatial dependence of the spin-orbit field.

Upon substitution of Eq. (19) into Eq. (18) we get the following form for the boundary conditions at the superconductor-ferromagnet interface:

$$\partial_I \gamma_S = \frac{1}{L_S \zeta_S} (1 - \gamma_S \tilde{\gamma}_F) N_F (\gamma_F - \gamma_S) + iA_T \gamma_S + i\gamma_S A_T^*, \quad (21a)$$

$$\partial_I \gamma_F = \frac{1}{L_F \zeta_F} (1 - \gamma_F \tilde{\gamma}_S) N_S (\gamma_F - \gamma_S) + iA_T \gamma_F + i\gamma_F A_T^*. \quad (21b)$$

ensure the continuity of the current flow through the interface:

$$L_j \zeta_j \hat{g}_{Rj} \tilde{\partial}_I \hat{g}_{Rj} = [\hat{g}_{R1}, \hat{g}_{R2}]. \quad (18)$$

Here $\tilde{\partial}_I$ is the gauge covariant derivative at the interface, j refers to the different materials comprising the hybrid system, with $j = 1, 2$ denoting the materials on the left and right side of the relevant interface, L_j represents the length of the material, and $\zeta_j = R_B/R_j$ is the interface parameter given by the ratio between the barrier resistance R_B and its bulk resistance R_j .

A. Riccati parametrization

To solve numerically Eq. (17) it is useful to introduce a parametrization for the quasiclassical Green's function. Here we employ the Riccati parametrization [62,78]:

$$\hat{g}_R = \begin{pmatrix} N(1 + \gamma\tilde{\gamma}) & 2N\gamma \\ -2\tilde{N}\tilde{\gamma} & -\tilde{N}(1 + \tilde{\gamma}\gamma) \end{pmatrix}, \quad (19)$$

with $N = (1 - \gamma\tilde{\gamma})^{-1}$ and $\tilde{N} = (1 - \tilde{\gamma}\gamma)^{-1}$ and the tilde conjugation denotes the operation $\tilde{\gamma}(s, \varepsilon) = \gamma^*(s, -\varepsilon)$. Therefore, with the use of this parametrization we have reduced the equation for the 4×4 matrix \hat{g}_R to one for the 2×2 matrix γ .

To study the system depicted in Fig. 2 we define the Usadel equation separately for a curved ferromagnet with spin-orbit coupling, and a straight s -wave superconductor. We will then solve the two Usadel equations self-consistently, employing the Kupriyanov-Lukichev boundary conditions at the SF interface.

Substituting Eq. (19) into Eq. (17) we get the Usadel equation for the ferromagnet and the superconductor, respectively:

The corresponding equations for $\tilde{\gamma}$ are simply obtained by tilde conjugation of Eqs. (20a) to (21b).

B. Weak proximity effect equations

To interpret the effects of the geometrical curvature and spin-orbit coupling components in our system, we will now study the curved ferromagnet in the limit of weak proximity effect. In this limit $|\gamma_{ij}| \ll 1$ and $N \sim 1$, so that $\gamma = f/2$, where $f = (f_0 + \mathbf{d} \cdot \boldsymbol{\sigma})i\sigma_2$. Here f is the anomalous Green's function, the off-diagonal block matrix in \hat{g}_R , and is defined in terms of the scalar function f_0 and the \mathbf{d} vector $\mathbf{d} = (d_T, d_N, d_B)$ representing the condensate functions for the singlet and triplet components, respectively.

For the system of Fig. 2 the components $\sigma_{T,N,B}(s)$ in the ferromagnet are obtained from the following set of

three unit vectors:

$$\hat{T}(s) = -\sin\theta(s)\hat{x} + \cos\theta(s)\hat{y}, \quad (22a)$$

$$\hat{N}(s) = -\cos\theta(s)\hat{x} - \sin\theta(s)\hat{y}, \quad (22b)$$

$$\hat{B}(s) \equiv \hat{z}, \quad (22c)$$

with $\theta(s) = \kappa s$. Consequently, we get the following form for the γ matrix:

$$\gamma = \frac{1}{2} \begin{pmatrix} (id_T + d_N)e^{-i\theta} & d_z + f_0 \\ d_z - f_0 & (id_T - d_N)e^{i\theta} \end{pmatrix}. \quad (23)$$

$$\frac{iD_F}{2} \partial_s^2 d_T - iD_F(\kappa + 2\alpha_N)\partial_s d_N - 2iD_F\alpha_B\partial_s d_z = f_0 h_T + \left\{ \varepsilon + \frac{iD_F}{2} [(\kappa + 2\alpha_N)^2 + 4\alpha_B^2] \right\} d_T, \quad (24a)$$

$$\frac{iD_F}{2} \partial_s^2 d_N + iD_F(\kappa + 2\alpha_N)\partial_s d_T = f_0 h_N + \left\{ \varepsilon + \frac{iD_F}{2} (\kappa + 2\alpha_N)^2 \right\} d_N - iD_F\alpha_B(\kappa + 2\alpha_N)d_N, \quad (24b)$$

$$\frac{iD_F}{2} \partial_s^2 d_z + 2iD_F\alpha_B\partial_s d_T = f_0 h_z + \left\{ \varepsilon + 2iD_F\alpha_B^2 \right\} d_z - iD_F\alpha_B(\kappa + 2\alpha_N)d_N, \quad (24c)$$

$$\frac{iD_F}{2} \partial_s^2 f_0 = \varepsilon f_0 + \mathbf{h} \cdot \mathbf{d}. \quad (24d)$$

By inspecting these equations it is possible to understand how the mechanism for singlet-triplet conversion works in the ferromagnet. Let us consider an exchange field along the \hat{T} direction: at the SF interface on the ferromagnet side, due to the proximity effect, singlets are present, which are partially converted into the SRT component d_T by the exchange field. The presence of geometrical curvature and/or spin-orbit coupling results then in the generation of LRT components d_N , d_z .

C. Physical interpretation of the weak proximity effect equations

The effect of κ , α_N , and α_B in Eqs. (24a) to (24c) is twofold: the triplets undergo spin precession and spin relaxation. The former can be identified with the terms having a first derivative of a triplet component and describes the rotation of the spin of superconducting triplet correlations while moving along the ferromagnet. The latter appears as an additional imaginary component of the triplet energy and represents a loss of spin information due to frequent impurity scattering. Consequently, both curvature and spin-orbit coupling independently provide a pathway for LRT generation. At the same time, if their value becomes too large, they become detrimental for the triplets. An estimate of the value for the crossover between the two regimes can be provided by comparison of the spin-precession prefactor $\epsilon_p \sim D_F\kappa/L_F$ and the spin-relaxation prefactor $\epsilon_r \sim D_F\kappa^2/2$, where we for simplicity consider geometric curvature only. Therefore, a transition from spin-precession dominated to spin-relaxation dominated regimes occurs when $\epsilon_p \sim \epsilon_r$, i.e., when $\kappa L_F \sim 2$ or $\kappa L_F/\pi \sim 0.6$. The inclusion of SOC terms will shift the transition towards 0 [79]. This effect is crucial for the results presented in this work and will be discussed in more detail in the next section.

Finally, we note that in Eqs. (24a) to (24c) κ and α_N always appear together in the same form, highlighting that they have

In this limit it becomes straightforward to identify the short-range triplet (SRT) $\mathbf{d}_{\parallel} = \mathbf{d} \cdot \mathbf{h}/|\mathbf{h}|$ and LRT $\mathbf{d}_{\perp} = \mathbf{d} \times \mathbf{h}/|\mathbf{h}|$ components. For instance, if the exchange field \mathbf{h} is directed along the \hat{T} direction the SRT can be identified with d_T , while d_N and d_B represent the LRTs.

The weak proximity limit allows us to consider only the terms linear in γ both in the Usadel equation and in the Kupriyanov-Lukichev boundary conditions. With the SO field given by Eq. (13) and the γ matrix of Eq. (23) the linearized Usadel equation in the ferromagnet takes the following form:

the same effect on the \mathbf{d} -vector components. It is therefore possible to define an “effective” curvature $\tilde{\kappa} = \kappa + 2\alpha_N$ and consider α_N as a factor which boosts the effects of the geometrical curvature.

IV. CURVATURE-CONTROLLED TRIPLET SPIN VALVE

In order to obtain numerical results for the hybrid system of Fig. 2, we look for a self-consistent solution to the Usadel equation given by Eqs. (20a) and (20b), with the boundary conditions of Eqs. (21a) and (21b), and the following gap equation [62]:

$$\Delta(s) = N_0\lambda \int_0^{\Delta_0 \cosh(1/N_0\lambda)} d\varepsilon \operatorname{Re}\{f_0(\varepsilon, s)\} \times \tanh\left(\frac{\pi}{2e^\gamma} \frac{\varepsilon/\Delta_0}{T/T_{c0}}\right), \quad (25)$$

where λ is the coupling constant between electrons, N_0 is the density of states at the Fermi level, $\gamma \simeq 0.577$ is the Euler-Mascheroni constant, and T is the temperature. Δ_0 and T_{c0} are the superconducting gap and critical temperature of the bulk superconductor, respectively.

To calculate the critical temperature numerically we make use of a binary search algorithm. With this, after calculating $\Delta(s, T)$ for N different values of T , we obtain the critical temperature with a precision of $T_{c0}/2^{N+1}$. The binary search algorithm is presented in [80] and can be found as part of the set of numerical programs GENEUS openly accessible on GitHub [81]. This code is modified to include geometric curvature via a change in coordinate system and Pauli matrices, as well as inclusion of position dependent exchange and spin-orbit fields in the curved ferromagnet, as presented in Sec. III.

Once a self-consistent solution is found, we can extract the critical temperature of the system for different values

of the geometrical curvature κ , the intrinsic and extrinsic (curvature-induced) spin-orbit coupling constants α_B and α_N , and ferromagnet and superconductor lengths L_F and L_S . The critical temperature plots were obtained through a spline interpolation of 17 data points for geometric curvature between 0 (straight wire) and $2\pi/L_F$ (ring). We consider the exchange field of the ferromagnet to be along the tangential direction $\mathbf{h} \parallel \hat{\mathcal{T}}$ and the interface parameter $\zeta = 3$. We normalize energies to the bulk gap of the superconductor at zero temperature Δ_0 , and lengths to its (diffusive) coherence length ξ_0 . Furthermore, we considered a conventional s -wave superconductor with the material parameter $N_0\lambda = 0.2$.

We note that the critical temperature of the hybrid system will always be smaller than the bulk critical temperature of the superconductor. This is due to the proximity effect, where singlet correlations leak into the ferromagnet. As is clear from Eq. (25) a decrease in singlets in the superconductor directly corresponds to a reduction of the singlet order parameter and consequently of the critical temperature.

Analyzing the curvature dependence of the critical temperature of the hybrid system, a range of parameters gives a significant variation with respect to the bulk critical temperature, suggesting a superconducting triplet spin-valve effect tunable via the geometrical curvature. To understand how this effect works we consider again the weak proximity effect limit.

As discussed in the previous section, curvature κ and spin-orbit coupling constants α_N and α_B have two effects on the SRT and LRT components: spin precession and spin relaxation. While the former, linear in curvature and SOC constants, converts SRTs into LRTs, the latter, proportional to the square curvature and SOC constants, causes their spin to decay while diffusing in the ferromagnet. Therefore, for small κ and/or α_N , α_B the precession mechanism dominates over the relaxation, and SRT correlations are converted into LRT allowing for more singlets to be converted in SRTs, thus reducing the number of singlets in the superconductor and lowering the critical temperature. On the other hand, when the relaxation term dominates, for high κ and/or α_N , α_B , as discussed in the previous section, the triplet components are subjected to spin relaxation, causing them to decay faster. Consequently, κ , α_N , and α_B result in an increased suppression of these superconducting correlations in this case, giving a higher critical temperature of the system.

To study this spin-valve effect, we start by considering the case of zero spin-orbit coupling. We consider two different lengths of the superconductor: $L_S = 0.55\xi_0$ and $L_S = \xi_0$. In Fig. 3 we plot the behavior of the critical temperature as a function of $\kappa L_F/\pi$, for $L_S = 0.55\xi_0$ and different lengths of the ferromagnet L_F . The quantity $\kappa L_F/\pi$ represents the angle (in units of π) which is spanned by the portion of circular ring formed by the ferromagnetic wire when keeping fixed its length L_F and changing its curvature κ . We see how, for a very short ferromagnetic wire, $L_F = 0.20\xi_0$, the critical temperature T_c of the SF structure undergoes a variation of $\sim 40\%$ of the value of the bulk critical temperature of the superconductor T_{c0} , thus giving a very good spin-valve effect. For such a short ferromagnet to be realizable, one would require a large coherence length ξ_0 . Considering $L_F = 0.40\xi_0$ and $L_F = 0.50\xi_0$ we still note a significant variation of T_c : $\sim 20\%$

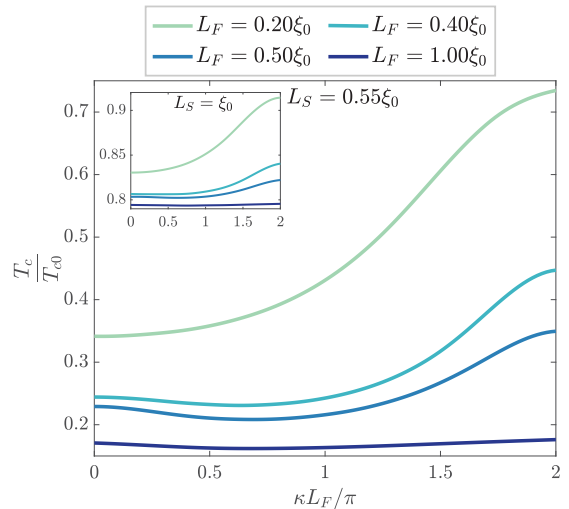


FIG. 3. Critical temperature of the system T_c divided by the critical temperature of the isolated superconductor T_{c0} as a function of curvature of the ferromagnet κ , for $L_S = 0.55\xi_0$ and $L_S = \xi_0$ (inset) and different lengths of the ferromagnet L_F , with $\mathbf{h} = 10\Delta_0\hat{\mathcal{T}}$ and zero spin-orbit coupling.

and $\sim 15\%$ of the value of T_{c0} , respectively. Interestingly, for $L_S = 0.55\xi_0$ and $L_F \neq 0.2\xi_0$ we note a nonmonotonic behavior of T_c : at small values of κ , T_c decreases and then starts to increase again, due to the interplay of spin-precession and relaxation mechanisms discussed above. There is no decrease in T_c at small κ for $L_S = 0.55\xi_0$ and $L_F = 0.2\xi_0$ because in this case the length of the ferromagnet is too small for the spin precession to contribute significantly. In the inset of Fig. 3, on the other hand, we plot the case $L_S = \xi_0$ and we note two differences: (i) the critical temperature of the hybrid system is much closer to that of the bulk superconductor and (ii) its variation when changing the curvature is substantially reduced. This is not surprising since we expect the superconductivity to be more robust with respect to proximity effects when increasing the length of the superconductor. Therefore, in order to have a stronger spin-valve effect, we will from now on consider the case $L_S = 0.55\xi_0$.

It is worth analyzing the effect of varying the magnitude of the exchange field \mathbf{h} in the curved ferromagnet. In Fig. 4 we plot the ratio T_c/T_{c0} as a function of the curvature κ for three values of the magnitude of the exchange field $|\mathbf{h}| = (\Delta_0, 10\Delta_0, 50\Delta_0)$ with $L_S = 0.55\xi_0$, $L_F = 0.50\xi_0$, and zero spin-orbit coupling. We note that increasing the magnitude of the exchange field reduces T_c . This is due to the inverse proximity effect, which produces a magnetization inside the superconductor proportional to the value of \mathbf{h} . The higher the value of the magnetization the more the singlet correlations are suppressed inside the superconductor, reducing the critical temperature of the system. Upon inspection of Fig. 4 we can conclude that an intermediate magnitude of the exchange field will result in greatest variation of T_c , without a significantly detrimental suppression of the overall value.

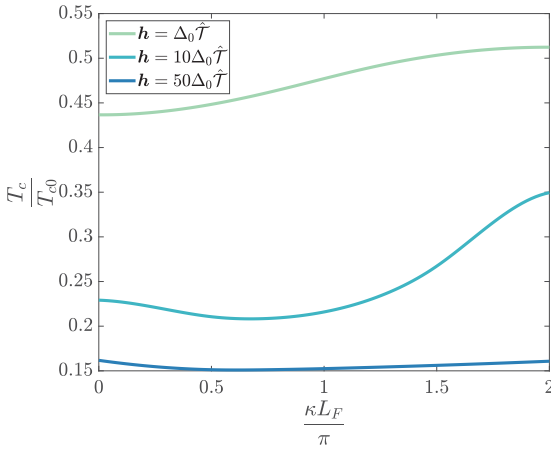


FIG. 4. Critical temperature of the system T_c divided by the critical temperature of the isolated superconductor T_{c0} as a function of curvature of the ferromagnet κ , for different values of the exchange field \mathbf{h} , with $L_S = 0.55\xi_0$, $L_F = 0.50\xi_0$, and zero spin-orbit coupling.

A. Spin-valve effect with curvature-induced SOC

We now consider the presence of curvature-induced spin-orbit coupling α_N . Since we previously saw that α_N is proportional to the curvature we can define it to be $\alpha_N = a\kappa$, with $a = \hbar\Lambda g|e|/4mc^2$. In Fig. 5 we plot T_c/T_{c0} as a function of κ for different lengths of the ferromagnet and four different values of the curvature-induced SOC proportionality constant a each, with $L_S = 0.55\xi_0$, $\mathbf{h} = 10\Delta_0\hat{T}$. Looking at the figure it is possible to note how the introduction of a finite a results in a rescaling of the $a = 0$ curves. As was noted in the previous section, in Eqs. (24a) to (24c) κ and α_N always appear together in a way that allows us to introduce an effective curvature $\tilde{\kappa} = \kappa + 2\alpha_N = \kappa(1 + 2a)$. Therefore,

the case of finite α_N can be considered as equivalent to the $a = 0$ case extended to higher curvatures. To make this more clear, in the inset of Fig. 5(b) we plot T_c/T_{c0} as a function of the curvature for κL_F ranging from 0 to 4π , for $L_S = 0.55\xi_0$, $L_F = 0.50\xi_0$, $\mathbf{h} = 10\Delta_0\hat{T}$, and $a = 0$. Comparing in Fig. 5(b) the $a = 0.5$ curve with the inset, we note that the two curves look equivalent, showing the effect quantitatively. This equivalency also shows that the weak proximity effect limit is a very good approximation to the full Usadel equation in this case.

We briefly note that the $a = 0$ curve was obtained by letting κ span from 0 to $4\pi L_F$ in the numerical calculations. This case is of course unrealistic since we cannot go over $\kappa = 2\pi L_F$ (closed ring), but it is useful for interpreting the results for $a \neq 0$. Another effect of the presence of the curvature-induced SOC is to broaden the variation over the curvature of T_c . This is not so evident in Fig. 5(a) for $L_F = 0.2\xi_0$, but in Fig. 5(b) for $L_F = 0.5\xi_0$ we note that for $a = 0.5$ the variation of the critical temperature is increased about 10%. Interestingly, we can see this effect also for the case $L_F = \xi_0$ in Fig. 5(c), where the superconductivity is quite weak: while for $a = 0$ the critical temperature undergoes a variation of $\sim 1\%$, if $a \neq 0$ it is possible to enlarge it, and for $a = 0.5$ we reach a change of $\sim 5\%$.

The effective curvature picture also helps to understand the second region of decreasing T_c in Figs. 5(a) and 5(b) for higher curvatures. In the same way as we defined an effective curvature, it is possible to define an effective exchange field (in Cartesian coordinates) $\tilde{\mathbf{h}} = h_0[-\sin(\kappa(1 + 2a)s), \cos(\kappa(1 + 2a)s), 0]$. This effective field has a smaller periodicity than the actual exchange field, which is 2π periodic, so if the geometric curvature is such that $\kappa L_F > 2\pi/(1 + 2a)$, the effective field will be parallel in any pair of points $s = u$ and $s' = L_F/(1 + 2a) + u$ with $u \in [0, 2aL_F/(1 + 2a)]$. Hence, at certain points in the ferromagnet, the triplet correlations will experience an effective exchange field pointing in the same direction, favoring a more robust spin precession. However, if κ is increased further, the relaxation term dominates again, suppressing the triplets and increasing T_c .

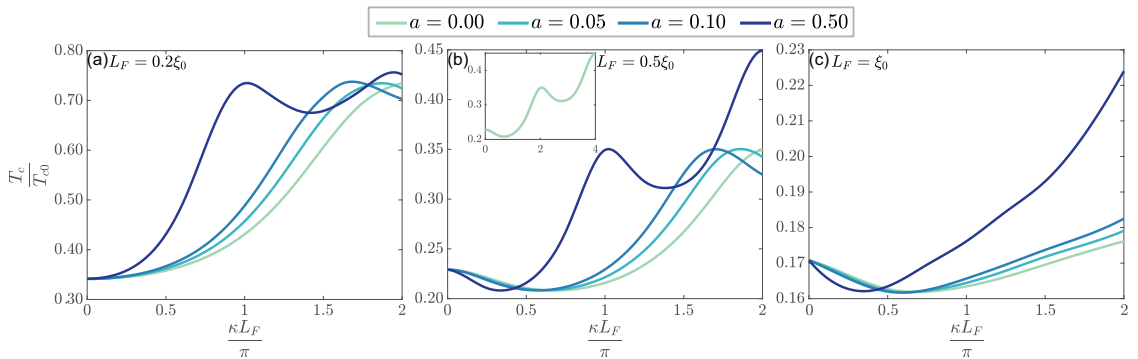


FIG. 5. Critical temperature of the system T_c divided by the critical temperature of the isolated superconductor T_{c0} as a function of curvature of the ferromagnet κ , for: (a) $L_F = 0.2\xi_0$, (b) $L_F = 0.5\xi_0$, (c) $L_F = \xi_0$, and different values of the curvature-induced spin-orbit proportionality constant a , with $L_S = 0.55\xi_0$, $L_F = 0.50\xi_0$, $\mathbf{h} = 10\Delta_0\hat{T}$, and $\alpha_B = 0$. The inset of (b) shows T_c/T_{c0} as a function of the curvature for $\kappa L_F/\pi$ values up to 4, for $\alpha_N = 0$.

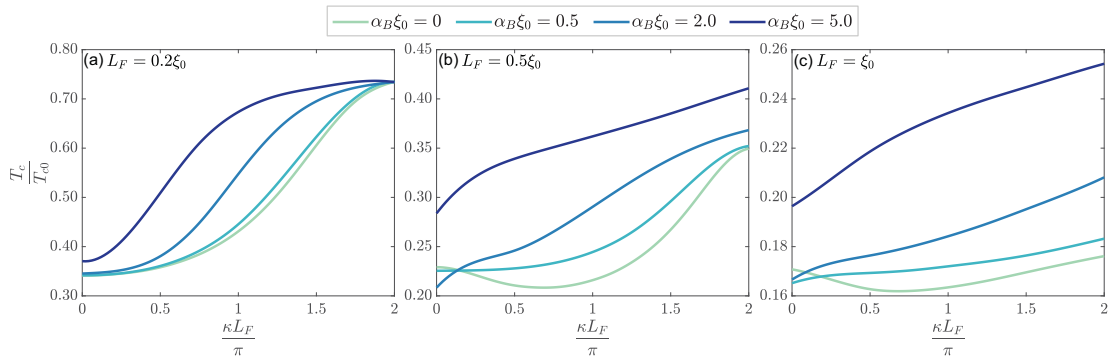


FIG. 6. Critical temperature of the system T_c divided by the critical temperature of the isolated superconductor T_{c0} as a function of curvature of the ferromagnet κ , for: (a) $L_F = 0.2\xi_0$, (b) $L_F = 0.5\xi_0$, (c) $L_F = \xi_0$, and different values of the intrinsic spin-orbit coupling α_B , with $L_S = 0.55\xi_0$, $\mathbf{h} = 10\Delta_0\hat{T}$, and $a = 0$.

B. Spin-valve effect with intrinsic SOC

Let us now neglect the curvature-induced SOC and focus only on the intrinsic term proportional to α_B . For the sake of completeness we note that this component of the spin-orbit coupling could also be induced extrinsically by generating an asymmetry in the confinement of the nanowire, for instance by an electric field pointing in the binormal direction.

In Fig. 6 we plot T_c/T_{c0} as a function of κ for different lengths of the ferromagnet and four different values of α_B each, with $L_S = 0.55\xi_0$, $\mathbf{h} = 10\Delta_0\hat{T}$. The overall effect of the inclusion of an intrinsic SOC $\alpha_B \neq 0$ is to increase the critical temperature of the system with respect to the $\alpha_B = 0$ curve, with the exception of the region of small κ . The different behavior close to $\kappa = 0$ may once again be understood in terms of the spin-precession and spin-relaxation mechanisms. For $L_F = 0.2\xi_0$ in Fig. 6(a), the length of the ferromagnet is so small that the spin precession is negligible. Hence, the addition of the intrinsic SOC simply intensifies the effect of the spin-relaxation term, suppressing the triplets and increasing T_c . On the other hand, for $L_F = 0.5\xi_0$ and $L_F = \xi_0$ in Figs. 6(b) and 6(c), where spin precession is not negligible anymore, at $\kappa = 0$ the critical temperature is decreased for values of $\alpha_B\xi_0$ up to 2, signaling that these values support a better singlet to triplet conversion compared to the $\alpha_B = 0$ case. However, when the SOC constant is big enough, $\alpha_B\xi_0 = 5$, we note a crossover: the contribution to the spin-relaxation term dominates over the spin precession, and the critical temperature is again increased. By comparison of Figs. 6(b) and 6(c) it can be seen that the range of values for which spin precession dominates over the spin relaxation is larger for the shorter wire: for $L_F = 0.5\xi_0$ at $\kappa = 0$ the critical temperature of the $\alpha_B\xi_0 = 2$ is smaller than the critical temperature of the $\alpha_B\xi_0 = 0.5$ curve, while the opposite is true for $L_F = \xi_0$.

In general, in Fig. 6 we note again that with the inclusion of SOC the critical temperature variation is broadened, although to a smaller extent with respect to the curvature-induced SOC, and the highest increase in the variation is about 5%. For instance, for $L_F = \xi_0$ in Fig. 6(c), the $\alpha_B = 0$ curve has a variation of $\sim 1\%$ while the $\alpha_B\xi_0 = 5$ curve has $\sim 6\%$. On the other hand, in Fig. 6(a) for $\alpha_B\xi_0 = 5$ the variation of T_c is

slightly reduced. Hence, the intrinsic SOC appears to be more advantageous for the improvement of the spin-valve effect if the ferromagnet is long rather than short.

C. Spin-valve effect with curvature-induced and intrinsic SOC

We conclude with an analysis of the case where both curvature-induced and intrinsic SOC are present. In Fig. 7 we plot T_c/T_{c0} as a function of κ for two values of the curvature-induced SOC proportionality constant a , each for four values of α_B , plotted together with the case of no SOC, with the parameters: $L_S = 0.55\xi_0$, $L_F = 0.5\xi_0$, $\mathbf{h} = 10\Delta_0\hat{T}$. Again we note a similar effect to the case of zero curvature-induced SOC: for small intrinsic SOC and curvature, the singlet-triplet conversion is favored, resulting in a smaller T_c with respect to the zero SOC case. Hence, at zero curvature between the values $\alpha_B\xi_0 = 0.5$ and $\alpha_B\xi_0 = 2$, we note a crossover from a case where T_c is diminished, to one where it is increased. In general, from Fig. 7 we see that increasing α_B progressively reduces the effects of the spin precession of the triplets, both for κ close to zero and close to the value where the periodicity of the effective exchange field mentioned above is met, until, we get a monotonic T_c vs κ dependence. This, for $a = 0.1$ in Fig. 7(a), can be seen at $\alpha_B\xi_0 = 2$, while for $a = 0.5$ in Fig. 7(b), happens around $\alpha_B\xi_0 = 5$.

V. DISCUSSION AND SUMMARY

The curvature-induced SOC constant normalized to the curvature $a = \alpha_N/\kappa$ depends primarily on two parameters: the deformation potential Λ and the effective mass m^* of the electrons. To obtain a rough estimate for the size of a we consider gallium manganese arsenide (Ga,Mn)As, a ferromagnetic semiconductor with effective mass $m^* \sim 0.09m_e$, where m_e is the bare electron mass [82]. Assuming that the deformation potential is similar to that in GaAs, $|e\Lambda| \sim 1$ to 10 eV [83], the resulting curvature-induced SOC constant in natural units is $a \sim 1 \times 10^{-5}$ to 1×10^{-4} , meaning that the effective curvature $\tilde{\kappa}$ is not significantly renormalized by the curvature-induced SOC in this case. Moreover, for the

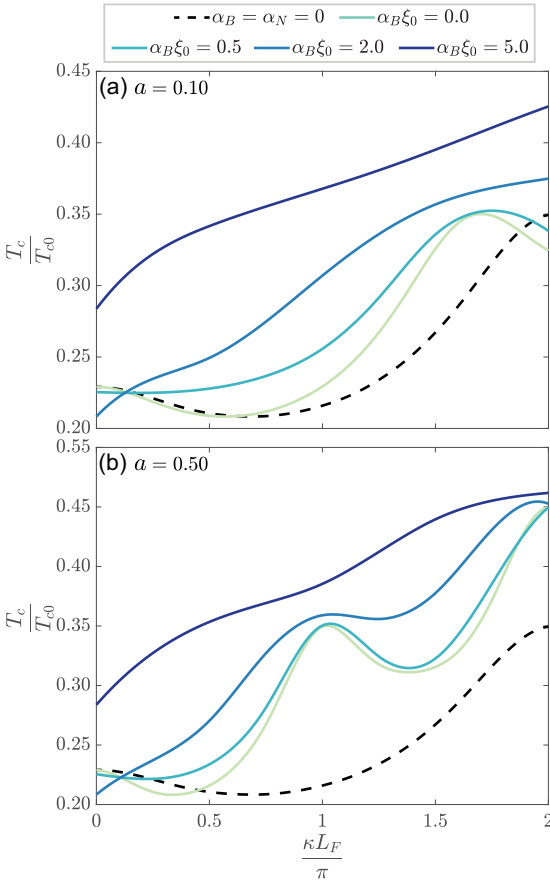


FIG. 7. Critical temperature of the system T_c divided by the critical temperature of the isolated superconductor T_{c0} as a function of curvature of the ferromagnet κ , for: (a) $a = 0.1$, (b) $a = 0.5$, and different values of the intrinsic spin-orbit coupling α_B compared to the case of zero SOC (black dashed curve), with $L_S = 0.55\xi_0$, $L_F = 0.5\xi_0$, $\hbar = 10\Delta_0\hat{\tau}$.

curvature-induced SOC to be significant Λ either has to be significantly larger than 1 eV or the effective mass has to be many orders of magnitude smaller than the electron mass, and a is therefore expected to be small for most materials following this analysis, in line with its relativistic origins. However, it is sometimes found that using the energy gap rather than the mass gap gives better estimates for the Rashba coefficient [84]. This would result in much larger values for α_N , possibly of the same order of magnitude as κ , and could therefore significantly affect the effective curvature $\tilde{\kappa}$. The precise magnitude of a is therefore difficult to predict. However, we point out that the main results do not rely on the size of a , as the effect of α_N is to boost the effect of the curvature, and does not introduce new effects.

We can also see that a wide range of values of $\alpha_B\xi_0/\hbar$ is in principle possible depending on the combination of ferromagnet and superconductor. The Rashba SOC strength varies greatly between materials, but typically lie in the range

TABLE I. Approximate exchange and anisotropy constants, and the resulting maximum curvature κ_c [26] for a few ferromagnetic materials at low temperatures.

Material	A (J/m)	$ K $ (J/m ³)	κ_c (nm ⁻¹)
Cobalt	$\sim 2 \times 10^{-11}$ [87]	$\sim 8 \times 10^5$ [88]	~ 0.1
Iron	$\sim 2 \times 10^{-11}$ [89,90]	$\sim 5 \times 10^4$ [90,91]	~ 0.03
Nickel	$\sim 1 \times 10^{-11}$ [90]	$\sim 1 \times 10^5$ [90,92]	~ 0.07

$\alpha_B m^*/\hbar \sim 1 \times 10^{-3}$ to 1×10^{-1} eV nm for semiconductors and heavy metals [84], meaning the dimensionless quantity $\alpha_B\xi_0/\hbar \sim 0.01-1 \xi_0[\text{nm}]m^*/m_e$. Estimating the diffusive coherence length $\xi_0 = \sqrt{l\bar{\xi}}$ using mean free path $l = 5$ nm and coherence lengths $\xi^{\text{Al}} = 1600$ nm and $\xi^{\text{Nb}} = 38$ nm for aluminum and niobium, respectively [65], we get $\xi_0^{\text{Al}} = 89$ nm and $\xi_0^{\text{Nb}} = 14$ nm, resulting in dimensionless Rashba coefficients $\alpha_B\xi_0/\hbar \sim 0.1-100 m^*/m_e$.

The curvature of the FM is expected to also affect the magnetic state [13], possibly inducing more complicated magnetization textures than a purely tangential field assumed in this study. SOC in general acts as a fieldlike torque on the spin [85], and thus geometric curvature, which acts as an effective SOC, would be expected to have a similar effect. However, Sheka *et al.* [26] showed theoretically for Heisenberg magnets that in a curved ferromagnetic wire with tangential uniaxial anisotropy, the magnetic ground state remained oriented in the tangential direction as long as the curvature was lower than a critical curvature $\kappa_c \approx 0.657\sqrt{|K|/A}$, where A and K are the exchange and anisotropy constants, respectively. The critical curvature is therefore inversely proportional to the domain wall length [86]. Assuming that a similar analysis is applicable also to metallic ferromagnets, one should use materials with strong uniaxial anisotropy to ensure a tangential exchange field. The critical curvatures, according to the results in Ref. [26], for a few ferromagnetic materials relevant for spintronics systems are given in Table I. Moreover, the effect of the curvature enters as the dimensionless constant κL_F , where the ferromagnet length is of the order of the superconducting coherence length. It is therefore likely beneficial to use superconductors with long coherence lengths in order to avoid curvature effects on the magnetization direction. For instance using $L_F = 0.5\xi_0^{\text{Al}}$, a half-circular wire results in a curvature $\kappa = \pi/L_F \approx 0.07 \text{ nm}^{-1}$, which is similar to the critical curvature of nickel, but below that of cobalt.

In summary, we have discussed the effects arising in geometrically curved diffusive nanostructures and presented a covariant formalism for the Usadel framework, allowing us to study an SF hybrid nanowire where the ferromagnet presents geometric curvature. By solving the Usadel equation we have calculated the critical temperature of the structure as a function of the geometric curvature, for various parameters, with and without spin-orbit coupling, which predicts the behavior for a broad range of possible material choices. We have found that our system presents promising characteristics for the realization of a superconducting spin valve: the critical temperature can be controlled by varying the curvature of the ferromagnet alone. For the right choice of parameters the critical temperature of the structure undergoes a consistent

variation when varying the curvature, up to 40% of the critical temperature of the bulk superconductor. Moreover, we have explored the effects of curvature-induced and intrinsic spin-orbit coupling and observed that in some cases their presence boosts the spin-valve effect. We also noted that analyzing the dependence of the critical temperature on the curvature can help understand how relevant the spin-orbit coupling is in the system. Furthermore, a possible extension of this study would be to consider the more general case of nonconstant curvature, which would modify the results quantitatively.

We have shown that geometric curvature alone can tune properties for which previously magnetic inhomogeneities or multiple spin-orbit coupling components were needed. Curvature control of the superconducting proximity effect and long-range triplet generation therefore open for many new possibilities in superconducting spintronics device designs and function. Realization and characterization of geometrically curved nanostructures, especially those including magnetic materials, is still in an early phase, so that many new possibilities are yet to be explored.

ACKNOWLEDGMENTS

We thank Mathias B. M. Svendsen for useful discussions and E. Rashba for helpful correspondence. The computations have been performed on the SAGA supercomputer provided by UNINETT Sigma2—the National Infrastructure for High Performance Computing and Data Storage in Norway. We acknowledge funding via the “Outstanding Academic Fellows” programme at NTNU, the Research Council of Norway Grant No. 302315, as well as through its Centres of Excellence funding scheme, Project No. 262633, “Center for Quantum Spintronics”.

APPENDIX: CURVILINEAR COORDINATE SYSTEMS

A vector in a three-dimensional curvilinear coordinate system can be described by the generalized coordinates q_α and basis vectors \mathbf{e}_α , with $\alpha = \{1, 2, 3\}$,

$$\mathbf{R} = q^\alpha \mathbf{e}_\alpha, \quad (\text{A1})$$

where the Einstein summation convention is used. From the above we see that the covariant basis vectors are given by

$$\mathbf{e}_\alpha = \partial_\alpha \mathbf{R}, \quad (\text{A2})$$

where we use the shorthand notation $\partial_\alpha = \partial/\partial q^\alpha$. In general the basis vectors are not orthogonal, and both the length and direction can vary in space [93]. The metric tensor is defined as

$$\hat{G}_{\alpha\beta} = \mathbf{e}_\alpha \cdot \mathbf{e}_\beta, \quad (\text{A3})$$

meaning the unit basis vectors are given by $\hat{\mathbf{e}}_\alpha = \mathbf{e}_\alpha/\sqrt{\hat{G}_{\alpha\alpha}}$. The contravariant basis vectors \mathbf{e}^α are related to the covariant basis vectors by $\mathbf{e}_\alpha \cdot \mathbf{e}^\beta = \delta_\alpha^\beta$.

The gradient of a scalar ϕ can be defined by considering the small change [69]

$$d\phi = \partial_\alpha \phi dq^\alpha = \partial_\alpha \phi \mathbf{e}^\alpha \cdot d\mathbf{R}, \quad (\text{A4})$$

where we have used $d\mathbf{R} = \mathbf{e}_\alpha dq^\alpha$ from Eq. (A1). In order to write the change in ϕ as

$$d\phi = \nabla \phi \cdot d\mathbf{R}, \quad (\text{A5})$$

we define the gradient operator [94]

$$\nabla = \mathbf{e}^\alpha \frac{\partial}{\partial q^\alpha} = \frac{\hat{\mathbf{e}}^\alpha}{\sqrt{\hat{G}_{\alpha\alpha}}} \partial_\alpha. \quad (\text{A6})$$

The fact that basis vectors can vary in space has consequences when considering the gradient of vectors. Considering the gradient of a contravariant vector $\mathbf{V} = V^\alpha \mathbf{e}_\alpha$, we get

$$\nabla \mathbf{V} = \mathbf{e}^\alpha \partial_\alpha V^\beta \mathbf{e}_\beta = \mathbf{e}^\alpha [(\partial_\alpha V^\beta) \mathbf{e}_\beta + V^\beta (\partial_\alpha \mathbf{e}_\beta)]. \quad (\text{A7})$$

Defining the Christoffel symbols of the second kind [93,94],

$$\Gamma_{\alpha\beta}^\gamma \mathbf{e}_\gamma = \partial_\beta \mathbf{e}_\alpha, \quad (\text{A8})$$

we get

$$\nabla_\alpha V^\beta = \partial_\alpha V^\beta + V^\gamma \Gamma_{\gamma\alpha}^\beta, \quad (\text{A9})$$

meaning the gradient of a vector can have additional terms in a general curvilinear coordinate system compared to, e.g., the Cartesian coordinate system.

From the relation between the covariant and contravariant basis vectors, we find an expression for the derivative of the contravariant basis vectors in terms of the Christoffel symbols [93],

$$\begin{aligned} 0 &= (\partial_\gamma \mathbf{e}_\alpha) \cdot \mathbf{e}^\beta + \mathbf{e}_\alpha \cdot (\partial_\gamma \mathbf{e}^\beta) \\ \Rightarrow \partial_\gamma \mathbf{e}^\beta &= -\Gamma_{\alpha\gamma}^\beta \mathbf{e}^\alpha. \end{aligned} \quad (\text{A10})$$

The gradient of a covariant vector is therefore given by

$$\nabla_\alpha V_\beta = \partial_\alpha V_\beta - V_\gamma \Gamma_{\alpha\beta}^\gamma. \quad (\text{A11})$$

In the main text we use the notation D_α for the gradient of covariant vector components to highlight the distinction from the gradient in a Cartesian coordinate system.

The Christoffel symbols can be expressed in terms of the metric as [93,94]

$$\Gamma_{\alpha\beta}^\gamma = \frac{1}{2} \hat{G}^{\gamma\lambda} [\partial_\beta \hat{G}_{\alpha\lambda} + \partial_\alpha \hat{G}_{\lambda\beta} - \partial_\lambda \hat{G}_{\alpha\beta}], \quad (\text{A12})$$

where we see that $\Gamma_{\alpha\beta}^\gamma$ is invariant when $\alpha \leftrightarrow \beta$.

Due to the variation of the length of the basis vectors in space, the components V_α of a vector do not necessarily have the correct physical dimensions. We therefore introduce the physical vector components

$$V_{(\alpha)} = \hat{\mathbf{e}}_\alpha \cdot \mathbf{V} = \frac{V_\alpha}{\sqrt{\hat{G}_{\alpha\alpha}}}. \quad (\text{A13})$$

In Cartesian coordinates the metric is the identity matrix, and therefore the notion of physical vector components is not necessary.

In the local coordinate system following a space curve parametrized by the arclength s as $\mathbf{r}(s)$, we can define a vector

$$\mathbf{R} = \mathbf{r}(s) + n\hat{\mathcal{N}}(s) + b\hat{\mathcal{B}}(s), \quad (\text{A14})$$

where $\hat{\mathcal{N}}$ and $\hat{\mathcal{B}}$ are the directions normal and binormal to the tangent $\hat{\mathcal{T}} = \partial_s \mathbf{r}$ of the curve at s , namely $\hat{\mathcal{N}} = \partial_s \hat{\mathcal{T}}/\kappa(s)$ and $\hat{\mathcal{B}} = \hat{\mathcal{T}} \times \hat{\mathcal{N}}$, with $\kappa = |\partial_s \hat{\mathcal{T}}|$. The derivatives of the tangent, normal and binormal vectors are related by the Frenet-Serret equations of motion in Eq. (2) in the absence of torsion.

The covariant basis vectors are then given by

$$\mathbf{e}_t = \partial_s \mathbf{R} = \eta(s, n) \hat{\mathcal{T}}, \quad (\text{A15a})$$

$$\mathbf{e}_n = \frac{\partial \mathbf{R}}{\partial n} = \hat{\mathcal{N}}, \quad (\text{A15b})$$

$$\mathbf{e}_b = \frac{\partial \mathbf{R}}{\partial b} = \hat{\mathcal{B}}, \quad (\text{A15c})$$

where we have defined $\eta(s, n) = 1 - n\kappa(s)$, and use the subscript t, n, b for the tangential, normal, and binormal components respectively. Using Eq. (A3) and the above basis vectors, we get the metric given in Eq. (3). Note that by definition the basis vectors are orthogonal, as seen by the diagonal form of the metric, but only \mathbf{e}_n and \mathbf{e}_b are always unit basis vectors.

The only nonzero derivatives of the elements of metric are $\partial_s \mathcal{G}_{tt} = 2\eta \partial_s \eta$ and $\partial_n \mathcal{G}_{tt} = 2\eta \partial_n \eta$, resulting in the Christoffel symbols [64]

$$\Gamma_{tt}^t = \frac{\partial_s \eta(s, n)}{\eta(s, n)}, \quad (\text{A16a})$$

$$\Gamma_{tt}^n = -\eta(s, n) \partial_n \eta(s, n), \quad (\text{A16b})$$

$$\Gamma_{tn}^t = \frac{\partial_n \eta(s, n)}{\eta(s, n)}. \quad (\text{A16c})$$

The physical components of a vector \mathbf{V} are given by

$$V_{T,N,B} = \mathbf{V} \cdot \{\hat{\mathcal{T}}, \hat{\mathcal{N}}, \hat{\mathcal{B}}\}, \quad (\text{A17})$$

where we use uppercase indexes to denote the physical components.

-
- [1] O. G. Schmidt and K. Eberl, *Nature (London)* **410**, 168 (2001).
- [2] P. Cendula, S. Kiravittaya, Y. F. Mei, C. Deneke, and O. G. Schmidt, *Phys. Rev. B* **79**, 085429 (2009).
- [3] S. Xu, Z. Yan, K.-I. Jang, W. Huang, H. Fu, J. Kim, Z. Wei, M. Flavin, J. McCracken, R. Wang, A. Badea, Y. Liu, D. Xiao, G. Zhou, J. Lee, H. U. Chung, H. Cheng, W. Ren, A. Banks, X. Li *et al.*, *Science* **347**, 154 (2015).
- [4] E. R. Lewis, D. Petit, L. Thevenard, A. V. Jausovec, L. O'Brien, D. E. Read, and R. P. Cowburn, *Appl. Phys. Lett.* **95**, 152505 (2009).
- [5] D. M. Burn, M. Chadha, S. K. Walton, and W. R. Branford, *Phys. Rev. B* **90**, 144414 (2014).
- [6] O. M. Volkov, A. Kákay, F. Kronast, I. Mönch, M.-A. Mawass, J. Fassbender, and D. Makarov, *Phys. Rev. Lett.* **123**, 077201 (2019).
- [7] G. Williams, M. Hunt, B. Boehm, A. May, M. Taverne, D. Ho, S. Giblin, D. Read, J. Rarity, R. Allenspach, and S. Ladak, *Nano Res.* **11**, 845 (2018).
- [8] J. Askey, M. O. Hunt, W. Langbein, and S. Ladak, *Nanomaterials* **10**, 429 (2020).
- [9] B. Dick, M. J. Brett, T. J. Smy, M. R. Freeman, M. Malac, and R. F. Egerton, *J. Vac. Sci. Technol. A* **18**, 1838 (2000).
- [10] B. Kundys, *Appl. Phys. Rev.* **2**, 011301 (2015).
- [11] S. Matzen, L. Guillemot, T. Maroutian, S. K. K. Patel, H. Wen, A. D. DiChiara, G. Agnus, O. G. Shpyrko, E. E. Fullerton, D. Ravelosona, P. Lecoeur, and R. Kukreja, *Adv. Electron. Mater.* **5**, 1800709 (2019).
- [12] L. Guillemeney, L. Lermusiaux, G. Landaburu, B. Wagnon, and B. Abécassis, *Commun. Chem.* **5**, 7 (2022).
- [13] R. Streubel, P. Fischer, F. Kronast, V. P. Kravchuk, D. D. Sheka, Y. Gaididei, O. G. Schmidt, and D. Makarov, *J. Phys. D* **49**, 363001 (2016).
- [14] D. D. Sheka, *Appl. Phys. Lett.* **118**, 230502 (2021).
- [15] R. Streubel, E. Y. Tsymbal, and P. Fischer, *J. Appl. Phys.* **129**, 210902 (2021).
- [16] D. D. Sheka, O. V. Pylypovskiy, P. Landeros, Y. Gaididei, A. Kákay, and D. Makarov, *Commun. Phys.* **3**, 128 (2020).
- [17] Y. Gaididei, V. P. Kravchuk, and D. D. Sheka, *Phys. Rev. Lett.* **112**, 257203 (2014).
- [18] S. Vojkovic, V. L. Carvalho-Santos, J. M. Fonseca, and Á. S. Núñez, *J. Appl. Phys.* **121**, 113906 (2017).
- [19] A. W. Teixeira, S. Castillo-Sepúlveda, S. Vojkovic, J. M. Fonseca, D. Altbir, Á. S. Núñez, and V. L. Carvalho-Santos, *J. Magn. Magn. Mater.* **478**, 253 (2019).
- [20] J. A. Otálora, J. A. López-López, P. Vargas, and P. Landeros, *Appl. Phys. Lett.* **100**, 072407 (2012).
- [21] D. Mancilla-Almonacid, M. Castro, J. Fonseca, D. Altbir, S. Allende, and V. Carvalho-Santos, *J. Magn. Magn. Mater.* **507**, 166754 (2020).
- [22] V. Carvalho-Santos, F. Apolonio, and N. Oliveira-Neto, *Phys. Lett. A* **377**, 1308 (2013).
- [23] O. M. Volkov, D. D. Sheka, Y. Gaididei, V. P. Kravchuk, U. K. Röbler, J. Fassbender, and D. Makarov, *Sci. Rep.* **8**, 866 (2018).
- [24] O. V. Pylypovskiy, D. Y. Kononenko, K. V. Yershov, U. K. Röbler, A. V. Tomilo, J. Fassbender, J. van den Brink, D. Makarov, and D. D. Sheka, *Nano Lett.* **20**, 8157 (2020).
- [25] V. P. Kravchuk, D. D. Sheka, R. Streubel, D. Makarov, O. G. Schmidt, and Y. Gaididei, *Phys. Rev. B* **85**, 144433 (2012).
- [26] D. D. Sheka, V. P. Kravchuk, and Y. Gaididei, *J. Phys. A: Math. Theor.* **48**, 125202 (2015).
- [27] G. Cantele, D. Ninno, and G. Iadonisi, *Phys. Rev. B* **61**, 13730 (2000).
- [28] H. Aoki, M. Koshino, D. Takeda, H. Morise, and K. Kuroki, *Phys. Rev. B* **65**, 035102 (2001).
- [29] M. Encinosa and L. Mott, *Phys. Rev. A* **68**, 014102 (2003).
- [30] C. Ortix and J. van den Brink, *Phys. Rev. B* **81**, 165419 (2010).
- [31] J.-S. Jeong, J. Shin, and H.-W. Lee, *Phys. Rev. B* **84**, 195457 (2011).
- [32] P. Gentile, M. Cuoco, and C. Ortix, *SPIN* **03**, 1340002 (2013).
- [33] Y.-L. Wang, H. Jiang, and H.-S. Zong, *Phys. Rev. A* **96**, 022116 (2017).
- [34] F. Nagasawa, D. Frustaglia, H. Saarikoski, K. Richter, and J. Nitta, *Nat. Commun.* **4**, 2526 (2013).
- [35] P. Gentile, M. Cuoco, and C. Ortix, *Phys. Rev. Lett.* **115**, 256801 (2015).
- [36] Z.-J. Ying, P. Gentile, C. Ortix, and M. Cuoco, *Phys. Rev. B* **94**, 081406(R) (2016).
- [37] Z.-J. Ying, M. Cuoco, C. Ortix, and P. Gentile, *Phys. Rev. B* **96**, 100506(R) (2017).
- [38] C.-H. Chang and C. Ortix, *Nano Lett.* **17**, 3076 (2017).

- [39] A. M. Turner, V. Vitelli, and D. R. Nelson, *Rev. Mod. Phys.* **82**, 1301 (2010).
- [40] G. Francica, M. Cuoco, and P. Gentile, *Phys. Rev. B* **101**, 094504 (2020).
- [41] A. G. Kutlin and A. S. Mel'nikov, *Phys. Rev. B* **101**, 045418 (2020).
- [42] P.-H. Chou, C.-H. Chen, S.-W. Liu, C.-H. Chung, and C.-Y. Mou, *Phys. Rev. B* **103**, 014508 (2021).
- [43] H. Imamura, P. Bruno, and Y. Utsumi, *Phys. Rev. B* **69**, 121303(R) (2004).
- [44] K.-W. Kim, H.-W. Lee, K.-J. Lee, and M. D. Stiles, *Phys. Rev. Lett.* **111**, 216601 (2013).
- [45] A. Kundu and S. Zhang, *Phys. Rev. B* **92**, 094434 (2015).
- [46] T. Salamone, M. B. M. Svendsen, M. Amundsen, and S. Jacobsen, *Phys. Rev. B* **104**, L060505 (2021).
- [47] M. Eschrig, *Phys. Today* **64**(1), 43 (2011).
- [48] J. Linder and J. W. A. Robinson, *Nat. Phys.* **11**, 307 (2015).
- [49] F. S. Bergeret, A. F. Volkov, and K. B. Efetov, *Rev. Mod. Phys.* **77**, 1321 (2005).
- [50] A. I. Buzdin, *Rev. Mod. Phys.* **77**, 935 (2005).
- [51] I. F. Lyuksyutov and V. L. Pokrovsky, *Adv. Phys.* **54**, 67 (2005).
- [52] F. S. Bergeret, A. F. Volkov, and K. B. Efetov, *Phys. Rev. Lett.* **86**, 4096 (2001).
- [53] J. W. A. Robinson, J. D. S. Witt, and M. G. Blamire, *Science* **329**, 59 (2010).
- [54] T. S. Khaire, M. A. Khasawneh, W. P. Pratt, and N. O. Birge, *Phys. Rev. Lett.* **104**, 137002 (2010).
- [55] F. S. Bergeret and I. V. Tokatly, *Phys. Rev. Lett.* **110**, 117003 (2013).
- [56] F. S. Bergeret and I. V. Tokatly, *Phys. Rev. B* **89**, 134517 (2014).
- [57] S. Oh, D. Youm, and M. R. Beasley, *Appl. Phys. Lett.* **71**, 2376 (1997).
- [58] L. R. Tagirov, *Phys. Rev. Lett.* **83**, 2058 (1999).
- [59] A. I. Buzdin, A. V. Vedyayev, and N. V. Ryzhanova, *Europhys. Lett.* **48**, 686 (1999).
- [60] J. Y. Gu, C.-Y. You, J. S. Jiang, J. Pearson, Y. B. Bazaliy, and S. D. Bader, *Phys. Rev. Lett.* **89**, 267001 (2002).
- [61] A. Potenza and C. H. Marrows, *Phys. Rev. B* **71**, 180503(R) (2005).
- [62] S. H. Jacobsen, J. A. Ouassou, and J. Linder, *Phys. Rev. B* **92**, 024510 (2015).
- [63] N. Banerjee, J. A. Ouassou, Y. Zhu, N. A. Stelmashenko, J. Linder, and M. G. Blamire, *Phys. Rev. B* **97**, 184521 (2018).
- [64] M. B. M. Svendsen, Master thesis, Norwegian University of Science and Technology (NTNU), 2021.
- [65] C. Kittel, *Introduction to Solid State Physics*, 8th ed. (Wiley, Hoboken, NJ, 2005).
- [66] C. Ortix, S. Kiravittaya, O. G. Schmidt, and J. van den Brink, *Phys. Rev. B* **84**, 045438 (2011).
- [67] J. Bardeen and W. Shockley, *Phys. Rev.* **80**, 72 (1950).
- [68] C. G. Van de Walle, *Phys. Rev. B* **39**, 1871 (1989).
- [69] D. J. Griffiths, *Introduction to Electrodynamics*, 4th ed. (Pearson, London, 2013).
- [70] V. P. Mineev and G. E. Volovik, *J. Low Temp. Phys.* **89**, 823 (1992).
- [71] J. Fröhlich and U. M. Studer, *Rev. Mod. Phys.* **65**, 733 (1993).
- [72] H. Jensen and H. Koppe, *Ann. Phys.* **63**, 586 (1971).
- [73] R. C. T. da Costa, *Phys. Rev. A* **23**, 1982 (1981).
- [74] C. Ortix, *Phys. Rev. B* **91**, 245412 (2015).
- [75] K. D. Usadel, *Phys. Rev. Lett.* **25**, 507 (1970).
- [76] W. Belzig, F. K. Wilhelm, C. Bruder, G. Schön, and A. D. Zaikin, *Superlattices Microstruct.* **25**, 1251 (1999).
- [77] M. Y. Kuprianov and V. Lukichev, *Zh. Eksp. Teor. Fiz.* **94**, 149 (1988) [*Sov. Phys. JETP* **67**, 1163 (1988)].
- [78] N. Schopohl and K. Maki, *Phys. Rev. B* **52**, 490 (1995).
- [79] For a finite α_N we have the condition $(\kappa + 2\alpha_N)L_F \sim 2$.
- [80] J. A. Ouassou, A. Di Bernardo, J. W. A. Robinson, and J. Linder, *Sci. Rep.* **6**, 29312 (2016).
- [81] J. A. Ouassou, Geneus, GitHub repository (2018), <https://github.com/jabirali/geneus>.
- [82] S. Ohya, K. Takata, and M. Tanaka, *Nat. Phys.* **7**, 342 (2011).
- [83] R. A. Mair, R. Prepost, E. L. Garwin, and T. Maruyama, *Phys. Lett. A* **239**, 277 (1998).
- [84] A. Manchon, H. C. Koo, J. Nitta, S. M. Frolov, and R. A. Duine, *Nat. Mater.* **14**, 871 (2015).
- [85] S. H. Jacobsen, I. Kulagina, and J. Linder, *Sci. Rep.* **6**, 23926 (2016).
- [86] M. E. Schabes and H. N. Bertram, *J. Appl. Phys.* **64**, 1347 (1988).
- [87] G. S. Abo, Y.-K. Hong, J. Park, J. Lee, W. Lee, and B.-C. Choi, *IEEE Trans. Magn.* **49**, 4937 (2013).
- [88] D. M. Paige, B. Szpunar, and B. K. Tanner, *J. Magn. Magn. Mater.* **44**, 239 (1984).
- [89] P. Vavassori, D. Biserio, F. Carace, A. di Bona, G. C. Gazzadi, M. Liberati, and S. Valeri, *Phys. Rev. B* **72**, 054405 (2005).
- [90] K. Niitsu, *J. Phys. D* **53**, 39LT01 (2020).
- [91] C. Graham Jr., *Phys. Rev.* **112**, 1117 (1958).
- [92] J. J. M. Franse and G. De Vries, *Physica* **39**, 477 (1968).
- [93] P. A. Kelly, in *Mechanics Lecture Notes Part III: Foundations of Continuum Mechanics* (University of Auckland, Auckland, 2021), Chap. 1, pp. 135–159.
- [94] B. R. Kusse and E. A. Westwig, in *Mathematical Physics: Applied Mathematics for Scientists and Engineers* (Wiley-VCH, Berlin, 2006), Chap. F, pp. 655–659.




III

REFERENCE

T. Salamone, H. G. Hugdal, S. H. Jacobsen, and M. Amundsen,
High magnetic field superconductivity in a two-band superconductor.
Physical Review B **107**, 174516 (2023)

CONTRIBUTIONS

MA and SHJ initiated and supervised the project. TS contributed to analytical calculations, to the writing of the manuscript and performed numerical simulations. HGH contributed to analytical calculations and numerical simulations. MA and SHJ contributed to analytical and numerical results. All authors contributed to discussions and revisions of the manuscript.

High magnetic field superconductivity in a two-band superconductorTancredi Salamone ¹, Henning G. Hugdal ¹, Sol H. Jacobsen,¹ and Morten Amundsen ²¹*Center for Quantum Spintronics, Department of Physics, NTNU, Norwegian University of Science and Technology, NO-7491 Trondheim, Norway*²*Nordita, KTH Royal Institute of Technology and Stockholm University, Hannes Alfvéns väg 12, SE-106 91 Stockholm, Sweden*

(Received 8 August 2022; revised 8 March 2023; accepted 12 May 2023; published 19 May 2023)

We present a mechanism allowing for superconductivity at high magnetic fields, beyond the Pauli-Chandrasekhar-Clogston limit. We consider spin splitting induced by an in-plane external magnetic field in a superconductor with two relevant bands close to the Fermi level. The magnetic field therefore controls which bands are available for Cooper pair formation. The presence of interband superconducting pairing, i.e., Cooper pairs formed by electrons with different band indices, produces high-field reentrant superconducting domains, whose critical magnetic field violates the Pauli-Chandrasekhar-Clogston limit. We analyze how the interband superconducting domains are influenced by the band parameters, and show that, for a certain range of parameters, the system presents two separate superconducting regions, for low and high magnetic field.

DOI: [10.1103/PhysRevB.107.174516](https://doi.org/10.1103/PhysRevB.107.174516)**I. INTRODUCTION**

Over the past two decades, multiband superconductors have been attracting great interest because of increasing experimental evidence of interesting effects not achievable in single-band systems. For instance, in the first-ever discovered multiband superconductor, MgB₂, Leggett modes have been observed [1] and more recently optically controlled [2]. Moreover, spontaneous time reversal symmetry breaking has been reported in Ba_{1-x}K_xFe₂As₂, Sr₂RuO₄, UPt₃ and many other multiband systems (for an exhaustive review see [3]).

Since the extension of the Bardeen-Cooper-Schrieffer (BCS) theory to multiband systems by Suhl, Matthias and Walker [4] and Moskalenko [5], many studies have focused on a theoretical understanding of the effects of a multiband description of superconductors [6–17]. In general, if two bands are close to each other or hybridized, it is possible to form interband Cooper pairs (see, e.g., [18]), where the electrons comprising the pairs come from two distinct bands. Research on interband pairing has been rather limited, but studies have found that it affects Josephson tunneling [7], it is an important factor in obtaining an anomalous Hall effect [19], it can produce gapless states [13], and it influences the BCS-BEC crossover [20]. We note that, in the context of this work, the term interband will always refer to Cooper pairs formed by electrons in distinct bands, and it must not be confused with the same term often found in the literature, also called pair-hopping, referring to the hopping of intraband pairs, i.e., formed by electrons in the same band, between different bands.

Among multiband superconductors, MgB₂ and Fe-based superconductors (FeBS) are particularly interesting because of their high critical temperatures and critical magnetic fields. For instance, the critical temperature is 39 K for MgB₂ [21], 55 K for SmO_{1-x}F_xFeAs [22], and 65 K in FeSe films on SrTiO₃ substrate [23], whereas the zero temperature estimated

values of the critical field are 25 T in single crystal MgB₂ [24], 70 T in C-doped MgB₂ thin films [25], and up to 300 T in FeBS [26–31]. It is worth noting, however, that these values are often extrapolated from low-magnetic field data obtained close to the critical temperature. Therefore, the extrapolated low-temperature dependence of the critical field and its $T = 0$ value may be a bad estimate. However, the application of pulsed fields allows one to reach higher magnetic field values and obtain more reliable estimations [30].

The simultaneous presence of superconductivity and magnetism is of great interest for the field of superconducting spintronics [32] where the proximity effect is exploited to achieve dissipationless information transport. However, these two phenomena are often mutually exclusive since two effects contribute to destroying superconductivity when an external magnetic field is applied: the orbital and Pauli paramagnetic pair-breaking effects [33,34]. The orbital effect describes the breaking of Cooper pairs when the kinetic energy of electrons, resulting from the momentum acquired in a magnetic field, exceeds the superconducting gap. On the other hand, paramagnetic pair breaking occurs when Cooper pairing becomes energetically unfavorable as the Zeeman energy of the electrons overcomes the superconducting gap. This happens when the exchange energy reaches a value given by the Pauli, or equivalently the Chandrasekhar-Clogston, limit $h_c = \Delta_0/\sqrt{2} = 1.86T_c$, where Δ_0 is the value of the superconducting gap at zero temperature and zero applied field, and T_c is the superconducting critical temperature.

Various mechanisms producing the limit violation, or enhancement of critical fields have been proposed, e.g., scattering by nonmagnetic impurities [35,36], spin-triplet superconductivity [37], Fulde-Ferrell-Larkin-Ovchinnikov (FFLO) pairing [38,39], strong superconducting coupling, spin-orbit coupling [40,41], application of a voltage bias [42,43], the proximity of two bands to each other [44–46], and pair hopping in three-band superconductors [47,48]. Furthermore,

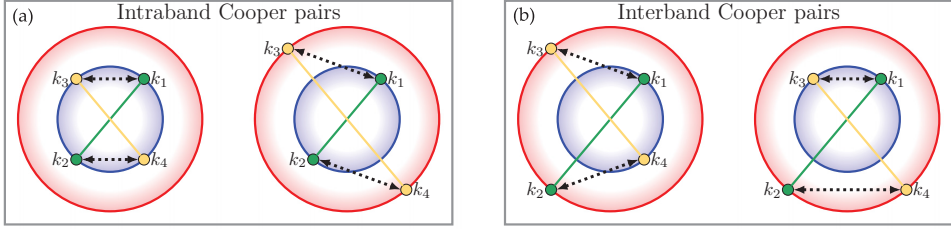


FIG. 1. Illustration of some of the superconducting pairing processes possible in a two-band system for (a) intraband and (b) interband Cooper pairs. The red and blue circles represent the Fermi surfaces of the two bands, the green and yellow lines identify the electrons forming the Cooper pairs, and the dotted lines indicate the scattering processes.

many experimental works have reported evidence for critical magnetic field violating the above limits in multiple superconductors, e.g., NbSe₂ [40,49], iron pnictides [50,51], lanthanide infinite-layer nickelate [52], moiré graphene [53], organic superconductors [54,55], Eu-Sn molybdenum chalcogenide [56], and URhGe [57]. References [53–57] are particularly interesting for the purpose of this work because their results present two disconnected superconducting domains, for small and large external magnetic field, due to non-spin-singlet Cooper pairs in Ref. [53] and to the Jaccarino-Peter effect in Refs. [54–56].

In this work, we present a simple mechanism which allows one to overcome the conventional limit. We consider a two-band *s*-wave superconductor in the presence of an in-plane external magnetic field, producing Zeeman splitting. We obtain the critical magnetic field by the paramagnetic pair-breaking effect and demonstrate that the inclusion of interband pairing allows one to overcome the limiting value of the critical field found in conventional superconductors. Within a BCS framework we show that for a certain range of parameters, our system exhibits superconductivity for significantly high values of the external magnetic field. Furthermore, we show that the system can exhibit two separate superconducting domains, for small and large external magnetic field, and we provide an explanation of the mechanism producing these results.

II. THEORY

We consider a two-band superconducting thin film with both intra- and interband spin-singlet superconducting coupling, and an in-plane external magnetic field producing Zeeman splitting. We ignore orbital pair-breaking effects and assume the system does not experience any magnetic flux. The mean-field Hamiltonian of the system is the

following:

$$\begin{aligned} \mathcal{H} = & \sum_{k\sigma} (\xi_k^{(1)} - E_c - \sigma h) c_{k\sigma}^{(1)\dagger} c_{k\sigma}^{(1)} \\ & + \sum_{k\sigma} (\xi_k^{(2)} + E_c - \sigma h) c_{k\sigma}^{(2)\dagger} c_{k\sigma}^{(2)} \\ & - \sum_k \sum_{\alpha,\alpha'=1,2} (\Delta_{\alpha\alpha'}(\mathbf{k}) c_{k\uparrow}^{(\alpha)\dagger} c_{-k\downarrow}^{(\alpha')\dagger} + \text{H.c.}), \end{aligned} \quad (1)$$

where the operator $c_{k\sigma}^{(\alpha)\dagger}$ ($c_{k\sigma}^{(\alpha)}$) creates (destroys) an electron in band α with dispersion $\xi_k^{(\alpha)} = \varepsilon_k^\alpha - \mu$ and spin σ , E_c is half the band separation, and h is the externally applied in-plane magnetic field. We note that the Hamiltonian in Eq. (1) is a generalization to a two-band spin-split superconductor of the one presented in Ref. [58] for a single band. The superconducting order parameters $\Delta_{\alpha\alpha'}(\mathbf{k})$ are defined by

$$\Delta_{\alpha\alpha'}(\mathbf{k}) = \frac{T}{V} \sum_{\omega_n} \sum_{\beta,\beta'=1,2} \sum_{\mathbf{k}'} g_{\alpha\alpha',\beta\beta'}(\mathbf{k},\mathbf{k}') F^{\beta\beta'}(\mathbf{k}',\omega_n), \quad (2)$$

where $\omega_n = (2n+1)\pi/\beta$ is the fermionic Matsubara frequency and $F^{\beta\beta'}$ is the anomalous component of the Green's function.

The superconducting coupling matrix $g_{\alpha\alpha',\beta\beta'}(\mathbf{k},\mathbf{k}')$ defines the different coupling processes, and the terms $g_{\alpha\alpha,\alpha'\alpha'}$ describe processes involving intraband Cooper pairs formed by electrons in the same band, hopping between the same band ($\alpha = \alpha'$) or different bands ($\alpha \neq \alpha'$). This last term is often referred to in the literature as interband scattering, or pair hopping, and must not be confused with the use we make of the term interband. Processes involving interband pairs instead are described by those elements $g_{\alpha\alpha',\beta\beta'}$ with $\alpha \neq \alpha'$ and/or $\beta \neq \beta'$. The superconducting pairing processes relevant for the purpose of this work are illustrated in Fig. 1 for a two-band system.

The terms Δ_{11} and Δ_{22} represent the intraband order parameters, while $\Delta_{12} = \Delta_{21}$ is the interband order parameter. In the basis defined by $\hat{\psi}_{\mathbf{k}}^\dagger = (c_{k\uparrow}^{(1)\dagger}, c_{-k\downarrow}^{(1)}, c_{k\uparrow}^{(2)\dagger}, c_{-k\downarrow}^{(2)})$ the inverse Green's function for the Hamiltonian of Eq. (1) is

$$\mathcal{G}_0^{-1} = \begin{pmatrix} (i\omega_n + h)\hat{\tau}_0 - \tilde{\xi}_1\hat{\tau}_3 + \Delta_{11}\hat{\tau}_1 & \Delta_{12}\hat{\tau}_1 \\ \Delta_{12}\hat{\tau}_1 & (i\omega_n + h)\hat{\tau}_0 - \tilde{\xi}_2\hat{\tau}_3 + \Delta_{22}\hat{\tau}_1 \end{pmatrix}, \quad (3)$$

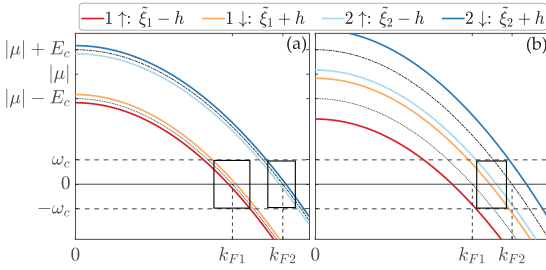


FIG. 2. Band structure of the system in the presence of an exchange field, for (a) small and (b) large values of the field and generic values of E_c , γ , ω_c , μ . The rectangles indicate the regions where Cooper pair formation can occur.

where $\tilde{\xi}_1 = \xi_k^{(1)} - E_c$, $\tilde{\xi}_2 = \xi_k^{(2)} + E_c$, and we restricted to s -wave pairing (real order parameter). The two branches of the BCS quasiparticle excitation spectrum, E_+ and E_- , are obtained by defining $\det \mathcal{G}_0^{-1} \equiv (\tilde{\omega}_n^2 + E_+^2)(\tilde{\omega}_n^2 + E_-^2)$, where $\tilde{\omega}_n = \omega_n - ih$. Inverting Eq. (3) we obtain the Green's function of the system which allows us to analyze when superconductivity occurs. Details of the form of the Greens function are given in Appendix A.

III. RESULTS

We consider a two-band system with spin-split holelike parabolic bands: $\xi_k^{(\alpha)} = -k^2/(2m_\alpha) - \mu$ with m_α the effective mass of the band α and μ the chemical potential. Defining the ratio between the two band masses as $\gamma = m_1/m_2$ we can write $\xi_k^{(2)} = \gamma \xi_k^{(1)} + (\gamma - 1)\mu$. The band structure of the system for generic values of E_c , γ , μ , and two different limits of h is represented in Fig. 2, where we also show the energy cutoff of the effective attractive interaction ω_c . By examining the case of small spin splitting represented in Fig. 2(a), we note that intraband pairing is favored, since bands with the same band index and opposite spin are close to each other. On the other hand, the presence of a large spin-splitting field can bring two bands with different band and spin indices closer to each other, favoring an interband pairing mechanism, as shown in Fig. 2(b).

To simplify the problem, we neglect those scattering processes connecting interband to intraband Cooper pairs and vice versa, i.e., we set $g_{\alpha\alpha,\alpha\beta} = g_{\alpha\beta,\alpha\alpha} = 0$ with $\alpha \neq \beta$. This simplification is justified by the fact that, for sufficiently large E_c , either interband or intraband pairing processes will dominate over the other, depending on h and γ . Simultaneously, the processes of intraband pair hopping in interband pairs, or vice versa, are either forbidden due to energy or momentum conservation, or strongly suppressed compared to the nonmixing processes, since they would meet energy and momentum conservation criteria for significantly smaller ranges.

With these simplifications, from Eq. (2), it is clear that the gap equation for the intraband and interband order parameters are decoupled and we can solve them separately. We set the chemical potential μ as the energy scale and choose the energy cutoff for the effective attractive interaction and the band separation to be $\omega_c = 0.2|\mu|$ and $E_c =$

$0.05|\mu|$, respectively. Furthermore, we consider dimensionless superconducting coupling constants: $\lambda_{\alpha\beta}^{\text{intra}} = N_\alpha(0)g_{\alpha\alpha,\beta\beta}$ and $\lambda^{\text{inter}} = N_1(0)g_{\alpha\beta,\alpha\beta}$, ($\alpha \neq \beta$), where $N_\alpha(0)$ is the density of states at the Fermi energy for the band α . Their values are chosen to be $\lambda_{11}^{\text{intra}} = 0.3$, $\lambda^{\text{inter}} = \lambda_{22}^{\text{intra}} = 2\lambda_{12}^{\text{intra}} = 0.2$. We assume that λ^{inter} can be taken to be larger than some $\lambda_{\alpha\beta}^{\text{intra}}$ because of the external magnetic field, which may bring two different bands with opposite spin very close to each other in energy; see, e.g., Fig. 2(b).

Having chosen the values of our parameters we can establish whether the system exhibits superconductivity. We determine the critical values of temperature T_c and exchange field h_c of our system for different values of the effective mass ratio γ by linearizing Eq. (2) with respect to $\Delta_{\alpha\alpha'}$, separately for interband ($\alpha \neq \alpha'$) and intraband ($\alpha = \alpha'$) superconducting pairing. The linearized gap equations are derived in Appendixes B and C. In the interband case we have the following equation:

$$\frac{1}{\lambda^{\text{inter}}} = \int_{-\omega_c}^{\omega_c} \frac{d\xi}{2(\tilde{\xi}_1 + \tilde{\xi}_2)} \sum_{\alpha=1,2} \left\{ \tanh \left[\frac{\beta_c}{2} (\tilde{\xi}_\alpha + h_c) \right] + \tanh \left[\frac{\beta_c}{2} (\tilde{\xi}_\alpha - h_c) \right] \right\}, \quad (4)$$

where $\beta_c = 1/T_c$, $\tilde{\xi}_1 = \xi - E_c$, and $\tilde{\xi}_2 = \gamma\xi + (\gamma - 1)\mu + E_c$. The interband critical parameters are the values satisfying Eq. (4). We note that by setting $E_c = 0$ and $\gamma = 1$, we get $\tilde{\xi}_1 = \tilde{\xi}_2 = \xi$, and Eq. (4) reduces to that of a single-band superconductor in external magnetic field, reported in Appendix B. In the intraband case we have the following system of equations:

$$\begin{pmatrix} \delta_1 \\ \delta_2 \end{pmatrix} \begin{pmatrix} \lambda_{11}I_1(T_c, h_c) - 1 & \lambda_{12}I_2(T_c, h_c) \\ \lambda_{21}I_1(T_c, h_c) & \lambda_{22}I_2(T_c, h_c) - 1 \end{pmatrix} = 0, \quad (5)$$

where the terms δ_α are defined through $\Delta_{\alpha\alpha} = \epsilon\delta_\alpha$, $\epsilon(T = T_c) = 0$, and

$$I_\alpha(T, h) = \int_{-\omega_c}^{\omega_c} \frac{d\xi}{4\tilde{\xi}_\alpha} \left\{ \tanh \left[\frac{\beta}{2} (\tilde{\xi}_\alpha + h) \right] + \tanh \left[\frac{\beta}{2} (\tilde{\xi}_\alpha - h) \right] \right\}, \quad (6)$$

with $\alpha = 1, 2$, and $\beta = 1/T$. The intraband critical parameters are found by setting to zero the determinant of the matrix in Eq. (5). More details on the procedure used to obtain the critical parameters are reported in Appendix E.

The results are shown in Fig. 3, displaying reentrant superconductivity. The figure shows the inter- and intraband superconducting domains, delimited by the $h_c(T)$ curves, for different values of γ ; the lines correspond to the critical values of temperature and exchange field, while the colored area identifies the superconducting region, with dark gray color identifying the interband regions and light gray the intraband. From Fig. 3, we immediately note a substantial difference between the superconductivity induced by each type of coupling. The intraband region develops around $h = 0$ for all the values of γ , with the highest critical temperature obtained in the absence of any external field. On the other hand, the interband regions show an interesting behavior: Except for the case $\gamma = 1.1$, they are not present in the zero-field case but around a certain finite value of h , thus their appearance is conditioned to the presence of an external field. Therefore,

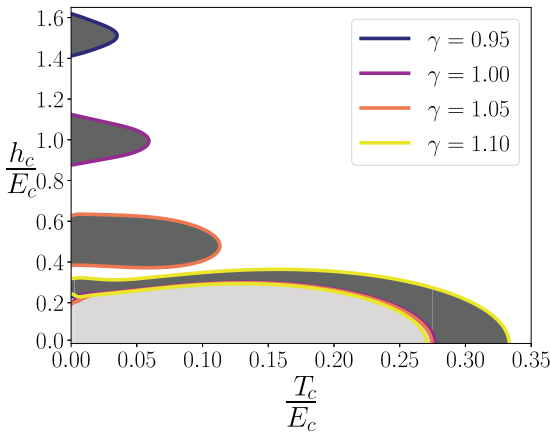


FIG. 3. Critical field h_c as a function of temperature T for different values of the band mass ratio γ , for $E_c = 0.05|\mu|$, $\lambda_{11}^{\text{intra}} = 0.3$, $\lambda_{22}^{\text{inter}} = \lambda_{22}^{\text{intra}} = 2\lambda_{12}^{\text{intra}} = 0.2$, and $\omega_c = 0.2|\mu|$. The dark (light) gray areas represent the region of interband (intra) superconducting coupling. Except for the case $\gamma = 1.1$, we note a reentrant superconductivity, with the two disconnected intra- and interband superconducting domains.

analyzing Fig. 3, we note that for certain values of γ it is possible to find two distinct/disconnected superconducting regions: the intraband one for low exchange field values and the interband one developing around substantially higher values of the exchange field. We note that the value $\gamma = 1.1$ as a certain significance, since it approximately corresponds to the point where the difference in band curvature compensates for the band separation $2E_c$, so that the Fermi momenta of the two bands become the same. Hence, any $h \neq 0$ has a detrimental effect for superconductivity.

These results can be explained by considering the band structure provided in Fig. 2 and the conditions for superconducting pairing to occur. In the BCS theory, Cooper pairs are formed by electrons with opposite momenta close to the Fermi momentum, and energies in a “shell” of width ω_c around the Fermi energy. Therefore, only electrons meeting these two criteria can form Cooper pairs. In a multiband system with spin-split bands, each band will have its own intervals of energies and momenta where this can be realized. When the intervals of two different bands overlap, Cooper pair formation among them is feasible. These overlap regions are represented by the rectangles in Fig. 2.

In the absence of spin splitting, and in the case of intraband pairing Cooper pair formation is of course always possible. When an external field is applied, instead, the spin-up and spin-down bands separate from each other, with their distance increasing with h , thus reducing the size of the overlap region where the formation of Cooper pairs is possible. Consequently, for purely intraband pairing, the critical temperature of the system has a maximum at zero field.

This picture changes when considering the case of interband pairing. While in the intraband case the exchange field pulls the two pairs of spin-split bands apart from each other, in the interband case it can have the opposite effect. Supercon-

ductivity involving interband pairs can result from different cases. With spin-split bands, we can have formation of Cooper pairs with (i), one electron in band 1 \downarrow and the other in 2 \uparrow and (ii), one electron in band 1 \uparrow and the other in band 2 \downarrow . Without spin splitting, instead, we have (iii), one electron in band 1 and the other in band 2. The choice of the parameters E_c , h , and γ determines the size of the overlap between the different bands and the size of the superconducting coupling constant λ^{inter} influences in which of the three cases superconductivity is realized.

Qualitatively, in each case the maximum in the size of the overlap, and thus in the superconducting critical temperature, occurs when the Fermi momenta of the two bands involved are equal to each other. Therefore, equating the Fermi momenta of the two bands for each of these cases, we can obtain, as a function of the other parameters, the value of h which determines the match of the momenta, allowing for Cooper pair formation. In case (i) we have $k_{F1\downarrow} = \sqrt{-2m(\mu + E_c - h)}$ and $k_{F2\uparrow} = \sqrt{-2m_1/\gamma(\mu - E_c + h)}$, equating the two we obtain:

$$h = \frac{\gamma - 1}{\gamma + 1}\mu + E_c. \quad (7)$$

In case (ii) we get $k_{F1\uparrow} = \sqrt{-2m_1(\mu + E_c + h)}$ and $k_{F2\downarrow} = \sqrt{-2m_1/\gamma(\mu - E_c - h)}$, yielding

$$h = -\frac{\gamma - 1}{\gamma + 1}\mu - E_c. \quad (8)$$

In case (iii) it is clear that $h = 0$.

We note that the value of h_c at which the interband superconducting domains present a maximum in T_c , depends only on the band parameters μ , E_c , and γ , and not on the superconducting coupling constants. These instead, together with other factors, such as, e.g., impurity scattering, influence the value of T_c , and therefore, whether superconductivity is realized.

Having determined the value of h which produces a maximum of the overlap in the different cases, with our choice of parameters we calculate numerically the critical temperature of the interband domains as a function of γ and h . The numerical results are plotted in Fig. 4 together with the theoretical prediction given by Eqs. (7) and (8).

We observe that for a good range of γ values ($0.95 \lesssim \gamma \lesssim 1.05$ and $1.15 \lesssim \gamma \lesssim 1.3$) the numerical results follow the analytical results and superconductivity comes from case (i) or case (ii), showing peaks in T_c for nonzero values of h . Instead, for $1.06 < \gamma < 1.14$, the superconducting domains are centered in $h = 0$, away from the analytical prediction, except for $\gamma \simeq 1.1$. Therefore, for this choice of parameters, and this range of γ values, the system favors superconductivity in the absence of spin splitting. Considering instead those points which do not exhibit superconductivity, for $\gamma < 0.95$ and $\gamma > 1.3$, we can state that the overlap between the bands is not large enough for the chosen value of the interband superconducting coupling constant. However, choosing a higher coupling would yield superconductivity for values of γ smaller than 0.95 and higher than 1.3.

Observing Fig. 4, we can see that peaks in T_c can be found for rather high values of the exchange field, up to $h \simeq 1.6E_c$. Therefore, when the system has both intraband and interband

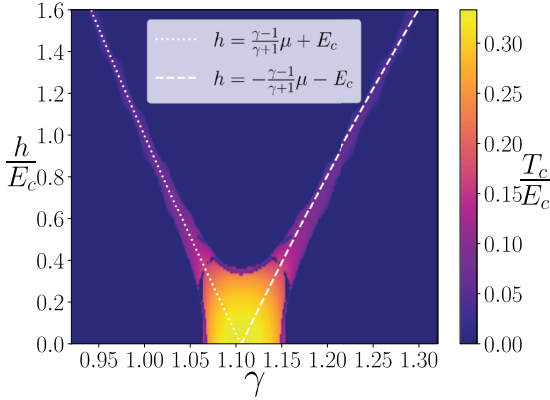


FIG. 4. Critical temperature of the interband superconducting domains as a function of γ and h , for $E_c = 0.05|\mu|$, $\lambda^{\text{inter}} = 0.2$, and $\omega_c = 0.2|\mu|$.

superconducting pairing, it can present two disconnected superconducting domains, one for low magnetic field due to the intraband pairing, and one for high magnetic field coming exclusively from interband pairing.

Finally, it is worth noting that the case of two electronlike bands would yield qualitatively similar results. The difference would be in the value of the band mass ratio γ at which the band overlap occurs. The case where there is a coupling between an electronlike and a holelike band is more complicated and would require a separate study.

IV. MINIMAL MODELS FOR TWO-DIMENSIONAL MgB_2 AND $\text{Ba}_{0.6}\text{K}_{0.4}\text{Fe}_2\text{As}_2$

The simple model presented in this work, for an ideal case, can be realized in a two-dimensional multiband superconductor with the application of an in-plane external magnetic field. On the material side many superconductors have been shown to have multiple holelike bands close to the Fermi energy at the Γ point. For instance, band structure calculations in few monolayers (MLs) MgB_2 in Ref. [59] have shown that each ML contributes to the band structure with a pair of σ bands, σ_1 , and σ_2 having different effective masses and chemical potential $\mu \simeq 500$ meV, with each pair of bands separated by $E_c \simeq 37.5$ meV. Therefore, we consider a minimal model for 2ML two-dimensional MgB_2 , taking only a pair of σ bands separated by 37.5 meV. In this case we retain the superconducting coupling constants representing scattering processes connecting interband to intraband Cooper pairs and *vice versa*, which were previously neglected. This means that in this case the intraband and interband order parameters are coupled, the resulting set of linearized gap equations is given in Appendix D. We reduce the indices of the $\lambda_{\alpha\alpha',\beta\beta'}$ coupling constants in the following way:

$$\alpha\alpha' \equiv \begin{cases} \alpha & \text{if } \alpha = \alpha', \\ 3 & \text{if } \alpha \neq \alpha'. \end{cases}$$

Therefore, the index 3 represents the interband pairing channel. Following Ref. [13] we consider the following su-

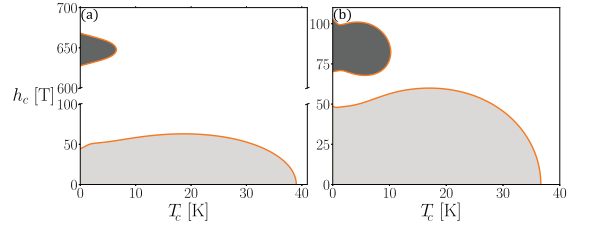


FIG. 5. Superconducting critical curves from a minimal model for (a) two-dimensional MgB_2 and (b) $\text{Ba}_{0.6}\text{K}_{0.4}\text{Fe}_2\text{As}_2$, with the highlighted high (dark gray) and low (light) field superconducting domains.

perconducting coupling matrix:

$$\hat{\lambda} = \begin{pmatrix} 0.275 & 0.032 & \lambda_{13} \\ 0.032 & 0.274 & \lambda_{23} \\ \lambda_{31} & \lambda_{32} & \lambda_{33} \end{pmatrix}, \quad (9)$$

where the upper 2×2 block represents the conventional superconducting coupling for a two-band system, the terms $\lambda_{\alpha 3}$ and $\lambda_{3\alpha}$, $\alpha = 1, 2$, represent interband Cooper pairs scattering to intraband Cooper pairs and *vice versa*. Finally λ_{33} represents purely interband scattering processes, and corresponds to the constant λ^{inter} . To obtain the correct value of the critical temperature at zero field ($T_c \approx 39$ K), we set $\lambda_{\alpha 3} = \lambda_{3\alpha} = 0.045$ and $\lambda_{33} = 0.2$. In Fig. 5(a) we report the superconducting domain delimited by the h_c - T_c critical curves. As in the previous section we find two disconnected superconducting domains for low and high magnetic field, with the high magnetic field one centered at a value $B = \mu_B E_c \approx 650$ T.

Also, among FeBS, many materials in the iron-pnictides family, like $\text{LaFeAsO}_{1-x}\text{F}_x$ [60–62] and $\text{Ba}_{1-x}\text{K}_x\text{Fe}_2\text{As}_2$ [63], exhibit multiple holelike bands at the Γ points, mainly originating from the 3-*d* Fe orbitals. Again, we consider a minimal model for optimally doped $\text{Ba}_{0.6}\text{K}_{0.4}\text{Fe}_2\text{As}_2$, with the two holelike α and β bands at the Γ point, separated by $E_c = 5$ meV [63]. Following Ref. [13] we take the superconducting coupling matrix to be

$$\hat{\lambda} = \begin{pmatrix} 0.51 & -0.005 & \lambda_{13} \\ -0.0025 & 0.39 & \lambda_{23} \\ \lambda_{31} & \lambda_{32} & \lambda_{33} \end{pmatrix}, \quad (10)$$

where the elements 12 and 21 are set to negative values as required by the s_{\pm} superconducting phase typical of FeBS. However, we note that the critical temperature and field of the system are not sensitive to this negative sign since the intraband gaps are effectively decoupled from the interband gap for the parameters used. Once more, we set $\lambda_{\alpha 3} = \lambda_{3\alpha} = 0.05$, $\alpha = 1, 2$, and $\lambda_{33} = 0.25$ to obtain the right critical temperature at zero field ($T_c \approx 36$ K) and report the results in Fig. 5(b). Again we note two disconnected superconducting domains with the high field one centered around $h_c \approx 90$ T.

V. CONCLUSIONS

In summary, we have considered a superconducting system with two relevant low-energy bands in the presence of a spin-splitting field. In the present treatment, we ignore or-

bital depairing effects and flux related phenomena, such as Abrikosov vortices, which would need to be added to the gap equation for estimates in bulk superconductors rather than thin films with an in-plane magnetic field. We have shown that the inclusion of interband superconducting pairing processes, i.e., allowing for the presence of Cooper pairs with the two electrons coming from two different bands, can result in reentrant superconducting domains centered at a high value of the spin-splitting field. These domains are exclusively due to the interband pairing and generally do not overlap with the superconducting domains originating from intraband pairing, which are always centered at zero spin-splitting field.

ACKNOWLEDGMENTS

Computations have been performed on the SAGA supercomputer provided by UNINETT Sigma2—the National Infrastructure for High Performance Computing and Data Storage in Norway. We acknowledge funding via the Outstanding Academic Fellows programme at NTNU, the Research Council of Norway, Grant No. 302315, as well as its Centres of Excellence funding scheme, Project No. 262633, QuSpin. Nordita is supported in part by NordForsk.

APPENDIX A: GREEN'S FUNCTION OF THE SYSTEM

The Green's function of the system is obtained by inverting Eq. (3) in the main text:

$$\mathcal{G}_0(\mathbf{k}, \omega_n) = \frac{1}{\det \mathcal{G}_0^{-1}} \begin{pmatrix} \hat{\mathcal{A}}^{11}(\mathbf{k}, \tilde{\omega}_n) & \hat{\mathcal{A}}^{12}(\mathbf{k}, \tilde{\omega}_n) \\ \hat{\mathcal{A}}^{21}(\mathbf{k}, \tilde{\omega}_n) & \hat{\mathcal{A}}^{22}(\mathbf{k}, \tilde{\omega}_n) \end{pmatrix}. \quad (\text{A1})$$

where $\det \mathcal{G}_0^{-1} = (\tilde{\omega}_n^2 + E_+^2)(\tilde{\omega}_n^2 + E_-^2)$ with $\tilde{\omega}_n = \omega_n - ih$. The two branches have the following expression:

$$E_{\pm}^2 = \frac{1}{2} \{ \tilde{E}_1^2 + \tilde{E}_2^2 + 2|\Delta_{12}|^2 \pm [(\tilde{E}_1^2 + \tilde{E}_2^2 + 2|\Delta_{12}|^2)^2 - 4(\tilde{E}_1^2 \tilde{E}_2^2 + |\Delta_{12}|^4 + 2\tilde{\xi}_1 \tilde{\xi}_2 |\Delta_{12}|^2 - 2\text{Re}\{\Delta_{11} \Delta_{22} \Delta_{12}^*\})]^{1/2} \}. \quad (\text{A2})$$

The components of the 2×2 matrices $\hat{\mathcal{A}}^{\alpha\beta}(\mathbf{k}, \omega_n)$ are

$$[\hat{\mathcal{A}}^{11}(\mathbf{k}, \tilde{\omega}_n)]_{11} = -(i\tilde{\omega}_n + \tilde{\xi}_1)(\tilde{\omega}_n^2 + \tilde{\xi}_2^2 + |\Delta_{22}|^2) - |\Delta_{12}|^2(i\tilde{\omega}_n + \tilde{\xi}_2), \quad (\text{A3a})$$

$$[\hat{\mathcal{A}}^{11}(\mathbf{k}, \tilde{\omega}_n)]_{12} = \Delta_{11}(\tilde{\omega}_n^2 + \tilde{\xi}_2^2 + |\Delta_{22}|^2) - \Delta_{12}^2 \Delta_{22}^*, \quad (\text{A3b})$$

$$[\hat{\mathcal{A}}^{12}(\mathbf{k}, \tilde{\omega}_n)]_{11} = (i\tilde{\omega}_n + \tilde{\xi}_1)\Delta_{12}\Delta_{22}^* + \Delta_{11}\Delta_{12}^*(i\tilde{\omega}_n + \tilde{\xi}_2), \quad (\text{A3c})$$

The expression of the anomalous Green's function is

$$F^{12}(\mathbf{k}, \omega_n - ih) = -\frac{(i\tilde{\omega}_n + \tilde{\xi}_1 + h)(i\tilde{\omega}_n - \tilde{\xi}_2 + h) - |\Delta_{12}|^2}{[(\omega_n - ih)^2 + E_+^2][(\omega_n - ih)^2 + E_-^2]} \Delta_{12}. \quad (\text{B5})$$

$$[\hat{\mathcal{A}}^{12}(\mathbf{k}, \tilde{\omega}_n)]_{12} = -(i\tilde{\omega}_n + \tilde{\xi}_1)(i\tilde{\omega}_n - \tilde{\xi}_2) - |\Delta_{12}|^2 \Delta_{12} - \Delta_{11}\Delta_{12}^* \Delta_{22}, \quad (\text{A3d})$$

$$[\hat{\mathcal{A}}^{21}(\mathbf{k}, \tilde{\omega}_n)]_{11} = [\hat{\mathcal{A}}^{12}(\mathbf{k}, -\tilde{\omega}_n^*)]_{11}^*, \quad (\text{A3e})$$

$$[\hat{\mathcal{A}}^{21}(\mathbf{k}, \tilde{\omega}_n)]_{12} = [\hat{\mathcal{A}}^{12}(\mathbf{k}, -\tilde{\omega}_n)]_{12}, \quad (\text{A3f})$$

$$[\hat{\mathcal{A}}^{\alpha\beta}(\mathbf{k}, \tilde{\omega}_n)]_{22} = -[\hat{\mathcal{A}}^{\alpha\beta}(\mathbf{k}, -\tilde{\omega}_n)]_{11}, \quad (\text{A3g})$$

$$[\hat{\mathcal{A}}^{\alpha\beta}(\mathbf{k}, \tilde{\omega}_n)]_{21} = [\hat{\mathcal{A}}^{\alpha\beta}(\mathbf{k}, \tilde{\omega}_n^*)]_{12}^*. \quad (\text{A3h})$$

where $\tilde{E}_\alpha = \sqrt{\tilde{\xi}_\alpha^2 + |\Delta_{\alpha\alpha}|^2}$, $\alpha = 1, 2$, with $\tilde{\xi}_1 = \xi_{\mathbf{k}}^{(1)} - E_c$, $\tilde{\xi}_2 = \xi_{\mathbf{k}}^{(2)} + E_c$.

The elements of $\hat{\mathcal{A}}^{22}(\mathbf{k}, \omega_n)$ are obtained by exchanging the indices 1 and 2 in the expressions for the elements of $\hat{\mathcal{A}}^{11}(\mathbf{k}, \omega_n)$. The inter- and intraband normal and anomalous Green's functions are given by

$$G^{\alpha\beta}(\mathbf{k}, \tilde{\omega}_n) = \frac{[\hat{\mathcal{A}}^{\alpha\beta}(\mathbf{k}, \tilde{\omega}_n)]_{11}}{(\tilde{\omega}_n^2 + E_+^2)(\tilde{\omega}_n^2 + E_-^2)}, \quad (\text{A4a})$$

$$F^{\alpha\beta}(\mathbf{k}, \tilde{\omega}_n) = \frac{[\hat{\mathcal{A}}^{\alpha\beta}(\mathbf{k}, \tilde{\omega}_n)]_{12}}{(\tilde{\omega}_n^2 + E_+^2)(\tilde{\omega}_n^2 + E_-^2)}. \quad (\text{A4b})$$

APPENDIX B: GAP EQUATION FOR THE INTERBAND ORDER PARAMETER

We derive the gap equation in the case of purely interband coupling, i.e., Cooper pairs formed exclusively by electrons in different bands. To do so we consider the following form of the coupling matrix:

$$g_{\alpha\alpha'\beta\beta'} = \begin{cases} g^{\text{inter}}, & \text{if } \alpha \neq \alpha', \beta \neq \beta' \\ 0, & \text{otherwise.} \end{cases} \quad (\text{B1})$$

Inserting this in Eq. (2) we obtain the following gap equation:

$$\Delta_{12} = \frac{g^{\text{inter}} T}{V} \sum_{k\omega_n} [F^{12}(\mathbf{k}, \omega_n - ih) + F^{21}(\mathbf{k}, \omega_n - ih)]. \quad (\text{B2})$$

Setting $\Delta_{11} = \Delta_{22} = 0$ in Eq. (A2) we get

$$E_{\pm} = \frac{\tilde{\xi}_1 - \tilde{\xi}_2}{2} \pm E_{12}, \quad (\text{B3})$$

with $E_{12} = \sqrt{(\tilde{\xi}_1 + \tilde{\xi}_2)^2/4 + |\Delta_{12}|^2}$. Using the relation, defined in the main text, between the two bands $\xi_{\mathbf{k}}^{(2)} = \gamma \xi_{\mathbf{k}}^{(1)} + (\gamma - 1)\mu$, we can write

$$E_{\pm} = \frac{(\xi_{\mathbf{k}}^{(1)} + \mu)(1 - \gamma)}{2} - E_c \pm E_{12}, \quad (\text{B4a})$$

$$E_{12} = \sqrt{\left(\frac{\xi_{\mathbf{k}}^{(1)}(1 + \gamma) - \mu(1 - \gamma)}{2} \right)^2 + |\Delta_{12}|^2}. \quad (\text{B4b})$$

After summing over the Matsubara frequency the gap equation Eq. (B2) takes the following form:

$$\begin{aligned} \frac{1}{g^{\text{inter}}} &= -\frac{1}{V} \sum_{\mathbf{k}} \frac{1}{2E_{12}} [n_F(E_+ - h) - n_F(-E_+ - h) - n_F(E_- - h) + n_F(-E_- - h)] \\ &= \frac{1}{V} \sum_{\mathbf{k}} \sum_{s=\pm} \frac{s}{4E_{12}} \left\{ \tanh \left[\frac{\beta}{2}(E_s + h) \right] + \tanh \left[\frac{\beta}{2}(E_s - h) \right] \right\}, \end{aligned} \quad (\text{B6})$$

where $n_F(\varepsilon) = (e^{\beta\varepsilon} + 1)^{-1}$ is the Fermi function and we have used

$$\begin{aligned} n_F(E_{\pm} - h) - n_F(-E_{\pm} - h) &= -\frac{\sinh \beta E_{\pm}}{\cosh \beta E_{\pm} + \cosh \beta h} \\ &= -\frac{1}{2} \left\{ \tanh \left[\frac{\beta}{2}(E_{\pm} + h) \right] + \tanh \left[\frac{\beta}{2}(E_{\pm} - h) \right] \right\}. \end{aligned}$$

We now switch from the summation over momenta to integral over the energy: $V^{-1} \sum_{\mathbf{k}} (\cdot) = \int d\xi_1 N_1(\xi_1) (\cdot)$, where $N_1(\xi_1)$ is the density of state of band 1. We then approximate the density of state with its value at the Fermi level $N_1(\xi_1) \simeq N_1(0)$ and, defining the dimensionless superconducting coupling constant as done in the main text, we obtain the final expression for the interband gap equation:

$$\frac{1}{\lambda^{\text{inter}}} = \int_{-\omega_c}^{\omega_c} d\xi \sum_{s=\pm} \frac{s}{4E_{12}(\xi)} \left\{ \tanh \left[\frac{\beta}{2}(E_s(\xi) + h) \right] + \tanh \left[\frac{\beta}{2}(E_s(\xi) - h) \right] \right\}. \quad (\text{B7})$$

To obtain critical temperature and critical field, we linearize Eq. (B7) with respect to Δ_{12} . The equation then takes the following simple form:

$$\frac{1}{\lambda^{\text{inter}}} = \int_{-\omega_c}^{\omega_c} \frac{d\xi}{2(\tilde{\xi}_1 + \tilde{\xi}_2)} \sum_{\alpha=1,2} \left\{ \tanh \left[\frac{\beta_c}{2}(\tilde{\xi}_{\alpha} + h_c) \right] + \tanh \left[\frac{\beta_c}{2}(\tilde{\xi}_{\alpha} - h_c) \right] \right\}. \quad (\text{B8})$$

We note that by setting $E_c = 0$ and $\gamma = 1$, we get $\tilde{\xi}_1 = \tilde{\xi}_2 = \xi$, the system reduces to a single-band superconductor. Therefore, Eq. (B8) takes the usual form for a single-band spin-split superconductor:

$$\frac{1}{\lambda} = \int_{-\omega_c}^{\omega_c} \frac{d\xi}{2\xi} \left\{ \tanh \left[\frac{\beta_c}{2}(\xi + h_c) \right] + \tanh \left[\frac{\beta_c}{2}(\xi - h_c) \right] \right\}. \quad (\text{B9})$$

APPENDIX C: GAP EQUATION FOR THE INTRABAND ORDER PARAMETERS

In order to consider purely intraband coupling we take the following form of the coupling matrix:

$$g_{\alpha\alpha'\beta\beta'} = \begin{cases} g_{\alpha\beta}^{\text{intra}}, & \text{if } \alpha = \alpha', \beta = \beta' \\ 0, & \text{otherwise} \end{cases}. \quad (\text{C1})$$

Using this expression in Eq. (2) we get the following coupled gap equations:

$$\Delta_{11} = \frac{g_{11}^{\text{intra}} T}{V} \sum_{\mathbf{k}\omega_n} F^{11}(\mathbf{k}, \omega_n - ih) + \frac{g_{12}^{\text{intra}} T}{V} \sum_{\mathbf{k}\omega_n} F^{22}(\mathbf{k}, \omega_n - ih), \quad (\text{C2a})$$

$$\Delta_{22} = \frac{g_{21}^{\text{intra}} T}{V} \sum_{\mathbf{k}\omega_n} F^{11}(\mathbf{k}, \omega_n - ih) + \frac{g_{22}^{\text{intra}} T}{V} \sum_{\mathbf{k}\omega_n} F^{22}(\mathbf{k}, \omega_n - ih). \quad (\text{C2b})$$

The two branches of the BCS quasiparticle spectrum are simply $E_+ = E_{11}$ and $E_- = E_{22}$ and we get the following expression for the anomalous Green's function:

$$F^{\alpha\alpha}(\mathbf{k}, \omega_n - ih) = \frac{\Delta_{\alpha\alpha}}{(i\omega_n + E_{\alpha\alpha} + h)(i\omega_n - E_{\alpha\alpha} + h)}. \quad (\text{C3})$$

Following the same steps as in the previous section we finally get the following:

$$\Delta_{\alpha\alpha} = \sum_{\beta=1,2} \lambda_{\alpha\beta} \Delta_{\beta\beta} \int_{-\omega_n}^{\omega_n} \frac{d\xi_{\beta}}{4E_{\beta\beta}} \left(\tanh \frac{E_{\beta\beta} + h}{2T} + \tanh \frac{E_{\beta\beta} - h}{2T} \right). \quad (\text{C4})$$

Linearizing Eq. (C4) with respect to the order parameters again allows one to obtain the superconducting critical temperature and critical field. We set $\Delta_{\alpha\alpha} = \epsilon\delta_{\alpha}$, where $\epsilon(T = T_c) = 0$, and obtain the following system:

$$\begin{pmatrix} \delta_1 \\ \delta_2 \end{pmatrix} \begin{pmatrix} \lambda_{11}I_1(T_c, h_c) - 1 & \lambda_{12}I_2(T_c, h_c) \\ \lambda_{21}I_1(T_c, h_c) & \lambda_{22}I_2(T_c, h_c) - 1 \end{pmatrix} = 0, \quad (\text{C5})$$

where

$$I_{\alpha}(T, h) = \int_{-\omega_c}^{\omega_c} \frac{d\xi}{4\tilde{\xi}_{\alpha}} \left\{ \tanh \left[\frac{\beta}{2} (\tilde{\xi}_{\alpha} + h) \right] + \tanh \left[\frac{\beta}{2} (\tilde{\xi}_{\alpha} - h) \right] \right\}, \quad (\text{C6})$$

with $\alpha = 1, 2$. The critical parameters are found by setting to zero the determinant of the matrix in Eq. (C5).

APPENDIX D: LINEARIZED GAP EQUATION FOR COUPLED INTERBAND AND INTRABAND ORDER PARAMETERS

When including the superconducting coupling constants representing scattering processes connecting interband to intraband Cooper pairs, the gap equations for the interband and intraband order parameters become coupled. In this case the linearized gap equation yields the following system:

$$\begin{pmatrix} \delta_1 \\ \delta_2 \\ \delta_3 \end{pmatrix} \begin{pmatrix} \lambda_{11}I_1(T_c, h_c) - 1 & \lambda_{12}I_2(T_c, h_c) & \lambda_{13}I_3(T_c, h_c) \\ \lambda_{21}I_1(T_c, h_c) & \lambda_{22}I_2(T_c, h_c) - 1 & \lambda_{23}I_3(T_c, h_c) \\ \lambda_{31}I_1(T_c, h_c) & \lambda_{32}I_2(T_c, h_c) & \lambda_{33}I_3(T_c, h_c) - 1 \end{pmatrix} = 0, \quad (\text{D1})$$

where the constants $\lambda_{\alpha 3}$ and $\lambda_{3\alpha}$, with $\alpha = 1, 2$, represent the scattering processes connecting interband to intraband Cooper pairs, and λ_{33} corresponds to λ^{inter} in the main text. The terms I_{α} , $\alpha = 1, 2$ are given in Eq. (C6), while I_3 corresponds to the energy integral in Eq. (B8). Again, the critical parameters are found by setting to zero the determinant of the matrix in Eq. (D1).

APPENDIX E: CRITICAL TEMPERATURE AND CRITICAL FIELD

We presented the linearized equations [Eqs. (B8) and (C5)] allowing one to obtain the curve $h_c(T)$ for the interband and intraband domains, respectively. A remark here is needed, since as is clear from Fig. 3 in the main text, in the interband curves, to each temperature (except the maximum one), correspond two solutions for h . This is a problem for the numerical solver. To address this, first we find the value of the critical field corresponding to the maximum temperature of the superconducting curve. This can be done through analytical considerations as explained in the main text [see Eqs. (7) and (8)]. Having obtained this value we then find separately a solution for the critical field higher and lower than this value, as a function of the temperature.

-
- [1] G. Blumberg, A. Mialitsin, B. S. Dennis, M. V. Klein, N. D. Zhigadlo, and J. Karpinski, Observation of Leggett's Collective Mode in a Multiband MgB₂ Superconductor, *Phys. Rev. Lett.* **99**, 227002 (2007).
- [2] F. Giorgianni, T. Cea, C. Vicario, C. P. Hauri, W. K. Withanage, X. Xi, and L. Benfatto, Leggett mode controlled by light pulses, *Nat. Phys.* **15**, 341 (2019).
- [3] S. K. Ghosh, M. Smidman, T. Shang, J. F. Annett, A. D. Hillier, J. Quintanilla, and H. Yuan, Recent progress on superconductors with time-reversal symmetry breaking, *J. Phys.: Condens. Matter* **33**, 033001 (2021).
- [4] H. Suhl, B. T. Matthias, and L. R. Walker, Bardeen-Cooper-Schrieffer Theory of Superconductivity in the Case of Overlapping Bands, *Phys. Rev. Lett.* **3**, 552 (1959).
- [5] V. A. Moskalenko, The theory of superconductivity with overlapping energy bands, *Sov. Phys. Usp.* **17**, 450 (1974).
- [6] F. Korchorbé and M. Palistrant, Superconductivity in a two-band system with low carrier density, *Zh. Eksp. Teor. Fiz.* **104**, 3084 (1993) [*JETP* **77**, 442 (1993)].
- [7] J. Tahir-Kheli, Interband pairing theory of superconductivity, *Phys. Rev. B* **58**, 12307 (1998).
- [8] S. Caprara, J. Biscaras, N. Bergeal, D. Bucheli, S. Hurand, C. Feuillet-Palma, A. Rastogi, R. C. Budhani, J. Lesueur, and M. Grilli, Multiband superconductivity and nanoscale inhomogeneity at oxide interfaces, *Phys. Rev. B* **88**, 020504(R) (2013).
- [9] M. Marciani, L. Fanfarillo, C. Castellani, and L. Benfatto, Leggett modes in iron-based superconductors as a probe of time-reversal symmetry breaking, *Phys. Rev. B* **88**, 214508 (2013).
- [10] L. Komendová, A. V. Balatsky, and A. M. Black-Schaffer, Experimentally observable signatures of odd-frequency pairing in multiband superconductors, *Phys. Rev. B* **92**, 094517 (2015).
- [11] T. Cea and L. Benfatto, Signature of the Leggett mode in the A_{1g} Raman response: From MgB₂ to iron-based superconductors, *Phys. Rev. B* **94**, 064512 (2016).
- [12] L. Komendová and A. M. Black-Schaffer, Odd-Frequency Superconductivity in Sr₂RuO₄ Measured by Kerr Rotation, *Phys. Rev. Lett.* **119**, 087001 (2017).
- [13] A. A. Vargas-Paredes, A. A. Shanenko, A. Vagov, M. V. Milošević, and A. Perali, Crossband versus intraband pairing in superconductors: Signatures and consequences of the interplay, *Phys. Rev. B* **101**, 094516 (2020).
- [14] V. Barzykin, Magnetic-field-induced gapless state in multiband superconductors, *Phys. Rev. B* **79**, 134517 (2009).
- [15] M. Iskin and C. A. R. Sá de Melo, BCS-BEC crossover of collective excitations in two-band superfluids, *Phys. Rev. B* **72**, 024512 (2005).

- [16] M. Iskin and C. A. R. Sá de Melo, Two-band superfluidity from the BCS to the BEC limit, *Phys. Rev. B* **74**, 144517 (2006).
- [17] Y. Yerin, H. Tajima, P. Pieri, and A. Perali, Coexistence of giant Cooper pairs with a bosonic condensate and anomalous behavior of energy gaps in the BCS-BEC crossover of a two-band superfluid Fermi gas, *Phys. Rev. B* **100**, 104528 (2019).
- [18] A. M. Black-Schaffer and A. V. Balatsky, Odd-frequency superconducting pairing in multiband superconductors, *Phys. Rev. B* **88**, 104514 (2013).
- [19] E. Taylor and C. Kallin, Intrinsic Hall Effect in a Multiband Chiral Superconductor in the Absence of an External Magnetic Field, *Phys. Rev. Lett.* **108**, 157001 (2012).
- [20] G. N. Bremm, M. A. Continentino, and T. Micklitz, BCS-BEC crossover in a two-band superconductor with odd-parity hybridization, *Phys. Rev. B* **104**, 094514 (2021).
- [21] J. Nagamatsu, N. Nakagawa, T. Muranaka, Y. Zenitani, and J. Akimitsu, Superconductivity at 39 K in magnesium diboride, *Nature (London)* **410**, 63 (2001).
- [22] R. Zhi-An, L. Wei, Y. Jie, Y. Wei, S. Xiao-Li, Zheng-Cai, C. Guang-Can, D. Xiao-Li, S. Li-Ling, Z. Fang, and Z. Zhong-Xian, Superconductivity at 55 K in iron-based f-doped layered quaternary compound $\text{Sm}[\text{O}_{1-x}\text{F}_x]\text{FeAs}$, *Chin. Phys. Lett.* **25**, 2215 (2008).
- [23] Q.-Y. Wang, Z. Li, W.-H. Zhang, Z.-C. Zhang, J.-S. Zhang, W. Li, H. Ding, Y.-B. Ou, P. Deng, K. Chang, J. Wen, C.-L. Song, K. He, J.-F. Jia, S.-H. Ji, Y.-Y. Wang, L.-L. Wang, X. Chen, X.-C. Ma, and Q.-K. Xue, Interface-induced high-temperature superconductivity in single unit-cell FeSe films on SrTiO_3 , *Chin. Phys. Lett.* **29**, 037402 (2012).
- [24] M. Xu, H. Kitazawa, Y. Takano, J. Ye, K. Nishida, H. Abe, A. Matsushita, N. Tsujii, and G. Kido, Anisotropy of superconductivity from MgB_2 single crystals, *Appl. Phys. Lett.* **79**, 2779 (2001).
- [25] V. Braccini, A. Gurevich, J. E. Giенcke, M. C. Jewell, C. B. Eom, D. C. Larbalestier, A. Pogrebnnyakov, Y. Cui, B. T. Liu, Y. F. Hu, J. M. Redwing, Q. Li, X. X. Xi, R. K. Singh, R. Gandikota, J. Kim, B. Wilkens, N. Newman, J. Rowell, B. Moeckly *et al.*, High-field superconductivity in alloyed MgB_2 thin films, *Phys. Rev. B* **71**, 012504 (2005).
- [26] A. S. Sefat, M. A. McGuire, B. C. Sales, R. Jin, J. Y. Howe, and D. Mandrus, Electronic correlations in the superconductor $\text{LaFeAsO}_{0.89}\text{F}_{0.11}$ with low carrier density, *Phys. Rev. B* **77**, 174503 (2008).
- [27] G. F. Chen, Z. Li, G. Li, J. Zhou, D. Wu, J. Dong, W. Z. Hu, P. Zheng, Z. J. Chen, H. Q. Yuan, J. Singleton, J. L. Luo, and N. L. Wang, Superconducting Properties of the Fe-Based Layered Superconductor $\text{LaFeAsO}_{0.9}\text{F}_{0.1-\delta}$, *Phys. Rev. Lett.* **101**, 057007 (2008).
- [28] Y. Jia, P. Cheng, L. Fang, H. Luo, H. Yang, C. Ren, L. Shan, C. Gu, and H.-H. Wen, Critical fields and anisotropy of $\text{NdFeAsO}_{0.82}\text{F}_{0.18}$ single crystals, *Appl. Phys. Lett.* **93**, 032503 (2008).
- [29] M. M. Altarawneh, K. Collar, C. H. Mielke, N. Ni, S. L. Bud'ko, and P. C. Canfield, Determination of anisotropic H_{c2} up to 60 T in $\text{Ba}_{0.55}\text{K}_{0.45}\text{Fe}_2\text{As}_2$ single crystals, *Phys. Rev. B* **78**, 220505(R) (2008).
- [30] H. Q. Yuan, J. Singleton, F. F. Balakirev, S. A. Baily, G. F. Chen, J. L. Luo, and N. L. Wang, Nearly isotropic superconductivity in $(\text{Ba},\text{K})\text{Fe}_2\text{As}_2$, *Nature (London)* **457**, 565 (2009).
- [31] M. P. Smylie, A. E. Koshelev, K. Willa, R. Willa, W.-K. Kwok, J.-K. Bao, D. Y. Chung, M. G. Kanatzidis, J. Singleton, F. F. Balakirev, H. Hebbeker, P. Niraula, E. Bokari, A. Kayani, and U. Welp, Anisotropic upper critical field of pristine and proton-irradiated single crystals of the magnetically ordered superconductor $\text{RbEuFe}_4\text{As}_4$, *Phys. Rev. B* **100**, 054507 (2019).
- [32] J. Linder and J. W. A. Robinson, Superconducting spintronics, *Nat. Phys.* **11**, 307 (2015).
- [33] A. M. Clogston, Upper Limit for the Critical Field in Hard Superconductors, *Phys. Rev. Lett.* **9**, 266 (1962).
- [34] B. S. Chandrasekhar, A note on the maximum critical field of highfield superconductors, *Appl. Phys. Lett.* **1**, 7 (1962).
- [35] A. Gurevich, Enhancement of the upper critical field by non-magnetic impurities in dirty two-gap superconductors, *Phys. Rev. B* **67**, 184515 (2003).
- [36] A. Gurevich, Limits of the upper critical field in dirty two-gap superconductors, *Physica C: Superconductivity* **456**, 160 (2007).
- [37] S. Ran, C. Eckberg, Q.-P. Ding, Y. Furukawa, T. Metz, S. R. Saha, I.-L. Liu, M. Zic, H. Kim, J. Paglione, and N. P. Butch, Nearly ferromagnetic spin-triplet superconductivity, *Science* **365**, 684 (2019).
- [38] A. Ptok and D. Crivelli, The fulde-ferrell-larkin-ovchinnikov state in pnictides, *J. Low Temp. Phys.* **172**, 226 (2013).
- [39] A. Ptok, Influence of s_{\pm} symmetry on unconventional superconductivity in pnictides above the Pauli limit – two-band model study, *Eur. Phys. J. B* **87**, 2 (2014).
- [40] X. Xi, Z. Wang, W. Zhao, J.-H. Park, K. T. Law, H. Berger, L. Forró, J. Shan, and K. F. Mak, Ising pairing in superconducting NbSe_2 atomic layers, *Nat. Phys.* **12**, 139 (2016).
- [41] H. Nam, H. Chen, T. Liu, J. Kim, C. Zhang, J. Yong, T. R. Lemberger, P. A. Kratz, J. R. Kirtley, K. Moler, P. W. Adams, A. H. MacDonald, and C.-K. Shih, Ultrathin two-dimensional superconductivity with strong spin-orbit coupling, *Proc. Natl. Acad. Sci.* **113**, 10513 (2016).
- [42] I. V. Bobkova and A. M. Bobkov, Recovering the superconducting state via spin accumulation above the pair-breaking magnetic field of superconductor/ferromagnet multilayers, *Phys. Rev. B* **84**, 140508(R) (2011).
- [43] J. A. Ouassou, T. D. Vethaak, and J. Linder, Voltage-induced thin-film superconductivity in high magnetic fields, *Phys. Rev. B* **98**, 144509 (2018).
- [44] S. V. Shulga, S.-L. Drechsler, G. Fuchs, K.-H. Müller, K. Winzer, M. Heinecke, and K. Krug, Upper Critical Field Peculiarities of Superconducting $\text{YNi}_2\text{B}_2\text{C}$ and $\text{LuNi}_2\text{B}_2\text{C}$, *Phys. Rev. Lett.* **80**, 1730 (1998).
- [45] A. Ghanbari, E. Erlandsen, A. Sudbø, and J. Linder, Going beyond the Chandrasekhar-Clogston limit in a flatband superconductor, *Phys. Rev. B* **105**, L060501 (2022).
- [46] S. Hörhold, J. Graf, M. Marganska, and M. Grifoni, Two bands Ising superconductivity from Coulomb interactions in monolayer NbSe_2 , *2D Mater.* **10**, 025008 (2023).
- [47] Y. Yerin, S.-L. Drechsler, and G. Fuchs, Ginzburg-landau analysis of the critical temperature and the upper critical field for three-band superconductors, *J. Low Temp. Phys.* **173**, 247 (2013).
- [48] A. M. Marques, R. G. Dias, M. A. N. Araújo, and F. D. R. Santos, In-plane magnetic field versus temperature phase diagram of a quasi-2d frustrated multiband superconductor, *Supercond. Sci. Technol.* **28**, 045021 (2015).

- [49] M. Kuzmanović, T. Dvir, D. LeBoeuf, S. Ilić, M. Haim, D. Möckli, S. Kramer, M. Khodas, M. Houzet, J. S. Meyer, M. April, H. Steinberg, and C. H. L. Quay, Tunneling spectroscopy of few-monolayer NbSe₂ in high magnetic fields: Triplet superconductivity and Ising protection, *Phys. Rev. B* **106**, 184514 (2022).
- [50] S. Ghannadzadeh, J. D. Wright, F. R. Foronda, S. J. Blundell, S. J. Clarke, and P. A. Goddard, Upper critical field of NaFe_{1-x}Co_xAs superconductors, *Phys. Rev. B* **89**, 054502 (2014).
- [51] X. Xing, W. Zhou, J. Wang, Z. Zhu, Y. Zhang, N. Zhou, B. Qian, X. Xu, and Z. Shi, Two-band and Pauli-limiting effects on the upper critical field of 112-type iron pnictide superconductors, *Sci. Rep.* **7**, 45943 (2017).
- [52] L. E. Chow, K. Y. Yip, M. Pierre, S. W. Zeng, Z. T. Zhang, T. Heil, J. Deuschle, P. Nandi, S. K. Sudheesh, Z. S. Lim, Z. Y. Luo, M. Nardone, A. Zitouni, P. A. van Aken, M. Goiran, S. K. Goh, W. Escoffier, and A. Ariando, Pauli-limit violation in lanthanide infinite-layer nickelate superconductors, [arXiv:2204.12606](https://arxiv.org/abs/2204.12606) 2022.
- [53] Y. Cao, J. M. Park, K. Watanabe, T. Taniguchi, and P. Jarillo-Herrero, Pauli-limit violation and re-entrant superconductivity in moiré graphene, *Nature (London)* **595**, 526 (2021).
- [54] L. Balicas, J. S. Brooks, K. Storr, S. Uji, M. Tokumoto, H. Tanaka, H. Kobayashi, A. Kobayashi, V. Barzykin, and L. P. Gor'kov, Superconductivity in an Organic Insulator at Very High Magnetic Fields, *Phys. Rev. Lett.* **87**, 067002 (2001).
- [55] S. Uji, H. Shinagawa, T. Terashima, T. Yakabe, Y. Terai, M. Tokumoto, A. Kobayashi, H. Tanaka, and H. Kobayashi, Magnetic-field-induced superconductivity in a two-dimensional organic conductor, *Nature (London)* **410**, 908 (2001).
- [56] H. W. Meul, C. Rossel, M. Decroux, O. Fischer, G. Remenyi, and A. Briggs, Observation of Magnetic-Field-Induced Superconductivity, *Phys. Rev. Lett.* **53**, 497 (1984).
- [57] F. Lévy, I. Sheikin, B. Grenier, and A. D. Huxley, Magnetic field-induced superconductivity in the ferromagnet URhGe, *Science* **309**, 1343 (2005).
- [58] G. Sarma, On the influence of a uniform exchange field acting on the spins of the conduction electrons in a superconductor, *J. Phys. Chem. Solids* **24**, 1029 (1963).
- [59] J. Bekaert, L. Bignardi, A. Aperis, P. van Abswoude, C. Mattevi, S. Gorovikov, L. Petaccia, A. Goldoni, B. Partoens, P. M. Oppeneer, F. M. Peeters, M. V. Milošević, P. Rudolf, and C. Cepek, Free surfaces recast superconductivity in few-monolayer MgB₂: Combined first-principles and ARPES demonstration, *Sci. Rep.* **7**, 14458 (2017).
- [60] G. Xu, W. Ming, Y. Yao, X. Dai, S.-C. Zhang, and Z. Fang, Doping-dependent phase diagram of LaOMAs (M = V–Cu) and electron-type superconductivity near ferromagnetic instability, *Europhys. Lett.* **82**, 67002 (2008).
- [61] I. I. Mazin, D. J. Singh, M. D. Johannes, and M. H. Du, Unconventional Superconductivity with a Sign Reversal in the Order Parameter of LaFeAsO_{1-x}F_x, *Phys. Rev. Lett.* **101**, 057003 (2008).
- [62] K. Haule, J. H. Shim, and G. Kotliar, Correlated Electronic Structure of LaO_{1-x}F_xFeAs, *Phys. Rev. Lett.* **100**, 226402 (2008).
- [63] H. Ding, K. Nakayama, P. Richard, S. Souma, T. Sato, T. Takahashi, M. Neupane, Y.-M. Xu, Z.-H. Pan, A. V. Fedorov, Z. Wang, X. Dai, Z. Fang, G. F. Chen, J. L. Luo, and N. L. Wang, Electronic structure of optimally doped pnictide Ba_{0.6}K_{0.4}Fe₂As₂: A comprehensive angle-resolved photoemission spectroscopy investigation, *J. Phys.: Condens. Matter* **23**, 135701 (2011).

ISBN 978-82-326-7292-9 (printed ver.)
ISBN 978-82-326-7291-2 (electronic ver.)
ISSN 1503-8181 (printed ver.)
ISSN 2703-8084 (online ver.)